MULTI-SCALE MODELLING OF GEOMECHANICAL BEHAVIOUR USING VCFEM

MULTI-SCALE MODELLING OF GEOMECHANICAL BEHAVIOUR USING THE VORONOI CELL FINITE ELEMENT METHOD (VCFEM) AND FINITE-DISCRETE ELEMENT METHOD (VCFEM-DEM)

By BRANDON KARCHEWSKI, B.ENG.MGMT

A Thesis Submitted to the School of Graduate Studies

in Partial Fulfillment of the Requirements for the Degree

Doctor of Philosophy

McMaster University

McMaster University DOCTOR OF PHILOSOPHY (2015) Hamilton, Ontario (Civil Engineering)

TITLE: Multi-Scale Modelling of Geomechanical Behaviour Using the Voronoi Cell Finite Element Method (VCFEM) and Finite-Discrete Element Method (VCFEM-DEM)

AUTHOR: Brandon Karchewski, B.Eng.Mgmt. (McMaster University)

SUPERVISORS: Professor D. Stolle, Professor P. Guo

NUMBER OF PAGES: xvi, 190, XXXII

Lay Abstract

The focus of the present work is the simulation of geomechanical behaviour at multiple scales. This ranges from simulating the interaction of grains of sand in a laboratory compression test to the seepage of water through and deformation of a large dam constructed of granular material. The simulations use a numerical tool called the Voronoi cell finite element method (VCFEM), which the present work extends to allow accurate analysis of the flow of fluid through a porous medium, deformation of a granular material under load and coupled analysis of these phenomena. The development and testing of this numerical tool for use in geomechanical analysis is itself a contribution. The present work also contains new insights into how localized stresses and strains in a granular material that are present well before the peak strength can have an important influence on the mode of failure.

Abstract

The present work applies the hybrid Voronoi cell finite element method (VCFEM) within geomechanics. Coupled seepage and deformation analysis using the VCFEM incorporating body forces allows accurate analysis of earth dams. The development of a novel approach for simulating granular material behaviour using the combined finite-discrete element method (VCFEM-DEM) provides new insights into strain localization in granular materials.

Chapter 1 provides background including summary literature reviews for all concepts in the title including seepage analysis, micromechanical and continuum mechanics theory, Voronoi diagrams, finite elements (FEM), discrete elements (DEM) and combined FEM-DEM. Chapter 1 concludes by detailing the contributions of the present work.

Chapter 2 presents the VCFEM for seepage analysis. The numerical examples include an investigation of mesh sensitivity and a comparison of conforming shape functions. Polygonal elements with more than four nodes show a decrease in mesh sensitivity in free surface problems, compared with four-node quadrilateral elements. The choice of conforming shape function within the VCFEM analysis did not affect the results.

Chapter 3 formulates and applies the VCFEM-DEM, showing that strain localization effects in granular materials are important at all scales. The VCFEM-DEM captures shear banding in biaxial compression tests, demonstrating that global shear strains and inhomogeneities in the shear stress field present after consolidation are early precursors to the failure mode. At the field scale, strain localization can lead to significant non-uniformity in subsurface stress distribution owing to self-weight.

Chapter 4 presents the coupled VCFEM for seepage and deformation. A practical example of the design of an earth dam demonstrates the application of general body forces within a hybrid formulation, notably lacking in the literature.

Chapter 5 concludes by summarizing the key observations of the present work, and providing direction for future research. The Appendix provides additional details related to numerical integration within the VCFEM.

Acknowledgements

The Natural Sciences and Engineering Research Council of Canada (NSERC) provided partial funding for the research work comprising this doctoral thesis. In particular, NSERC provided a CGS M grant for 2011-12 and a PGS D grant for 2012-15. The NSERC USRA program also provided support for several summer research terms during my undergraduate studies and for collaborations during my graduate studies. The opportunity to participate in research at the undergraduate level played a key role in my decision to pursue graduate studies. I gratefully acknowledge the financial support of fundamental and applied research by NSERC, and by extension, the Canadian taxpayers.

I would next like to give my thanks to the members of my supervisory committee. I could always count on Spencer Smith and Michael Tait to provide candid advice on how to organize my research activities most efficiently, and on what aspects of the results are most interesting to those outside my specialization.

I would also like to thank Dieter Stolle and Peijun Guo for their outstanding supervision. I began working with these gentlemen following the second year of my undergraduate studies in civil engineering. I learned at an early stage about the excitement and frustration of both laboratory investigations and numerical modelling in geomechanics. The patience and good nature of my supervisors played a pivotal role in my development as an academic and in my decision to pursue a career in teaching and research.

Most of all I would like to thank my wife, Anna Pekinasova. Anna has been the most outspoken supporter of my work on a day-to-day basis through nearly a decade of post-secondary education. Our discussions about the nature of geological materials, though to some they may seem a strange activity for a Friday evening, have often led to interesting insights. In recent years, I have had the opportunity to formally collaborate on research with Anna, and I look forward to continuing to collaborate for many years to come. I am deeply thankful to Anna for all of her support in my development.

Though in research we are not always sure of what, if anything, we will find, we can be sure that we will rarely find anything if we are not searching.

Table of Contents

List of Figures

List of Tables

List of Abbreviations and Symbols

Table 0.1 Acronyms and abbreviations

Abbreviation	Description
1-D, 2-D, 3-D	one dimension, two dimensions, three dimensions
DEM	discrete/distinct element method
FEM	finite element method
VCFEM	Voronoi cell finite element method

Table 0.2 Units

Symbol	Base Units	Description
L	-	length
M	-	mass
T	-	time
F	$M \cdot L \cdot T^{-2}$	force
kg	-	kilogram
m	-	metre
s	-	second
N	$kg \cdot m \cdot s^{-2}$	Newton
Pa	$N \cdot m^{-2}$	Pascal
°	-	degrees

Table 0.3 Solution variables

Symbol	Units	Description
$\mathbf{a}_h$, $\mathbf{a}_u$, $\tilde{\mathbf{a}}_u$	L	nodal values of h, $\mathbf{u}$, $\tilde{\mathbf{u}}$
$\mathbf{a}_p$	$F \cdot L^{-2}$	nodal values of p
$\mathbf{f}_b$	$F \cdot L^{-3}$	volumetric body force vector
$\mathbf{f}_g$	$F \cdot L^{-3}$	volumetric gravitational force vector
$\mathbf{f}_j$	$F \cdot L^{-3}$	volumetric seepage force vector
h, h^*	L	hydraulic head in V or V_e, on S_e
$\hat{h}$	L	prescribed hydraulic head
$\mathbf{i}$	-	hydraulic gradient
p	$F \cdot L^{-2}$	pressure
$\mathbf{q}$	$L \cdot T^{-1}$	specific discharge
$\hat{q}$	$L \cdot T^{-1}$	prescribed specific discharge
t	T	time
$\hat{\boldsymbol{t}}$	$F \cdot L^{-2}$	prescribed traction
$\mathbf{u}$, $\mathbf{u}^*$	L	displacement in V or V_e, on S_e
$\tilde{\mathbf{u}}$	L	displacement in local coordinates for interface element
$\hat{\mathbf{u}}$	L	prescribed displacement
$\mathbf{v}_f$	$L \cdot T^{-1}$	pore fluid velocity
$\boldsymbol{\beta}_q$, $\boldsymbol{\beta}_\sigma$	-	flux interpolation coefficients for $\mathbf{q}$, $\boldsymbol{\sigma}'$
$\boldsymbol{\beta}_g$, $\boldsymbol{\beta}_j$, $\boldsymbol{\beta}_p$	-	body force interpolation coefficients for $\mathbf{f}_g$, $\mathbf{f}_j$, p
$\gamma_{ij} = 2\varepsilon_{ij}$	-	engineering shear strain components, $i,j \in \{ x, y, z \}$, $i \neq j$
$\boldsymbol{\varepsilon}$, $\tilde{\boldsymbol{\varepsilon}}$, $\boldsymbol{\varepsilon}_e$, $\boldsymbol{\varepsilon}_p$	-	strain tensor, global, local, elastic, plastic
ε_{ij}	-	strain components, $i,j \in \{ x, y, z \}$
ε_ξ, ε_η	-	interface shear, normal strain components
ζ	-	plastic hardening parameter
$\boldsymbol{\sigma}$, $\boldsymbol{\sigma}'$, $\tilde{\boldsymbol{\sigma}}$, $\boldsymbol{\sigma}_0$, $\boldsymbol{\sigma}^*$	$F \cdot L^{-2}$	stress tensor, total, effective, local, initial, trial
σ_i	$F \cdot L^{-2}$	principal stresses, $i \in \{ 1, 2, 3 \}$
σ_n	$F \cdot L^{-2}$	normal stress
σ_ξ, σ_η	$F \cdot L^{-1}$	shear and normal stress in interface element
τ	$F \cdot L^{-2}$	shear stress
$\psi(\mathbf{x})$	$L^2 \cdot T$	potential/streamline function

Table 0.4 Material parameters and constants

Symbol	Units	Description
$A_{\check{\zeta}}$, A_η	-	parameters for nonlinear elastic constitutive model
c, c'	$F \cdot L^{-2}$	cohesion
$\mathbf{D}$, $\mathbf{D}_e$, $\mathbf{D}_{ep}$	$F \cdot L^{-2}$	constitutive tensor, $e \rightarrow$ elastic, $ep \rightarrow$ elastoplastic
d	L	nominal particle size
E	$F \cdot L^{-2}$	Young's modulus
e, e_0	-	void ratio, $0 \rightarrow$ initial
G, G_r	$F \cdot L^{-2}$	shear modulus, $r \rightarrow$ residual
G_s, G_f	-	specific gravity, $s \rightarrow$ solid, $f \rightarrow$ fluid
$\mathbf{g}$	$L \cdot T^{-2}$	gravitational acceleration vector
g	$L \cdot T^{-2}$	gravitational acceleration
$\mathbf{K}$	$L \cdot T^{-1}$	hydraulic conductivity tensor
K_{ij}	$L \cdot T^{-1}$	hydraulic conductivity components, $i, j \in \{ x, y, z \}$
K_i	$L \cdot T^{-1}$	principal hydraulic conductivities, $i \in \{ x, y, z \}$
l_e	L	length of interface element
M, M_0, M_r	$F \cdot L^{-2}$	constrained modulus, $0 \rightarrow$ compressive, $r \rightarrow$ residual
m	-	number of flux coefficients in $\boldsymbol{\beta}_i$
N_e	-	number of elements, number of cells in Voronoi diagram
n	-	number of degrees of freedom in element
r	-	required number of kinematic constraints
s	T^{-1}	seepage source term
S_s	L^{-1}	specific storage
α_p, α_j	-	effective stress coefficients for pressure, seepage force
γ	$F \cdot L^{-3}$	unit weight, ρg
γ_μ, $\gamma_{\pm\sigma}$	$F \cdot L^{-3}$	mean, ± one standard deviation unit weight lines
δ_e	L	characteristic length for interface elements
ϑ	-	material parameter, coefficient of $\Delta\varepsilon_\xi^p$ in $\Delta\zeta$
κ_η	$F \cdot L^{-2}$	parameter for nonlinear elastic constitutive model
κ	-	swelling index
λ	-	compression index
ν	-	Poisson's ratio
ρ, ρ_f, ρ_w	$M \cdot L^{-3}$	density of bulk material, fluid, water
ϕ	-	porosity
φ', φ_f, φ_c	°	internal friction angle, effective, peak, critical

Table 0.5 Other symbols

Symbol	Units	Description
$a(\zeta)$	$F \cdot L^{-2}$	hardening function
a_0	$F \cdot L^{-2}$	centre of loading surface at e_0
B_{ij}	L	edge between contiguous Voronoi cells V_i and V_j
D_{ij}	L	dominance region of Voronoi cell point i over j
$\mathbf{F}_I$, $\mathbf{F}_E$	F	global force vectors, $I \rightarrow$ internal, $E \rightarrow$ external
$\mathbf{F}_{I(g)}$, $\mathbf{F}_{I(i)}$	F	internal force vectors, $g \rightarrow$ grain, $i \rightarrow$ interface
$\mathbf{F}_{\hat{t}}$, $\mathbf{F}_g$, $\mathbf{F}_j$, $\mathbf{F}_p$	F	external force vectors for tractions, gravity, seepage, pressure
$\mathbf{F}_0$	F	internal force vector for initial stresses
$F(\boldsymbol{\sigma}')$	$F \cdot L^{-2}$	failure function (Mohr-Coulomb)
$f(\boldsymbol{\sigma}', \zeta)$	$(F \cdot L^{-2})^2$	loading function
$\mathbf{G}_{qh}$, $\mathbf{G}_{\sigma u}$	-	element boundary equilibrium matrix for $\mathbf{q}$, $\boldsymbol{\sigma}'$
$\mathbf{G}_{gu}$, $\mathbf{G}_{ju}$, $\mathbf{G}_{pu}$	-	element boundary body force matrix for $\mathbf{f}_g$, $\mathbf{f}_j$, p
H, H_e, H_p	-	hardening coefficients, $e \rightarrow$ elastic, $p \rightarrow$ plastic
$\mathbf{H}_{qq}$, $\mathbf{H}_{\sigma\sigma}$	-	element flux matrix for $\mathbf{q}$, $\boldsymbol{\sigma}'$
$\mathbf{K}_{hh}$	$L^2 \cdot T^{-1}$	hydraulic conductivity matrix
$\mathbf{K}_{uu}$, $\mathbf{K}_{uu(g)}$, $\mathbf{K}_{uu(i)}$	$F \cdot L^{-1}$	stiffness matrix, $(g) \rightarrow$ grain, $(i) \rightarrow$ interface
$\mathbf{K}_{uu(0)}$	$F \cdot L^{-1}$	initial (elastic) stiffness matrix
$\hat{\mathbf{K}}$	$F \cdot L^{-1}$	effective (dynamic) stiffness matrix
$\mathbf{L}_{qh}$, $\mathbf{L}_{\sigma u}$, $\mathbf{L}_{iu}$	L^{-1}	linear differential operators
$\mathbf{M}$, $\mathbf{M}'$	M	lumped, consistent mass matrix
$\mathbf{N}_h$, $\mathbf{N}_u$	-	shape function matrices in V_e for h, $\mathbf{u}$
$\mathbf{N}_h^*$, $\mathbf{N}_u^*$	-	shape function matrices on S_e for h^*, $\mathbf{u}^*$
$\tilde{\mathbf{N}}_u$	-	shape function matrix for interface element
N_1, N_2	-	interface shape functions
$\mathbf{n}_q$, $\mathbf{n}_\sigma$	-	unit normal vector representations
n_i	-	normal vector components, $i \in \{ x, y, z \}$
$\mathbf{P}_q$, $\mathbf{P}_\sigma$	-	flux interpolation matrices for $\mathbf{q}$, $\boldsymbol{\sigma}'$
$\mathbf{Q}_q$	$L^3 \cdot T^{-1}$	element flux vector
$\mathbf{T}$, $\mathbf{T}_0$	-	transformation/rotation matrices
ΔU, ΔU_e	$F \cdot L$	strain energy increment, $e \rightarrow$ element
V, V_ϕ	L^3	domain volume, pore volume
V_e, V_i	L^3	body/grain element volume, interface element volume
V_{ijk}	L	vertex of three contiguous Voronoi cells V_i, V_j, V_k
r^2	-	coefficient of determination for fitted curves
S, S_e, S_i	L^2	domain surface, element surface, internal surface

S_h, S_q, S_u, S_t	L^2	boundary condition surfaces
$\mathbf{w}$	-	vector of integration point weights
$\mathbf{x}$, $\tilde{\mathbf{x}}$	L	position vector in global, local coordinates
x, y, z	L	Cartesian space coordinates
$\mathbf{x}_c$	L	element/cell centroid coordinates
$\mathbf{x}_e$	L	cell point for Voronoi cell V_e, $\mathbf{x}_e \neq \mathbf{x}_c$ in general
$\mathbf{x}_s$	L	local coordinates in V_e
$\dot{A} = \partial A/\partial t$	$A \times T^{-1}$	time derivative of A
$\mathbf{A}^T$	same as $\mathbf{A}$	transpose of matrix/vector $\mathbf{A}$
$\mathbf{A}^{-1}$	inverse of $\mathbf{A}$	inverse of matrix $\mathbf{A}$
$\|\mathbf{A}\|$	same as $\mathbf{A}$	Euclidean norm of vector/matrix $\mathbf{A}$
Π_{HW}	F·L	Hu-Washizu functional
Π_{TPE}	F·L	total potential energy functional
Π_{MCE}	F·L	modified complementary energy (hybrid) functional
Π_h	$L^4 \cdot T^{-1}$	functional for conventional FEM seepage, analogous to Π_{TPE}
Π_{qh}	$L^4 \cdot T^{-1}$	hybrid functional for seepage, analogous to Π_{MCE}
$\boldsymbol{\alpha}_u$	L	modal displacement vector
α	-	width-to-height ratio for quadrilateral meshes
$\boldsymbol{\delta}$	-	Kronecker delta, identity tensor
δ	-	step size parameter for nonlinear solver
ε_a	-	approximate relative error
ε_s	-	stopping criterion for approximate relative error
η, ξ	-	local coordinates for interface element
θ	°	orientation of interface element
$\Delta\mu$	-	plastic multiplier
$\boldsymbol{\Phi}$	-	moment fitting matrix
$\boldsymbol{\Phi}_u$	-	eigenmode matrix
$\boldsymbol{\phi}$	-	vector of exact integrals of weighted basis functions
$\boldsymbol{\varphi}_{u(k)}$	-	eigenmode vector, k^{th} column of $\boldsymbol{\Phi}_u$
$\boldsymbol{\Psi}_q$	$L^3 \cdot T^{-1}$	residual flux vector for seepage analysis
$\boldsymbol{\Psi}_\sigma$	F	residual load vector for deformation analysis
Ω_d, Ω_w	-	unsaturated and saturated domains for unconfined seepage
$\omega_{(k)}$	T^{-1}	angular natural frequency of mode k

Declaration of Academic Achievement

This doctoral thesis contains the original work of the author. As all modern education and research is and should be collaborative, the work was influenced by the work of past researchers, and produced in cooperation with colleagues. Where the work relies or builds on the work of past researchers, appropriate reference is given. For original content produced in cooperation with others, which includes all sections of Chapters 2, 3 and 4, footnotes cite associated publications or presentations, crediting the co-authors. That said, the development of the novel features of the modelling approaches used in the present work, their implementation as a scientific computing code, the generation of simulation results and the writing presenting the formulation and discussing the results are all primarily the work of the author. In particular, the author notes that A. Pekinasova contributed significantly to the code implementation, results generation and interpretation of results for Chapters 2 and 4 as part of research collaborations made possible by grants from the Natural Sciences and Engineering Research Council of Canada (NSERC) Undergraduate Student Research Award (USRA) program during the summers of 2014 and 2015.

1 Introduction

1.1 General Background and Literature Review

As with all records of significant research, the title necessarily compresses much detail into as few words as possible – particularly with the short title, which must fit on the spine of the binding at a reasonable font size. Therefore, an excellent way to introduce the content of this thesis is by unpacking the title and defining the terms contained within it:

MULTI-SCALE MODELLING *OF* ***GEOMECHANICAL BEHAVIOUR*** *USING THE* ***VORONOI CELL FINITE ELEMENT METHOD*** *(VCFEM) AND THE FINITE-****DISCRETE ELEMENT METHOD*** *(VCFEM-DEM)*

1.1.1 Multi-scale modelling

A primary interest of the present work is that the behaviour of geological materials such as soil and rock depends on phenomena at different length scales. Practical applications of mechanics in civil engineering are most often concerned with behaviour at the macro-scale. Examples include seepage of water through an earth dam, transport of a contaminant through an aquifer, forces on a retaining wall supporting a soil slope and the dynamic behaviour of a structure subjected to seismic excitation. In these examples, the length scale of interest is metres or even kilometres. However, in studying the behaviour of geological materials, the author has come to realize that to understand the fundamental reasons for the behaviour, consideration of small-scale features is important. For example, the rate at which

a porous material conducts a particular pore fluid under a specified hydraulic gradient depends on the permeability of the porous material – a geometric property of the pore structure – and the material properties of the pore fluid. For another example, the deformation of a material composed of discrete grains, such as sand or gravel, depends on the interactions between individual grains. In these examples, the length scale of interest is millimetres or even micrometres. Therefore, in modelling geological materials, capturing the physics means somehow accounting for behaviours at a broad range of length scales, which the present work refers to as multi-scale modelling. This approach to modelling is itself not novel, but recognizing this should help the reader to understand the motivation behind the present work. The literature on multi-scale modelling comprises a significant amount of research across multiple disciplines, and the body of the present work introduces related work where the context is appropriate.

1.1.2 Geomechanical behaviour

Geomechanical behaviour means phenomena observed in geological materials such as soil and rock that we can describe using mechanics, which is a branch of physics. This differs from other methods of describing phenomena related to geological materials including field mapping, dating techniques – relative or absolute – and descriptive geometry, although one cannot deny the importance of these methods in understanding the origin of geological materials. Part of understanding the mechanical behaviour of geological materials is knowing that such materials, as they exist in their natural state, are porous and therefore consist of a solid component and a (potentially multi-phase) fluid

component that resides in the pores [1-4]. Common pore fluids of interest in geomechanical modelling are water, air and aqueous or non-aqueous phase contaminants [4-6]. The focus of this thesis has not been on unsaturated geomechanics (involving water and air as pore fluids) or on contaminant transport (involving water and contaminants as pore fluids), and as such the pore fluid is restricted to water in its liquid phase. Another aspect important in understanding the behaviour of geological materials is the physics behind the deformation of the solid phase, which consists of grains of solid material that move relative to one another, causing it to behave in a way that is distinct from the traditional definitions of solid, liquid or gas [7].

In addition to the phenomenological understanding of geological materials described above, geomechanics also includes the mathematical modelling of such phenomena and computing solutions using numerical analysis. Numerical analysis is a sub-discipline of applied mathematics wherein one simulates natural phenomena using mathematical models with the aims of understanding and making predictions regarding such phenomena. Sections 1.1.4-1.1.6 and the body chapters describe the numerical analysis techniques used in the present work. Prior to discussing numerical analysis techniques, this section introduces the governing equations used as mathematical models for the geomechanical phenomena of interest. The descriptions introduce the key solution variables, mathematical operators and material parameters along with their units enclosed in brackets $[\cdot]$, taking the fundamental units as L = length, M = mass and T = time, and for convenience the derived unit $F = M \cdot L \cdot T^{-2}$ = force. Figure 1.1 shows a

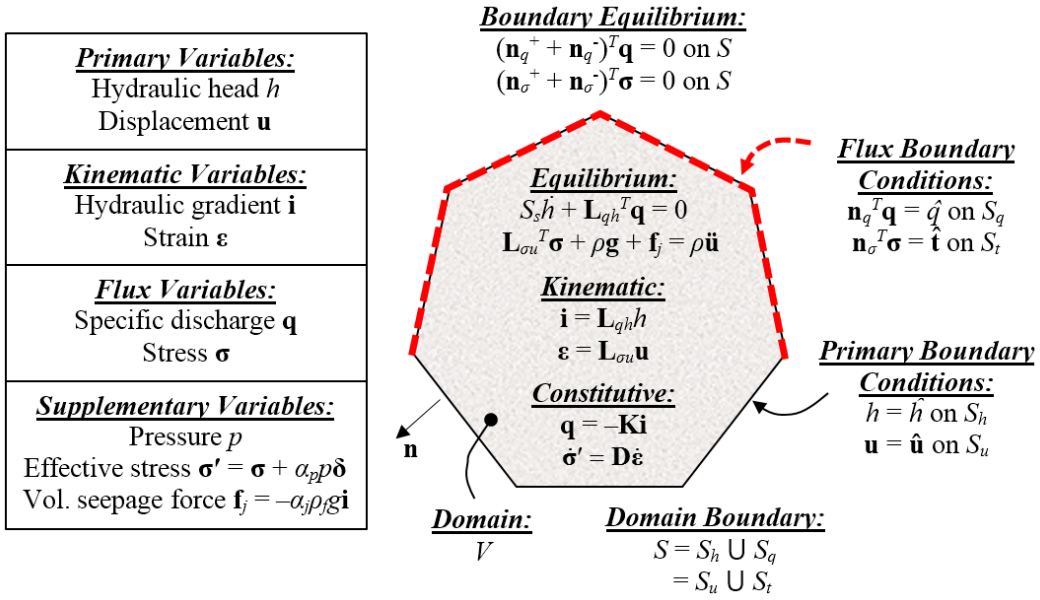

Figure 1.1 Schematic of domain for analysis of geomechanical behaviour

schematic of the analysis domain and a summary of key solution variables, governing equations and boundary conditions for the analysis of geomechanical behaviour of interest within the present work.

The first phenomenon of interest in the present work is the seepage of a single-phase fluid through the pores of a geological material, described by the well-known transient groundwater equations for Darcian flow [4] in a volume V [L^3], as Figure 1.1 shows,

$$S_s\dot{h} + \mathbf{L}_{qh}^T\mathbf{q} = 0 \tag{1.1.1}$$

$$\mathbf{i} = \mathbf{L}_{qh}h \tag{1.1.2}$$

$$\mathbf{q} = -\mathbf{K}\mathbf{i} \tag{1.1.3}$$

The key solution variables in these equations are the hydraulic head h [L], hydraulic gradient $\mathbf{i}$ [-] and specific discharge $\mathbf{q}$ [$L \cdot T^{-1}$]. Superposed dots imply derivatives with respect to time t so $\dot{h} = \partial h/\partial t$. The symbol $\mathbf{L}_{qh} = \{ \partial/\partial x, \partial/\partial y, \partial/\partial z \}^T$ represents a linear differential operator and $\{\cdot\}^T$

represents the transpose operation. Thus, $\mathbf{L}_{qh}h$ means the gradient of h and $\mathbf{L}_{qh}^{T}\mathbf{q}$ means the divergence of $\mathbf{q}$. The hydraulic head h is a potential that includes contributions from pressure potential and gravitational potential through the relation $h = p/\rho_f g + y$ where p [$\mathrm{F\cdot L^{-2}}$] is the pressure, ρ_f [$\mathrm{M\cdot L^{-3}}$] is the density of the pore fluid, g [$\mathrm{L\cdot T^{-2}}$] is the gravitational acceleration and y [L] is the elevation relative to an arbitrary datum. The specific discharge $\mathbf{q} = \{ q_x, q_y, q_z \}^T$ is a vector quantity representing the volumetric flow rate of the pore fluid per total unit area of porous material, resolved here in the Cartesian coordinate system with position vectors given by $\mathbf{x} = \{ x, y, z \}^T$. The specific discharge is smaller in magnitude than the actual pore fluid velocity $\mathbf{v}_f$ [L/T] since the pores only make up a portion of the total volume given by the porosity $\phi = V_\phi/V$ where subscript ϕ refers to the pores. We may relate the average pore fluid velocity to the specific discharge $\mathbf{q}$ by $\mathbf{v}_f = \phi^{-1}\mathbf{q}$. Additional material parameters are the specific discharge S_s [$\mathrm{L^{-1} = L^3\cdot L^{-3}\cdot L^{-1}}$], whose peculiar units derive from its definition as the volume of fluid released from storage in a unit volume of porous material per unit decline in hydraulic head [4], and the hydraulic conductivity $\mathbf{K}$ [$\mathrm{L\cdot T^{-1}}$],

$$\mathbf{K} = \begin{bmatrix} K_{xx} & K_{xy} & K_{xz} \\ K_{yx} & K_{yy} & K_{yz} \\ K_{zx} & K_{zy} & K_{zz} \end{bmatrix} \tag{1.1.4}$$

which is a second-order tensor relating the specific discharge $\mathbf{q}$ to the hydraulic gradient $\mathbf{L}_{qh}h$ [-] through equation (1.1.3), which the literature commonly refers to as Darcy's law [4]. The latter is not truly a "law", as it is often referred to, but a constitutive equation originally derived by Henry Darcy based on empirical evidence of water flowing through sand [8]. Whitaker [9] presents a

phenomenological derivation of Darcy's Law based on the Navier-Stokes momentum balance equations for a fluid flowing through a porous medium using a volume averaging or homogenization process and neglecting the inertial and viscous forces in the fluid. We often presume that the hydraulic conductivity tensor **K** has all positive diagonal entries and vanishing non-diagonal entries when we align the coordinate axes with the principal directions of the material fabric,

$$\mathbf{K} = \begin{bmatrix} K_x & 0 & 0 \\ 0 & K_y & 0 \\ 0 & 0 & K_z \end{bmatrix} \tag{1.1.5}$$

which from the theory of eigenanalysis implies that **K** for an arbitrary orientation of the coordinate axes should be symmetric and positive definite, i.e. $\mathbf{K} = \mathbf{K}^T$ and $\mathbf{x}^T\mathbf{K}\mathbf{x} > 0 \ \forall \mathbf{x}$. For partially saturated domains, note that $\mathbf{K} = \mathbf{K}(p)$ when $p < 0$ making equation (1.1.3) nonlinear – a fact that Chapters 2 and 4 exploit to solve problems of unconfined seepage wherein the free surface of the pore fluid within the porous medium must be located as part of the solution. A special case of equation (1.1.1) that applies on an internal surface S_i where $S_s = 0$ is,

$$\left(\mathbf{n}_q^+ + \mathbf{n}_q^-\right)^T \mathbf{q} = 0 \tag{1.1.6}$$

where $\mathbf{n}_q{}^+ = \{ n_x{}^+, n_y{}^+, n_z{}^+ \}^T = -\mathbf{n}_q{}^-$ represent the unit normals to S_i in opposite directions. This alternate form is useful in deriving certain approximate solution schemes, which Chapter 2 discusses in more detail. To close the seepage formulation, there are also the boundary conditions,

$$h = \hat{h}(\mathbf{x},t) \text{ on } S_h \tag{1.1.7}$$

$$\mathbf{n}_q^T\mathbf{q} = \hat{q}(\mathbf{x},t) \text{ on } S_q \tag{1.1.8}$$

where $\hat{h}(\mathbf{x},t)$ and $\hat{q}(\mathbf{x},t)$ are the prescribed hydraulic head and prescribed flux (specific discharge) on their respective parts of the domain boundary S_h and S_q, the total domain boundary $S = S_h \cup S_q$ and $\mathbf{n}_q = \{ n_x, n_y, n_z \}^T$ represents the outward pointing unit normal to S. Although the formulations presented herein extend readily to three dimensions, it often suffices for demonstrative examples and simplicity of presentation to perform two-dimensional analysis in the xy-plane, assuming $q_z \approx 0$ and ignoring all components involving z in $\mathbf{q}$, $\mathbf{L}_{qh}$, $\mathbf{K}$ and $\mathbf{n}_q$. For seepage analysis, the present work only considers cases of steady seepage wherein $\dot{h} = 0$, $\hat{h}(\mathbf{x},t) = \hat{h}(\mathbf{x})$ and $\hat{q}(\mathbf{x},t) = \hat{q}(\mathbf{x})$. Despite the simplifications, the formulations can adequately represent problems of importance in civil engineering such as the flow of water around a sheet pile into an excavation and the seepage of water through an earth dam, as Chapter 2 demonstrates.

The second phenomenon of interest in the present work is the strength and deformation of solid geological materials composed of discrete grains when subjected to loading from boundary tractions and body forces. Prior to presenting the formulation and assumptions employed in the present work, it is worthwhile to begin with a summary of the literature on the behaviour of granular materials, to elucidate the important phenomena that a model of such material should aim to capture. The earliest definition of a strength criterion for granular materials comes from Coulomb [10], who in investigating retaining walls proposes a linear relationship between the shear strength of the material τ_f [F·L^{-2}] and the normal stress (tension positive) applied on a plane of interest σ_n [F·L^{-2}],

$$F(\tau, \sigma_n) = |\tau| + \sigma_n \tan\varphi_f - c \leq 0 \tag{1.1.9}$$

where φ_f [-] is the internal angle of friction, c [F·L^{-2}] is the inherent shear strength or cohesion and τ_f corresponds to the case that $F = 0$. Despite its simplicity, the linear frictional law of Coulomb, with some modifications, remains useful in practical engineering applications to the present day. A key modification to the description of strength criteria in geomechanics is that of "effective" stress σ' [F·L^{-2}] related to the "total" stress σ [F·L^{-2}] by,

$$\sigma' = \sigma + p \tag{1.1.10}$$

where p is the pore pressure, as defined previously. Note that tension is positive for σ' and σ whereas compression is positive for p in this form. Terzaghi [1] lays the foundations of soil mechanics and geotechnical engineering in a seminal series of papers describing key phenomena related to soil mechanics, among which is the realization that the behaviour of soils depends on the effective stress, rather than the total stress. Note that this concept influences the normal components of stress only, leaving the shear stress components unchanged. Therefore, any criterion describing the failure of a geomaterial should use the effective stress when referring to normal stress components. Another modification to the Coulomb frictional law stems from the fact that it does not specify how to determine the plane on which failure occurs in a mass of geological material. For a granular material, one should consider a plane on which a critical combination of normal and shear stress maximizes F for a given state of stress. For this, it is best to re-write the criterion in terms of the principal effective stresses (tension positive) $\sigma_1' > \sigma_2' > \sigma_3'$ in the well-known form,

$$F\left(\sigma_1', \sigma_3'\right) = \tfrac{1}{2}\left(\sigma_1' - \sigma_3'\right) + \tfrac{1}{2}\left(\sigma_1' + \sigma_3'\right)\sin\left(\varphi_f'\right) - c'\cos\left(\varphi_f'\right) \leq 0 \tag{1.1.11}$$

Although this form of the failure function accounts for orientation of principal stresses, it ignores the influence of the intermediate principal stress σ_2', and assumes that the material is homogeneous and isotropic. One may account for the influence of the intermediate principal stress using, for example, the modified form of Matsuoka and Nakai [11], although the present work ignores this aspect of geomechanical behaviour. For heterogeneous materials, such as jointed rock where the joints form planes that may have significantly different strength parameters to the matrix material, one should also examine failure through these joints [12,13]. This idea will be useful in Chapter 3 of the present work. An approach to accounting for anisotropic behaviour in geomaterials is to modify the failure criterion to include tensors describing the inherent and induced orientation of the principal directions of the material fabric. Oda [14] introduces this concept and incorporates the fabric tensors into an anisotropic plasticity formulation. Pietruszczak and Mróz [15,16] present a similar approach incorporating a microstructure tensor to describe the fabric. Duveau et al. [17] provide a review of other failure criteria for anisotropic materials, including geomaterials as a subset. These approaches have value in allowing the macroscopic analysis of anisotropic materials using a continuum-based formulation, but require a priori specification of a material fabric tensor describing how the fabric varies in the domain of interest. The difficulty in obtaining such a description in general for real geomaterials aside, this approach is restrictive in that it may be especially difficult to incorporate local variations in material fabric, which are important in understanding strain localization behaviour in geomaterials.

It is worth noting at this point that granular materials, which most geological materials are, are discontinuous in nature. They display anomalous behaviour relative to the traditional definitions of solid, fluid or gaseous materials [18] and defy definition of governing equations based on continuum mechanics starting from a differential basis without accounting for the geometric fabric of the granular structure and the so-called stress-geometry or stress-force-fabric equation [19- 31].

Reynolds [32] first described the phenomenon of dilatancy, which is the tendency of a dense granular material to expand when loaded. Nearly a century later, Rowe [33] returns to this issue and finds that the strength and dilatancy of a granular assembly subjected to deviatoric loading depends on the friction between particles, the orientation of the granular fabric and the amount of energy dissipation during sample preparation. Matsuoka [34] describes the complex relationship between stress ratios and dilatancy in soils, finding that the dilatancy depends on the ratio of shear and effective normal stress on the mobilized failure plane, rather than the ratio of deviator and effective mean stress in the specimen. Capturing such behaviour is possible to an extent at the constitutive modelling level, but dilatancy at failure in granular materials occurs in a nonuniform manner, which requires careful treatment in modelling. Wan and Guo [35] propose a constitutive model accounting for the stress-dilatancy effect using a critical void ratio dependent factor, and later [36-39] extend this approach to incorporate the evolution of microstructure fabric. They observe that failure associated with a loss of stability resulting from the buckling of force chains in

the granular structure can occur even for dense granular material when subjected to certain strain paths.

Cosserat and Cosserat [40] advance the theory of micropolar elasticity, which includes rotations of material points into the formulation, in addition to the usual descriptions of deformation. This approach was the first real step toward a theoretical description of the mechanics of granular materials. Goodman and Cowin [41] propose a formulation for granular flow that accounts for the volume distribution of the material as a kinematic variable, thereby providing a description that allows static equilibrium under gradients of density and under shear stress, which is not possible in a fluid. A key observation of Goodman and Cowin [41] is that the principal axes of stress and deformation may not coincide for granular materials. Drescher and de Josselin de Jong [42] confirm this result experimentally using photoelastic discs as a proxy for granular materials. They also confirm other phenomena predicted by micropolar theory including sub-division of the granular assembly into sliding elements and rotation of the grains during deformation. Although confirming these key phenomena, Ammi et al. [43] point out that polygons provide a better geometric representation of the grains when comparing the packing structures of regular polygons with disc packings. Chang and Ma [44] advance the micropolar theory of granular materials by deriving the constitutive coefficients in terms of the properties at the contacts or interfaces between grains, thereby allowing computation using numerical approximation with finite elements (see Section 1.1.4). Their results show good comparison with simulations using the discrete element method (see Section 1.1.5) supporting the ability of continuum descriptions of granular materials using

micropolar theory to solve boundary value problems of interest. De Borst [45] incorporates the micropolar description into a generalized plasticity flow theory and shows through numerical simulation the ability of the modelling framework to capture bands of strain localization of finite thickness in direct shear and biaxial compression simulations. Further review of approaches to modelling strain localization specifically is provided later in this section.

Steinmann [46] provides a brief review of the developments in micropolar theory up to the mid-90s beginning from the Cosserats [40] and including key contributions from Günther [47], Koiter [48], Mindlin [49], Toupin [50], Neuber [51], Schaefer [52], Eringen [53], Lippmann [54], Besdo [55] and Reissner [56]. Steinmann [46] also notes the difficulty of mesh dependence in the numerical modelling of strain softening behaviour within a continuum description of granular materials, and notes the approach of regularization citing studies by Mühlhaus and Vardoulakis [57], Mühlhaus [58], de Borst [59,60], de Borst and Mühlhaus [61], Steinmann and Willam [62] and Dietsche et al. [63]. Steinmann [46] combines micropolar hyperelasticity with multiplicative elastoplasticity to enhance the configuration space of the solution, thereby describing the fabric of the granular medium within a finite deformation and finite rotation theory.

The text of Cambou [64] compiles the important observations of granular behaviour from experimental evidence, and the main approaches to modelling this behaviour. Cambou [64] states that there are two main modelling approaches. The first is micromechanical analysis based on micropolar theory, homogenization techniques and DEM, which are useful in understanding the micro-scale

behaviour in granular materials. The second approach is continuum-based analysis incorporating the phenomenological descriptions of granular behaviour into a numerical analysis tool such as the finite element method. Cambou [64] points out that these approaches are not in opposition, but support each other in a mutually beneficial way. Micromechanical analysis reveals the details of the phenomena, and continuum-based analysis facilitates solution of practical boundary value problems. For example, Huntley [65] examines the force distribution in an irregular pile of grains and Kolb et al. [66] analyze the fluctuation of forces in a column of granular material, both using a micromechanical approach to understand the details of the phenomena. Sterpi [67], on the other hand, models strain softening effects using two different approaches to simulate the behaviour of granular material around a tunnel, an important application in geotechnical engineering.

The 20th century saw much development of the theory of granular materials, but a comprehensive theoretical basis still proved elusive. Rothenburg [19] examines idealized granular assemblies consisting of discs and spheres, developing relationships between the interparticle forces and granular fabric at the micro-scale, and the macroscopic definition of stress through statistical homogenization. Bathurst and Rothenburg [20] provide further insight into these relationships. Rothenburg and Bathurst [21] and Ouadfel and Rothenburg [26] extend the stress-force-fabric relation for idealized assemblies of planar elliptical and ellipsoidal particles, respectively. Ball and Grinev [19] examine the stress transmission in periodic arrays of granular material and find that the geometric disorder of the grain contacts has an important influence. Edwards and Grinev

[24,25] seek to derive governing continuum equations for the transmission of stress in granular materials and find that there is a missing set of equations linking the geometry and the stress transmission through interparticle force and torque balance. They propose that a self-consistent continuum theory for granular materials should include the concept of compactivity, which describes the position of particles with respect to its nearest neighbours, into the volume averaging or homogenization process. A closely related concept is that of the coordination number, which is an integer value giving the number of neighbouring particles in contact with a given particle, which for 2-D assemblies of uniform particle size can range from 4 (loose) to 6 (dense), and the evolution of which provides a local measure of compactivity as an assembly approaches critical state [68]. Kruyt and Rothenburg [27] summarize the kinematic and static assumptions involved in the statistical homogenization process used to relate microscopic descriptions of a granular assembly to macroscopic definitions of stress and strain. Rycroft [29] accounts for multi-scale behaviour in granular flows using a spot model that relates particle rearrangement at the micro-scale to displacements of particle groups at the meso-scale leading to accurate and efficient large-scale simulations of dense granular flows using the discrete element method. Hill and Selvadurai [69], Cambou et al. [70] and Maugin and Metrinke [71] present texts summarizing the state-of-the-art for micromechanical modelling of granular materials and other generalized continuum theories at the end of the first decade of the 21st century.

More recently, Miehe et al. [72] present a two-scale simulation approach considering elliptical shaped plane particles with frictional contact laws and

various boundary constraints. Pietruszczak and Guo [73] demonstrate a multi-laminate approach for modelling inherently anisotropic granular media that accounts for the sliding and separation associated with softening by incorporating the shear band thickness into the model. De Giuli [30] derives the missing stress-geometry equation mentioned previously by defining the stress tensor using a discrete potential function and introducing a fabric tensor describing the geometry of the granular structure, and uses statistical mechanics to model the fluctuations of contact forces in the granular network. Tordesillas et al. [74] examine vortices in granular media and support the evidence from triaxial experiments and discrete element simulations that strain localization at failure derives from grain motions present even at very early stages of the loading. Kang et al. [75] study the orientation of pores within shear bands at failure in biaxial compression simulations and find that whether the pores elongate parallel to the shear band, the minor principal stress or major principal stress depends on the shape of the particles, the size of the pores and the initial conditions of the granular packing.

The literature specifically on strain localization or shear banding in granular materials itself is voluminous. This section presents only a brief summary sufficient to elucidate the key observations from experiments and simulations regarding the factors driving strain localization failure. Rudnicki and Rice [76] examine the conditions for strain localization in brittle rock as a bifurcation problem resulting from an instability in the homogeneous deformation field. Vardoulakis et al. [77] report on theoretical and experimental investigations to compare the solutions for orientation of shear band proposed by Coulomb [10] and by Roscoe [78]. The former involves a stress discontinuity at the shear band,

which separates two rigid bodies, whereas the latter maintains stress continuity and separates two deforming bodies. Vardoulakis et al. [77] show that both can be correct theoretically and experimentally depending on the material's constitutive behaviour and the loading configuration. The Coulomb orientation follows from cases where the principal stress axes do not rotate during compression testing, thus the orientation of principal stress axes and principal strain rate axes are different. The Roscoe orientation follows from cases where the principal stress axes always coincide with the principal strain rate axes. Vardoulakis [79] completes the comparison, showing that the Coulomb and Roscoe orientations are theoretical upper and lower bounds. Mühlhaus and Vardoulakis [80] investigate the thickness of shear bands in granular materials comparing theoretical predictions with experimental results and find that the shear band thickness is on the order of 10 to 20 times the mean particle diameter. Shuttle and Smith [81] simulate the initiation of shear band formation in granular soils and find that they can be induced both by inhomogeneities in the granular structure and by imperfect boundary conditions. Bardet [82] and the references therein provide a detailed review of the developments in the experimental investigation, theoretical modelling and numerical simulation of strain localization up to the late 20th century. Bardet [82] notes that the strain localization theory of elastoplasticity up to that point does not properly account for the shear band orientation in all cases and notes discrepancies between theoretical predictions and experimental observations. The present author supposes that the discrepancies stem from the attempt to force a continuum-based description of a discontinuous material without properly accounting for the microstructure, noted in the literature on the

development of stress-geometry equations described earlier. Vermeer [83] continues the theoretical investigation of shear band orientation with the aim of explaining the particle size dependence observed experimentally. Vermeer [83] extends the theoretical analysis by allowing the material outside the shear band to unload elastically, thereby allowing post-peak analysis, and observes that the Coulomb orientation is the weakest failure mode in this regime, explaining why it occurs. However, the implied stress discontinuity of this mode makes its formation unstable, which is why Roscoe orientations can also occur.

Lade [84] describes various modes of failure in granular materials, noting that large plastic strains under decreasing stresses may lead to unstable liquefaction under undrained conditions, but that localization of plastic strains under drained conditions leads to shear bands that are stable, but lead to decreasing load capacity. Noting the observation of Vardoulakis [79] that the out-of-axes shear modulus of a granular medium plays an important role in the formation of shear bands, Desrues and Chambon [85] propose an approach to determine the value of such shear moduli, despite the inability of laboratory tests to obtain it directly. They propose an inverse analysis that calibrates the out-of-axis shear modulus to experimental triaxial compression results. Gajo et al. [86] develop a small-strain constitutive model capable of capturing the effect of multiple shear band formation by accounting for the unloading of shear bands after formation. This leads to oscillation of the stress-strain curve in the post-peak regime prior to strong softening.

Tordesillas et al. [87] present a continuum-based analysis framework for the formation of shear bands by returning to micropolar theory and deriving a

constitutive description whose parameters have direct physical interpretations, as opposed to fitting parameters that are not well understood. They conclude based on their observations that the shear band thickness can vary theoretically from zero to infinity, but only decreasing shear band thickness is consistent with the post-peak softening observed in experiments and that strain localization emerges from inhomogeneities in the granular structure coupled with a specific set of boundary conditions. Gudehus and Nübel [88] and Nübel and Huang [89] examine the formation of shear bands in sand and find that local inhomogeneities in the grain structure can lead to spontaneous formation of internal shear bands under isotropic global stress and kinematic boundary conditions. Such internal shear bands ultimately coalesce into global shear bands as loading progresses. Gajo et al. [90] examine the constitutive and kinematic parameters that influence the formation of shear bands in sands and find that parameters such as elastic anisotropy and membrane compliance, though they do not influence the pre-peak loading response of the material, may strongly influence the post-peak behaviour. Rechenmacher et al. [91] examine force chain evolution in shear bands formed in granular materials and observe through digital image based displacement analyses that force chain formation and collapse plays an important role in the kinematics of shear bands. Tordesillas et al. [92] show that the buckling of force chains in the region of shear bands provides an explanation for the stress-dilatancy effect described earlier, as there is significant local dilation associated with the collapse of force chains.

Several studies [93- 99] investigate the evolution of void distribution, volumetric strain and fabric within shear bands and find that the development of

critical state is associated with inhomogeneities in the void distribution in the strain localization zone leading to a terminal void ratio, vanishing volumetric strain rate and elongation of so-called meso-domains of particles in contact. Borja et al. [100] demonstrate that, not only is the shear band characterized by local changes in the void distribution, but that initial spatial density variations in the granular structure can determine the location of the persistent shear band at failure. Gu et al. [101] simulate biaxial compression tests and find that lower initial density and higher confining pressure during the shearing phase can delay the formation of the global shear band. They also show that the laboratory apparatus has an influence on the shear band formation, modelling the membrane used to apply confinement to the specimen explicitly. Desrues and Andò [102] examine the formation of shear bands in granular material both at the continuum level and at the grain scale. They find that strain localization precursors exist well before the peak stress, and that particle shape plays an important role in the formation of shear bands since it influences the manner in which particles interact with and rotate relative to their neighbours.

Guo [103] and Guo and Stolle [104] recently revisited the influence of pore pressure on the formation of shear bands in coupled analysis of saturated granular materials. They found that shear bands form in loose saturated sand during contraction as the deviator stress is increasing, in which case the dilatancy of the material governs the orientation of the band, which corresponds to the Roscoe angle. However, for low permeability densely compacted sand, shear banding occurs at or beyond the peak stress, and the orientation is consistent with the Coulomb angle.

The complex nature of granular materials and the phenomenon of strain localization continue to captivate researchers today, as in the 19th century. In fact, we still seek to understand the same fundamental phenomena that caught the interest of early investigators. Walker et al. [105] examine the evolution of shear bands in dense granular media, which is driven by local dilation in the region of the shear band. Chen et al. [106] simulate the formation of periodic patterns in granular material when subjected to pure shear, observing how the patterned local shear bands ultimately coalesce into a dominant global band owing to local variations in grain structure. These two studies demonstrate that the study of granular material behaviour still has the same fundamental focus as when Reynolds [32] investigated dilatancy in dense granular media and when Faraday [107] observed the formation of periodic patterns in grains subjected to acoustic excitation. The volume of recent work [cf. 108- 114] related to the multi-scale behaviour of granular materials demonstrates that this is still very much an active area of research across a broad range of disciplines.

A single work cannot realistically hope to resolve all current outstanding questions related to granular materials. Chapter 3 of the present work focusses on the strain localization issue and presents a novel approach to accounting for the influence of such variations in material fabric by modelling the grain structure directly, while retaining a continuum based formulation. Sections 1.1.4-1.1.6 of the present chapter provide further background context for the analysis techniques developed in the present work, in particular related to the influences of microstructure on the behaviour of geomaterials.

For now, it is sufficient to present the governing equations from a continuum mechanics perspective, with the understanding that the present work does not seek a continuum basis for the entire domain. Rather, the present work develops a novel framework for analyzing granular materials accounting for the influence of the grain structure by subdividing the domain into different types of sub-domain wherein the continuum description suffices to describe the behaviour. The sub-domain types correspond to individual grains or representative volumes of grains with linear elastic constitutive behaviour and to the interface regions where the grains interact with nonlinear constitutive behaviour. The equations describing the dynamic equilibrium of a solid continuum saturated with a pore fluid in a domain of interest V, as Figure 1.1 shows, are,

$$\rho\ddot{\mathbf{u}} = \mathbf{L}_{\sigma u}^{T}\boldsymbol{\sigma} + \mathbf{f}_{b} \tag{1.1.12}$$

$$\boldsymbol{\varepsilon} = \mathbf{L}_{\sigma u}\mathbf{u} \tag{1.1.13}$$

$$\dot{\boldsymbol{\sigma}}' = \mathbf{D}\dot{\boldsymbol{\varepsilon}} \tag{1.1.14}$$

The solution variables in this system are the displacement $\mathbf{u} = \{ u_x, u_y, u_z \}^T$ [L], the strain $\boldsymbol{\varepsilon}$ [-], the total stress $\boldsymbol{\sigma}$ [F·L^{-2}] and the effective stress $\boldsymbol{\sigma}'$ [F·L^{-2}]. The present work assumes, where applicable, that coupling of the solid deformation to the fluid phase is one way through the principle of effective stress [2, 115],

$$\boldsymbol{\sigma}' = \boldsymbol{\sigma} + \alpha_p p\boldsymbol{\delta} \tag{1.1.15}$$

and through the body forces $\mathbf{f}_b$ where the pressure field p and the body force field – in particular, gravity forces and seepage forces – are known a priori and are not influenced by the solid deformation. Clearly this only applies when the deformations are small, which the present work also assumes. The strain $\boldsymbol{\varepsilon}$ and the

stress **σ** (or **σ′**) are second-order tensors, which in three dimensions have nine components,

$$\boldsymbol{\varepsilon} = \begin{bmatrix} \varepsilon_{xx} & \varepsilon_{xy} & \varepsilon_{xz} \\ \varepsilon_{yx} & \varepsilon_{yy} & \varepsilon_{yz} \\ \varepsilon_{zx} & \varepsilon_{zy} & \varepsilon_{zz} \end{bmatrix} \tag{1.1.16}$$

$$\boldsymbol{\sigma}' = \boldsymbol{\sigma} + \alpha_p p \boldsymbol{\delta} = \begin{bmatrix} \sigma_{xx} & \sigma_{xy} & \sigma_{xz} \\ \sigma_{yx} & \sigma_{yy} & \sigma_{yz} \\ \sigma_{zx} & \sigma_{zy} & \sigma_{zz} \end{bmatrix} + \alpha_p p \begin{bmatrix} 1 & 0 & 0 \\ 0 & 1 & 0 \\ 0 & 0 & 1 \end{bmatrix} \tag{1.1.17}$$

with extension positive for normal strains ε_{ii}, tension positive for normal stresses σ_{ii} and compression positive for pressure p. As the strain represents deformation of the material, the argument that rigid body rotations do not cause strains implies that **ε** is symmetric. Similarly, in the absence of point-wise applied moment couples, moment equilibrium implies that **σ** is symmetric. As the latter is always the case in the present work, both **ε** and **σ** have only six independent components. Therefore, the present work uses the compact vector notation to represent symmetric second- and fourth-order tensor quantities for convenience. Helnwein [116] comments on some of the mathematical details and implications of this representation, and the references therein provide examples from the literature on numerical and theoretical analysis making use of this notation. Within the present work,

$$\boldsymbol{\varepsilon} = \begin{Bmatrix} \varepsilon_{xx} & \varepsilon_{yy} & \varepsilon_{zz} & \gamma_{xy} & \gamma_{yz} & \gamma_{zx} \end{Bmatrix}^T \tag{1.1.18}$$

$$\boldsymbol{\sigma} = \begin{Bmatrix} \sigma_{xx} & \sigma_{yy} & \sigma_{zz} & \sigma_{xy} & \sigma_{yz} & \sigma_{zx} \end{Bmatrix}^T \tag{1.1.19}$$

$$\boldsymbol{\delta} = \begin{Bmatrix} 1 & 1 & 1 & 0 & 0 & 0 \end{Bmatrix}^T \tag{1.1.20}$$

where $\gamma_{ij} = 2\varepsilon_{ij}$ for $i \neq j$ is the so-called engineering strain. Taking this into account, the differential operator $\mathbf{L}_{\sigma u}$ is,

$$\mathbf{L}_{\sigma u} = \begin{bmatrix} \frac{\partial}{\partial x} & 0 & 0 & \frac{\partial}{\partial y} & 0 & \frac{\partial}{\partial z} \\ 0 & \frac{\partial}{\partial y} & 0 & \frac{\partial}{\partial x} & \frac{\partial}{\partial z} & 0 \\ 0 & 0 & \frac{\partial}{\partial z} & 0 & \frac{\partial}{\partial y} & \frac{\partial}{\partial x} \end{bmatrix}^T \tag{1.1.21}$$

The body forces $\mathbf{f}_b = \mathbf{f}_g + \mathbf{f}_j$ of interest in the present work are the gravitational force $\mathbf{f}_g = \rho\mathbf{g}$ [F·L^{-3}] and the volumetric seepage force $\mathbf{f}_j$ [F·L^{-3}]. The magnitude of the gravitational force is $\rho\|\mathbf{g}\|$ and the direction is $\mathbf{g}/\|\mathbf{g}\|$ where $\mathbf{g}$ [L·T^{-2}] is the gravitational acceleration vector, often $\mathbf{g} = \{ 0, -g \}^T$ where $g = \|\mathbf{g}\|$ for a coordinate system with the y direction aligned with, but in the opposite direction of the gravitational acceleration field. The volumetric seepage force is [117],

$$\mathbf{f}_j = -\alpha_j \rho_f g \mathbf{i} = \alpha_j \rho_f g \mathbf{K}^{-1} \mathbf{q} \tag{1.1.22}$$

where it is clear that it is oriented in the direction of flow $\mathbf{q}/\|\mathbf{q}\|$ with magnitude $\alpha_j \rho_f g \|\mathbf{i}\|$ where $\mathbf{q}$ and $\mathbf{i}$ are the specific discharge and hydraulic gradient vectors, respectively, as defined previously. The material parameters are the bulk density ρ [M·L^{-3}] of the mixture of solid and pore fluid, the coefficients α_p and α_j representing the influence of the fluid phase on the stress field – both equal to unity for granular materials [2, 117] – and the constitutive operator $\mathbf{D}$ [F·L^{-2}] relating stress rates to strain rates. If the solid obeys a linear elastic constitutive model, then $\mathbf{D} = \mathbf{D}_e$ is constant and equation (1.1.14) reduces to Hooke's law [118],

$$\boldsymbol{\sigma}' = \mathbf{D}_e \boldsymbol{\varepsilon} \tag{1.1.23}$$

where strains result only from changes in effective stress and if the material is isotropic, $\mathbf{D}_e$ contains only two independent material parameters. The assumption of linear elasticity and isotropy are not adequate to describe the behaviour of large volumes of granular material, wherein the stress-strain relation is nonlinear owing to the development of unrecoverable strains and the fabric of the granular structure is inherently anisotropic. However, the linear elastic isotropic constitutive model remains useful in the present work where the sub-domain of interest is a single grain or a representative volume of grains undergoing small enough strains that the behaviour is approximately linear elastic and isotropic. For sub-domains where the behaviour is truly nonlinear, such as at the interfaces between grains, the present work uses either nonlinear elasticity where $\mathbf{D} = \mathbf{D}(\boldsymbol{\varepsilon})$ or a form of flow plasticity where the rate form of equation (1.1.14) or an equivalent incremental form must be retained. The present work captures anisotropy through the discretization of the domain into convex polygonal regions using techniques described in Section 1.1.3, which directly captures the shape of the grains and the orientations of the interfaces on which they interact. Chapter 3 introduces the details of the formulations for the polygonal and interface sub-domains, as applicable. As with the seepage formulation, a special case of equation (1.1.12) on an internal surface S_i of zero volume that is useful in some formulations is,

$$\left(\mathbf{n}_\sigma^+ + \mathbf{n}_\sigma^-\right)^T \boldsymbol{\sigma} = \mathbf{0} \tag{1.1.24}$$

where $\mathbf{n}_\sigma^+ = -\mathbf{n}_\sigma^-$ represent the unit normals to S_i in opposite directions consistent with the vector representation of $\boldsymbol{\sigma}$,

$$\mathbf{n}_\sigma = \begin{bmatrix} n_x & 0 & 0 & n_y & 0 & n_z \\ 0 & n_y & 0 & n_x & n_z & 0 \\ 0 & 0 & n_z & 0 & n_y & n_x \end{bmatrix}^T \tag{1.1.25}$$

Again, to close the formulation, there are the boundary conditions,

$$\mathbf{u} = \hat{\mathbf{u}}(\mathbf{x},t) \text{ on } S_u \tag{1.1.26}$$

$$\mathbf{t} = \mathbf{n}_\sigma^T \boldsymbol{\sigma} = \hat{\mathbf{t}}(\mathbf{x},t) \text{ on } S_t \tag{1.1.27}$$

where $\hat{\mathbf{u}}(\mathbf{x},t)$ and $\hat{\mathbf{t}}(\mathbf{x},t)$ are the prescribed displacements and the prescribed tractions on S_u and S_t and the total domain boundary $S = S_u \cup S_t$.

At this point, the reader may be experiencing a sense of déjà vu, and quite rightly, as the set of governing equations for seepage and solid deformation bear a striking resemblance. Tonti [119] presents a general framework for understanding mathematical models of physical phenomena. This framework recognizes that many such models include a primary variable (h or $\mathbf{u}$), a flux variable ($\mathbf{q}$ or $\boldsymbol{\sigma}$) and a kinematic variable ($\mathbf{i}$ or $\boldsymbol{\varepsilon}$). The governing equations relating these variables in a volume of interest V consist of a balance equation (equation (1.1.1) or (1.1.12)), a kinematic equation (equation (1.1.2) or (1.1.13)) and a constitutive equation (equation (1.1.3) or (1.1.14)). To close the formulation, there are the kinematic/primary/Dirichlet boundary conditions (equation (1.1.7) or (1.1.26)) and the natural/flux/Neumann boundary conditions (equation (1.1.8) or (1.1.27)). There exist other special types of boundary conditions, but these are the classical forms. Tonti [119] also presents a method for mapping out how the governing equations relate the solution variables, which the author finds useful in understanding both the exact form of the equations and how approximate forms

derive from them. A description and presentation of this tool are outside of the scope of the present work, but the approach is worth acknowledging.

1.1.3 Voronoi cell

The term Voronoi cell derives from the concept of a Voronoi diagram, or Dirichlet tessellation, which is a structure that subdivides a domain V into a set of subdomains V_e based on their geometric distance to a set of cell points with coordinates $\mathbf{x}_e \; \forall e \in \{ 1, 2, \ldots N_e \}$ where N_e is the number of cell points. When V is infinite, the set of all V_e may consist of some finite and some infinite cells. When V is itself finite, all V_e will also be finite, and the diagram is sometimes qualified as a constrained or clipped Voronoi diagram. The present work uses only the latter type. The present work refers to Voronoi cells alternatively as polygonal elements, body elements or grain elements at various points, so e stands for "element". The names Dirichlet tessellation and Voronoi diagram derive from the mathematicians Dirichlet and Voronoi who pioneered their use within the context of proving the unique reducibility of quadratic forms [120,121]. The Voronoi diagram has found usefulness in a broad range of disciplines, attracting interest from mathematicians, computer scientists, natural scientists and engineers alike. The literature on this topic is vast, and a complete review is well beyond the scope of the present work. Aurenhammer [122] provides a comprehensive review of the origins of, applications of and literature on Voronoi diagrams up to 1991. This section presents only the components necessary to understand the application of the Voronoi diagram or Voronoi cells within the present work. In particular, although the concept of a Voronoi diagram extends to dimensions of arbitrary

order, the present discussion restricts itself only to planar Voronoi diagrams in two dimensions (2-D).

Consider a set of N_e cell points $\mathbf{x}_e$ $\forall e \in \{ 1, 2, \ldots N_e \}$ within a finite domain V, as Figure 1.2(a) shows for a case where $N_e = 17$. For two cell points $\mathbf{x}_i$ and $\mathbf{x}_j$ where $i \neq j$ and $i,j \in \{ 1, 2, \ldots N_e \}$, the dominance D_{ij} of $\mathbf{x}_i$ over $\mathbf{x}_j$ is the subdomain of V that is at least as close to $\mathbf{x}_i$ as to $\mathbf{x}_j$,

$$D_{ij} = \left\{ \mathbf{x} \in V : \left\| \mathbf{x} - \mathbf{x}_i \right\| \leq \left\| \mathbf{x} - \mathbf{x}_j \right\| \right\} \tag{1.1.28}$$

where $\|\mathbf{x} - \mathbf{x}_i\|$ represents the Euclidean distance between the points $\mathbf{x}$ and $\mathbf{x}_i$. The Voronoi cell V_i for cell point $\mathbf{x}_i$ is the intersection of the dominance regions of $\mathbf{x}_i$ relative to $\mathbf{x}_j$ $\forall j \neq i \in \{ 1, 2, \ldots N_e \}$,

$$V_i = \bigcap_{j \neq i} D_{ij} = \left\{ \mathbf{x} \in V : \left\| \mathbf{x} - \mathbf{x}_i \right\| \leq \left\| \mathbf{x} - \mathbf{x}_j \right\|, \forall j \neq i \right\} \tag{1.1.29}$$

The Voronoi diagram therefore has the following properties,

$$\begin{aligned} \bigcup_{e=1}^{N_e} V_e &= V \\ \bigcap_{e=1}^{N_e} V_e &= 0 \end{aligned} \tag{1.1.30}$$

which is to say that the set of subdomains V_e $\forall e \in \{ 1, 2, \ldots N_e \}$ subdivides the domain V with no gaps. As Figure 1.2(b) demonstrates, this construction guarantees that Voronoi cells are always convex polygons, provided that the domain boundary is a convex. An edge B_{ij} between contiguous Voronoi cells V_i and V_j is,

$$B_{ij} = \left\{ \mathbf{x} \in V : \left\| \mathbf{x} - \mathbf{x}_i \right\| = \left\| \mathbf{x} - \mathbf{x}_j \right\| < \left\| \mathbf{x} - \mathbf{x}_l \right\|, \forall l \neq i, j \right\} \tag{1.1.31}$$

which is a segment of the bisector line perpendicular to the line segment connecting

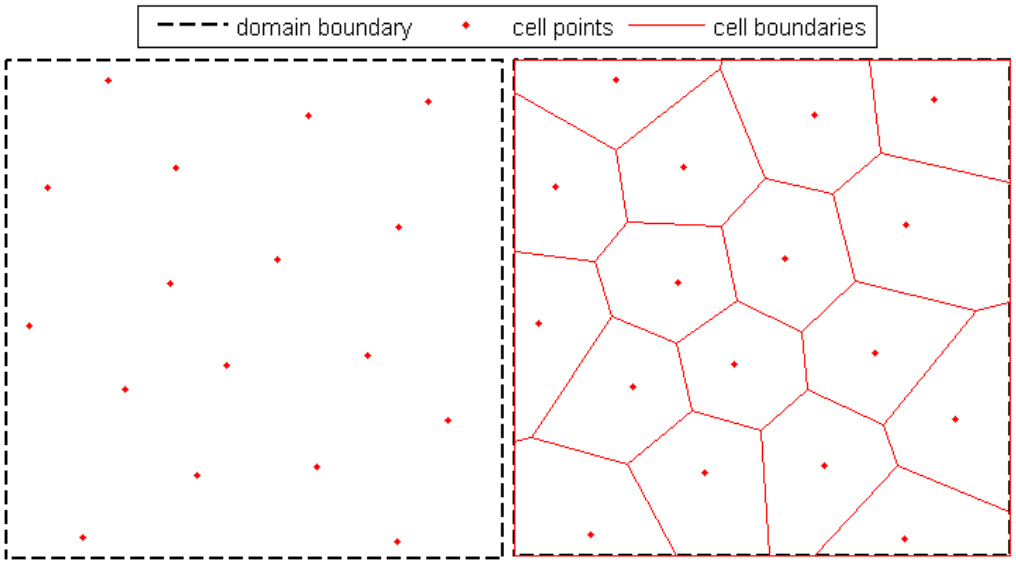

Figure 1.2 Example of a constrained Voronoi diagram. (a) A finite domain *V* and a set of cell points $\mathbf{x}_e$. (b) Domain subdivided into Voronoi cells V_e.

$\mathbf{x}_i$ and $\mathbf{x}_j$. A vertex V_{ijk} of three mutually contiguous Voronoi cells V_i, V_j and V_k is,

$$V_{ijk} = \left\{ \mathbf{x} \in V : \left\| \mathbf{x} - \mathbf{x}_i \right\| = \left\| \mathbf{x} - \mathbf{x}_j \right\| = \left\| \mathbf{x} - \mathbf{x}_k \right\| < \left\| \mathbf{x} - \mathbf{x}_l \right\|, \forall l \neq i, j, k \right\} \quad (1.1.32)$$

which, by its equidistance from $\mathbf{x}_i$, $\mathbf{x}_j$ and $\mathbf{x}_k$, implies that it is the centre of a circle having these three points on its circumference and no other cell points inside it.

From the definitions above, one may conceive of several approaches to generating the Voronoi diagram. Green and Sibson [123] present a recursive algorithm making use of the definition V_{ijk} to find nodes and contiguities by traversing clockwise around $\mathbf{x}_i$ finding the vertices of the cell V_i by locating the centres of circles V_{ijk} containing no other $\mathbf{x}_l$ $\forall l \neq i,j,k$. They note that degenerate vertices can occur if there exist circles with four cell points on their circumference and no other cell points inside, such as in a regular grid arrangement of cell points, which requires special treatment. Ghosh and Mukhopadhyay [124], using the algorithm of Green and Sibson [123] as a basis, discuss techniques for obtaining constrained Voronoi diagrams of concave domains by inserting cell

points mirrored about the bisector line through each concave vertex. This technique is also useful when one wishes to guarantee a node at a particular location on a boundary segment, for example, when the boundary conditions change at that point. Rycroft [125] presents a library for generating three-dimensional (3-D) Voronoi cell diagrams. The basis of the mesh generation algorithm in this library is the use of the bisector line definition in equation (1.1.31), which are used to recursively slice parts of the total domain V from each cell. The author used the concepts from [123-125], along with the general definitions of a Voronoi cell diagram in 2-D described above, to implement a mesh generator for the present body of work.

1.1.4 Finite element method

The finite element method (FEM) is a branch of numerical analysis wherein one discretizes mathematical models for physical phenomena into finite subdomains and interpolates key variables in a manner that satisfies certain governing equations, continuity and/or compatibility requirements, often based on an energy stationarity principle or an expression of virtual work. As the present work involves application of different types of finite element formulation to geomechanical modelling, this section has two aims: i) to define some important types of finite element formulation along with their advantages and limitations, and ii) to provide a brief review of the literature on applications of finite elements to geomechanical analysis. This section does not provide the complete details of the formulations used in the present work, since the body chapters provide this.

Rather, this section provides the necessary background motivating the present work.

Finite element formulations begin with a variational principle or an expression of virtual work. Washizu [126] provides one of the earliest, but still one of the most comprehensive views on variational methods for continuum-based solid mechanics problems. For example, considering the set of equations describing the solid deformation in Section 1.1.2, the most general form of variational principle for a linear elastic solid under static unsaturated conditions where $\boldsymbol{\sigma} = \mathbf{D}_e\boldsymbol{\varepsilon}$, $\ddot{\mathbf{u}} = \mathbf{0}$ and $\boldsymbol{\sigma} = \boldsymbol{\sigma}'$ is the Hu-Washizu principle,

$$\begin{aligned}\Pi_{HW}\left[\mathbf{u},\boldsymbol{\varepsilon},\boldsymbol{\sigma},\mathbf{t}\right] = \int_V \left(\tfrac{1}{2}\boldsymbol{\varepsilon}^T\mathbf{D}_e\boldsymbol{\varepsilon} - \mathbf{u}^T\mathbf{f}_b\right)dV - \int_V \boldsymbol{\sigma}^T\left(\boldsymbol{\varepsilon} - \mathbf{L}_{\sigma u}\mathbf{u}\right)dV \\ - \int_{S_t}\left(\mathbf{u}^T\hat{\mathbf{t}}\right)dS - \int_{S_u}\mathbf{t}^T\left(\mathbf{u}-\hat{\mathbf{u}}\right)dS\end{aligned} \tag{1.1.33}$$

The statement of the variational principle is that for all of the kinematically and statically admissible fields $\mathbf{u}$, $\boldsymbol{\varepsilon}$, $\boldsymbol{\sigma}$ and $\mathbf{t}$, the actual solution is given by the set of fields that achieve stationarity of Π_{HW}, which is to say that the first variation $\delta\Pi_{HW}$ vanishes. It is important to use the term stationarity, since the solution when $\delta\Pi_{HW} = 0$ could represent a minimum, maximum or saddle-point of the functional space. Applying the first variation gives,

$$\begin{aligned}\delta\Pi_{HW} = \int_V \delta\boldsymbol{\varepsilon}^T\left(\mathbf{D}_e\boldsymbol{\varepsilon} - \boldsymbol{\sigma}\right)dV - \int_V \delta\boldsymbol{\sigma}^T\left(\boldsymbol{\varepsilon} - \mathbf{L}_{\sigma u}\mathbf{u}\right)dV - \int_V \delta\mathbf{u}^T\left(\mathbf{L}_{\sigma u}^T\boldsymbol{\sigma} + \mathbf{f}_b\right)dV \\ + \int_{S_t}\delta\mathbf{u}^T\left(\mathbf{t}-\hat{\mathbf{t}}\right)dS - \int_{S_u}\delta\mathbf{t}^T\left(\mathbf{u}-\hat{\mathbf{u}}\right)dS + \int_{S_u}\delta\mathbf{u}^T\left(\mathbf{n}_\sigma^T\boldsymbol{\sigma} - \mathbf{t}\right)dS = 0\end{aligned} \tag{1.1.34}$$

from which it is clear that for arbitrary variations $\delta\mathbf{u}$, $\delta\boldsymbol{\varepsilon}$, $\delta\boldsymbol{\sigma}$ and $\delta\mathbf{t}$ the governing equations give the conditions for stationarity of $\delta\Pi_{HW}$. Such a general principle gives a firm mathematical basis for the theory of finite elements. However, its

generality is both its strength and its weakness. The introduction to this section stated that the other key component of the finite element method is the interpolation of the unknown fields satisfying the continuity, compatibility and/or equilibrium conditions implied by the variational principle or statement of virtual work on which it is based. The Hu-Washizu principle, with four independently varying fields, simply has too many such requirements to satisfy. Therefore, all finite element methods of practical importance select a subset of the governing equations to satisfy in the "strong" sense – that is, satisfying the governing equations directly – and only including a subset of the "weak" or integrated residual forms in the underlying principle.

Perhaps the most popular example is the principle of minimum total potential energy, which assumes strong form satisfaction of all governing equations except for equilibrium – equation (1.1.12) – and the traction boundary conditions – equation (1.1.27) – giving the following form,

$$\Pi_{TPE}\left[\mathbf{u}\right] = \int_V \left(\tfrac{1}{2}\boldsymbol{\varepsilon}^T \mathbf{D}_e \boldsymbol{\varepsilon} - \mathbf{u}^T \mathbf{f}_b\right) dV - \int_{S_t} \left(\mathbf{u}^T \hat{\mathbf{t}}\right) dS \tag{1.1.35}$$

where ones assumes satisfaction of the kinematic relation $\boldsymbol{\varepsilon} = \mathbf{L}_{\sigma u}\mathbf{u}$ in the strong sense. An equivalent expression for seepage analysis is,

$$\Pi_h\left[h\right] = \int_V \left(-\tfrac{1}{2}\mathbf{i}^T \mathbf{K} \mathbf{i}\right) dV - \int_{S_q} \left(h\hat{q}\right) dS \tag{1.1.36}$$

where again one assumes $\mathbf{i} = \mathbf{L}_{qh}h$. A large body of literature on the theory and application of finite elements based on such principles exists, and a complete bibliography is beyond the scope of the present work. Clough [127,128] discusses the early history of the development of the FEM. Melosh [129] discusses

techniques for assessing the convergence of FEM solutions to acceptable error tolerance, and Oden [130] discusses techniques for adaptive refinement of the mesh and the order of interpolation functions to obtain the "best" solution to a given problem. Examples of general texts on the FEM, focussed in large part on this approach, are that of Bathe [131], Cook et al. [132], Strang and Fix [133] and Zienkiewicz et al. [134]. This approach is the most popular because of its elegance – beauty arising from simplicity and effectiveness – since it has only a single solution variable **u**. It requires interpolation of **u** such that one can compute $\boldsymbol{\varepsilon} = \mathbf{L}_{\sigma u}\mathbf{u}$ directly, continuity of **u** between elements and satisfaction of $\mathbf{u} = \hat{\mathbf{u}}$ on S_u (or equivalent requirements for seepage analysis). For elements with simple shapes such as triangles and quadrilaterals in 2-D or tetrahedra and hexahedra in 3-D, this is straightforward to accomplish. Methods based on Π_{TPE} are also easy to extend to account for nonlinear constitutive behaviour, which is important in geomechanics since linear elasticity certainly does not apply throughout the domain. The elegance of this approach has led to its adoption by the developers of most popular commercial finite element software packages. Owing to its popularity, the present work sometimes refers to this principle as the "conventional" approach. Of course, within the context of scientific and engineering research, the term conventional often implies to the reader that the author really means "outdated" and that their "new and improved" approach is somehow better. The author does not generally intend this alternate meaning, unless explicitly stated. Indeed, the ease with which this approach handles nonlinear behaviour makes it a good choice for representing the interactions between grains in geomaterials, as Chapter 3 of the present work demonstrates.

However, there are certain cases when alternate approaches provide advantages over the Π_{TPE} approach. For example, while the triangular/quadrilateral (tetradhedral/hexahedral in 3-D) shaped elements usually employed in analyses using this approach are well suited to discretizing continua, they do not provide adequate geometric representation of the grains in geomaterials. Polygons (polyhedra) provide a better geometric representation of such grains. While conforming shape functions for **u** or *h* satisfying continuity requirements exist [135- 143], they are not in closed form for polygonal elements with >4 nodes. This means that direct computation of $\boldsymbol{\varepsilon} = \mathbf{L}_{\sigma u}\mathbf{u}$ is not possible and one must resort to numerical approximations [144]. Therefore, to represent a polygonal subdomain using conventional triangular elements and standard interpolation functions, one must discretize the polygon into several triangular elements – a hexagon becomes six triangles. It would be more efficient to represent such a subdomain with a single element, if possible. Another consequence of the conventional Π_{TPE} formulation is that, since it uses a single primary solution variable (**u** or *h*), it computes the values of the secondary variables (**ε** and **σ** or **i** and **q**) through differentiation of the approximate interpolated values of the primary variable. Since differentiation is a subtractive process, the positive and negative errors in the approximate **u** or *h* fields tend to accumulate [145]. The consequence is that the values of the secondary variables can be quite inaccurate and equilibrium is generally not satisfied at an arbitrary point in the domain.

Finite elements that use more than one primary solution variable – called mixed or hybrid finite element methods [146-148] – circumvent some of the

disadvantages of the Π_{TPE} approach. Again, the literature on mixed and hybrid finite elements is vast, and the author does not intend to present a complete review of this literature here. This paragraph summarizes the approach, advantages and limitations of a specific class of hybrid finite element method first presented by Pian [149], formalized by Tong and Pian [150,151] and extended for polygonal and polyhedral elements by Ghosh and co-workers [152- 157], all within the context of solid mechanics analysis. The hybrid principle begins with a modified statement of complementary energy,

$$\Pi_{MCE}\left[\mathbf{u}^*,\boldsymbol{\sigma}\right] = -\tfrac{1}{2}\int_V \left(\boldsymbol{\sigma}^T\mathbf{D}_e^{-1}\boldsymbol{\sigma}\right)dV + \int_S \mathbf{u}^{*T}\left(\mathbf{n}_\sigma^T\boldsymbol{\sigma}\right)dS - \int_{S_t}\left(\mathbf{u}^{*T}\hat{\mathbf{t}}\right)dS \qquad (1.1.37)$$

Chapter 2 shows that an equivalent principle for seepage analysis is,

$$\Pi_{qh}\left[h^*,\mathbf{q}\right] = \tfrac{1}{2}\int_V \left(\mathbf{q}^T\mathbf{K}^{-1}\mathbf{q}\right)dV + \int_S h^*\left(\mathbf{n}_q^T\mathbf{q}\right)dS - \int_{S_q}\left(h^*\hat{q}\right)\,dS \qquad (1.1.38)$$

Compared with the Π_{TPE} approach, the key differences with this approach are:

i) there are two primary solution variables ($\mathbf{u}^*$ and $\boldsymbol{\sigma}$ or h^* and $\mathbf{q}$),

ii) one need only interpolate $\mathbf{u}^* \subset \mathbf{u}$ (or $h^* \subset h$) on the boundaries of an element, and

iii) the interpolation of $\boldsymbol{\sigma}$ or $\mathbf{q}$ must satisfy the equilibrium equations.

The consequence of (i) and (ii) is that the kinematic variable ($\boldsymbol{\varepsilon}$ or $\mathbf{i}$) need not be determined in the solution, though one could determine them through the constitutive relation, if desired. The flux variables $\boldsymbol{\sigma}$ and $\mathbf{q}$ need not be continuous between elements since the second term in Π_{MCE} satisfies equilibrium between elements in a weak sense. As such, constructing interpolations of the flux variables that satisfy the homogeneous equilibrium equations in the domain of a

polygonal element with an arbitrary number of nodes is straightforward using a potential function approach – Airy's stress function [cf. 118] for solid mechanics, or a streamline function for seepage. Owing to the lack of continuity requirements for the flux field interpolation, one may eliminate the unknown coefficients of the potential function at the element level, which means that the global system of equations for a hybrid finite element mesh has the same number of equations as a conventional finite element mesh with the same number of nodes. The use of a potential function seems to restrict the hybrid approach to cases of linear constitutive behaviour. Ghosh and Moorthy [155] describe a method for incorporating elastoplastic constitutive behaviour into a hybrid finite element solution, though in later work Hu and Ghosh [158] move to a so-called "local enhancement" approach that actually replaces hybrid elements with conventional elements in regions where inelastic behaviour occurs. The present author found the implementation of elastoplasticity within a hybrid formulation to be awkward at best. Nonetheless, when the constitutive behaviour is linear, hybrid polygonal elements provide certain advantages in terms of representing the geometry of the microstructure of geomaterials.

This section concludes with a brief review of some specialized finite elements used to model discontinuities in geomaterials and/or strain localization in granular materials, as this provides the necessary context for Chapter 3 of the present work. The focus is on two distinct approaches. The first is the use of special elements representing strong discontinuities in the material, such as rock joints or interfaces between grains, for which one may prescribe the geometry a priori. The second approach is the generation of localization zones within

continuum finite elements, which requires careful consideration of the criterion for the propagation of strain localization zones and the mesh sensitivity associated with the softening regime.

The earliest example of a finite element for a strong discontinuity is the joint element developed by Goodman et al. [159], which uses an iterative correction procedure to account for the differing constitutive behaviour in jointed rock under compression and separation regimes. Zienkiewicz et al. [160] examine behaviour in jointed rock by formulating the interface element as an isoparametric finite element accounting for nonlinear behaviour. Katona [161] examines soil-structure interaction around buried culverts using an interface element based on a constrained virtual work principle accounting for various deformation modes. Herrmann [162] improves the element of Goodman et al. [159] by introducing constraint conditions and accounting for sliding and debonding constitutive behaviour. Desai et al. [163] propose a thin-layer element that accounts for the finite thickness of the interface, rather than zero thickness as in earlier formulations, and also incorporates stick, slip, debonding and rebonding deformation modes into the analysis. Wang et al. [164] use special shear band elements to examine cases of shear band kinking – the intersection of multiple shear bands at the macro-scale. This approach requires a mesh updating procedure to avoid pathological behaviour owing to undesirable element aspect ratios. Wang et al. [164] prescribe the location of the shear band to demonstrate the technique, so it should be noted that the approach could not predict the generation of shear bands. Selvadurai and Yu [165] examine the behaviour at a discontinuity in a geomaterial, which one could interpret at the macro-scale as a rock joint, or at the

micro-scale as the contact between two grains. In particular, they noted the importance of considering the different behaviour in different deformation modes including frictional shear and dilation. They also examined the influence of surface topography on the behaviour at the interface, which can lead to failure of the parent material or incompatible movements of the contacting material.

An example of embedding strain localization zones within continuum-based finite elements is the approach of Pietruszczak and Mróz [166], who capture softening behaviour in granular materials. They use an associated flow rule with a simple yield function based on the Coulomb criterion with variable cohesion. They prescribe the thickness of the shear band as a parameter, which controls the tangent stiffness of the element. They also determine the orientation of the shear band from the Coulomb orientation relative to the orientation of the principal stresses. Therefore, one should still regard such analysis as phenomenological since it cannot predict the orientation or thickness of the shear band from fundamental characteristics of the granular material such as the grain structure. Belytschko et al. [167] advance this approach using a three-field mixed formulation in which a bifurcation analysis on the element level determines the formation of the strain localization zone, though they note that the analysis still does not determine the thickness of the shear band. The condition for shear band formation in their analysis is a loss of ellipticity of the governing equations associated with the softening regime, and they show that there is little mesh sensitivity for sufficiently refined meshes. Wan et al. [168] generate embedded localization zones within continuum-based finite elements to capture strain localization leading to collapse of soil slopes. In their approach, they represent the

localization zone with a special element, and incorporate discontinuities into the interpolation functions for the parent continuum element. This allows generation of strain localization zones within elements along an orientation determined by a prescribed criterion – for example, Mohr-Coulomb – as the analysis progresses without having to regenerate the original mesh. Pietruszczak and Niu [169] examine the embedded localization zone approach further, incorporating a characteristic length scale determined by partitioning the element area, virtually eliminating mesh sensitivity in the results. Larsson et al. [170] apply the concept of regularization to supposedly eliminate mesh sensitivity in the formation of strain localization bands. However, it is worth noting that Larsson et al. [170] only demonstrate mesh insensitivity with regard to mesh density, and the orientation of the strain localization zone still seems to follow the orientation of the mesh of triangular elements. The present author points out that this is the more important form of mesh sensitivity for a mesh of continuum based finite elements not accounting for the microstructure of the material. Chen et al. [171] introduce an internal length scale and show that the regularization technique can be applied to obtain true mesh insensitivity using a meshfree approximation to simulate the generation of multiple strain localization bands propagating from an asymmetric imperfection. They demonstrate that the results are insensitive to the mesh when comparing different levels of mesh refinement and when comparing regular and irregular mesh configurations. Wang et al. [172] combine their earlier work on special shear band elements with regularization techniques and a Mohr-Coulomb strength model to generate shear band elements as part of the simulation. This overcomes the issues associated with prescribing the location of shear band

elements, allowing prediction of shear band formation while avoiding mesh sensitivity. However, the use of the Mohr-Coulomb criterion to prescribe the orientation of the shear band contradicts the evidence cited in Section 1.1.2 that shear bands may form at other orientations, theoretically bounded by the Roscoe and Coulomb orientations. Samaniego and Belytschko [173] also achieve mesh insensitivity analyzing similar examples as in [171] using the extended finite element method (XFEM) to incorporate shear band propagation. Within the XFEM, the shear bands may be inserted at arbitrary orientations within the mesh according to an appropriate fracture propagation criterion, resulting in insensitivity to the mesh configuration. Such mesh insensitivity is desirable for continuum-based models of damage in metals, which was the application area in [171] and [173]. However, the present author questions whether insensitivity to mesh configuration is truly desirable for granular materials where irregularities in the grain structure are important in the generation of shear bands. An alternative approach is to harness the "mesh sensitivity" by constructing the mesh in a manner that represents the physical grain structure, as in the present work.

1.1.5 Discrete element method

The discrete or distinct element method (DEM) is an alternative approach to numerical modelling of granular materials wherein the method represents individual grains and their interactions. Cundall [174] proposes the DEM as a method for analyzing blocky rock systems. Cundall and Strack [175] present the DEM as a general approach to modelling assemblies of grains, whether these represent blocks in a jointed rock system or grains in a granular material. The

earliest version represents the grains as disc-shaped particles [175], but Cundall [176] and Hart et al. [177] later extend the method for use with convex polyhedral blocks. Ting et al. [178], Ng [179] and Lin and Ng [180] present the modifications necessary to employ the DEM to elliptical and ellipsoidal shaped particles. Clearly, models using simpler grain shapes such as spheres or ellipsoids make detection of contact easier, but may not accurately reflect the grain shape of many granular materials that have angular or subangular grains. Polyhedral grains better represent granular materials, but require tracking of a larger number of interaction types (point-to-point, point-to-edge, point-to-face, edge-to-face, face-to-face). Cundall [176] introduces the common plane approach to reduce the number of tests required by testing only for contact with a plane between two potentially contacting blocks. Most of the early approaches assume that the discrete elements are rigid since the deformation of particles is often small in comparison to their relative movements. Barbosa and Ghaboussi [181] extend the DEM to account for deformation of the discrete particles by sub-discretizing each particle with a FEM mesh. Boon [182] closely examines contact detection and block generation in DEM analyses of jointed rock masses involving polygonal or polyhedral elements, and develops novel and efficient algorithms for this purpose.

Within the DEM, the normal force between contacting grains is proportional to their overlapping volume. The shear force transfer may be non-slip if frictional dissipation is not of interest, or may account for frictional sliding using Coulomb frictional resistance. Grains may be rigid or deformable with the former preferred when the deformation of the grains is small compared to the deformation caused by relative movement between grains. When deformable polyhedral blocks are

desirable, the blocks are typically discretized into an internal mesh of finite elements [177].

Cambou [64] cites DEM as one of the principal numerical approaches used to understand the micromechanics of granular materials. Indeed, several of the studies cited in Section 1.1.2 use the DEM to simulate strain localization in granular materials [29,72,74,75,93,96,97,101]. This is just a small sampling of the vast body of literature applying the DEM to numerical modelling of discontinua. The present work does not present the details of the formulation of the DEM, as it not the focus. Radjaï and Dubois [183] and Cambou et al. [70] compile works representing the state-of-the-art as of the end of the first decade the 21st century. The present author recognizes the advantages of the DEM with regard to modelling the details of the behaviour of granular material. Chapter 3 of the present work develops an alternative approach, with its own set of advantages and disadvantages, but the aim is not to diminish the advantages of the DEM approach. To paraphrase Cambou in the preface to [64] when describing the complementary nature of micromechanical, DEM and FEM analyses, the alternative technique presented herein is complementary to the foregoing approaches and seeks to contribute to a better understanding of the behaviour of granular materials.

1.1.6 Combined finite-discrete element method

The approaches of the finite element method and the discrete element method are extreme cases in which the formulation assumes a continuum and a collection of interacting grains, respectively. Another class of analysis techniques

used to model geological materials is the combined finite-discrete element method (FEM-DEM), which makes use of ideas from these two categories. The modelling framework presented in Chapter 3 of the present work fits best into this category. This section presents a brief summary of the literature on FEM-DEM modelling approaches. It is worth noting that the definition of FEM-DEM is somewhat vague. The present work takes a loose definition as any numerical analysis technique that uses some form of continuum formulation, but breaks the domain into sub-regions that interact in a manner different from that of the basic continuum elements. Therefore, some of the methods described in this section may not even call themselves FEM-DEM, though they combine ideas from both analysis frameworks. In all such methods, one must define the rules governing the contact between the sub-regions. For granular materials, these rules should capture the fact that grain interfaces have negligible resistance to separation, high stiffness in compression and nonlinear dissipative constitutive behaviour in shear.

Material point method (MPM) models including a contact algorithm have been used to model a variety of micro-scale contact problems [184,185] and macro-scale problems involving multiple material phases [186]. The “material points” carry relevant calculation data – material properties, stresses, velocities – and move through a fixed calculation grid. The solution at each time step uses a three part explicit algorithm to account for interaction between contacting bodies: i) solution of velocities assuming all material points are a single body, ii) solution of velocities for each individual body ignoring the influence of surrounding bodies and iii) velocity correction based on the difference between the velocities determined in the first and second phases. The presumption is that the calculated

velocities from phases (i) and (ii) will differ only when bodies are interacting. This approach can handle grains of arbitrary shape and does not require pair-wise comparison to determine which specific grains are interacting. The MPM combines a formulation loosely based on a dynamic FEM formulation in phases (i) and (ii) with the idea of accounting for interaction between discrete particles from DEM in phase (iii). This approach is able to account for grain interactions, but apparently requires many material points to represent each grain and small numerical time steps. This leads to simulations that are computationally expensive even for a modest number of grains.

Munjiza et al. [187] propose the combined finite-discrete element method (FEM-DEM) within the context of modelling the transient dynamics of fracturing solids such as rock and concrete. The text of Munjiza [188] provides the most complete description of the method and its applications to date. The FEM-DEM approach uses a combination of constant strain triangular body finite elements to represent volumes of material with linear elastic constitutive behaviour and joint elements to account for the nonlinear behaviour associated with fracture propagation [189]. This approach differs from the discrete finite element method described in reference [181] in that it accounts for grain interactions using interface finite elements rather than relying on contact detection algorithms based on overlapping element volumes. This has the advantage of reducing the complication involved in modelling grain interaction, but sacrifices the ability to model large strain behaviour wherein the contact relationships between grains may change during the simulations. Mahabadi et al. [189] describe the most recent version of the FEM-DEM model. This approach is sufficient for modelling

fracture propagation in materials such as concrete and rock, which was the focus of applications of this group. However, triangular elements may not accurately reflect the shape of the grains in granular materials, which plays an important role in the strain localization phenomena described in Section 1.1.2.

Chapter 3 of the present work focusses on extending the FEM-DEM approach using convex polygonal Voronoi cell elements in an approach termed VCFEM-DEM. As the body of that chapter discusses in detail, this modification allows the VCFEM-DEM to capture many of the important phenomena associated with strain localization in granular materials.

1.2 Summary of Contributions

This section provides a summary of the key research contributions of the present work. The topic of this thesis is the modelling of geomaterials using the Voronoi cell finite element method (VCFEM), and where applicable, VCFEM combined with elements accounting for interactions between the VCFEM elements. Two of the most important phenomena of practical importance in the modelling of geomaterials are transport of fluid through the pores and their deformation response to applied loads. Since geological materials, whether in situ or when used as a construction material, are exposed to the natural environment, these two phenomena often occur simultaneously. Methods for analyzing certain aspects of these phenomena already exist, each with its own advantages and disadvantages, as Section 1.1 discussed. The present work adds to this body of knowledge by exploring techniques for analyzing geomaterials using VCFEM and VCFEM-DEM. This exploration revealed certain situations when this approach

has its own advantages, but it is important to note that the author does not purport it to be a solution for all numerical analysis issues or necessarily a replacement for existing techniques. The following lists the most important technical contributions of this work, with a brief description of each and references to the corresponding body sections that provide further details.

Extension of VCFEM to seepage analysis, including location of free surface in unconfined seepage

The key feature of this contribution is the application of the hybrid VCFEM functional to field problems described by the Laplace equation. Previous applications of hybrid FEM and hybrid VCFEM were in the context of solid mechanics, and the extension of the hybrid VCFEM to field problems is of academic interest. This part of the work also included an investigation of the sensitivity of the solution to mesh configuration and choice of conforming shape function, with particular focus on the solution of unconfined seepage problems, which require iteration to locate the free surface. With regard to mesh sensitivity, hybrid FEM analysis using four-node quadrilateral elements displayed sensitivity in terms of the location of the free surface, whereas hybrid VCFEM using polygonal elements having greater than four nodes – primarily six-node hexagonal elements – did not show significant mesh sensitivity. The choice of conforming shape function did not have a significant influence on the results. Section 2.1 presents the details of the formulation and a discussion of the results.

Simulation of strain localization in biaxial compression tests on granular material using static and dynamic VCFEM-DEM

The phenomenon of strain localization is a behaviour observed in geomaterials at the macro-scale, but develops because of interactions at the grain-scale. Examples of this include shear band failure in laboratory compression tests and slope failure where a distinct failure surface forms. Such strain localization in granular materials is akin to fracture propagation in metals and rock, but the modelling details differ owing to the lack of any tensile resistance between the grains. The literature on the various approaches to modelling this behaviour is extensive, as Section 1.1.2 discussed. The present work examines both static and dynamic VCFEM-DEM models for granular behaviour. The key feature of this modelling approach is that it employs two types of element: i) polygonal VCFEM body elements representing the grains or representative volumes of material where the constitutive behaviour is linear elastic and ii) interface elements that capture the interaction between grains with nonlinear constitutive behaviour owing to the frictional sliding that occurs. In the static model, the interface elements use a form of nonlinear elastic constitutive model with stress correction according to the Coulomb yield criterion. Consideration of rotation of coordinate axes is not necessary here since the interface defines the local failure plane. The dynamic model uses a form of isotropic combined volumetric-deviatoric hardening plasticity to capture the nonlinear interactions at the grain interfaces. Both types of model are capable of capturing the strain localization phenomenon in laboratory scale simulations. Although several modelling frameworks for strain localization exist, the most important contribution of this work and the VCFEM-

DEM approach is that it allows for the development of strain localization owing to the material fabric, as opposed to stress concentrations at boundary conditions, prescribed variations in void ratio or arbitrary mesh orientations. It does this by discretizing the domain so that mesh sensitivity – a topic often discussed in the literature on numerical analysis of granular materials with the aim of its elimination [167,170-173] – becomes a representation of the actual material fabric rather than an artificial numerical artifact. In addition, scrutiny of the shear stresses in the grains during the simulations reveals strong inhomogeneities in the shear stress distribution, even after the initial consolidation phase, which form the "fingerprint" of the failure of the granular specimen. The author forwards that such inhomogeneities in the stress field are as important to understanding the strength of granular materials as dislocations and imperfections are in understanding the real strength of metals. Section 3.1 discusses the formulation of the static VCFEM-DEM model and some preliminary results, Section 3.2 provides additional results and completes the discussion using the static model and Section 3.3 contains the formulation and discussion of results using the dynamic VCFEM-DEM model.

Examination of deformation patterns in granular materials using dynamic VCFEM-DEM and tangent eigenanalysis

In addition to capturing strain localization and stress inhomogeneity in laboratory simulations, the dynamic VCFEM-DEM modelling framework allows the examination of deformation modes in granular materials through eigenanalysis. This sort of analysis is not possible within DEM frameworks that do not necessarily construct global mass and stiffness matrices. Examination of

the deformation modes reveals two primary categories. The first category consists of "global" modes where the grains deform together as a structure. The second, and more interesting, category consists of "local" modes where there is significant relative movement between grains. Modes in the latter category correspond to various failure modes observed in laboratory testing of granular materials. The character and relative importance of the modes to the deformation of the specimen depend on the levels of stress and accumulated plastic strain in the interface elements, and change as the test progresses. The eigenanalysis of the deformation modes provides an additional technique for understanding the characteristic length scale of the failure of granular materials in laboratory tests. Sections 3.3.2.5 and 3.3.3.2 present the details of the formulation and discussion of the results related to this contribution.

Examination of influence of force chaining in granular materials on subsurface stress distribution owing to self-weight using VCFEM-DEM

Estimations of the subsurface stress distribution for practical applications typically assume idealized conditions with stress increasing linearly with depth. The real subsurface stress distribution for granular materials may be more complex owing to heterogeneities in material properties and material fabric. The present work examines the statistical distribution of subsurface stress with the realization that the stress due to soil self-weight at a given point in the subsurface is not entirely due to the soil directly above it. Using the VCFEM-DEM modelling framework, with the implementation of body forces owing to gravity, the present work examines the influence of the material fabric on the distribution of subsurface vertical stress. The length scale over which non-uniformities in

subsurface stress exist – stress "fingers" –is similar to the length scale of shear banding in laboratory simulations. Since this is approximately 3-10 grains, such variations are not important for sands and fine gravels, but may be significant for granular materials such as blocky rock or glacial tills, which can have large variations in grain size. Section 3.4 discusses the details of this contribution.

Coupled modelling of seepage through and deformation of geomaterials using VCFEM

Analysis of coupled hydromechanical behaviour of porous materials is important in many geotechnical engineering problems. For example, the design of an earth dam requires prediction of the seepage through the dam including location of the free surface, as well as the deformation and effective stress distribution. The key solution variables are pore pressure, specific discharge, effective stress and displacement, with the accuracy of all four being important. The present work extends the implementation of body forces in the hybrid VCFEM to account for self-weight, pore fluid pressure and seepage forces. Assuming that the distribution of pore pressure and specific discharge influences the stress and deformation of the solid, but not vice versa, the calculation proceeds in two phases. The first phase determines the pore pressure and specific discharge distributions using the VCFEM formulation from Chapter 2. The second phase determines the deformation and stress in the solid phase using the pore pressure and volumetric seepage force – determined from the specific discharge field – distributions as known body force fields. The key contribution here is the successful implementation of body forces in a hybrid formulation, which the developers of hybrid finite elements proposed at an early stage, but for which

there is a notable lack of examples in the literature. Chapter 4 presents the formulation and demonstrates the performance on a problem of practical interest in geotechnical engineering.

2 Seepage Analysis using VCFEM

2.1 Journal Paper #1: Investigation of a hybrid polygonal finite element formulation for confined and unconfined seepage[1]

2.1.1 Introduction

Our objective in this paper is to present the formulation and implementation of hybrid polygonal finite elements within the context of field problems described by Laplace's equation, taking steady state seepage through porous media as the focus. The solution of such problems using analytical methods and numerical methods such as finite elements, finite differences and finite volumes comprises a large body of literature [190- 205] and these schemes are indeed capable of obtaining accurate solutions. Our motivation in investigating the hybrid polygonal element formulation is two-fold: (i) the attractiveness of the improvement in flux field accuracy obtained by satisfying equilibrium (mass balance), a priori [149,150,153] without significant additional complexity in the formulation; and (ii) an interest in extending the analysis to a discontinuous FEM also involving flow through pore or fracture networks for which polygonal elements better represent the micro-scale geometry of geomaterials. Toward the latter motivation, in the present work we examine the hybrid polygonal FEM for analysis of continua, in particular with regard to sensitivity to mesh configuration. The purpose is to build confidence for later studies of discontinua, that sensitivity to

[1] Karchewski B, Pekinasova A, Stolle D, Guo P. Investigation of a hybrid polygonal finite element formulation for confined and unconfined seepage. Submitted 01/2015 to *International Journal for Numerical and Analytical Methods in Geomechanics*.

mesh configuration derives from real physical influences of the material fabric, rather than artificial influences from the mesh. For simplicity, in the present study we assume deterministic material properties, although one can extend the analysis to include stochastic analysis that takes into account the influence of material inhomogeneity.

Conventional finite element formulations for field problems use a single primary variable – for steady state seepage typically hydraulic head or pressure – and determine the flux variable through gradients of the interpolation functions for the primary variable. Section 2.1.2 of this paper compares the conventional and hybrid formulations, to examine the consequences of determining the flux variable through gradients of the approximate solution for the primary variable. We also discuss the manner in which the hybrid formulation overcomes some of the unattractive features of the conventional approach with respect to flux field accuracy. Section 2.1.2 closes by presenting the hybrid formulation for polygonal elements and extending the hybrid formulation for cases of unconfined seepage. Section 2.1.3 presents a series of numerical examples including confined seepage beneath a dam with a sheet pile, unconfined seepage through a rectangular earth dam and unconfined seepage through an inhomogeneous earth dam with a clay core. Section 2.1.4 gives concluding remarks on the performance of the hybrid polygonal finite element and goals for the future development of this approach.

2.1.2 Formulation

We begin by defining the problem within the context of steady seepage of a single fluid phase through a saturated homogeneous porous medium. Without loss

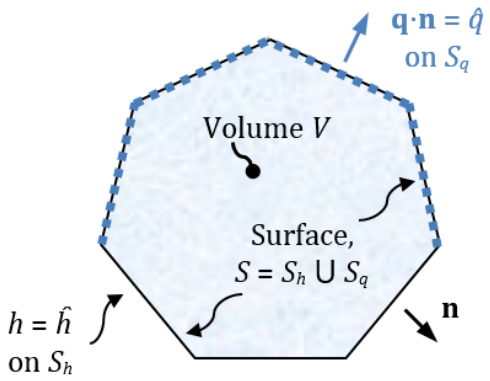

Figure 2.1 Domain of steady seepage problem with classical boundary conditions

of generality, consider Figure 2.1, which shows a convex polygonal domain V with outer surface S. The well-known Euler equations that must be satisfied in V are,

$$\mathbf{i} = \mathbf{L}_{qh} h \tag{2.1.1}$$

$$\mathbf{q} = -\mathbf{K}\mathbf{i} \tag{2.1.2}$$

$$\mathbf{L}_{qh}^{T}\mathbf{q} - s = 0 \tag{2.1.3}$$

where h is the total hydraulic head, $\mathbf{i}$ represents the hydraulic gradient, $\mathbf{q}$ is the specific discharge, $\mathbf{K}$ is the second order tensor representing hydraulic conductivity, s is a source term (assumed zero herein), $\mathbf{L}_{qh} = \{\ \partial/\partial x,\ \partial/\partial y\ \}^T$ is a linear differential operator, $\{\cdot\}^T$ represents the transpose operation and italic and bold face represent scalar and tensor quantities, respectively. In unconfined seepage analysis, we must also determine the pressure p in the fluid phase, since this determines whether a point is above or below the phreatic surface; i.e. whether it is in the saturated or unsaturated zone. We calculate the pressure from the hydraulic head using the well-known relation $p = (h - y)\rho_f g$ where y is the

elevation head relative to an arbitrary datum, ρ_f is the fluid density and g is gravitational acceleration. The classical boundary conditions for this problem are,

$$h = \hat{h} \text{ on } S_h \tag{2.1.4}$$

$$\mathbf{n}_q^T \mathbf{q} = \hat{q} \text{ on } S_q \tag{2.1.5}$$

where $\hat{h}$ is a prescribed hydraulic head, $\hat{q}$ is a prescribed flux, S_h and S_q are the corresponding boundaries on which these conditions are applied over the outer surface $S = S_h \cup S_q$, and $\mathbf{n}_q = \{ n_x, n_y \}^T$ is the outward pointing unit normal vector to S.

In the remainder of this section, we give two variational approximations for the above system, drawing on the generalized framework for parameterized variational principles that Felippa [206,207] presents, to make critical comparisons of the relative merits of each formulation.

2.1.2.1 Conventional finite element formulation

Zienkiewicz et al. [193] present the first FEM formulation of the seepage problem, which minimizes a potential energy functional in terms of h only, with $\mathbf{q}$ being determined through gradients of the approximate h field and Darcy's law. We will refer to this as the "conventional" formulation, not in any derogatory sense, but simply meaning that it has become popular for its simplicity and widespread adoption by commercial FEM software. Although this formulation is not the focus of the present work, we digress with the aim of demonstrating the consequences of this approach with regard to accuracy of the flux field. We also aim to compare it with the hybrid formulation developed here for use with polygonal elements. The conventional formulation maintains strong links between

h and **i** through equation (2.1.1) and between **i** and **q** through equation (2.1.2). As such, **i** and **q** are secondary to the primary variable *h*. This formulation also enforces the kinematic boundary condition in equation (2.1.4) strongly. Derivation of the approximate solution begins by weakening equations (2.1.3) and (2.1.5) as follows,

$$\delta\Pi_{BE} = -\int_V \delta\left(\mathbf{L}_{qh}h\right)^T \mathbf{KL}_{qh}h \; dV + \int_{S_q} \delta h \; \mathbf{n}_q^T\left(\mathbf{KL}_{qh}h\right) dS = 0 \qquad (2.1.6)$$

$$\delta\Pi_{FBC} = -\int_{S_q} \delta h\left[\; \mathbf{n}_q^T\left(\mathbf{KL}_{qh}h\right) + \hat{q}\right] dS = 0 \qquad (2.1.7)$$

where the application of the divergence theorem is implicit in equation (2.1.6) and the symbol δ indicates a variation. The weighting function is $\pm\delta h$ for both $\delta\Pi_{BE}$ and $\delta\Pi_{FBC}$ since it is the "work" conjugate of **q** and one adjusts the sign to obtain convenient cancellation of terms. Summing the weighted residuals and cancelling the $\mathbf{n}^T(\mathbf{KL}_{qh}h)$ term leads to,

$$\delta\Pi_h = -\int_V \delta\left(\mathbf{L}_{qh}h\right)^T \mathbf{KL}_{qh}h \; dV - \int_{S_q} \delta h \; \hat{q} \; dS = 0 \qquad (2.1.8)$$

One may view equation (2.1.8) as a virtual work expression that allows approximate solution of the problem defined by equations (2.1.1)-(2.1.3) given the boundary conditions in equations (2.1.4) and (2.1.5). In this case, equation (2.1.8) also leads to a variational principle corresponding to the minimization of,

$$\Pi_h[h] = -\tfrac{1}{2}\int_V \left(\mathbf{L}_{qh}h\right)^T \mathbf{KL}_{qh}h \; dV - \int_{S_q} h\hat{q} \; dS \qquad (2.1.9)$$

which is analogous to the total potential energy functional in linear elastic solid mechanics [126,134,208]. The units of the functional given in equation (2.1.9) are not in terms of energy; however, multiplying all flux terms by the unit weight of

the fluid rectifies this. Since the governing equations assume incompressible flow, implying that the unit weight of the fluid is constant over the domain, one can factor it out without changing the nature of the variational principle.

Implementation of this formulation within the FEM framework requires appropriate interpolation functions for h and $\hat{q}$ over an element subvolume V_e and the flux boundary S_q, respectively. Such interpolation functions for triangular and quadrilateral elements are well-known in the FEM literature, and we refer the reader to, for example, Zienkiewicz and Taylor [134] for the details. For polygonal elements of higher order (i.e. n-gons where $n > 4$), the solution for such interpolation functions over an element domain V_e is not as well known in the FEM literature. Indeed, since the conditions for a "conforming" shape function – to wit, forming a partition of unity, being bounded by zero and unity, interpolating nodal data, possessing linear completeness and reducing to interpolation between adjacent nodes on an edge – are not sufficient to provide a unique solution, there are, in theory, infinite possibilities. Sukumar and co-workers [140,142] summarize the most commonly used shape functions for polygonal elements including Laplace [135,136], Wachspress [137], discrete harmonic [138] and metric coordinate [139] using a common notation. Sukumar [141] presents an additional approach to constructing polygonal interpolants based on a maximum entropy principle. These interpolating functions are usually not in explicit form, which increases the difficulty of computing the gradient $\mathbf{L}_{qh}h$ [144], which is necessary in equation (2.1.8). Section 2.1.2.2 shows that the hybrid formulation does not require interpolation of h over the element domain for the linear case of confined seepage. Section 2.1.2.5 demonstrates that the interpolation of h in the

element domain is necessary for unconfined seepage in which we must estimate the pressure to determine the local hydraulic conductivity. Nonetheless, computation of **L***h* is not necessary in the hybrid formulation.

Prior to demonstrating the hybrid formulation, we discuss two potential sources of error in the conventional formulation, which the hybrid formulation attempts to alleviate. Namely,

i. *Amplification of error in the flux approximation*. Differentiation is a subtractive process wherein positive and negative errors accumulate, rather than cancel as with integration [145]. Since the conventional formulation computes **q** from the gradient of the approximate *h* field, the order of error for **q** is one order lower than that for *h*. The magnitude of error decreases as the mesh is refined, but only at the rate determined by the order of error. Regardless, analysts using modern computers achieve acceptable tolerance for error in analysis of continua simply by using a very fine mesh or adaptive refinement in regions of high error. However, for our future work developing a discontinuous FEM for seepage analysis, where the elements may represent physical material regions that cannot be refined, we must be conscious of this source of error.

ii. *Mass balance is only satisfied locally at the nodes*. Since the conventional formulation weakens equation (2.1.3), it only satisfies mass balance at the nodes. This implies that local error in mass balance is inherent to the approximation. It is unreasonable to expect that the interpolated values of **q** will satisfy the strong form mass balance equation at an arbitrary point in the domain. In other words, the

conventional formulation satisfies global equilibrium without ensuring that each element is in equilibrium. The consequence is that global error in the conventional formulation may be small even when local errors in mass balance and distribution of the flux are large. As the following section discusses, the hybrid formulation partially overcomes this issue by satisfying mass balance, a priori, in the domain of each element, while satisfying mass balance between elements in an integrated or average sense.

2.1.2.2 Hybrid finite element formulation

Finite element methods based on hybrid formulations have shown promise in alleviating issues analogous to the aforementioned in solid mechanics. Hybrid and mixed formulations are a general class of approximate solutions wherein one solves for more than one field variable directly [126,133,134,146-148]. Since the numerical analysis literature uses the word “hybrid” for a variety of purposes, we make a distinction here between hybrid formulations and hybrid methods that combine single field finite element formulations with boundary element methods [195,196,209,210] and methods using conventional finite element solutions with streamline and/or particle tracking methods for generating flow nets [197,198]. Pian [149] presents the earliest hybrid formulation for linear elastic solid mechanics. Tong and Pian [150,151] refine this formulation, in particular by showing the requirements for interpolation of stress to ensure that the element stiffness matrix has sufficient rank for inversion. Further development of hybrid

principles led to improved performance in plate and shell problems where continuity of the primary variable and its derivatives are difficult to satisfy [211].

Recent work in hybrid finite elements for the analysis of solids demonstrates its capability to handle the influence of heterogeneities in a natural way at the element level [152,154-157]. An interesting advantage of such hybrid constructions is that the element shape is not restricted to simple polygons such as triangles and quadrilaterals; indeed the method handles any convex polygon equally well. Ying and Henriquez [212] successfully apply a hybrid formulation within the context of electrical flux of biological cells, itself a phenomena partially described by the Poisson equation. Harder et al. [213] present a mixed-hybrid formulation for the Darcy equation, although their work limits itself to triangular elements. A complete review of hybrid and mixed FEM formulations is outside of the scope of the present work, and we refer to [126,134,146-148,206-208] for the theoretical details.

We now present a hybrid formulation as an alternative approach to solving seepage problems. The hybrid formulation differs from the variational principle in the previous section in that it explicitly considers the subdivision of the domain V into subdomains V_e, which are the finite elements, as shown in Figure 2.2. Following the generalized notation of Felippa [206,207], the hybrid variational principle is the summation of two terms: an interior functional and an interface potential. In this formulation there are two primary variables in the solution, hydraulic head – denoted as h in V_e and as h^* on S_i – and specific discharge or flux $\mathbf{q}$. The integration surface S is now $S_h \cup S_q \cup S_i$ where S_i traverses the set of internal surfaces twice – once in each direction – as Figure 2.2 shows.

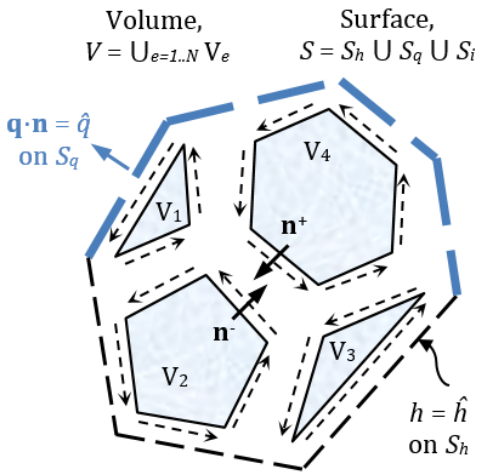

Figure 2.2 Subdivided domain of hybrid functional

To derive the hybrid formulation, we consider two additional strong form equations,

$$\mathbf{i}^h - \mathbf{i}^q = \mathbf{L}_{qh} h - \left(-\mathbf{K}^{-1}\mathbf{q}\right) = 0 \quad \text{in } V_e \tag{2.1.10}$$

$$\mathbf{q}^T\left(\mathbf{n}_q^+ + \mathbf{n}_q^-\right) = 0 \quad \text{on } S_i \tag{2.1.11}$$

where $\mathbf{i}^h$ and $\mathbf{i}^q$ are the hydraulic gradients computed through equations (2.1.1) and (2.1.2), respectively, and $\mathbf{n}_q^+$ and $\mathbf{n}_q^-$ are the outward pointing unit normals for elements on opposite sides of an internal surface. Equation (2.1.10) is the strong link between hydraulic gradients derived through the kinematic relation of equation (2.1.1) and through the constitutive relation of equation (2.1.2). Equation (2.1.11) represents mass balance on the boundaries between elements.

Following the approach of Felippa [206] for the hybrid formulation for solid mechanics problems, we weaken equations (2.1.4) and (2.1.10) to form the following weighted residuals,

$$\delta\Pi_{PBC} = \int_{S_h} \mathbf{n}_q^T \delta\mathbf{q}\left(\hat{h} - h\right) dS = 0 \tag{2.1.12}$$

$$\delta\Pi_{ii} = \int_{V_e} \delta\mathbf{q}^T \left(\mathbf{L}_{qh} h + \mathbf{K}^{-1}\mathbf{q}\right) dV = 0 \tag{2.1.13}$$

where we choose the multipliers $\delta\mathbf{q}$ and $\mathbf{n}_q{}^T\delta\mathbf{q}$ through work conjugate relationships. Next, we apply the divergence theorem to obtain,

$$\int_{V_e} \delta\mathbf{q}^T \mathbf{L}_{qh} h \; dV = -\int_{V_e} \delta\left(\mathbf{L}_{qh}^T \mathbf{q}\right) h \; dV + \int_{S_h} \mathbf{n}_q^T \delta\mathbf{q} h \; dS \tag{2.1.14}$$

in which the strong enforcement of $\mathbf{L}_{qh}{}^T\mathbf{q} = 0$ in V_e and $\mathbf{n}_q{}^T\mathbf{q} = \hat{q}$ over S_q cause their corresponding variations to vanish.

We now examine the interface potential, which is the weakened form of equation (2.1.11), itself a statement of point wise continuity of flux from one element to another along an interface. That is, we weaken mass balance only at the interfaces between elements as follows,

$$\delta\Pi_{int} = \int_{S_i} \left(\mathbf{n}_q^T \mathbf{q} \delta h^* + \mathbf{n}_q^T \delta\mathbf{q} h^*\right) dS = 0 \tag{2.1.15}$$

We consider variations of both h^* and $\mathbf{q}$ in $\delta\Pi_{int}$ since they are both primary variables. For convenience in developing element matrices and vectors, we use the following relation to rewrite the integrations over S_i,

$$\int_{S_i} f dS = \int_{S} f dS - \int_{S_h} f dS - \int_{S_q} f dS \tag{2.1.16}$$

where f is a scalar function. Summing $\delta\Pi_{PBC}$, $\delta\Pi_{ii}$, and $\delta\Pi_{int}$ taking into account equations (2.1.14) and (2.1.16), along with the strong enforcement of $h^* = \hat{h}$ on S_h gives,

$$\delta\Pi_{qh} = \int_{V} \delta\mathbf{q}^T \mathbf{K}^{-1}\mathbf{q} dV + \int_{S} \left(\mathbf{n}_q^T \delta\mathbf{q} h^* + \mathbf{n}_q^T \mathbf{q} \delta h^*\right) dS - \int_{S_q} \delta h^* \hat{q} \; dS = 0 \tag{2.1.17}$$

The variational statement in equation (2.1.17) implies stationarity of the following hybrid functional,

$$\Pi_{qh}\left[\mathbf{q}, h^*\right] = \tfrac{1}{2}\int_V \mathbf{q}^T\mathbf{K}^{-1}\mathbf{q}dV + \int_S h^*\mathbf{n}_q^T\mathbf{q}dS - \int_{S_q} h^*\hat{q}\ dS \qquad (2.1.18)$$

In combining equations (2.1.13), (2.1.14) and (2.1.15), we cancelled the terms containing the integrands $\mathbf{n}_q{}^T\delta\mathbf{q}h$ and $\mathbf{n}_q{}^T\delta\mathbf{q}h^*$, implying that their integrals are equal. Only equality of the integrands guarantees equality of these integrals, in general, which implies that the interpolation of h in V_e should satisfy $h^* \subset h$ on S. As discussed previously, interpolations satisfying this constraint on an arbitrary convex polygon – e.g. Laplace [135,136], Wachspress [137], discrete harmonic [138], metric coordinate [139] – are not unique. Notwithstanding, it is important to recognize that any conforming interpolant satisfies the assumptions of the hybrid formulation. We also observe that the h field in V_e is not consistent with the flux field $\mathbf{q}$, since we weaken the link between these variables, which is a fundamental difference between the hybrid and conventional finite element formulations. Owing to this, the hybrid formulation eliminates the issue of decreased order of error in the approximation of $\mathbf{q}$ as it does not depend on $\mathbf{L}_{qh}h$, but rather is itself a primary variable that we obtain directly. However, there are limits to the accuracy as the order of error in $\mathbf{q}$ is still constrained by the order of its interpolation, which Section 2.1.2.3 discusses further. The hybrid formulation does not weaken equation (2.1.3), thereby preserving mass balance in the domain of an element, if the interpolation of $\mathbf{q}$ satisfies mass balance, a priori. We also preserve mass balance or continuity at the nodal locations connecting elements

and satisfy mass balance is on the interelement boundaries in an average sense owing to the weak form $\delta\Pi_{int}$, which vanishes in the exact solution.

2.1.2.3 Interpolation of primary variables

In this section, we detail the interpolation of h^* and $\mathbf{q}$ to implement a finite element approximation based on the hybrid functional developed in the previous section. We also present the interpolation of h in the element domain, since this is necessary for the unconfined seepage case, as discussed further in Section 2.1.2.5.

The interpolation of h^* is straightforward as it only appears in surface integrals of $\Pi_{qh}[\mathbf{q},h^*]$. Examining the form of equation (2.1.17), the interpolation must guarantee (i) uniqueness of h^* on S_i (i.e. C^0 continuity) and (ii) satisfaction of equation (2.1.4) on S_h. The simplest way to achieve this is by linear interpolation of h^* between nodal values at adjacent nodes, which is the technique that we adopt herein,

$$h^* = \mathbf{N}_h^* \mathbf{a}_h = \begin{bmatrix} 1-\xi & \xi \end{bmatrix} \begin{Bmatrix} a_{h1} \\ a_{h2} \end{Bmatrix} \tag{2.1.19}$$

where a_{h1} and a_{h2} are the values of hydraulic head at adjacent nodes 1 and 2, and ξ is a local coordinate running from $\xi = 0$ at $\mathbf{x} = \mathbf{x}_1$ to $\xi = 1$ at $\mathbf{x} = \mathbf{x}_2$. Interpolation of h in the domain is of the form,

$$h = \mathbf{N}_h(\mathbf{x})\mathbf{a}_h \tag{2.1.20}$$

where for a polygonal element with n nodes, $\mathbf{N}_h$ has n columns and $\mathbf{a}_h$ contains the nodal values of h. Owing to the constraint that $h^* \subset h$ on S_i, equation (2.1.20) should reduce to equation (2.1.19) on an edge. Sukumar and co-workers [140,142] summarize the constraints on conforming interpolating shape functions including

that $\mathbf{N}_h^T\mathbf{N}_h = 1$ (partition of unity), $0 \leq \mathbf{N}_h \leq 1$ (bounded by zero and unity) and $\mathbf{x} = \mathbf{N}_h(\mathbf{x})\mathbf{x}_h$ (linear completeness) where $\mathbf{x}_h$ are the nodal coordinates. As Sukumar and co-workers present, these constraints are not sufficient to obtain a unique solution for $\mathbf{N}_h(\mathbf{x})$ for a polygonal domain, and there exist several shape functions satisfying these constraints. We refer the reader to references [140,142] for a detailed summary of the literature on shape functions for polygonal elements and their computation in a consistent notation.

Following references [150,153], we assume the following form for interpolation of $\mathbf{q}$ in the domain,

$$\mathbf{q} = \mathbf{P}_q\boldsymbol{\beta}_q \tag{2.1.21}$$

where $\mathbf{P}_q$ is a matrix of basis functions and $\boldsymbol{\beta}_q$ is a vector of unknown coefficients. The selection of the basis functions in $\mathbf{P}_q$ requires careful consideration as they must ensure (i) satisfaction of equation (2.1.3), (ii) insensitivity of the results to orientation of the coordinate system (i.e. spatial isotropy) and (iii) rank sufficiency of the volume integral of $\mathbf{P}_q^T\mathbf{K}^{-1}\mathbf{P}_q$ with respect to inversion. Within the context of 2-D solid mechanics, one may achieve (i) by using Airy's stress function [118,150] or consideration of independent stress modes [214]. Within the context of the potential flow involved in seepage problems, satisfaction of the homogeneous mass balance equation (i.e. when $s = 0$) is guaranteed for 2-D problems if we derive $\mathbf{q}$ from a potential function $\psi(\mathbf{x})$, as follows,

$$\mathbf{q} = \begin{Bmatrix} q_x \\ q_y \end{Bmatrix} = \begin{Bmatrix} \dfrac{\partial \psi}{\partial y} \\ -\dfrac{\partial \psi}{\partial x} \end{Bmatrix} \tag{2.1.22}$$

Spatial isotropy necessitates that $\psi(\mathbf{x})$ be symmetric with respect to the coordinates $\mathbf{x}$. We assume polynomial form for $\psi(\mathbf{x})$, which implies that $\psi(\mathbf{x})$ should be a complete polynomial. For rank sufficiency, Tong and Pian [150] showed that finite elements interpolating the flux variable as in equation (2.1.21) require that the number of coefficients $\boldsymbol{\beta}_q$ (or columns in $\mathbf{P}_q$) satisfy the inequality,

$$m \geq n - r \tag{2.1.23}$$

where m is the number of coefficients, n is the number of primary degrees of freedom per element, and r is the minimum number of kinematic (primary) boundary conditions necessary for a well-posed problem. Since h is a scalar field, n simply equals the number of nodes in the element. For steady 2-D seepage problems r is unity as it is only necessary to specify h at a single node [190,194]. For computational efficiency, we employ $\psi(\mathbf{x})$ of minimum order to satisfy the above constraints for an element with a given number of nodes. Indeed, the limitation principle states that one cannot improve the convergence rate by arbitrarily increasing the order of interpolation for $\mathbf{q}$ without also increasing the order of interpolation for h^* [215]. Comparing solutions obtained using the lowest allowable order $\mathbf{P}_q$ and higher order $\mathbf{P}_q$ in all elements verifies this. Using third order $\psi(\mathbf{x})$ gives,

$$\mathbf{P}_q = \begin{bmatrix} 1 & 0 & y & x & 0 & y^2 & 2xy & x^2 & 0 \\ 0 & 1 & 0 & -y & -x & 0 & -y^2 & -2xy & -x^2 \end{bmatrix} \tag{2.1.24}$$

where for elements with n=3, 4≤n<7, and 7≤n≤10, we use the first two, five and nine columns, respectively. In practice, automatic mesh generation based on Dirichlet or Voronoi tessellation [122-124] rarely results in polygons exceeding ten nodes [153]. Observing that $\mathbf{P}_q$ gives constant $\mathbf{q}$ for a triangular element, the

hybrid formulation for a mesh constructed entirely of such elements gives the same solution as the conventional formulation using 3-noded triangular elements, as one would expect.

To avoid dominance of higher order terms leading to numerical error [157], we compute $\mathbf{P}_q$ in terms of local coordinates,

$$\mathbf{x}_s = \mathbf{x} - \mathbf{x}_c \tag{2.1.25}$$

where $\mathbf{x}_s$ are the local coordinates, $\mathbf{x}$ are the global coordinates, and $\mathbf{x}_c$ are the coordinates of the element centroid. This form also has the advantage that the first order moments vanish when performing element level integrations. The implementation of this transformation is straightforward since the Jacobian of this transformation is unity, so we simply replace $\mathbf{x} = \{ x, y \}^T$ with $\mathbf{x}_s = \{ x_s, y_s \}^T$ in $\mathbf{P}_q$.

2.1.2.4 Hybrid finite element hydraulic conductivity matrix and flux vector

We now finalize the formulation by presenting the element hydraulic conductivity matrix $\mathbf{K}_{hh}$ and applied flux vector $\mathbf{Q}_q$ for the hybrid FEM approximation. Substituting equations (2.1.19) and (2.1.21) into equation (2.1.18) gives the hybrid functional for an element,

$$\Pi_{qh}\left[\boldsymbol{\beta}_q, \mathbf{a}_h\right] = -\tfrac{1}{2}\boldsymbol{\beta}_q{}^T\mathbf{H}_{qq}\boldsymbol{\beta}_q + \boldsymbol{\beta}_q{}^T\mathbf{G}_{qh}\mathbf{a}_h - \mathbf{a}_h^T\mathbf{Q}_q \tag{2.1.26}$$

where $\boldsymbol{\beta}_q$ and $\mathbf{a}_h$ are the element flux coefficients and nodal hydraulic heads, respectively, and,

$$\begin{aligned}
\mathbf{H}_{qq} &= -\tfrac{1}{2}\int_{V_e} \mathbf{P}_q^T\mathbf{K}^{-1}\mathbf{P}_q \; dV \\
\mathbf{G}_{qh} &= \int_S \left(\mathbf{n}_q^T\mathbf{P}_q\right)^T \mathbf{N}_h^* \; dS \\
\mathbf{Q}_q &= \int_{S_q} \mathbf{N}_h^{*T}\hat{q} \; dS
\end{aligned} \tag{2.1.27}$$

We could obtain exact integration of the polynomial basis functions over a polygonal domain using Green's Theorem [cf. 216]. For computational efficiency, we opt instead for exact numerical integration of the polynomial basis functions over irregular convex polygonal elements using techniques for constructing quadrature rules proposed in [217] and over element boundaries using standard Gaussian quadrature rules.

Taking the first variation of Π_{MCE} with respect to unknowns $\boldsymbol{\beta}_q$ and $\mathbf{a}_h$ gives the following pair of equations that must be satisfied simultaneously for arbitrary $\delta\boldsymbol{\beta}_q$ and $\delta\mathbf{a}_h$,

$$\begin{Bmatrix} \delta\boldsymbol{\beta}_q \\ \delta\mathbf{a}_h \end{Bmatrix}^T \left(\begin{bmatrix} -\mathbf{H}_{qq} & \mathbf{G}_{qh} \\ \mathbf{G}_{qh}^T & \mathbf{0} \end{bmatrix} \begin{Bmatrix} \boldsymbol{\beta}_q \\ \mathbf{a}_h \end{Bmatrix} - \begin{Bmatrix} \mathbf{0} \\ \mathbf{Q}_q \end{Bmatrix} \right) = \mathbf{0} \tag{2.1.28}$$

One may achieve this directly,

$$\begin{bmatrix} -\mathbf{H}_{qq} & \mathbf{G}_{qh} \\ \mathbf{G}_{qh}^T & \mathbf{0} \end{bmatrix} \begin{Bmatrix} \boldsymbol{\beta}_q \\ \mathbf{a}_h \end{Bmatrix} = \begin{Bmatrix} \mathbf{0} \\ \mathbf{Q}_q \end{Bmatrix} \tag{2.1.29}$$

and solve using penalty methods [152] or, following [150] by using,

$$\boldsymbol{\beta}_q = \mathbf{H}_{qq}^{-1}\mathbf{G}_{qh}\mathbf{a}_h \tag{2.1.30}$$

to condense $\boldsymbol{\beta}_e$ out of equation (2.1.26) and rewrite Π_e in terms of $\mathbf{h}_e^*$ only,

$$\Pi_{qh}\left[\mathbf{a}_h\right] = \tfrac{1}{2}\mathbf{a}_h^T\mathbf{K}_{hh}\mathbf{a}_h - \mathbf{a}_h^T\mathbf{Q}_q \tag{2.1.31}$$

where,

$$\mathbf{K}_{hh} = \mathbf{G}_{qh}^T\mathbf{H}_{qq}^{-1}\mathbf{G}_{qh} \tag{2.1.32}$$

is the element hydraulic conductivity matrix. We opt for the latter approach herein to reduce the number of global equations. Letting the first variation of equation (2.1.31) vanish leads to a linear system of equations,

$$\mathbf{K}_{hh}\mathbf{a}_h = \mathbf{Q}_q \tag{2.1.33}$$

We construct the global hydraulic conductivity matrix and flux vector by summing $\mathbf{K}_{hh}$ and $\mathbf{Q}_q$ over all elements taking into account the C^0 continuity of $\mathbf{a}_h$. We apply the kinematic boundary conditions by specifying the known nodal values for $\hat{h}$ in $\mathbf{Q}_q$ and setting the corresponding rows in $\mathbf{K}_{hh}$ to zeros except for a one on the diagonal; in essence, replacing the corresponding equilibrium equation with the constraint equation. After solving for the global nodal $\mathbf{a}_h$ values, we compute the seepage flux distribution using equations (2.1.21) and (2.1.30).

2.1.2.5 Algorithm for solution of unconfined seepage

The solution of the global system of equations for cases of confined seepage is a linear problem because the values of the constitutive parameters, i.e. the hydraulic conductivity coefficients, K_x and K_y, are known a priori. We now consider the solution algorithm for cases of unconfined seepage, such as that through an earth dam, as shown in Figure 2.3. In this case, the location of the "free surface" S_4 separating the saturated part of the domain Ω_w and the dry part of

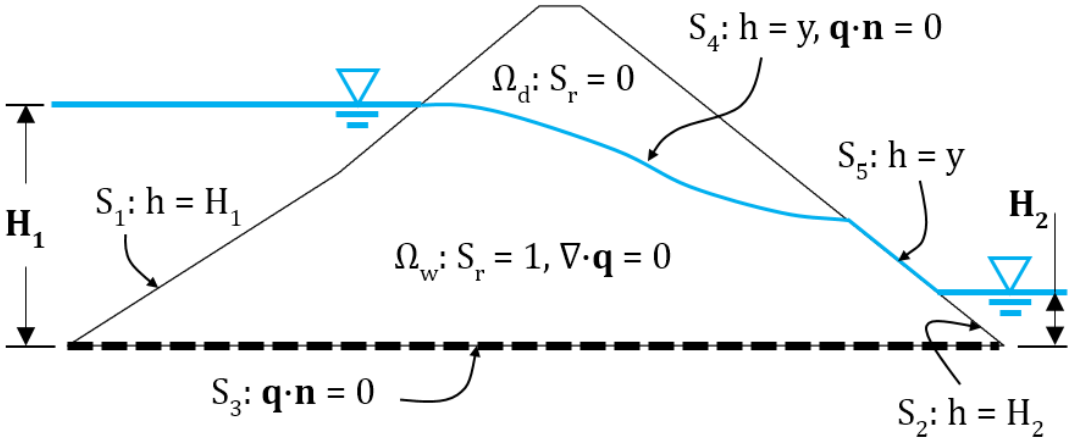

Figure 2.3 Schematic of domain for unconfined seepage analysis

the domain Ω_d is unknown. Under these conditions, we know that $\mathbf{n}_q^T\mathbf{q} = 0$ and $h = y$ on S_4, implying that S_4 is itself a streamline. For partially saturated conditions, we still define S_4 as the phreatic surface where $h = y$ holds, but $\mathbf{n}_q^T\mathbf{q} \neq 0$ in general, so S_4 may no longer be a streamline. We only require the condition that $h = y$ to solve for S_4 in the present study. Past studies locate S_4 using a variety of iterative approaches. France et al. [200] update the mesh such that they only analyze the saturated zone. Bathe and Khoshgoftaar [194] update the constitutive parameters to account for the negligible flux in the unsaturated zone. López-Querol et al. [205] update the boundary conditions to account for the zero flux condition on the portion of the boundary above the free surface. Numerous studies have investigated these approaches and their relative merits. A detailed literature review and comparison of methods is out of the scope of the present work. We adopt the approach of updating the constitutive parameters in the present study owing to the inefficiency of the updated mesh approach and the need for a transient analysis in the updated boundary conditions approach. For simplicity, we assume a step function for hydraulic conductivity K_i,

$$K_i = \begin{cases} K_{i,sat} & \text{when } p > 0 \\ 1\times10^{-a} K_{i,sat} & \text{otherwise} \end{cases} \tag{2.1.34}$$

where $i \in \{x, y\}$, $K_{i,sat}$ is the maximum value of hydraulic conductivity in the i direction when the domain is saturated, p is the gauge pressure relative to atmospheric conditions and a is a positive integer chosen such that K_i in Ω_d is small relative to $K_{i,sat}$, but non-zero for numerical stability. The present study adopts a modified Newton-Raphson scheme similar to that proposed by Bathe and Khoshgoftaar [194] within the context of conventional finite element analysis. We

first initialize the nodal values of hydraulic head to the magnitude of the highest expected value of prescribed head, except at nodes on S_h where we prescribe the values of h. At each iteration j, we compute the residual flux vector $\boldsymbol{\Psi}_q^{(j)}$ as,

$$\boldsymbol{\Psi}_q^{(j)} = \mathbf{Q}_q - \mathbf{K}_{hh}^{(j)} \mathbf{a}_h^{(j)} \tag{2.1.35}$$

where $\mathbf{K}_{hh}^{(j)}$ is the global hydraulic conductivity matrix evaluated at step j using equations (2.1.32) and (2.1.34) and $\mathbf{a}_h^{(j)}$ are the estimated nodal values of hydraulic head. In forming $\mathbf{K}_{hh}^{(j)}$ we evaluate equation (2.1.34) at each integration point when integrating $\mathbf{H}_{qq}$ as in equation (2.1.27). The resolution of the free surface solution depends on the number of integration points in an element. After applying the prescribed head boundary conditions, we estimate the increments to nodal head $\Delta\mathbf{a}_h^{(j)}$ by solving,

$$\mathbf{K}_{hh}^{(0)} \Delta\mathbf{a}_h^{(j)} = \boldsymbol{\Psi}_q^{(j)} \tag{2.1.36}$$

where we use the initial global hydraulic conductivity matrix $\mathbf{K}_{hh}^{(0)}$ for efficiency. We accelerate convergence by updating the global nodal heads as follows,

$$\mathbf{a}_h^{(j+1)} = \mathbf{a}_h^{(j)} + \delta^{(j)} \Delta\mathbf{a}_h^{(j)} \tag{2.1.37}$$

where $\delta^{(j)}$ is a step size determined at each iteration using a linear search as proposed by Borja [218] to ensure that $||\boldsymbol{\Psi}_q^{(j+1)}|| < ||\boldsymbol{\Psi}_q^{(j)}||$ where $||\cdot||$ is the standard 2-norm of a vector. The algorithm has converged when the approximate relative error $\varepsilon_a = ||\delta^{(j)}\Delta\mathbf{a}_h^{(j)}|| \,/\, ||\mathbf{a}_h^{(j+1)}||$ becomes less than a stopping criterion ε_s taken in the present study as 1×10^{-3}. Although this algorithm had not previously been applied within the context of hybrid polygonal finite elements, we found that its performance is similar to that when used in conjunction with conventional finite elements, with convergence typically occurring in fewer than ten iterations.

2.1.3 Numerical Examples

To demonstrate the performance of the hybrid VCFEM for confined and unconfined seepage, we present three numerical examples along with comparisons to the results of past studies. The salient features that we examine include: (i) accuracy of the flux results in comparison to existing approaches as well as (ii) mesh sensitivity and (iii) sensitivity to choice of conforming interpolant for h in cases of unconfined seepage wherein we must locate the free surface. The first example involves confined seepage around a sheet pile supporting an excavation wherein we examine the predicted equipotential lines and the flux field compared with a conventional FEM solution, as well as the global mass balance error for the hybrid FEM formulation of the present study. The second example is unconfined seepage through a rectangular earth dam with homogeneous material properties wherein we examine the sensitivity of the solution to element aspect ratio for hybrid quad meshes and to orientation and irregularity for hybrid polygonal meshes. The third example is unconfined seepage through an inhomogeneous earth dam with a low hydraulic conductivity clay core wherein we investigate the sensitivity of the solution to the choice of interpolating shape functions for three irregular polygonal meshes. We performed the analysis using a computer program *vcfem_seep* written in Matlab [219], implementing the formulation presented in Sections 2.1.2.2 through 2.1.2.5.

2.1.3.1 Example 1 – Sheet pile supporting excavation

Figure 2.4 shows the mesh for Example 1, which is a 10 m high sheet pile wall supporting an excavation. The sheet pile has an embedment of 5 m and

maintains a head difference of 8 m. Owing to symmetry we only model half of the 10 m wide excavation. The stratigraphy consists of a single layer of orthotropic sand with the bottom boundary being an impermeable bedrock layer 10 m below the base of the excavation. The quadrilateral mesh consists of 219 nodes and 182 elements. We capture the singularity at the base of the sheet pile using duplicate node numbers – we assign a different node index to the node at the base of the sheet pile in each adjacent element, thereby allowing hydraulic head to have different values in each element. To make a direct comparison of results based on the conventional and hybrid formulations, we analysed this problem using the quadrilateral mesh shown in Figure 2.4 under isotropic conditions with $K_x = K_y = 1.0\times10^{-5}$ m/s using both formulations. To examine the quality of the solution in terms of global mass balance error, we also analysed the problem using

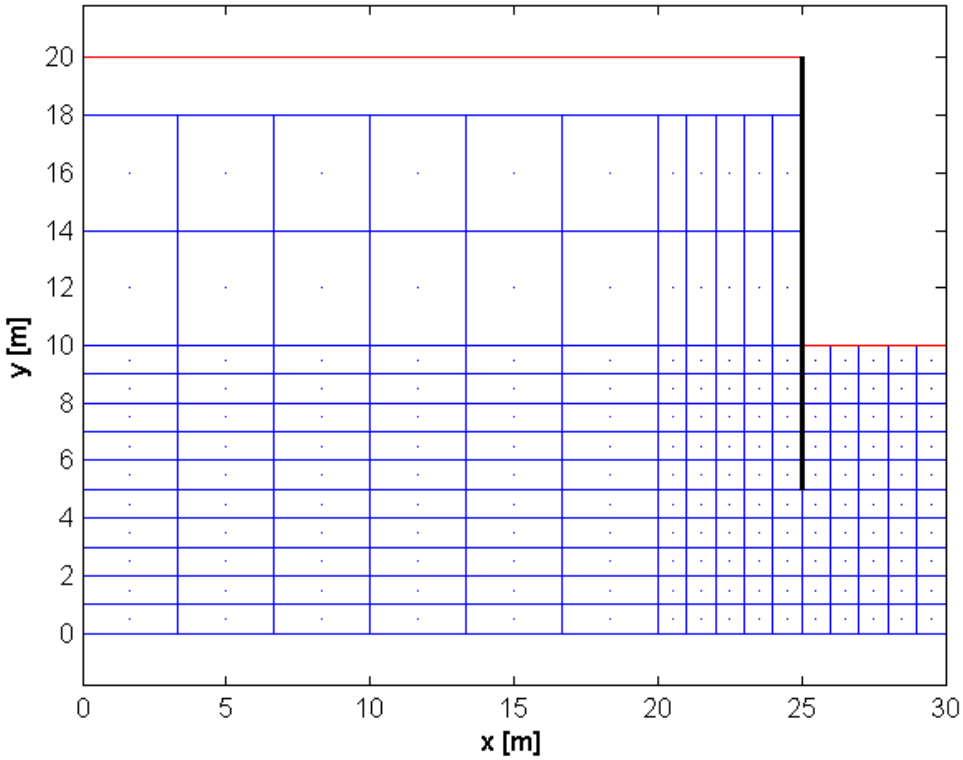

Figure 2.4 Quadrilateral mesh for Example 1 (sheet pile wall)

the hybrid FEM for various degrees of anisotropy taking $K_x = 1.0\times10^{-5}$ m/s and $K_x/K_y \in [1,16]$.

Figure 2.5 shows superimposed contours of total hydraulic head h from the conventional FEM and hybrid VCFEM solutions, respectively. The results from the two approaches show good agreement. Figure 2.6 through Figure 2.8 show the distributions of net pore water pressure on the sheet pile wall, $\mathbf{n}_q^T\mathbf{q}$ along the water table and $\mathbf{n}_q^T\mathbf{q}$ along the excavation, respectively. The results of the conventional and hybrid FEM compare well in terms of magnitude and distribution. Integrating $\mathbf{n}_q^T\mathbf{q}$ gives a total seepage flux of 2.402 m^3/day and 2.237 m^3/day based on the results of the conventional and hybrid FEM, respectively, which are in good agreement. When computing the global mass

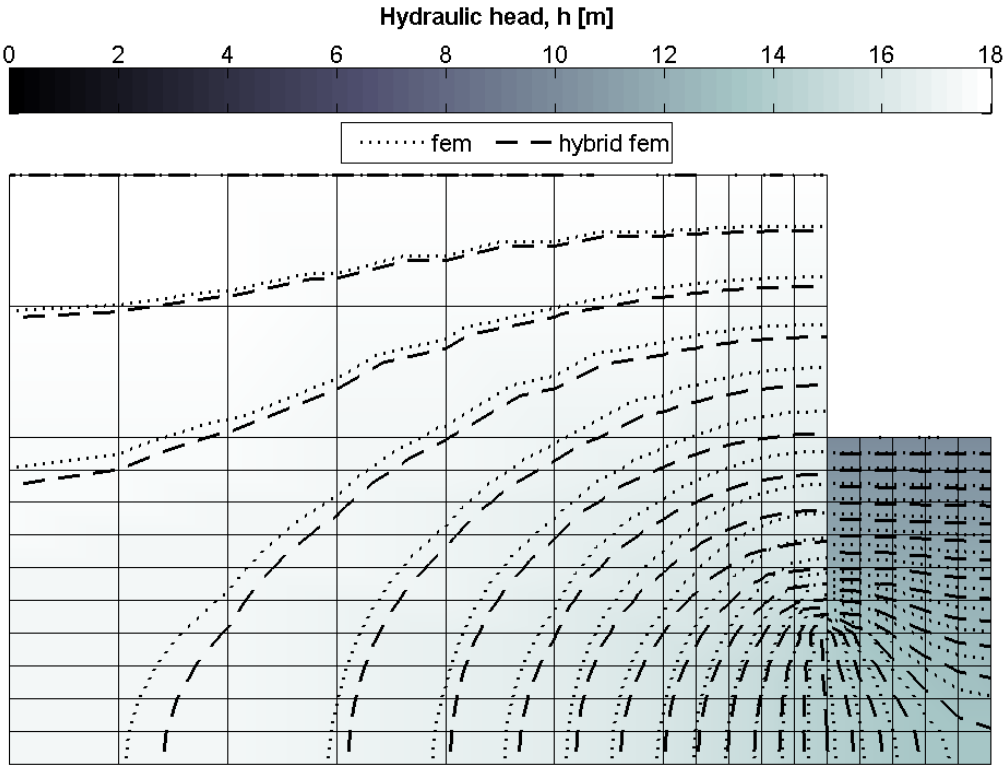

Figure 2.5 Plot of total hydraulic head h and seepage flux q for Example 1 using conventional FEM and hybrid VCFEM formulations with quadrilateral elements

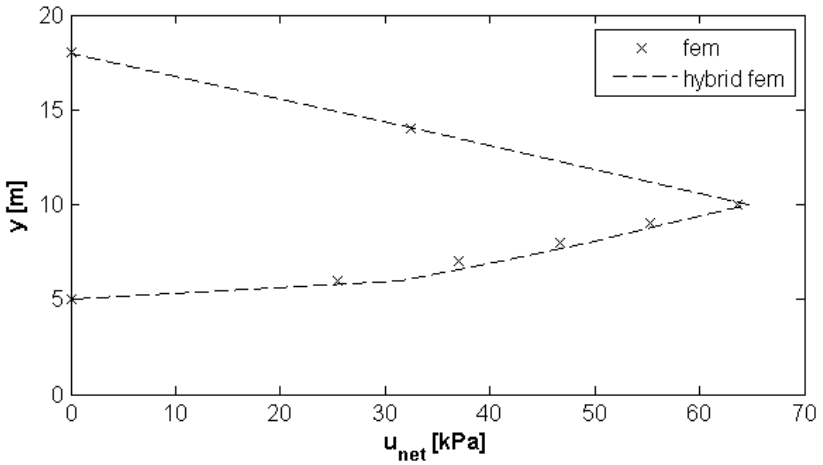

Figure 2.6 Net pore water pressure distribution on sheet pile for Example 1 comparing conventional FEM and hybrid FEM under isotropic conditions

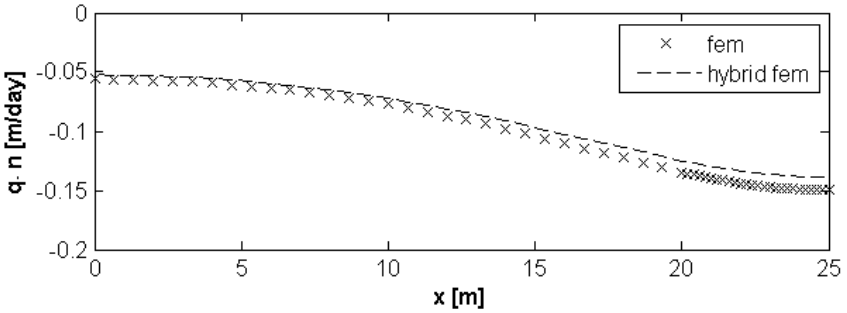

Figure 2.7 Seepage flux along water table (left of sheet pile wall) for Example 1 comparing conventional FEM and hybrid FEM under isotropic conditions

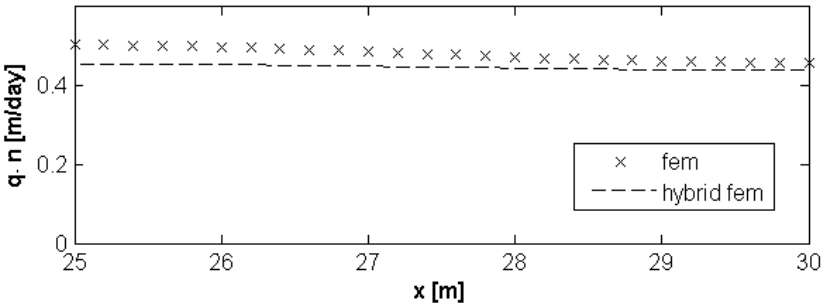

Figure 2.8 Seepage flux along base of excavation for Example 1 comparing conventional FEM and hybrid FEM under isotropic conditions

balance error by summing the total seepage flux at the water table and excavation levels, we obtain errors of 4.298×10^{-5} m^3/day and 3.752×10^{-8} m^3/day, respectively, for the conventional and hybrid FEM. This improvement in mass balance error is small in magnitude, but it is notable that there are three orders of

magnitude difference going from the conventional to the hybrid FEM. We ascribe this to the a priori satisfaction of the mass balance equation in the formulation. When refining the mesh, the difference in global mass balance error decreases. However, it is notable that the hybrid FEM solution converges in terms of this measure of performance more quickly than the conventional FEM results. Figure 2.9 shows the total discharge around the sheet pile per unit width at the water table and excavation for various degrees of anisotropy computed using the hybrid FEM. The global mass balance error was negligible in all cases.

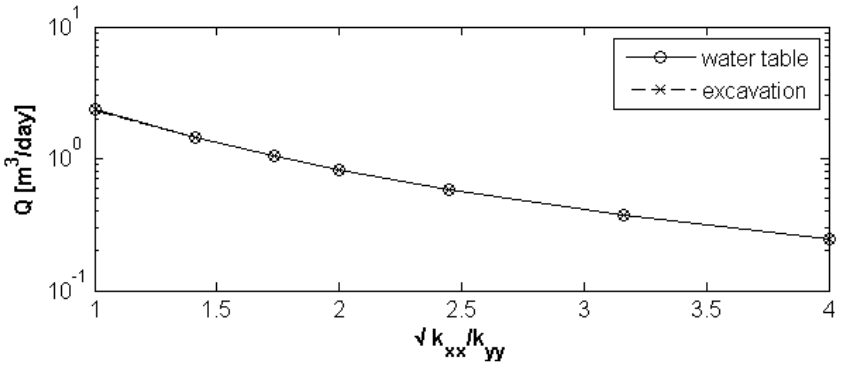

Figure 2.9 Mass balance computed from hybrid FEM solution for Example 1

2.1.3.2 Example 2 – Unconfined seepage through rectangular earth dam

Figure 2.10 shows a schematic of Example 2, which is a 16'×16' (4.9 m×4.9 m) earth dam composed of homogeneous isotropic material with $K_x = K_y = 1$ ft/hr (0.3048 m/hr), a constant head boundary condition of $h = 16'$ (4.9 m) on the right side, a zero pressure boundary condition, i.e. $h = y$, on the left side and zero flux boundary conditions on the top and bottom. The figure also shows a sample mesh of 800 hybrid quadrilateral elements with a width-to-height ratio of 0.5. Herbert [220] examines this problem using resistance network analogues, France et al. [200] using conventional FEM with updated mesh and Bathe and Khoshgoftaar [194] using conventional FEM without mesh iteration,

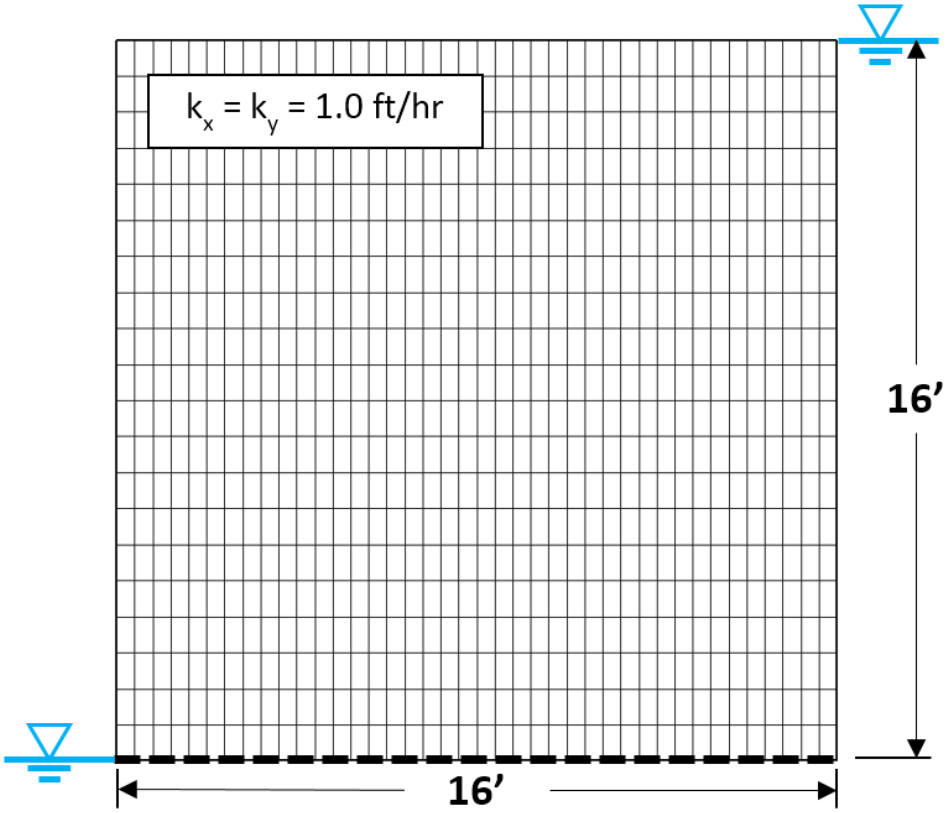

Figure 2.10 Schematic of Example 2 with a quad mesh of 800 elements and width-to-height ratio of 0.5

similar to the algorithm presented in Section 2.1.2.5 of the present paper. We select this example for its simplicity and use it to examine mesh sensitivity by comparing the results of analysis using hybrid quadrilateral elements of varying aspect ratio and hybrid polygonal elements of varying orientation and irregularity, as Figure 2.11 depicts.

Figure 2.12 shows the results for the location of the free surface using hybrid quadrilateral meshes of varying width-to-height ratios. We only present the results obtained using the metric coordinate shape function to interpolate *h* in the domain of an element here, but the results using other shape functions are essentially the same. The results show good agreement with the results of previous studies and the individual simulation results are consistent in an average

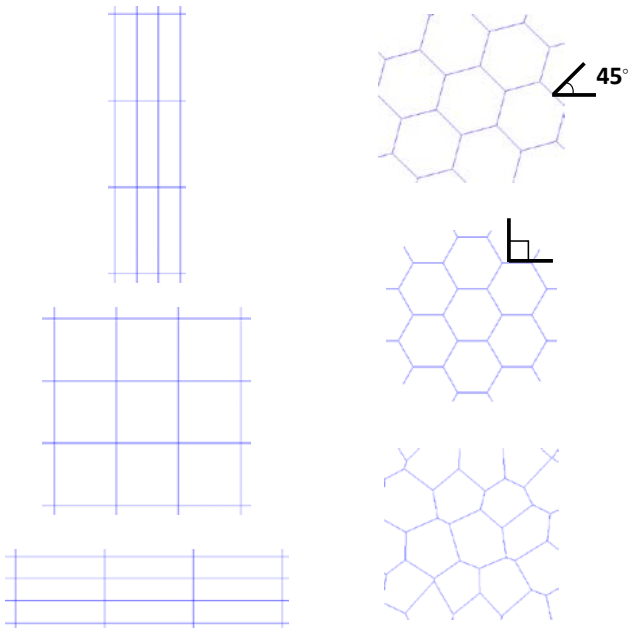

Figure 2.11 Several mesh types considered for Example 2. Hybrid quadrilateral meshes (left) with width-to-height ratios of 0.25 (top), 1.0 (middle) and 4 (bottom) and hybrid polygonal meshes (right) with regular hexagonal elements of varying orientation (top and middle) and irregular polygonal elements (bottom).

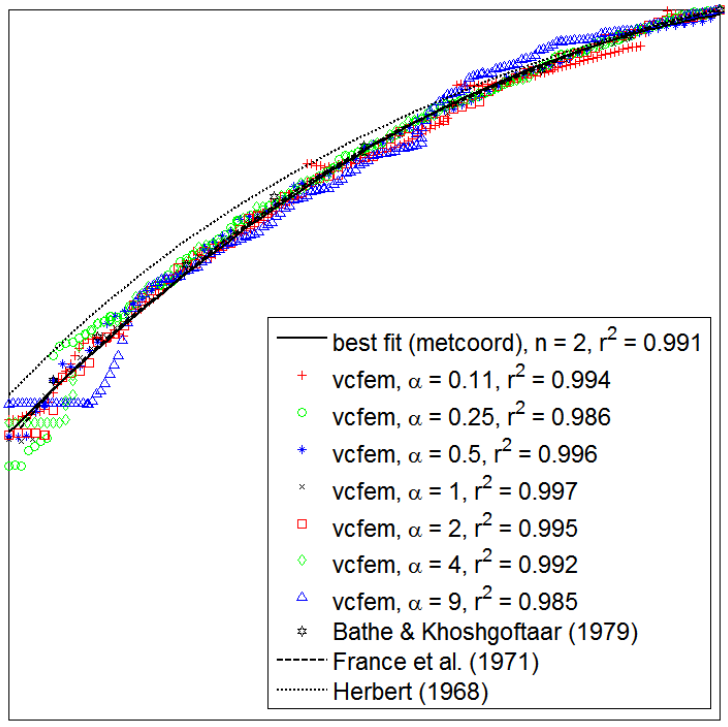

Figure 2.12 Free surface results for Example 2 using hybrid quad meshes of varying width-to-height ratio α and metric coordinate shape function. Best-fit curve is a second-order polynomial obtained using least squares regression.

sense with each other as demonstrated by the best-fit curve. We observe, however, that in the neighbourhood of the downstream side of the free surface there is significant mesh sensitivity in the solution when using quadrilateral elements. Owing to the boundary conditions, i.e. two nodes in each element adjacent to this boundary are fixed to zero pressure, and the linear interpolation to which the shape functions reduce in a quadrilateral element, the free surface is forced to be horizontal in this region. As the mesh is refined, the differences in the solutions for various width-to-height ratios decrease, along with the size of the region influenced by the fixed boundary conditions, but the influence of element shape for coarse meshes is worth noting.

Figure 2.13 shows the results of the same problem using hybrid polygonal meshes of varying orientation and irregularity. The polygonal meshes consist primarily (>85%) of hexagonal elements. We also show the results of a hybrid quadrilateral analysis using elements with width-to-height ratio of 1.0 for comparison. We obtained this set of results using the discrete harmonic shape function, with negligible difference in the results using other shape functions. We observe that the results are generally smoother with the polygonal meshes compared to those obtained with the quadrilateral meshes of similar density. We cannot ascribe this to higher order interpolation of the flux, since it is linear for both quadrilateral and hexagonal elements, as equation (2.1.24) shows. However, there is higher order interpolation of h in the domain of each element – regardless of the choice of conforming shape function – as the number of nodes increases. This is the most probable reason for the improved resolution of the free surface. In addition, there is significant reduction of the mesh sensitivity in the neighbourhood

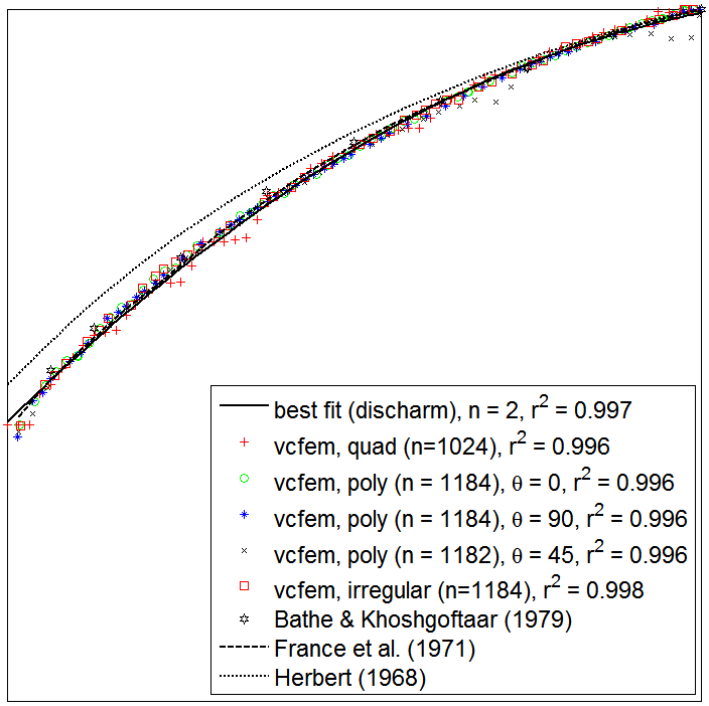

Figure 2.13 Free surface results for Example 2 using hybrid polygonal meshes of varying orientation θ and irregularity using discrete harmonic shape function. Polygonal meshes consist primarily (>85%) of hexagonal elements.

of the downstream side of the domain when using polygonal elements. We attribute this to the increased number of free nodes in a downstream polygonal element compared with a quadrilateral element, i.e. the boundary condition of two nodes with fixed head puts less constraint on the interpolation of *h* in an element as the number of nodes increases.

2.1.3.3 Example 3 – Unconfined seepage through zoned earth dam with low hydraulic conductivity core and toe filter

The final example that we examine is a more complex case involving a heterogeneous dam with a clay core and a toe filter, shown in Figure 2.14. The boundary conditions are fixed hydraulic head *h* of 60 m on the left boundary, zero pressure or $h = y$ on the right boundary, zero flux on the left side of the bottom boundary and on the top boundary and fixed hydraulic head *h* of 0 m on the right

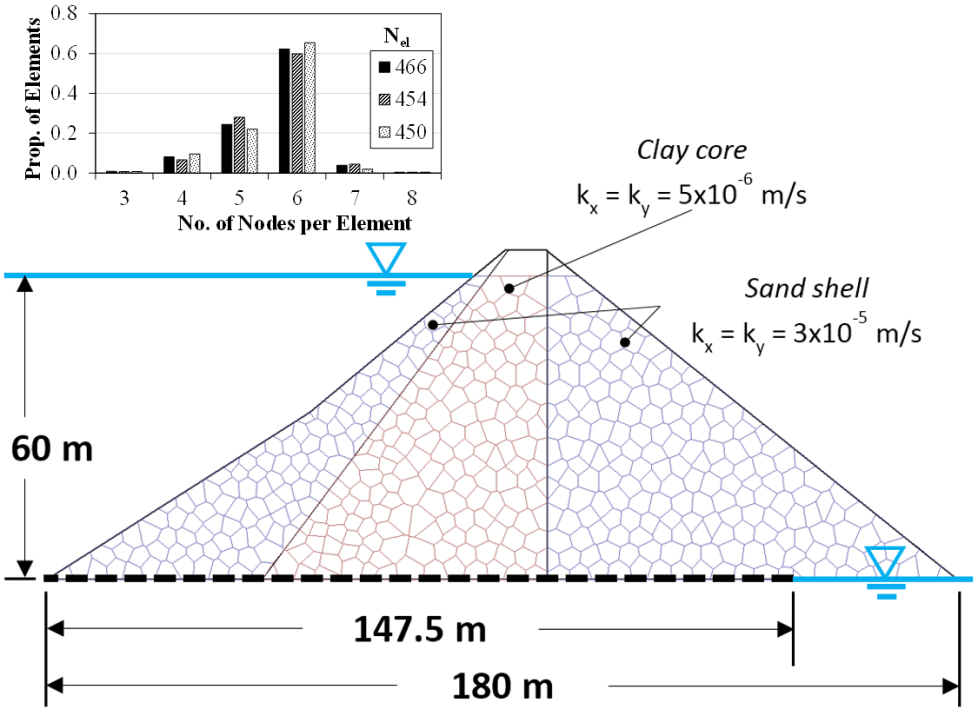

Figure 2.14 Schematic of Example 3 with an irregular polygonal mesh of 466 elements and (inset) distribution of nodes per element for two similar irregular meshes

side of the bottom boundary. The latter boundary condition represents a high hydraulic conductivity filter at the toe of the dam. We handle the mixed boundary condition at the meeting point of the impermeable and permeable parts of the bottom boundary by duplicating the node at that location. This example was examined previously by Lambe and Whitman [221] using flow nets, by Lacy and Prevost [204] using conventional FEM with a penalty function approach to integrating the element hydraulic conductivity matrix and by Bazyar and Graili [222] using scaled boundary FEM, among others.

Our focus in this example is on comparing the results obtained using irregular polygonal meshes and the various shape functions for interpolating head in the domain of an element: Laplace [135,136], Wachspress [137], discrete harmonic [138] and metric coordinate [139]. Figure 2.14 shows a schematic of an

irregular polygonal mesh with 466 polygonal elements, of which most (>60%) are hexagonal elements. We also analysed the problem using two other irregular polygonal meshes with similar number and composition of elements, as shown in the inset of Figure 2.14.

Figure 2.15 shows the results of the analysis for all three meshes and all four shape functions, a total of 12 analysis results. There is good agreement with the results of past studies by Lacy and Prevost [204] and Bazyar and Graili [222]. In particular, we note better agreement with the latter in in the clay core and with the former near the outflow at the filter. The solutions of the present study and of Lacy and Prevost [204] near the filter are in better agreement with the mechanics of potential flow described by the Laplace equation since the free surface, which is a streamline, is perpendicular to the constant head boundary at the filter, which is an equipotential line. It would appear that the updated mesh procedure employed in the scaled boundary FEM of reference [222] has difficulty achieving

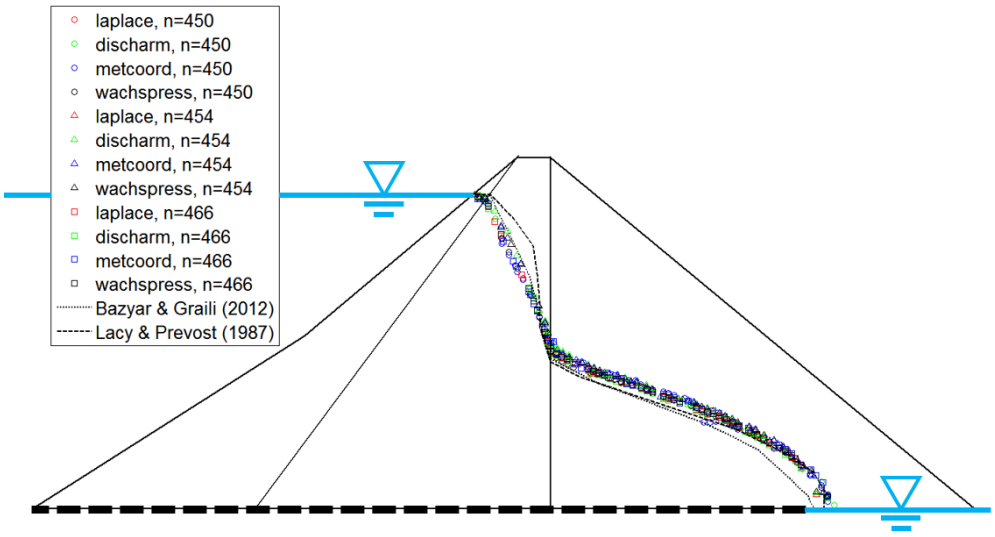

Figure 2.15 Free surface results for Example 3 using irregular polygonal meshes (n = 450, 454, 466) and various shape functions for interpolating h in the domain of the elements

this, insofar as the reported result implies. We observe excellent agreement between the results for the different irregular polygonal meshes, indicating negligible mesh sensitivity when using irregular polygonal meshes to solve continuous problems. There is no significant difference in the results when using the different shape functions, indicating that although the constraints specified for interpolating shape functions are not sufficient to provide a unique solution [140,142], they do constrain the form of the shape function enough that it does not significantly influence the location of the free surface within an element.

2.1.4 Conclusions

This study implemented a hybrid formulation and the consistent polygonal FEM approximation for steady potential flow through a saturated porous medium. A summary of key observations is as follows,

- Interpolation of flux **q** inside polygonal elements satisfying mass balance a priori using interpolation based on a streamline function $\psi(\mathbf{x})$ slightly improves global mass balance error. Having said that, the improvement in error is not very significant when compared with the error in the input data.
- Analysis of unconfined seepage problems using hybrid quadrilateral elements may result in mesh sensitivity in terms of the shape of the free surface near constant pressure boundaries. Hybrid polygonal elements with more than four nodes alleviate this issue through increased flexibility of the interpolation of head inside the element.

- The free surface solution is not sensitive to the choice of conforming shape function for interpolation of head in the domain of hybrid polygonal elements. Any conforming shape function will provide an adequate solution, which reduces the choice to the relative computational efficiency of the shape functions, an analysis of which is outside the scope of the present study.

The authors are presently engaged in extending the hybrid polygonal FEM for analysis of seepage through continua to the case of discontinua wherein the polygonal elements represent regions of intact material and significant seepage may occur in the pore or fracture networks between these regions. The results of the present study build confidence that sensitivities to mesh configuration in the discontinuous framework represent true physical behaviour and not artificial numerical influences produced by different configurations of polygonal elements or different interpolating shape function options.

3 Multi-scale Geomechanical Modelling using VCFEM-DEM

3.1 Conference Paper #1: Simulation of lab scale tests on granular media using assumed stress polygonal finite elements and nonlinear joint elements[2]

3.1.1 Introduction

Granular materials such as sand and gravel are fundamentally different from continuous solids such as metals since they are composed of discrete solid grains that interact by sliding relative to one another [7]. Although one may approximate the macroscopic behaviour of granular materials through continuum models with volume-averaged properties, understanding the behaviour involving grain interactions at the micro-scale is fundamental to understanding the macroscopic behaviour.

Equilibrium of contact forces between the grains governs their interaction with the stiffness associated with intergrain normal and shear deformation being

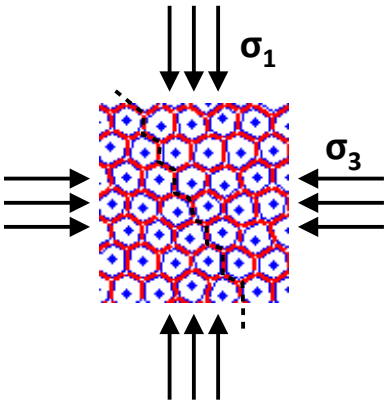

Figure 3.1 Schematic of localized failure in granular material

[2] Karchewski B, Guo P, Stolle D. Simulation of lab scale tests on granular media using assumed stress polygonal finite elements and nonlinear joint elements. *Proceedings of the 67th Canadian Geotechnical Conference, Sep 28-Oct 1, Regina, SK,* 2014.

significantly different from the stiffness of individual grain deformation. Modelling of inter-granular force equilibrium must adequately account for the details of grain interaction. Adjacent grains have negligible resistance to separation (tension), but high stiffness in compression. Shear deformation between grains may involve a recoverable elastic component as well as an unrecoverable sliding component if the applied shear exceeds the available frictional resistance. Existing models for this behaviour fit into three categories: micromechanical models [26,30,40,41,44,69,70,223,224], discrete element models with rigid or deformable grains [174-177,181,187-189] and material point models [184,185].

Micromechanical models examine the behaviour of granular materials by reducing the analysis to a small enough region that a continuum model explicitly accounting for individual grains through interface tracking becomes tractable. Such models use either Eulerian or arbitrary Lagrangian-Eulerian analysis tracking the particle behaviour in a volume of interest. Although this approach provides insight into the behaviour of granular materials at the micro-scale, they suffer from the inability to scale the region of interest even to the size of a laboratory test owing to the prohibitive computational cost.

Discrete element (DEM) models typically assume the grains to be rigid bodies having simple shapes such as discs/spheres [175], ellipses/ellipsoids [178-180,225] or polygons/polyhedra [174,176,177,181]. One determines if there is contact between these bodies through pair-wise comparison of overlapping volume. Models using spherical or ellipsoidal grains have the advantage of simplicity in detecting contact, but may not accurately reflect the grain shape of

many granular materials. Systems involving polyhedral grains or blocks more accurately represent the shape of geomaterials, but necessitate modelling of a greater number of interaction types: point-to-point, point-to-edge, point-to-face, edge-to-face and face-to-face. The common plane approach [176] reduces the number of tests required by testing two potentially contacting blocks for contact with a plane between them, rather than for direct contact with each other. Once DEM models determine which grains are in contact, they determine the normal contact force between grains in proportion to the overlapping volume of adjacent grains. Shear force transfer may be non-slip or may account for frictional resistance, which is proportional to the normal contact force and a material dependent friction coefficient. Grains may be rigid or deformable. The former is often preferred since the deformation of the grains is assumed small compared to the deformation caused by relative movement between grains and since methods for calculating deformation of particles having general polygonal shape are not as well established. When deformable polyhedral blocks are desirable, the blocks may be sub-discretized into an internal mesh of finite elements [181]. Recently developed DEM models involving deformable body elements, called combined FEM-DEM models, use a combination of body finite elements to represent linear elastic regions and interface finite elements to account for relative movement of these regions [187-189]. This approach has the advantage of reducing the complication involved in modelling many types of particle interaction, but models of this type have restricted the body element type to constant strain triangular finite elements, which do not provide accurate stress field approximation unless the mesh is greatly refined. In addition, the triangular shape of these elements

does not accurately reflect the shape of particles in granular media. This was sufficient for applications of the FEM-DEM to date, which were mostly related to modelling of fracture in rock and concrete.

Models using the material point method (MPM) including a contact algorithm are a novel approach to modelling a variety of contact problems. Bardenhagen and co-workers [184,185] apply this approach to micro-scale analysis of granular materials and Jassim et al. [186] model macro-scale problems involving multiple material phases such as pile driving. In this approach, material points carrying information about material properties, stresses and velocities move through a fixed calculation grid. The solution at each time step uses an explicit algorithm involving three main parts: solution of velocities assuming all material points are a single body, solution of velocities for each individual body ignoring the influence of surrounding bodies and velocity correction based on the difference between the velocities determined in the first and second phases. The velocities from the first two phases will differ only when bodies are interacting. In the context of micromechanical modelling, this approach can handle grains of arbitrary shape and has the advantage of not requiring pair-wise comparison to determine which specific grains are interacting. The disadvantages of such models are that they may require many material points to represent each grain and that the explicit solution algorithm requires small time steps leading to simulations that are computationally expensive even for a modest number of grains.

It is worth noting that all of the above methods have the advantage of being able to capture anisotropy in granular materials naturally through the initial topology of the set of grains. This is in contrast to continuum-based methods,

which analyze granular materials at the macro-scale and must resort to complex constitutive models to capture anisotropy [cf. 15,16]. Furthermore, since continuum-based models smear the effects of grain interactions at the micro-scale, they do not provide a means of examining the mechanism of failure in granular materials.

The present work presents a form of FEM-DEM model in which the body elements are deformable, have convex polygonal shape and provide accurate internal stress field approximation. The model accomplishes this by using hybrid assumed stress polygonal elements to represent the grains or representative volumes of grains and joint elements with non-linear constitutive behaviour to represent the interaction between body elements. The unrecoverable component of deformation resulting from frictional sliding in the joint elements satisfies the Coulomb yield criterion.

The remaining sections of this paper provide a brief overview of the model formulation, preliminary numerical results modelling biaxial tests on granular material, a discussion of observations from the numerical results and some concluding remarks including future steps in the model development and application.

3.1.2 Formulation

The FEM-DEM model presented here consists of two types of element: polygonal body elements representing grains or representative volumes of granular material and non-linear joint elements modelling the interaction between grains. This section presents an overview of the formulation of both element types

and a summary of the iterative solution algorithm for non-linear behaviour. The present work restricts itself to the case of static equilibrium for simplicity, although the non-linear solution algorithm is extendable to dynamic analysis and future work will examine this extension. The present work also assumes a priori knowledge of the pair-wise contiguity of body elements, which does not change during the course of the analysis. Future developments involving dynamic analysis including post-failure behaviour will necessitate additional steps to update this contiguity.

3.1.2.1 Polygonal body elements

The formulation of the polygonal body elements representing grain deformation follows a hybrid principle that Pian [149] proposes and Tong and Pian [150] formalize. The original developers noted that one might implement such a hybrid principle in polygonal elements with an arbitrary number of nodes [150], but practical implementation for polygons with 5 or more nodes was not presented until later by Ghosh and co-workers [152,153]. Ghosh and Moorthy [155] extend the formulation to allow for non-linear behaviour in hybrid polygonal elements. The present work assumes linear elastic behaviour in the polygonal body elements since the joint elements account for the non-linear response.

Following Tong and Pian [150], the formulation of the body elements begins with a modified statement of total complementary energy that also includes an interface potential, which accounts for traction equilibrium between elements,

$$\Pi_{MCE}\left[\boldsymbol{\sigma}', \mathbf{u}^*\right] = -\tfrac{1}{2}\int_{V_e}\left(\boldsymbol{\sigma}'^T \mathbf{D}_e^{-1}\boldsymbol{\sigma}'\right)dV + \int_{S_e}\left(\mathbf{n}_\sigma^T\boldsymbol{\sigma}'\right)^T \mathbf{u}^* dS - \int_{S_t}\left(\mathbf{u}^{*T}\hat{\mathbf{t}}\right)dS \quad (3.1.1)$$

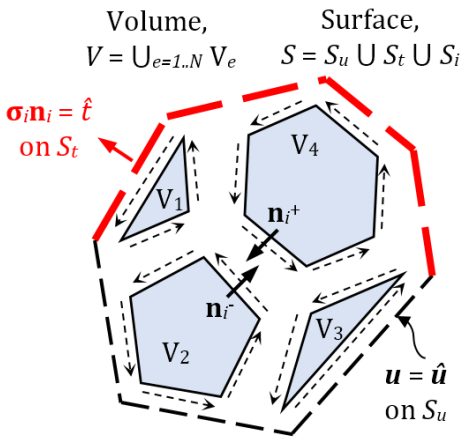

Figure 3.2 Discretization in hybrid VCFEM

where V_e is the volume of the polygonal element, S_e is the outer surface of the element, S_t is a surface over which there is an applied traction, $\boldsymbol{\sigma}' = \{ \sigma_{xx}', \sigma_{yy}', \sigma_{xy}' \}^T$ represents the effective stress tensor, $\mathbf{D}_e^{-1}$ represents the elastic compliance tensor relating strain to stress, $\mathbf{u}^* = \{ u_x, u_y \}^T$ is the displacement along the surface S_e, $\mathbf{n}_\sigma$ represents the outward pointing unit normal of the element, $\hat{\mathbf{t}}$ is an applied traction and $\{\cdot\}^T$ represents the transpose operation. The formulation herein uses the compact Voigt notation to represent symmetric tensors as vectors and matrices. For plane strain analysis,

$$\mathbf{D}_e^{-1} = \frac{1+\nu}{E}\begin{bmatrix} 1-\nu & -\nu & 0 \\ -\nu & 1-\nu & 0 \\ 0 & 0 & 2 \end{bmatrix} \tag{3.1.2}$$

$$\mathbf{n}_\sigma = \begin{bmatrix} n_x & 0 & n_y \\ 0 & n_y & n_x \end{bmatrix}^T \tag{3.1.3}$$

where E is the elastic modulus, ν is the Poisson ratio and subscripts $\{\cdot\}_x$ and $\{\cdot\}_y$ refer to the horizontal and vertical coordinate directions, respectively. Interpolation of stress in the element interior is of the form,

$$\boldsymbol{\sigma}' = \mathbf{P}_\sigma \boldsymbol{\beta}_\sigma \tag{3.1.4}$$

where $\mathbf{P}_\sigma$ contains a set of polynomial basis functions satisfying equilibrium (e.g. using Airy's stress functions) and $\boldsymbol{\beta}_\sigma$ is a vector of unknown coefficients. Interpolation of displacement on the element boundary is,

$$\mathbf{u}^* = \mathbf{N}_u^* \mathbf{a}_u \tag{3.1.5}$$

where $\mathbf{N}$ contains linear shape functions interpolating between the adjacent nodal values of displacement $\mathbf{a}^*$ along the boundary of an element. Substituting equations (3.1.4) and (3.1.5) into (3.1.1) gives,

$$\Pi_{MCE}\left[\boldsymbol{\beta}_\sigma, \mathbf{a}_u\right] = -\tfrac{1}{2}\boldsymbol{\beta}_\sigma^T \mathbf{H}_{\sigma\sigma}\boldsymbol{\beta}_\sigma + \boldsymbol{\beta}_\sigma^T \mathbf{G}_{\sigma u}\mathbf{a}_u - \mathbf{a}_u^T \mathbf{F}_{\hat{t}} \tag{3.1.6}$$

where,

$$\mathbf{H}_{\sigma\sigma} = \int_{V_e} \left(\mathbf{P}_\sigma^T \mathbf{D}_e^{-1} \mathbf{P}_\sigma\right) dV \tag{3.1.7}$$

$$\mathbf{G}_{\sigma u} = \int_{S_e} \left(\mathbf{n}_\sigma^T \mathbf{P}_\sigma\right)^T \mathbf{N}_u^* dS \tag{3.1.8}$$

$$\mathbf{F}_{\hat{t}} = \int_{S_t} \left(\mathbf{N}_u^{*T} \hat{\mathbf{t}}\right) dS \tag{3.1.9}$$

The analysis herein performs the integration of equation (3.1.7) using the technique for construction of exact quadrature over a convex polygonal domain described by Mousavi and Sukumar [217] and the surface integrations in equations (3.1.8) and (3.1.9) using standard Gaussian quadrature rules. Allowing the first variations of equation (3.1.8) with respect to unknowns $\boldsymbol{\beta}_\sigma$ and $\mathbf{a}_u$ to vanish and noting that the $\boldsymbol{\beta}_\sigma$ coefficients need not be continuous between elements gives,

$$\boldsymbol{\beta}_\sigma = \mathbf{H}_{\sigma\sigma}^{-1} \mathbf{G}_{\sigma u} \mathbf{a}_u \tag{3.1.10}$$

where Tong and Pian [150] state the requirements for rank sufficiency and invertibility of $\mathbf{H}_{\sigma\sigma}$. Substituting equation (3.1.10) into equation (3.1.6) gives the functional Π_{MCE} in terms of unknown $\mathbf{a}_u$ only,

$$\Pi_{MCE}\left[\mathbf{a}_u\right] = \tfrac{1}{2}\mathbf{a}_u^T\mathbf{K}_{uu}\mathbf{a}_u - \mathbf{a}_u^T\mathbf{F}_{\hat{t}} \tag{3.1.11}$$

where $\mathbf{K}_{uu}$ is the element stiffness matrix,

$$\mathbf{K}_{uu} = \mathbf{G}_{\sigma u}^T\mathbf{H}_{\sigma\sigma}^{-1}\mathbf{G}_{\sigma u} \tag{3.1.12}$$

For a more detailed discussion of the origin, formulations and applications of hybrid finite elements, refer to [146-148]. Ghosh [157] provides further details within the context of polygonal hybrid elements.

3.1.2.2 Non-linear joint elements

The formulation herein accommodates the deformation component due to relative movement between grains (compression, separation and/or sliding) using a form of non-linear joint element proposed by Stolle and Guo [226] in the context of slope stability analysis. Evaluation of joint element stiffness begins by examining the strain energy increment for an element,

$$\Delta U_e\left[\Delta\tilde{\boldsymbol{\sigma}}', \Delta\tilde{\boldsymbol{\varepsilon}}\right] = \int_{V_e}\left(\Delta\tilde{\boldsymbol{\varepsilon}}^T\tilde{\boldsymbol{\sigma}}'\right)dV + \tfrac{1}{2}\int_{V_e}\left(\Delta\tilde{\boldsymbol{\varepsilon}}^T\Delta\tilde{\boldsymbol{\sigma}}'\right)dV \tag{3.1.13}$$

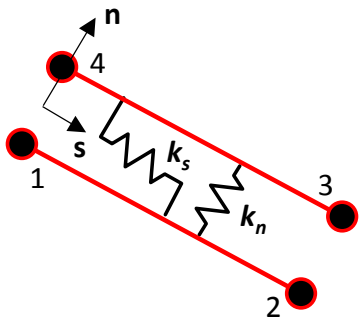

Figure 3.3 Schematic of nonlinear joint element

where $\Delta\tilde{\boldsymbol{\varepsilon}} = \delta_e^{-1}\Delta\tilde{\mathbf{u}}$ is the strain increment, δ_e is a small distance representing the thickness of the joint element, $\Delta\tilde{\mathbf{u}}$ is the relative displacement increment between the "top" and "bottom" of the joint element, $\tilde{\boldsymbol{\sigma}}'$ is the initial stress state, $\Delta\tilde{\boldsymbol{\sigma}}'$ is the stress increment and superposed ~ indicates that a variable is in the local coordinate system of the joint element. The stress increment $\Delta\tilde{\boldsymbol{\sigma}}'$ is related to the strain increment through the constitutive relation,

$$\Delta\tilde{\boldsymbol{\sigma}}' = \begin{Bmatrix} \Delta\sigma_\xi \\ \Delta\sigma_\eta \end{Bmatrix} = \begin{bmatrix} G & 0 \\ 0 & M \end{bmatrix} \begin{Bmatrix} \Delta\varepsilon_\xi \\ \Delta\varepsilon_\eta \end{Bmatrix} = \mathbf{D}\Delta\tilde{\boldsymbol{\varepsilon}} \tag{3.1.14}$$

The tangent shear modulus G follows the non-linear relation,

$$G = G_r - \frac{F}{\left|\tilde{\varepsilon}_\xi\right| + A_\xi} \tag{3.1.15}$$

where G_r is the residual shear modulus at high shear strain, we define the Coulomb yield function as $F = |\sigma_\xi| + \sigma_\eta \tan(\varphi') - c' \leq 0$ and A_ξ is a model parameter that prevents the denominator from vanishing when the shear displacement is zero and defines the shape of the shear stiffness degradation curve. The tangent constrained modulus M is constant in compression and diminishes rapidly in tension,

$$M = \begin{cases} M_0 & \varepsilon_\eta \leq 0 \\ M_r + \dfrac{\kappa_\eta}{\varepsilon_\eta + A_\eta} & \varepsilon_\eta > 0 \end{cases} \tag{3.1.16}$$

where M_0 is the constrained modulus in compression, M_r is the residual constrained modulus in tension and κ_η and $A_\eta = \kappa_\eta / (M_0 - M_r)$ are model parameters defining the shape of the normal stiffness degradation curve. The relative displacement of the joint elements are linearly interpolated between nodes as,

$$\tilde{\mathbf{u}} = \tilde{\mathbf{N}}_u \tilde{\mathbf{a}}_u \tag{3.1.17}$$

where $\tilde{\mathbf{N}}_u$ contains interpolating shape functions and $\tilde{\mathbf{a}}_u$ is a column vector of nodal displacements in local coordinates. For a joint element with 4 nodes numbered locally in counter-clockwise order and linear interpolation of relative displacement, the interpolation matrix $\tilde{\mathbf{N}}$ is,

$$\tilde{\mathbf{N}} = \begin{bmatrix} -N_1 & 0 & -N_2 & 0 & N_2 & 0 & N_1 & 0 \\ 0 & -N_1 & 0 & -N_2 & 0 & N_2 & 0 & N_1 \end{bmatrix} \tag{3.1.18}$$

where $N_1 = 1\text{-}\xi$, $N_2 = \xi$, $\xi = \sqrt{[(x\text{-}x_1)^2 + (y\text{-}y_1)^2]}/l_e$, $\{ x_i, y_i \}$ are the global coordinates of node i and l_e is the length of the interface element. The nodal displacements are transformed from global to local coordinates using the familiar form,

$$\tilde{\mathbf{a}}_u = \mathbf{T}\mathbf{a}_u \tag{3.1.19}$$

where $\mathbf{T}$ is,

$$\mathbf{T} = \begin{bmatrix} \mathbf{T}_0 & \mathbf{0} & \mathbf{0} & \mathbf{0} \\ \mathbf{0} & \mathbf{T}_0 & \mathbf{0} & \mathbf{0} \\ \mathbf{0} & \mathbf{0} & \mathbf{T}_0 & \mathbf{0} \\ \mathbf{0} & \mathbf{0} & \mathbf{0} & \mathbf{T}_0 \end{bmatrix} \tag{3.1.20}$$

and the matrix $\mathbf{T}_0$ rotates the coordinate system at a point,

$$\mathbf{T_0} = \begin{bmatrix} \cos\theta & \sin\theta \\ -\sin\theta & \cos\theta \end{bmatrix} \tag{3.1.21}$$

where $\theta = \tan^{-1}[(y_2\text{-}y_1)/(x_2\text{-}x_1)]$ defines the orientation of the interface element. Substituting equations (3.1.14), (3.1.17) and (3.1.19) into (3.1.13) gives the strain energy increment as,

$$\Delta U_e = \Delta \mathbf{a}_u^T \int_{V_e} \delta_e^{-1} \left(\mathbf{T}^T \tilde{\mathbf{N}}_u^T \tilde{\boldsymbol{\sigma}}' \right) dV + \tfrac{1}{2} \Delta \mathbf{a}_u^T \mathbf{K}_{uu(i)} \Delta \mathbf{a}_u \tag{3.1.22}$$

where $\mathbf{K}_{uu(i)}$ is the tangent stiffness matrix defined as,

$$\mathbf{K}_{uu(i)} = \int_{V_e} \delta_e^{-2} \left(\mathbf{T}^T \tilde{\mathbf{N}}_u^T \mathbf{D} \tilde{\mathbf{N}}_u \mathbf{T} \right) dV \tag{3.1.23}$$

The analysis herein performs the integrations in equations (3.1.22) and (3.1.23) using standard Gauss quadrature rules.

For a finite relative displacement increment $\Delta\tilde{\mathbf{u}}$ at an integration point, equation (3.1.14) only provides an estimate of the stress increment $\Delta\tilde{\boldsymbol{\sigma}}'$. To correct the stress state according to elastic perfectly plastic behaviour, the implementation herein uses a stable return mapping algorithm [227,228] wherein the estimated stress state $\tilde{\boldsymbol{\sigma}}'^*$ is,

$$\tilde{\boldsymbol{\sigma}}'^* = \tilde{\boldsymbol{\sigma}}' + \Delta\tilde{\boldsymbol{\sigma}}' \tag{3.1.24}$$

If the failure function $F^*(\tilde{\boldsymbol{\sigma}}'^*) \leq 0$ then it is an elastic step. Otherwise, use a first order Taylor series expansion of the yield function about the estimated stress state,

$$F = F^* + \left(\frac{\partial F}{\partial \tilde{\boldsymbol{\sigma}}'^*} \right)^T \Delta\tilde{\boldsymbol{\sigma}}'^* = 0 \tag{3.1.25}$$

and write the stress correction $\Delta\tilde{\boldsymbol{\sigma}}'^*$ using an associated flow rule,

$$\Delta\tilde{\boldsymbol{\sigma}}'^* = -\Delta\mu \mathbf{D} \left(\frac{\partial F}{\partial \tilde{\boldsymbol{\sigma}}'^*} \right) \tag{3.1.26}$$

where $\Delta\mu$ is determined by substituting equation (3.1.26) into (3.1.25) to obtain,

$$\Delta\mu = F^* \Big/ H_e \tag{3.1.27}$$

where,

$$H_e = \left(\frac{\partial F}{\partial \tilde{\boldsymbol{\sigma}}'^*} \right)^T \mathbf{D} \left(\frac{\partial F}{\partial \tilde{\boldsymbol{\sigma}}'^*} \right) \tag{3.1.28}$$

Finally, the stress state and yield function are updated iteratively according to,

$$\boldsymbol{\sigma}^* = \boldsymbol{\sigma}^* - \lambda \mathbf{k}\left(\frac{\partial f}{\partial \boldsymbol{\sigma}^*}\right) \tag{3.1.29}$$

$$F^* = F^* - \Delta\mu H_e \tag{3.1.30}$$

until $F^* \leq 0$. It is therefore necessary to incrementally increase the applied load, iteratively estimating displacement increments and correcting the stress state until the residual of the sum of external (applied) tractions and internal forces approaches zero.

3.1.2.3 Average strain measure

In examining the results of numerical examples simulating biaxial tests on granular material, it is of interest to calculate an average strain measure to determine the degree of induced anisotropy. Define the average strain as,

$$\overline{\boldsymbol{\varepsilon}} = \tfrac{1}{V}\int_V \boldsymbol{\varepsilon} dV \tag{3.1.31}$$

where for plane strain analysis $\boldsymbol{\varepsilon} = \{ \varepsilon_{xx}, \varepsilon_{yy}, \gamma_{xy} \}^T = \{ \partial u_x/\partial x, \partial u_y/\partial y, (\partial u_x/\partial y + \partial u_y/\partial x) \}^T$ is the engineering strain and V is the total volume of the domain. Based on the application of Green's theorem, which allows transformation of an area integral into a contour integral on a closed contour S,

$$\iint_A (\nabla \mathbf{u})\, dA = \int_S (\mathbf{u} \otimes \mathbf{n})\, dS \tag{3.1.32}$$

in which $\mathbf{u}$ is the displacement in the domain, $\mathbf{n}$ is the outward pointing unit normal to the domain and $\otimes$ represents an outer product between two vectors. Taking S as the outer surface of the analysis domain, as Figure 3.4 shows, the average strain contained by the contour is,

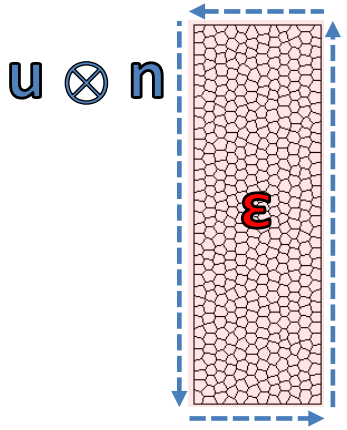

Figure 3.4 Schematic of contour used to compute average strain measures

$$\bar{\boldsymbol{\varepsilon}} = \begin{Bmatrix} \bar{\varepsilon}_{xx} \\ \bar{\varepsilon}_{yy} \\ \bar{\gamma}_{xy} \end{Bmatrix} = \frac{1}{A} \begin{Bmatrix} \int_S (u_x n_x)\, dS \\ \int_S (u_y n_y)\, dS \\ \int_S (u_x n_y + u_y n_x)\, dS \end{Bmatrix} \tag{3.1.33}$$

One can then determine the average principal strains as,

$$\bar{\varepsilon}_{1,3} = \tfrac{1}{2}\left(\bar{\varepsilon}_{xx} + \bar{\varepsilon}_{yy}\right) \pm \sqrt{\left(\bar{\varepsilon}_{xx} - \bar{\varepsilon}_{yy}\right)^2 + \bar{\gamma}_{xy}^2} \tag{3.1.34}$$

The remaining sections demonstrate the performance of the VCFEM-DEM formulation with deformable polygonal body elements and joint elements with nonlinear constitutive behaviour by simulating plane strain biaxial compression on granular materials.

3.1.3 Numerical Examples

Figure 3.5 shows representative meshes used to simulate biaxial compression on a granular material. The domain has a height of 0.15 m and a width of 0.05 m and the analysis assumes plane strain conditions. The coarse, medium and fine meshes have 75, 192 and 432 body elements and 186, 513 and 1201 joint elements, respectively.

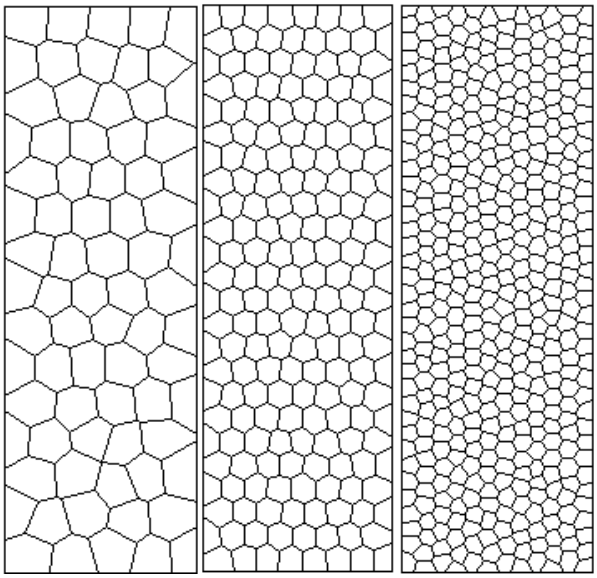

Figure 3.5 Representative meshes with 75 (left), 192 (centre) and 432 (right) body elements

Fixed vertical displacement along the bottom boundary and fully fixed conditions at the bottom left node define the kinematic boundary conditions. Simulation of biaxial compression consists of two analysis phases for the natural boundary conditions: uniform consolidation up to a confining pressure of 200 kPa followed by shear failure induced by increasing the vertical stress.

The body elements have an elastic modulus $E = 50.0 \times 10^6$ kPa and Poisson's ratio $\nu = 0.3$. Stolle and Guo [226] in examining slope stability using joint elements with the stiffness model described in Section 3.1.2.2 suggest that the ultimate load capacity predicted by the model is insensitive to the joint element stiffness parameters. These parameters should only influence the shape of the stress-strain curve with the strength parameters φ' and c' dictating the ultimate resistance. Shear deformation between particles of a granular material occurs more readily than shear deformation of the particles themselves and interpenetration of particles is not possible. Therefore, the shear stiffness of joint

elements should be significantly less than the shear stiffness of body elements and the normal stiffness of joint elements should be significantly higher than the constrained modulus of the body elements. For the analysis herein, we define the stiffness of joint elements as $G_r = 1\times10^3$ kPa, $A_\xi = 1\times10^{-5}$, $M_0 = 1\times10^8$ kPa, $M_r = 1\times10^6$ kPa, $\kappa_\eta = 1$ kPa and $A_\eta = 1.01\times10^{-8}$. One may consider these as curve fitting parameters that one should calibrate to the shape of the stress-strain curve obtained from laboratory results. To simulate a cohesionless granular material, the analysis herein assumes the interface strength parameters as $\varphi' = 30°$ and $c' = 0$ kPa.

3.1.4 Results and Discussion

The results of biaxial compression simulation demonstrate stress-strain curves that are representative of laboratory compression testing results. Figure 3.6 shows representative stress-strain curves for the various levels of mesh coarseness. Note that as the number of elements increases, the initial stiffness of the system decreases owing to the greater flexibility of the system resulting from a greater number of joint elements. This implies that values of joint element stiffness calibrated to laboratory results depend on the level of mesh refinement used in calibration. Further examination of the relationship between joint element stiffness coefficients and level of mesh refinement is required.

The maximum principal stress differences at failure (under confining pressure of 200 kPa) for the simulations shown in Figure 3.6 are 442 kPa, 488 kPa, 541 kPa for the coarse, medium and fine meshes, respectively. These are consistent with bulk friction angles in the range 30° to 35° for joint element friction

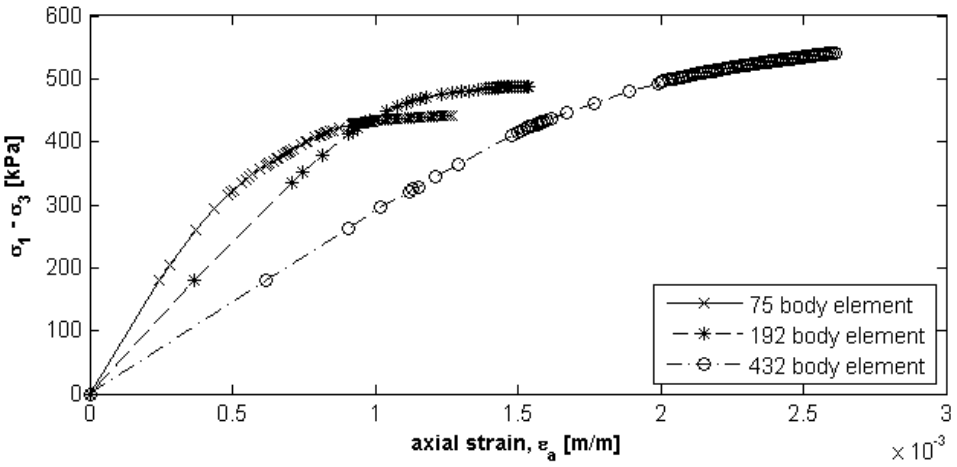

Figure 3.6 Representative stress-strain curves for meshes with different degrees of refinement

angle of 30°. There is an apparent increase in peak load with number of elements for the curves shown. Note, however, that these are representative curves taken from single trials rather than average curves and some variation exists when holding the number of elements constant and varying the initial arrangement of body elements. This reinforces the observation that calibrated strength and stiffness properties in the proposed model depend on the mesh coarseness in the model. This is owing to the fact that large body elements do not represent individual grain properties, but rather volume averaged properties. As the body elements become smaller, the properties should approach that of grains of intact material. Understanding of how to calibrate the body and joint element properties for field scale analyses requires further investigation.

Formation of classical "shear band" failure occurs at different levels of mesh coarseness, as Figure 3.7 illustrates. Depending on the initial topology of the elements representing the grains, it is also possible for localized failure modes to develop. Figure 3.8 shows examples of localized failures, partially attributable to the traction boundary conditions, which act directly on the body elements representing

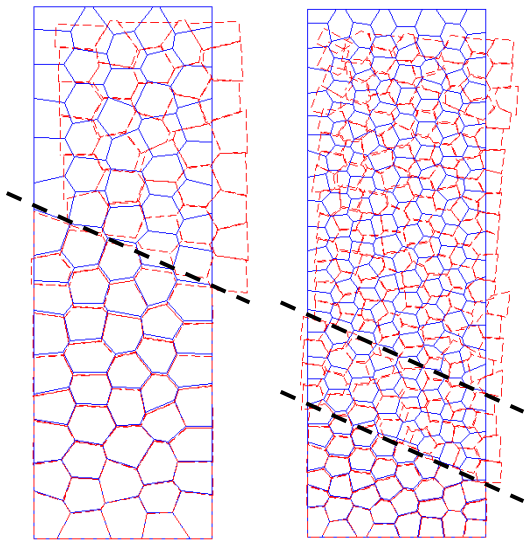

Figure 3.7 Plot of failure mode for representative meshes with 75 (left) and 192 (right) body elements (displacements magnified 23x for plotting)

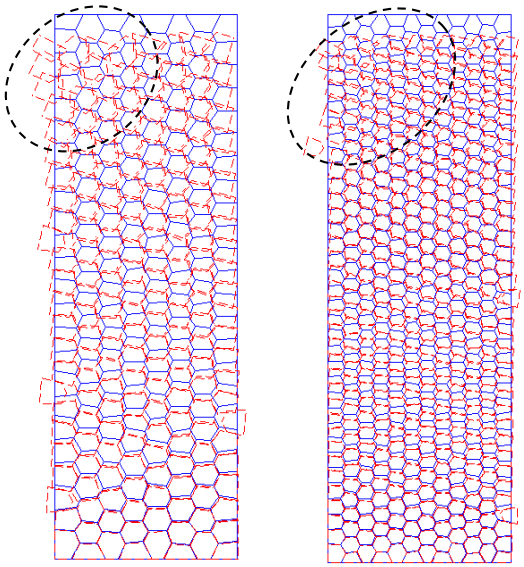

Figure 3.8 Examples of localized failure modes for meshes with 192 (left) and 432 (right) elements

the granular material. In a real laboratory experiment, a rigid loading cap exists to maintain a level surface at the top of the specimen. Further testing to determine whether the presence of elements representing the loading cap eliminates development of localized failure in simulations is necessary (see Sections 3.2 and 3.3).

Figure 3.9 shows a plot of principal strains at the end of the isotropic consolidation phase. The diagonal line is the isotropic strain line along which one would expect strains in an isotropic material to plot under isotropic stress conditions. Examination of the plot shows evidence that anisotropic strain conditions can develop under isotropic consolidation owing to the configuration of the grains (elements). Liu et al. [229], for example, observed this behaviour in tests on sand. The predicted principal strains after isotropic consolidation at 200 kPa were found to increase with the number of elements owing to the increased flexibility of the system from an increased number of joint elements. In generating sample meshes, randomized packing of polygonal elements was achieved by shifting alternate rows or columns of element centroids in the horizontal or vertical directions, respectively, followed by randomized shifting of element centroids.

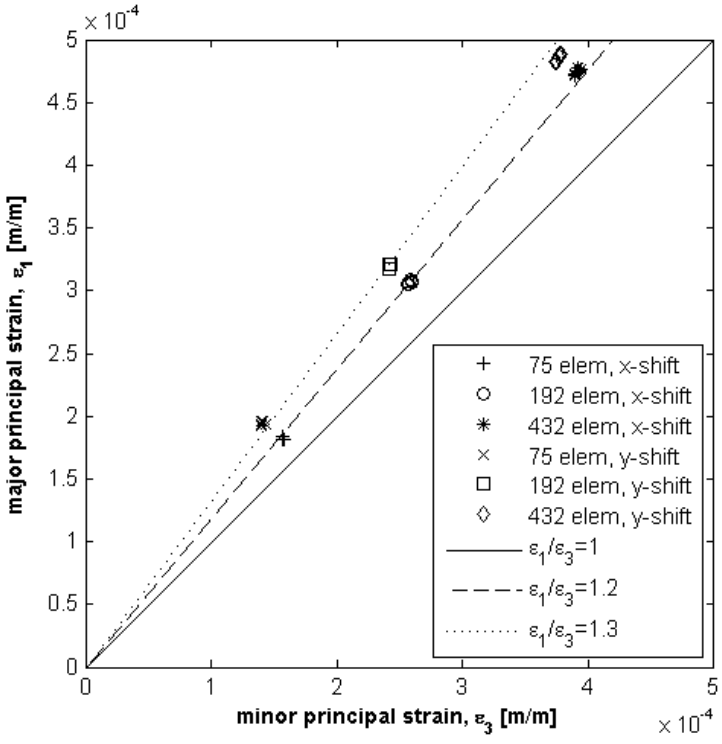

Figure 3.9 Plot of principal strains (contraction positive) after isotropic consolidation at 200 kPa

The resulting meshes therefore were more likely to have many joint elements oriented close to the vertical or horizontal directions, respectively. One can see examples of the former in the 75 and 192 element meshes and of the latter in the 432 element mesh in Figure 3.5. Examination of Figure 3.9 reveals that this anisotropy of joint element orientation has an influence on the degree of induced strain anisotropy, which may indicate a similar effect to that of "bedding planes" in real granular materials. Further investigation of the influence of joint element orientation on the degree of induced strain anisotropy is required to establish a clear relationship.

3.1.5 Conclusions and Future Work

This paper presented a formulation for a hybrid Voronoi cell finite-discrete element method (VCFEM-DEM) using polygonal body elements with linear elastic deformation and interface elements with nonlinear constitutive behaviour to represent interactions between body elements. Numerical examples demonstrated the capacity of this model to simulate the shear deformation of granular material at the laboratory test scale. Examination of the results showed that the ultimate load capacity of the system depends on the strength parameters of the joint elements, with influence from mesh coarseness and arrangement. Calibration of stiffness and strength parameters in the model from laboratory data is thus valid for a specified level of mesh coarseness. The initial topology of the mesh influences both the failure mode and the degree of induced strain anisotropy, as one would expect for real granular materials, owing to the influence

of particle shape and the orientation of the bedding plane during particle deposition.

The present work limited the analysis to static equilibrium and small displacements in which the contiguity of neighbouring body elements remained constant throughout the analysis. In order to simulate post peak conditions and dynamic loading, future work will extend the present analysis to account for dynamic equilibrium and potential changes in body element contiguity in the course of the analysis. Future work should also include parametric studies on the influence of the body and joint element stiffness properties on the shape of the stress strain curve as well as the influence of joint element orientation on the degree of induced strain anisotropy.

3.2 Conference Presentation #1: Simulation of lab scale tests on granular media using assumed stress polygonal finite elements and nonlinear joint elements[3]

3.2.1 Introduction

We examine here the results of additional quasi-static simulations of biaxial compression of granular material using the model presented in Section 3.1. We are interested in the influence of the grain structure or "fabric" of the material – a grain-scale property of the material – on the development of the global failure mode and formation of localized failures. In other words, how does the microstructure of the material influence its macroscopic behaviour? The following section provides further discussion of the results in Section 3.1.4 and presents additional results of a simulation of biaxial compression of a uniform medium to coarse sand with a nominal grain diameter of approximately 1 mm.

3.2.2 Results and Discussion

Typically, in continuum-based modelling, one should ensure that the results are not sensitive to the mesh [cf. 166,167,170-173], as the mesh is a numerical abstraction not representing a real property of the material. Even in some hybrid FEM-DEM modelling approaches using representative volumes of discrete elements, mesh sensitivity is something to be eliminated since the orientation and division between these representative volumes is arbitrary. Such models capture

[3] Karchewski B, Guo P, Stolle D. Simulation of lab scale tests on granular media using assumed stress polygonal finite elements and nonlinear joint elements. Presented at the *67th Canadian Geotechnical Conference, Sep 28-Oct 1, Regina, SK*, 2014.

localized shear strains and shear banding developing as a result of stress concentrations at the boundaries [81,166], local variations in void ratio and density [100] or on prescribed orientations determined by the mesh [164,170]. Capturing shear banding on prescribed planes by preparing the mesh or fabric in such a manner only demonstrates that an obviously weaker zone will govern the failure, as one would expect.

In Figure 3.7, we saw that the present modelling framework is capable of capturing strain localization in simulations of biaxial compression tests. Figure 3.10 shows additional examples of this phenomenon. We emphasize that in these results, strain localization develops primarily because of local variations in grain structure. Another way of saying this is that the results of the simulation are sensitive to the mesh configuration, which is often viewed as a negative feature in the finite element literature. However, in this case the mesh is not an arbitrary numerical abstraction, but rather represents a physical property of the granular material:

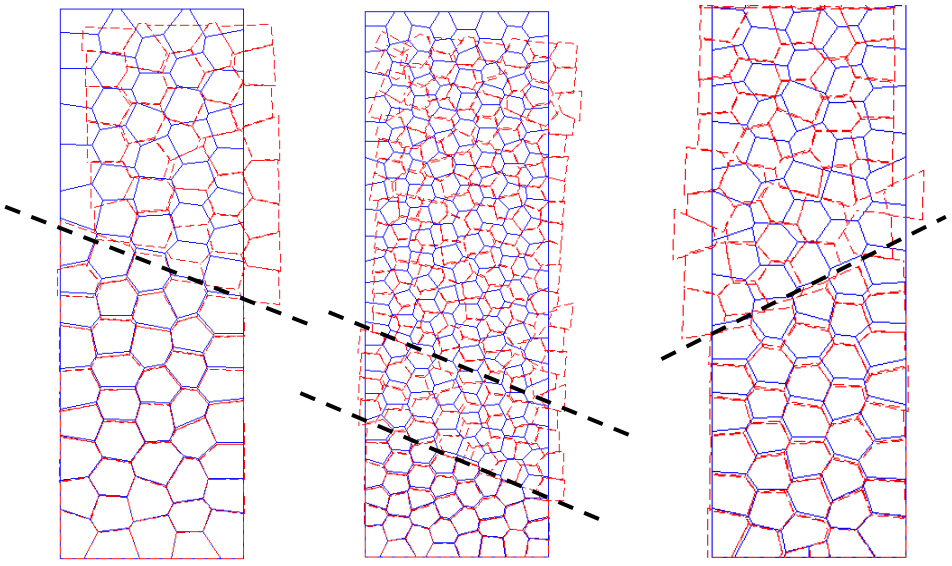

Figure 3.10 Additional examples of strain localization observed in biaxial compression simulations

the material's fabric or structure. There was no need to introduce artificial local variations in void ratio (or joint strength, or joint stiffness). Stress concentrations near the boundaries were not necessarily the driving factor in the strain localization. Wang et al. [164,172] capture this with a kinematic remeshing technique using discrete finite elements in which they generate special shear band elements after detecting strain localization. However, this approach requires the a priori specification of shear band thickness as a material property, and ultimately remains continuum based in that it does not capture the influences of grain structure. Samaniego and Belytschko [173] capture shear banding using the extended finite element method in a method similar to fracture mechanics, and the criterion used to generate shear band propagation is the loss of hyberbolicity of the initial boundary value problem. Their approach is apparently capable of generating shear bands of arbitrary orientation, although their presented examples only show shear bands propagating from stress concentrations at boundary conditions or from imperfections specified a priori. The present results differ in that they harnesses mesh sensitivity in a manner that captures physical influences of grain structure, though we use a continuum-based FEM formulation for both the body elements and the joint elements. The primary advantages are that we obtain details about the stresses in the grains, we accurately model the constitutive behaviour of the frictional contacts and we obtain detailed information about the joint orientations, stresses and strains throughout the simulation. A disadvantage of the present modelling framework is that we model all particle contacts as edge-edge contacts – or at best, we average the effect of point-edge and point-point contacts locally as an equivalent edge-edge contact. In the present form of the

model, we also assume that the contact relations between particles do not change throughout the simulation, which limits the analysis to small strains. We could overcome the latter by incorporating a contact detection step, such as that of Cundall [174,176], into the analysis, but careful consideration would need to be given to how the characteristic length and nonlinear joint stiffness coefficients should be initialized for new contacts.

We observed in Figure 3.8 that localized failure develops near boundary tractions during load-controlled simulations not modelling the loading cap explicitly. This behaviour is not artificial, since if one loaded granular material in a laboratory directly, one would expect similar localized failures. In laboratory tests, one prevents this by using a stiff loading cap to ensure that the load spreads evenly to the top of the specimen. We alleviated this issue in subsequent simulations in the same manner, by modelling a loading cap and the frictional contacts between the loading cap and the granular material explicitly.

Figure 3.11 shows the deformation pattern at failure of a simulation of a test on a uniform sand ($d \approx 1$ mm), along with the material properties of the body and joint elements. For this grain size, the mesh consists of 9168 body elements and 23 300 interface elements in the granular subdomain. The properties of the joint elements at the cap-granular boundary were taken as the same as those of the internal granular contacts. As the cap is not a granular material, the properties of the joint elements were set such that only linear elastic behaviour occurred.

We observe in Figure 3.11 a deformation pattern that is typical of laboratory compression tests on granular material with greater lateral deformation in the middle of the specimen than near the boundaries. We carried out the simulation

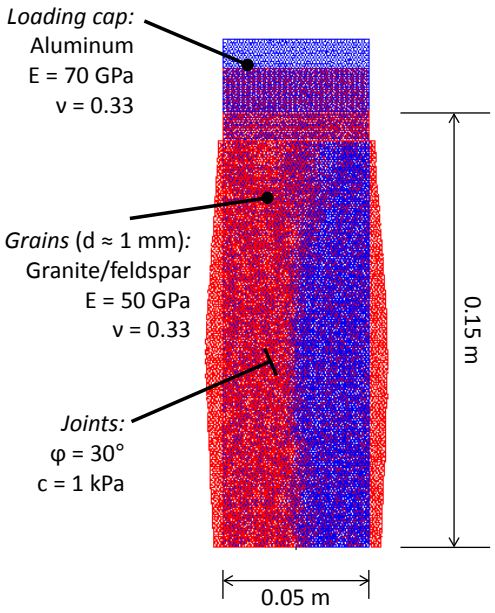

Figure 3.11 Biaxial compression test on uniform sand under confining pressure of 200 kPa and peak deviatoric stress of 398 kPa. Displacements magnified by approximately 350x for plotting.

with a constant lateral confining pressure of 200 kPa, which gave a peak deviatoric stress of 398 kPa. These results imply an internal friction angle of 29.8°, which is consistent with the joint contact friction angle of 30°. Therefore, the results are qualitatively and quantitatively similar to what one would observe in a typical laboratory test on such material.

We now examine the additional information about the internal behaviour of the specimen provided by the simulation results. Figure 3.12 (inset) and Figure 3.13 show the grain structure and the distribution of contact normal directions, respectively, being irregular hexagons with contact normals primarily at angles of $60n°$ for $n \in \{1, 2, \ldots, 5\}$. Figure 3.12 also shows the pattern of failed joint elements at the peak deviatoric stress. That is, joint elements that reached the Coulomb yield criterion and required stress correction in the final calculation step. We observe a distinct wedge shape formed below the loading cap, which we

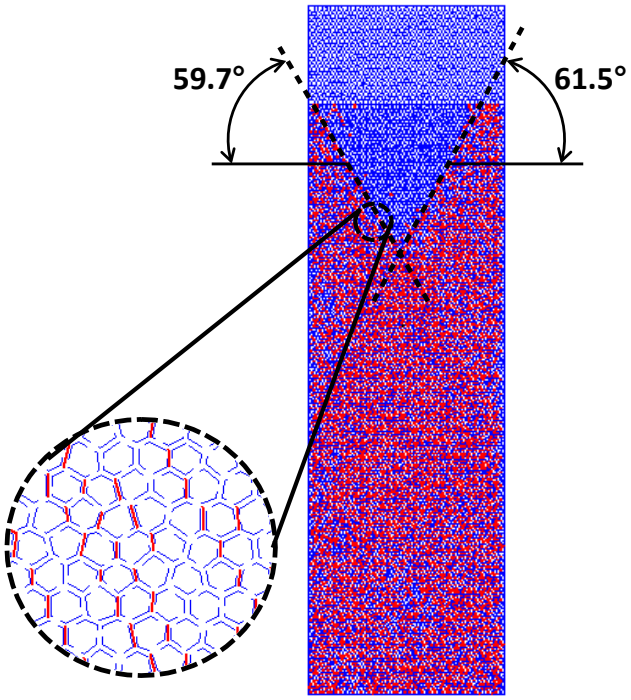

Figure 3.12 Failed joint elements in biaxial compression test on uniform sand under confining pressure of 200 kPa and peak deviatoric stress of 398 kPa and (inset) detailed image of grain shape and failure pattern.

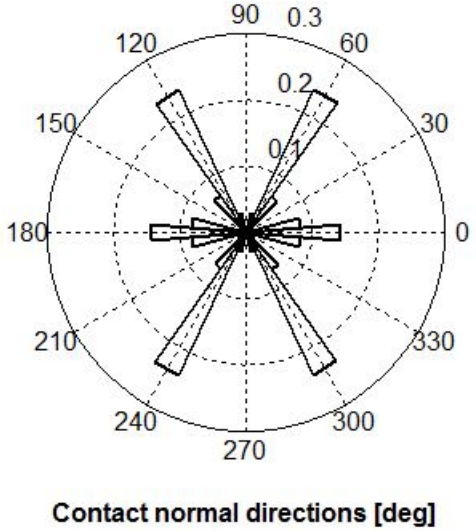

Figure 3.13 Histogram of joint element normal directions

attribute to the frictional behaviour at the cap-granular interface. However, the width of the loading cap does not govern the side angles of the frictional wedge, but rather they make an angle of approximately 60° with the horizontal. This failure plane angle is consistent with that predicted by the well-known Mohr-

Coulomb failure criterion, which is 45° + $\varphi'/2$ where $\varphi' \approx 30°$ in this case. This result also demonstrates why laboratory compression tests on granular material are not true material tests since the stress and strain conditions in the specimen are not uniform, a remark made by several others [cf. 230].

We also observe the shear stress distribution in the granular elements, as Figure 3.14 shows, for evidence of strain localization. The shear stress in the grain elements at a peak deviatoric stress of 398 kPa is between 400 kPa and 500 kPa. The range of shear stresses in the grains is consistent with the peak deviatoric stress level, but slightly higher in magnitude owing to the non-uniform stress distribution in the specimen. Since the granular elements have linear elastic constitutive behaviour, zones of high shear stress correspond directly to zones of shear strain localization. Examining a representative volume of grains in the inset

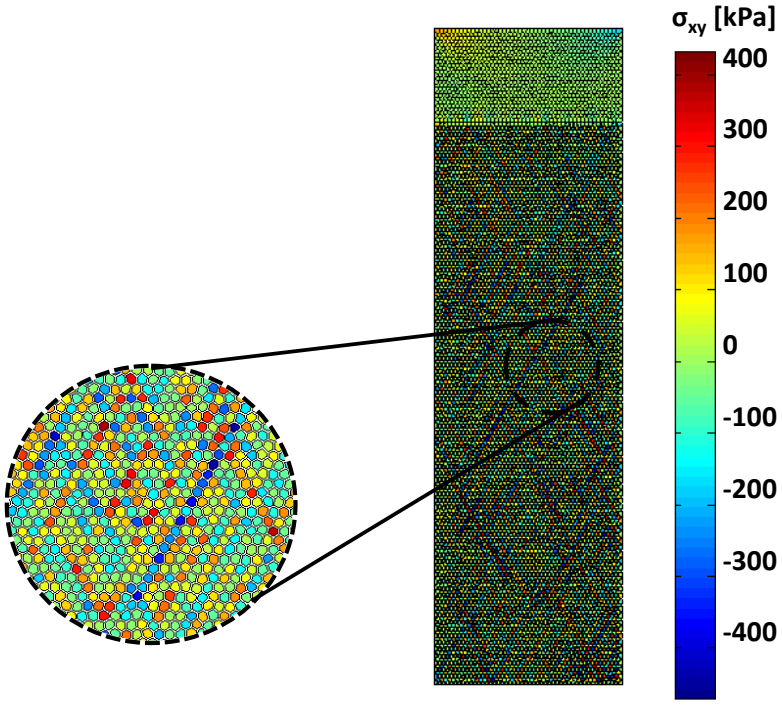

Figure 3.14 Shear stress in the grains in biaxial compression test on uniform sand under confining pressure of 200 kPa and peak deviatoric stress of 398 kPa and (inset) a detailed view of patterns of high shear stress and strain localization

of Figure 3.14, we observe that the distance separating zones of high shear stress – that is, the size of the shear band – is approximately 3-20 grains, which is consistent with observations in the literature [80,88,89,93,94,101]. We observe in the present set of simulation results that the orientation of the bands of high shear stress is consistent with the orientation of the failure planes developed beneath the loading cap. We observe in the inset of Figure 3.14 that the orientation of these planes results from the grain structure rather than from any artificial influences at the boundaries. However, the formation of bands of high shear stress is chaotic in the sense that it is highly sensitive to local variations in particle orientation and angularity, making it difficult or impossible to know a priori where such a plane will form.

3.2.3 Conclusions and Future Work

We examined the results of laboratory scale simulations of granular material obtained using the modelling framework presented in Section 3.1. The simulation results show behaviour consistent with what one would observe in laboratory compression tests on granular material. Additionally, we observed in the simulation results detailed information about the internal response of the specimen to the loading conditions. We captured strain localization in the specimen that resulted from the granular structure of the specimen rather than artificial influences such as the boundary conditions or arbitrary variations in material properties or mesh configuration assigned a priori.

Having successfully modelled laboratory scale results on dry granular material within this framework, we aim to extend this work in two directions. In

Sections 3.3, we examine the influence of grain structure on failure patterns in laboratory biaxial compression tests using a dynamic VCFEM-DEM formulation coupled with tangent eigenanalysis. In Section 3.4, we analyse subsurface stress distributions at the field scale to understand how grain structure affects the transfer of gravity loads. In future work, we aim to combine the VCFEM-DEM for the solid component of granular material with the modelling of flow through discrete pore or fracture networks using the model described in Section 2.1 to obtain a hydro-mechanical coupled model of granular material behaviour. Toward this goal, Section 4.1 first examines a coupled VCFEM model incorporating the seepage analysis of Section 2.1 with a continuous VCFEM model for solid mechanics, i.e. not modelling granular contacts.

3.3 Journal Paper #2 / Conference Paper #2: Multi-scale analysis of deformation modes in granular material using a dynamic hybrid polygonal finite element-discrete element formulation[4]

3.3.1 Introduction

To understand the behaviour of granular materials, it is important to realize that they differ fundamentally from solids such as metals. Whereas one may consider metals to be continuous solids even at the microscopic scale, granular materials consist of discrete solid grains – often visible to the naked eye – that interact by frictional sliding. This fundamental difference has captivated researchers from the age of enlightenment [10], through the 19th and early 20th centuries [2,32,107] up to the present day [7,231]. Indeed, the distinctly different manner in which granular materials behave compared with solids, liquids and gasses has led some to classify them as a distinct form of matter [18,232]. Many of the details of phenomena observed in granular material behaviour are not fully understood, and a complete review of the literature is outside of the scope of this article; we refer to Section 1.1.2 and references [7,18,26,64,69,70,108,110-114,232] for further details. In engineering science and géotechnique, it often suffices to approximate the macroscopic behaviour of granular materials using continuum models with volume-averaged properties. However, we must contend that a true understanding of the behaviour of granular material necessitates a multi-scale analysis accounting for particle interactions and their influence on

[4] Karchewski B, Guo P, Stolle D. Multi-scale analysis of deformation modes in granular material using a dynamic hybrid polygonal finite element-discrete element formulation. Submitted 07/2015 to the *4th GeoChina International Conference, July 25-27, Shandong, China*.

macro-scale behaviour. This is particularly true in cases where there is significant strain localization, which may occur at the laboratory scale in the form of shear banding and at the field scale when slopes fail.

The key features that govern the dynamic behaviour of assemblies of grains are the equilibrium of normal and tangential contact forces between grains and the dissipative frictional sliding that occurs when grains interact. The grains themselves may be considered rigid or deformable. The former is certainly an attractive assumption when "grains" in the model correspond to individual physical grains since the deformation of a grain assembly is governed by relative motion of grains. Incorporating deformable "grains" into the model allows scalability from lab scale to field scale behaviour [cf. 233,234], where in the latter case grains in the model are representative volumes of the geomaterial. Modelling of the inter-grain force equilibrium must adequately account for the fact that grains have negligible resistance to separation, high stiffness in compression and nonlinear dissipative constitutive behaviour in shear. We divide models for strain localization in granular materials into four broad categories: i) micromechanical, ii) discrete or distinct element (DEM), iii) material point method and iv) finite element with element enrichment accounting for strain localization. We shall discuss each briefly to put the model presented herein in context.

Micromechanical models reduce the analysis to a small enough region that a model explicitly accounting for individual grains and tracking their interactions with a high level of detail becomes tractable [26,30,40,41,44,69,70,223,224]. This form of model uses Eulerian, arbitrary Eulerian-Lagrangian or micropolar Cosserat continuum mechanics equilibrium equations with appropriate boundary

conditions and interface tracking to track all particles and interfaces in a volume of interest. This approach certainly allows detailed analysis of the behaviour of granular materials at the micro-scale, but lacks the ability to up-scale the region of interest owing to the exponentially increasing computational cost of tracking many individual particles and interfaces.

Discrete element (DEM) models reduce the complexity involved in micromechanical models by introducing grain elements having simple shapes such as discs/spheres [175], ellipses/ellipsoids [178-180,225] or polygons/polyhedra [174,176,177]. This approach simplifies the analysis of the behaviour at contacting interfaces, with the contact between grains determined through pair-wise comparison of overlapping volume. Clearly, models using simpler grain shapes such as spheres or ellipsoids make detection of contact easier, but may not accurately reflect the grain shape of many granular materials that have angular or subangular grains. Polyhedral grains better represent such granular materials, but require tracking of a larger number of interaction types (point-to-point, point-to-edge, point-to-face, edge-to-face, face-to-face). Cundall [176] introduces the common plane approach to reduce the number of tests required by testing only for contact with a plane between two potentially contacting blocks. The normal force between contacting grains is proportional to their overlapping volume. The shear force transfer may be non-slip if frictional dissipation is not of interest, or may account for frictional sliding using Coulomb frictional resistance. Grains may be rigid or deformable with the former preferred when the deformation of the grains is small compared to the deformation caused by relative movement between grains. When deformable polyhedral blocks are

desirable, the blocks are typically discretized into an internal mesh of finite elements [181]. A novel approach developed recently called FEM-DEM [187-189] uses a combination of body finite elements to represent linear elastic regions and interface finite elements to account for the nonlinear behaviour associated with fracture propagation. This approach has the advantage of reducing the complication involved in modelling many types of grain interaction, but sacrifices the ability to model large strain behaviour wherein the contact relationships between grains may change.

Material point method (MPM) models including a contact algorithm have been used to model a variety of micro-scale contact problems [184,185] and macro-scale problems involving multiple material phases [186]. The "material points" carry relevant calculation data – material properties, stresses, velocities – and move through a fixed calculation grid. The solution at each time step uses a three part explicit algorithm to account for interaction between contacting bodies. The first step solves for the material point velocities assuming all material points are part of a single body. The second step solves for the material point velocities for each individual body (grain) ignoring the influence of surrounding bodies. The third step corrects the velocities based on the difference between the velocities determined in the first and second phases, presuming that these will differ only when bodies are interacting. This approach can handle grains of arbitrary shape and does not require pair-wise comparison to determine which specific grains are interacting. The MPM approach is novel, but when modelling granular materials it suffers from similar disadvantages to micromechanical models, viz. requiring many material points to represent each grain and small numerical time steps,

leading to simulations that are computationally expensive even for a modest number of grains.

The present work uses a type of FEM-DEM model to capture multi-scale behaviour in granular materials. The model uses polygonal Voronoi cell elements to represent the grains, hence we call the model VCFEM-DEM. Previous work by the present authors [233] demonstrated a form of this model based on static equilibrium. The present work extends this modelling framework to account for dynamic behaviour, which allows modelling of the post-failure response when strain softening occurs. We model the interactions between grains using a type of interface element accounting for nonlinear constitutive behaviour. Section 1.1.4 provided a review of the literature on finite elements for modelling interfaces and strain localization, so we do not repeat it here. The interface elements in the present study use a combined volumetric deviatoric hardening flow plasticity formulation. Section 3.3.2 describes the formulation, Section 3.3.3 presents representative results of biaxial compression simulations and Section 3.3.4 summarizes the important contributions of the present study.

3.3.2 Formulation

3.3.2.1 Governing Equations

Figure 3.2 and Figure 3.3 schematically represent the discretization of a domain V into subdomains V_e representing grains and V_i representing interactions between grains. The equation governing the dynamic momentum balance for the overall grain structure in V is,

$$\rho\ddot{\mathbf{u}} = \mathbf{L}_{\sigma u}^{T}\boldsymbol{\sigma} + \rho\mathbf{g} \tag{3.3.1}$$

where ρ is the material density, $\mathbf{u} = \{ u_x, u_y, u_z \}^T$ represents the displacement field, $\boldsymbol{\sigma} = \{ \sigma_{xx}, \sigma_{yy}, \sigma_{zz}, \sigma_{xy}, \sigma_{yz}, \sigma_{zx} \}^T$ is the total stress tensor written in Voigt vector notation [cf. 116] and $\mathbf{g}$ is a vector representing the body acceleration field. We ignore body forces herein for simplicity since the focus is on biaxial compression test simulations, which is to say that $\mathbf{g} = \mathbf{0}$ in the present work. Superposed dots represent derivatives with respect to time t and $\mathbf{L}_{\sigma u}$ is a linear differential operator defined in matrix notation as,

$$\mathbf{L}_{\sigma u} = \begin{bmatrix} \frac{\partial}{\partial x} & 0 & 0 & \frac{\partial}{\partial y} & 0 & \frac{\partial}{\partial z} \\ 0 & \frac{\partial}{\partial y} & 0 & \frac{\partial}{\partial x} & \frac{\partial}{\partial z} & 0 \\ 0 & 0 & \frac{\partial}{\partial z} & 0 & \frac{\partial}{\partial y} & \frac{\partial}{\partial x} \end{bmatrix}^T \tag{3.3.2}$$

For plane strain analysis, we ignore the third row in $\mathbf{u}$, the third, fifth and sixth rows in $\boldsymbol{\sigma}$ and $\mathbf{L}_{\sigma u}$ and the third column in $\mathbf{L}$.

It is common in numerical analysis using continuum-based approaches such as the finite element method to discretize the domain such that the equation of motion becomes,

$$\mathbf{M}\ddot{\mathbf{a}}_u + \mathbf{F}_I(t) = \mathbf{F}_E(t) \tag{3.3.3}$$

where $\mathbf{M}$ is the mass matrix for the discretized system, $\mathbf{F}_I(t)$ is a vector of internal forces at time t and $\mathbf{F}_E(t)$ is a vector of external applied forces at time t. In the model developed for the present study, the internal force vector $\mathbf{F}_I$ has a linear elastic component $\mathbf{F}_{I(g)}$ coming from the internal stresses in the grain elements and a nonlinear component $\mathbf{F}_{I(i)}$ coming from the stresses at the interfaces between

grains. Sections 3.3.2.2 and 3.3.2.3 describe how we form the mass matrix and internal force vector for the grain elements and the interface elements, respectively. Section 3.3.2.4 discusses the time stepping scheme used to integrate equation (3.3.3) in time. Section 3.3.2.5 presents the eigenanalysis formulation for the structure of grain elements and interface elements.

3.3.2.2 Hybrid Polygonal Element (Grain Element)

Here we briefly derive the element stiffness for the polygonal elements representing the solid grains. The derivation is based on the hybrid principle of Pian and co-workers [149,150]. The authors note in the original presentation that the formulation is appropriate for elements with an arbitrary number of nodes [150], although it was not until much later that Ghosh and Mallett [153] provide the details for the practical implementation for polygons with more than four nodes. Ghosh and co-workers also extended the formulation to account for nonlinear constitutive behaviour in polygonal elements [155], as well as inclusions inside the elements [152,154,155]. For the present work, we restrict ourselves to the linear elastic case for the polygonal elements, assuming that the material grains remain linear elastic, whereas the interface elements – representing interactions between the grains – account for nonlinear constitutive behaviour.

Following the formulation of Tong and Pian [150], the stiffness of the polygonal elements derives from a modified complementary energy functional,

$$\Pi_{MCE}\left[\boldsymbol{\sigma}', \mathbf{u}^*\right] = -\tfrac{1}{2}\int_{V_e}\left(\boldsymbol{\sigma}'^T \mathbf{D}_e^{-1}\boldsymbol{\sigma}'\right)dV + \int_{S_e}\mathbf{u}^{*T}\left(\mathbf{n}_\sigma^T\boldsymbol{\sigma}\right)dS - \int_{S_t}\left(\mathbf{u}^{*T}\hat{\mathbf{t}}\right)dS \quad (3.3.4)$$

where V_e is the element volume, S_e is the outer surface of the element, S_t is a surface over which there is an applied traction, $\mathbf{D}_e^{-1}$ is the elastic compliance tensor relating strain to stress, $\boldsymbol{\sigma}' = \{ \sigma_{xx}', \sigma_{yy}', \sigma_{xy}' \}^T$ represents the "effective" stress tensor – the part of the stress causing strain, $\boldsymbol{\sigma}$ represents the total stress tensor, $\mathbf{u}^* = \{ u_x, u_y \}^T$ is the displacement on S_e, $\mathbf{n}_\sigma$ represents the outward pointing unit normal of the element and $\hat{\mathbf{t}}$ is an applied traction. Note that the "modifying" term in the complementary energy functional is the second term in equation (3.3.4) – called the interface potential – that accounts for traction equilibrium at the element boundaries. For plane strain analysis,

$$\mathbf{D}_e^{-1} = \frac{1+\nu}{E}\begin{bmatrix} 1-\nu & -\nu & 0 \\ -\nu & 1-\nu & 0 \\ 0 & 0 & 2 \end{bmatrix} \tag{3.3.5}$$

$$\mathbf{n}_\sigma = \begin{bmatrix} n_x & 0 & n_y \\ 0 & n_y & n_x \end{bmatrix}^T \tag{3.3.6}$$

where E is the elastic modulus of the grain, ν is the Poisson ratio and n_x and n_y refer to the components of the outward pointing unit normal in Cartesian coordinates. We interpolate stress inside the grain elements using Airy's stress functions with unknown coefficients. This satisfies equilibrium a priori, and is of the form,

$$\boldsymbol{\sigma} = \mathbf{P}_\sigma \boldsymbol{\beta}_\sigma + \boldsymbol{\sigma}_0 \tag{3.3.7}$$

where $\mathbf{P}_\sigma$ contains a set of monomial basis functions and $\boldsymbol{\beta}_\sigma$ is a vector of coefficients, whose values are to be determined in the finite element analysis. The $\mathbf{P}_\sigma\boldsymbol{\beta}_\sigma$ term in the stress interpolation represents the effective stress field $\boldsymbol{\sigma}'$ component owing to deformation of the grains and $\boldsymbol{\sigma}_0$ represents a background

initial stress field, which we assume to be constant herein. Interpolation of displacement on the element boundaries is of the form,

$$\mathbf{u}^{*} = \mathbf{N}_{u}^{*}\mathbf{a}_{u} \tag{3.3.8}$$

where $\mathbf{N}_u^*$ contains linear shape functions interpolating between the adjacent nodal values of displacement $\mathbf{a}_u$. Substituting equations (3.3.7) and (3.3.8) into (3.3.4) gives the discretized form of the two parameter hybrid functional for polygonal elements,

$$\Pi_{MCE}\left[\boldsymbol{\beta}_{\sigma}, \mathbf{a}_{u}\right] = -\tfrac{1}{2}\boldsymbol{\beta}_{\sigma}^{T}\mathbf{H}_{\sigma\sigma}\boldsymbol{\beta}_{\sigma} + \boldsymbol{\beta}_{\sigma}^{T}\mathbf{G}_{\sigma u}\mathbf{a}_{u} - \mathbf{a}_{u}^{T}\mathbf{F}_{\hat{t}0} \tag{3.3.9}$$

where $\mathbf{F}_{\hat{t}0} = \mathbf{F}_{\hat{t}} - \mathbf{F}_0$ and,

$$\mathbf{H}_{\sigma\sigma} = \int_{V_e}\left(\mathbf{P}_{\sigma}^{T}\mathbf{D}_{e}^{-1}\mathbf{P}_{\sigma}\right)dV \tag{3.3.10}$$

$$\mathbf{G}_{\sigma u} = \int_{S_e}\left(\mathbf{n}_{\sigma}^{T}\mathbf{P}_{\sigma}\right)^{T}\mathbf{N}_{u}^{*}\,dS \tag{3.3.11}$$

$$\mathbf{F}_{\hat{t}} = \int_{S_t}\left(\mathbf{N}_{u}^{*T}\hat{\mathbf{t}}\right)dS \tag{3.3.12}$$

$$\mathbf{F}_{0} = \int_{S_e}\mathbf{N}_{u}^{*T}\left(\mathbf{n}_{\sigma}^{T}\boldsymbol{\sigma}_{0}\right)\,dS \tag{3.3.13}$$

Recognizing that stationarity of equation (3.3.9) requires that the variations with respect to $\boldsymbol{\beta}_\sigma$ and $\mathbf{a}_u$ vanish, and noting that the $\boldsymbol{\beta}_\sigma$ coefficients need not be continuous between elements, leads to the following relation,

$$\boldsymbol{\beta}_{\sigma} = \mathbf{H}_{\sigma\sigma}^{-1}\mathbf{G}_{\sigma u}\mathbf{a}_{u} \tag{3.3.14}$$

where Tong and Pian [150] present the requirements for rank sufficiency and invertibility of $\mathbf{H}_{\sigma\sigma}$. Substitution of equation (3.3.14) into (3.3.9) gives the hybrid functional in terms of $\mathbf{a}_u$ only,

$$\Pi_{MCE}\left[\mathbf{a}_{u}\right] = \tfrac{1}{2}\mathbf{a}_{u}^{T}\mathbf{K}_{uu(g)}\mathbf{a}_{u} - \mathbf{a}_{u}^{T}\mathbf{F}_{t0} \tag{3.3.15}$$

where $\mathbf{K}_{uu(g)}$ is the element stiffness matrix for the polygonal grain elements,

$$\mathbf{K}_{uu(g)} = \mathbf{G}_{\sigma u}^{T}\mathbf{H}_{\sigma\sigma}^{-1}\mathbf{G}_{\sigma u} \tag{3.3.16}$$

We presented here only a brief overview of the hybrid polygonal element formulation. References [146-148] provide a more detailed literature review on the origin, formulation and application of hybrid finite elements and reference [157] provides further details regarding polygonal elements.

In the present work, we perform volume integrals over the domain of polygonal elements using exact quadrature rules generated according to the approach of Mousavi and Sukumar [217] and surface integrals using standard Gauss quadrature rules (for details, see the Appendix). As the grain elements remain linear elastic, we assemble the global stiffness component owing to grain elements through summation accounting for connectivity of nodal degrees of freedom between elements. The global nodal displacement vector $\mathbf{a}_u$ is the union of the element nodal displacement vectors. The component of internal force $\mathbf{F}_I(t)$ owing to body element deformation $\mathbf{F}_{I(g)}(t)$ is then the product of $\mathbf{K}_{uu(g)}$ and $\mathbf{a}_u(t)$,

$$\mathbf{F}_{I(g)}(t) = \mathbf{K}_{uu(g)}\mathbf{a}_u(t) \tag{3.3.17}$$

We shall now examine the formation of the element mass matrix for the grain elements. We compute the consistent mass matrix $\mathbf{M}'$ using the well-known [134] relation,

$$\mathbf{M}' = \int_{V_e}\left(\mathbf{N}_u^{T}\rho\mathbf{N}_u\right)dV \tag{3.3.18}$$

where $\mathbf{N}_u$ is a matrix containing shape functions that interpolate between nodal values of displacement (or velocity, or acceleration) inside V_e. This is also possible for polygonal elements, though it is worth noting that the solution for

conforming shape functions over polygons with more than four nodes not unique [140,142] as it is for the well-known triangular or quadrilateral elements [134]. Whether the choice of conforming shape function used to construct such a consistent mass matrix for polygonal grain elements significantly influences the dynamic solution is outside of the scope of the present study. In the present study we opt for a lumped mass approach for computational efficiency, with the understanding that this may introduce a small amount of numerical damping into the solution and influence the critical time step [235]. We form the lumped mass matrix **M** by setting the diagonal entries to the row sums of the consistent mass matrix and the off diagonal values to zero,

$$\mathbf{M}_{(i,j)} = \begin{cases} \sum_{j=1}^{N_{dof}} \mathbf{M}'_{(i,j)} & \text{for } i = j \\ 0 & \text{otherwise} \end{cases} \tag{3.3.19}$$

where the subscripts (*i*,*j*) refer to the row and column indices in the matrix and N_{dof} is the number of degrees of freedom in the element. We then form the global mass matrix through summation accounting for the connectivity of degrees of freedom. We assume that all mass in the system comes from the grain elements, with the interfaces between the grains being massless. This concludes the basic formulation of the element stiffness and mass matrices for the polygonal grain elements. The following section outlines the formulation of the interface elements.

3.3.2.3 Interface Element (Grain Interaction Element)

We now examine the formulation of the interface element representing the interactions between grains. In past studies, the use of interface elements has

primarily been applied within the contexts of soil-structure interaction and jointed rock. Section 1.1.4 provided a review of the literature on special finite elements for modelling interfaces and strain localization, so it is not repeated here.

In the present study, we define the constitutive behaviour of the interface element using an isotropic combined volumetric-deviatoric hardening elastoplastic formulation [cf. 236]. We base the interface element formulation on an incremental strain energy relation as follows,

$$\Delta U_i\left[\Delta\tilde{\boldsymbol{\sigma}}', \Delta\tilde{\boldsymbol{\varepsilon}}\right] = \int_{V_i}\left(\Delta\tilde{\boldsymbol{\varepsilon}}^T\tilde{\boldsymbol{\sigma}}'\right)dV + \tfrac{1}{2}\int_{V_i}\left(\Delta\tilde{\boldsymbol{\varepsilon}}^T\Delta\tilde{\boldsymbol{\sigma}}'\right)dV \tag{3.3.20}$$

where $\Delta\tilde{\boldsymbol{\varepsilon}} = \{\ \Delta\varepsilon_\xi,\ \Delta\varepsilon_\eta\ \}^T$ is the local strain increment, $\tilde{\boldsymbol{\sigma}}' = \{\ \sigma_\xi',\ \sigma_\eta'\ \}^T$ is the previous effective stress state and $\Delta\tilde{\boldsymbol{\sigma}}'$ is a finite effective stress increment. To wit, the strain energy increment in an interface element derives from the integration over the interface volume V_i of the strain energy density increment. For small finite increments to stress, the strain energy density increment has two components: (i) the work done by the strain increment at the current state of stress and (ii) the strain energy density increment owing to the product of the strain increment with the stress increment. The first and second terms in equation (3.3.20) capture (i) and (ii), respectively.

The aim in the finite element formulation is to determine an equivalent incremental strain energy expression in terms of the discretized nodal displacements at the element level that looks like,

$$\begin{aligned}\Delta U_e\left[\Delta\mathbf{a}_u\right] &= \Delta\mathbf{a}_u^T\left[\int_{V_e}\left(\mathbf{B}^T\tilde{\boldsymbol{\sigma}}'\right)dV + \tfrac{1}{2}\int_{V_e}\left(\mathbf{B}^T\mathbf{D}_{ep}\mathbf{B}\right)dV\Delta\mathbf{a}_u\right] \\ &= \Delta\mathbf{a}_u^T\mathbf{F}_{I(i)} + \tfrac{1}{2}\Delta\mathbf{a}_u^T\mathbf{K}_{uu(i)}\Delta\mathbf{a}_u\end{aligned} \tag{3.3.21}$$

where $\Delta\mathbf{a}_u$ is a vector of nodal displacement increments, $\mathbf{B}$ is a kinematic matrix relating global displacements to local strains and $\mathbf{D}_{ep}$ is the tangent elastoplastic interface constitutive matrix. Examining the second line in equation (3.3.21), $\mathbf{F}_{I(i)}$ is the internal force vector in an interface element and its summation over all interface elements accounting for connectivity of nodal degrees of freedom gives the component of $\mathbf{F}_I(t)$ owing to interface element internal forces $\mathbf{F}_{I(i)}(t)$.

We derive the local strain increments $\Delta\tilde{\boldsymbol{\varepsilon}}$ from the local displacement increments $\Delta\tilde{\mathbf{u}}$ on the "bottom" and "top" side of the interface in the local $\{\xi, \eta\}$ coordinate system as follows,

$$\Delta\tilde{\boldsymbol{\varepsilon}} = \begin{Bmatrix} \Delta\varepsilon_\xi \\ \Delta\varepsilon_\eta \end{Bmatrix} = \delta_e^{-1} \begin{bmatrix} -1 & 0 & 1 & 0 \\ 0 & -1 & 0 & 1 \end{bmatrix} \begin{Bmatrix} \Delta u_\xi^{bot} \\ \Delta u_\eta^{bot} \\ \Delta u_\xi^{top} \\ \Delta u_\eta^{top} \end{Bmatrix} = \mathbf{L}_{iu}\Delta\tilde{\mathbf{u}} \tag{3.3.22}$$

where δ_e is a representative thickness for the interface and $\mathbf{L}_{iu}$ is a difference operator that approximates a linear differential operator assuming linear interpolation of displacements in the η direction. We note that $\Delta\varepsilon_\xi$ and $\Delta\varepsilon_\eta$ represent increments to shear strain and normal strain in the η direction, respectively. We assume that normal strains in the ξ direction are negligible. In this way, we maintain stress continuity over the interfaces [166]. We transform from global to local coordinates as,

$$\begin{Bmatrix} \xi \\ \eta \end{Bmatrix} = \begin{bmatrix} \tilde{n}_y & -\tilde{n}_x \\ \tilde{n}_x & \tilde{n}_y \end{bmatrix} \begin{Bmatrix} x \\ y \end{Bmatrix} = \mathbf{T}_0\mathbf{x} \tag{3.3.23}$$

where $\tilde{\mathbf{n}} = \{ \tilde{n}_x, \tilde{n}_y \}^T$ is a unit normal vector pointing in the positive η direction. We assume linear interpolation of the displacement increments between the nodes of an interface element according to,

$$\Delta\mathbf{u} = \tilde{\mathbf{N}}_u \Delta\mathbf{a}_u \tag{3.3.24}$$

where $\tilde{\mathbf{N}}_u$ is a matrix containing interpolating shape functions in local coordinates and $\Delta\mathbf{a}_u$ is a column vector of nodal displacement increments in global coordinates. For an interface element with 4 nodes numbered locally in counter-clockwise order, we define $\tilde{\mathbf{N}}_u$ as,

$$\tilde{\mathbf{N}}_u = \begin{bmatrix} N_1 & 0 & N_2 & 0 & 0 & 0 & 0 & 0 \\ 0 & N_1 & 0 & N_2 & 0 & 0 & 0 & 0 \\ 0 & 0 & 0 & 0 & N_2 & 0 & N_1 & 0 \\ 0 & 0 & 0 & 0 & 0 & N_2 & 0 & N_1 \end{bmatrix} \tag{3.3.25}$$

where $N_1 = 1\text{-}\xi$ and $N_2 = \xi$. Combining the notions in equations (3.3.20), (3.3.22), (3.3.23) and (3.3.24) and comparing with equation (3.3.21) leads to the definition of the kinematic matrix **B** as,

$$\mathbf{B} = \mathbf{L}_{iu}\mathbf{T}\tilde{\mathbf{N}}_u \tag{3.3.26}$$

where we define **T** as,

$$\mathbf{T} = \begin{bmatrix} \mathbf{T}_0 & \mathbf{0} \\ \mathbf{0} & \mathbf{T}_0 \end{bmatrix} \tag{3.3.27}$$

which rotates the displacements on both bottom and top surfaces of the interface.

Following an isotropic combined volumetric-deviatoric elastoplastic strain hardening approach as in [236], we define the incremental stress-strain relation for an interface element as,

$$\Delta\tilde{\boldsymbol{\sigma}}' = \begin{Bmatrix} \Delta\sigma_\xi' \\ \Delta\sigma_\eta' \end{Bmatrix} = \begin{bmatrix} G & 0 \\ 0 & M \end{bmatrix} \begin{Bmatrix} \Delta\varepsilon_\xi^e \\ \Delta\varepsilon_\eta^e \end{Bmatrix} = \mathbf{D}_e \Delta\tilde{\boldsymbol{\varepsilon}}_e \tag{3.3.28}$$

where $\mathbf{D}_e$ is the elastic constitutive matrix and $\Delta\tilde{\boldsymbol{\varepsilon}}_e$ is the elastic strain increment for the interface with G and M being the elastic shear and constrained moduli. Use of the constrained modulus M to derive the normal stress in the η direction is consistent with the assumption that normal strains in the ξ direction are negligible. In this case, $\Delta\varepsilon_\eta$ also represents the volumetric strain increment for the interface. Examining the constitutive relation in equation (3.3.28), we assume additivity of elastic and plastic strain increments, $\Delta\tilde{\boldsymbol{\varepsilon}}_e = \Delta\tilde{\boldsymbol{\varepsilon}} - \Delta\tilde{\boldsymbol{\varepsilon}}_p$. The stress state during active loading lies on an expanding loading surface $f(\tilde{\boldsymbol{\sigma}}', \zeta) = 0$, which we define to be elliptical, following the modified critical state approach [237,238],

$$f\left(\tilde{\boldsymbol{\sigma}}', \zeta\right) = \left(\sigma_\eta' - a\right)^2 + \left(\sigma_\xi' \Big/ \tan\varphi_c\right)^2 - a^2 = 0 \tag{3.3.29}$$

where ζ is a hardening parameter, φ_c is the critical state friction angle and $a = a(\zeta)$ is a hardening function that determines the centre of the loading surface. Within the critical state approach, we define $a(\zeta)$ as,

$$a = a_0 \exp\left(\frac{-\zeta}{\lambda - \kappa}\right) \tag{3.3.30}$$

where a_0 is the centre of the loading surface at the stress state corresponding to an initial void ratio e_0, and λ and κ are the compression index and the swelling index, respectively. Following from this, the elastic constrained modulus M is actually proportional to the normal stress σ_η' [236] according to the following relation,

$$M = \frac{1 + e_0}{\kappa}\sigma_\eta' \tag{3.3.31}$$

Active loading satisfies the consistency condition,

$$\Delta f = \left(\frac{\partial f}{\partial \tilde{\boldsymbol{\sigma}}'} \right)^T \Delta \tilde{\boldsymbol{\sigma}}' + \frac{\partial f}{\partial \zeta} \Delta \zeta = 0 \tag{3.3.32}$$

where the stress increment comes from the constitutive relation in equation (3.3.28) and the increment to the hardening parameter is,

$$\Delta \zeta = \vartheta \Delta \varepsilon_{\xi}^{p} - \left(1 + e_0\right) \Delta \varepsilon_{\eta}^{p} \tag{3.3.33}$$

where the coefficient ϑ is a material parameter specifying the component of the increment to the hardening parameter ζ owing to plastic shear strain increments. We assume that at failure the interface stresses satisfy the Mohr-Coulomb failure criterion $F(\tilde{\boldsymbol{\sigma}}) = \sigma_{\xi}' - \sigma_{\eta}' \tan\varphi_f = 0$ where φ_f is the friction angle at failure. This assumption constrains the value of ϑ to be,

$$\vartheta = \tfrac{1}{2}\left(1 + e_0\right) \frac{\tan\varphi_f}{\tan\varphi_c} \left[\left(\frac{\tan\varphi_c}{\tan\varphi_f} \right)^2 - 1 \right] \tag{3.3.34}$$

which vanishes for $\varphi_c = \varphi_f$ reducing the model to purely isotropic volumetric hardening. To derive a symmetric positive definite tangent elastoplastic constitutive operator $\mathbf{D}_{ep}$, we assume an associated plastic flow rule as follows,

$$\Delta \tilde{\boldsymbol{\varepsilon}}_p = \frac{\partial f}{\partial \tilde{\boldsymbol{\sigma}}'} \Delta \mu \tag{3.3.35}$$

where $\Delta\mu$ is the plastic multiplier obtained for strain-controlled loading by substituting equations (3.3.28), (3.3.33) and (3.3.35) into equation (3.3.32) to obtain,

$$\Delta \mu = \frac{1}{H} \left(\frac{\partial f}{\partial \tilde{\boldsymbol{\sigma}}'} \right)^T \mathbf{D}_e \Delta \tilde{\boldsymbol{\varepsilon}} \tag{3.3.36}$$

where $H = H_e + H_p$ and,

$$H_e = \left(\frac{\partial f}{\partial \tilde{\boldsymbol{\sigma}}'} \right)^T \mathbf{D}_e \frac{\partial f}{\partial \tilde{\boldsymbol{\sigma}}'} \tag{3.3.37}$$

$$H_p = -\frac{\partial f}{\partial \zeta} \left(\vartheta \frac{\partial f}{\partial \sigma_{\xi}'} - (1 + e_0) \frac{\partial f}{\partial \sigma_{\eta}'} \right) \tag{3.3.38}$$

Finally, we substitute equations (3.3.35) and (3.3.36) into equation (3.3.28) to obtain the tangent elastoplastic constitutive operator as,

$$\mathbf{D}_{ep} = \mathbf{D}_e - \frac{1}{H} \mathbf{D}_e \frac{\partial f}{\partial \tilde{\boldsymbol{\sigma}}'} \left(\frac{\partial f}{\partial \tilde{\boldsymbol{\sigma}}'} \right)^T \mathbf{D}_e \tag{3.3.39}$$

We may now identify the internal force vector $\mathbf{F}_{I(i)}$ and tangent stiffness matrix $\mathbf{K}_{uu(i)}$ of an interface element as,

$$\mathbf{F}_{I(i)} = \int_{V_{ie}} \left(\mathbf{B}^T \tilde{\boldsymbol{\sigma}}' \right) dV \tag{3.3.40}$$

$$\mathbf{K}_{uu(i)} = \int_{V_{ie}} \left(\mathbf{B}^T \mathbf{D}_{ep} \mathbf{B} \right) dV \tag{3.3.41}$$

This form is useful for the eigenanalysis to visualize the deformation modes and how they change over the course of the simulation owing to changes in the distribution of stress and strain within the domain, as explained in Section 3.3.2.5.

We conclude this section by examining the stress correction procedure for the interface elements. For finite increments to nodal displacements $\Delta \mathbf{a}_u$, we update the stress state to ensure that we always satisfy $f(\tilde{\boldsymbol{\sigma}}', \zeta) \leq 0$. First, we compute the total strain increment $\Delta \tilde{\boldsymbol{\varepsilon}} = \mathbf{B} \Delta \mathbf{a}_u$ and compute a trial stress state $\tilde{\boldsymbol{\sigma}}'^*$ assuming an elastic step,

$$\tilde{\boldsymbol{\sigma}}'^* = \tilde{\boldsymbol{\sigma}}' + \mathbf{D}_e \Delta \tilde{\boldsymbol{\varepsilon}} \tag{3.3.42}$$

$$\zeta^* = \zeta \tag{3.3.43}$$

If we have $f^*(\tilde{\boldsymbol{\sigma}}'^*, \zeta^*) \leq 0$, then the step was indeed elastic and we do not perform stress correction. Otherwise, we employ a stable return mapping algorithm based on a first order Taylor series expansion of the yield function about the trial stress state [228],

$$f = f^* + \left(\frac{\partial f}{\partial \tilde{\boldsymbol{\sigma}}'^*} \right)^T \Delta \tilde{\boldsymbol{\sigma}}'^* + \frac{\partial f}{\partial \zeta^*} \Delta \zeta^* = 0 \tag{3.3.44}$$

where we note that the derivatives are with respect to the uncorrected stress and hardening parameter states. Assuming a linear stress correction $\tilde{\boldsymbol{\sigma}}'^* = \tilde{\boldsymbol{\sigma}}'^* + \Delta\tilde{\boldsymbol{\sigma}}'^*$, we compute $\Delta\boldsymbol{\sigma}'^*$ as,

$$\Delta \boldsymbol{\sigma}'^* = -\mathbf{D}_e \frac{\partial f}{\partial \tilde{\boldsymbol{\sigma}}'^*} \Delta\mu \tag{3.3.45}$$

where we now determine the plastic multiplier $\Delta\mu$ by combining equations (3.3.33) (3.3.44) and (3.3.45) to obtain,

$$\Delta\mu = f^* \Big/ H \tag{3.3.46}$$

where H is as we defined it previously, except that we evaluate the derivatives in equations (3.3.37) and (3.3.38) with respect to the trial stress state. We perform the stress correction procedure iteratively until we have $f^*/\|\tilde{\boldsymbol{\sigma}}'^*\|^2 < \varepsilon_s$ where ε_s is a stopping criterion for the relative error.

We note that in the hardening plasticity model described above, the use of an elliptical loading surface implies that in some cases, the corrected stress state $\tilde{\boldsymbol{\sigma}}'^*$ may lie outside of the Coulomb failure envelope. Since we assume such states of stress to be inadmissible, we also perform stress correction to ensure that we satisfy the yield criterion. We do this using an elastic-perfectly plastic flow plasticity formulation wherein the failure function $F(\tilde{\boldsymbol{\sigma}}')$ is,

$$F\left(\tilde{\boldsymbol{\sigma}}'\right) = \sigma_{\xi}' - \sigma_{\eta}' \tan\left(\varphi_f\right) \leq 0 \tag{3.3.47}$$

Using a similar stable return mapping approach as above, beginning from a trial stress state $\tilde{\boldsymbol{\sigma}}'^{*}$, if equation (3.3.47) is not satisfied, we write the first order Taylor series of F about $\tilde{\boldsymbol{\sigma}}'^{*}$ as,

$$F = F^{*} + \left(\frac{\partial F}{\partial \tilde{\boldsymbol{\sigma}}'^{*}}\right)^{T} \Delta\tilde{\boldsymbol{\sigma}}'^{*} = 0 \tag{3.3.48}$$

The stress correction $\Delta\tilde{\boldsymbol{\sigma}}'^{*}$ is written as in equation (3.3.45), but now the plastic multiplier is,

$$\Delta\mu = F^{*} \Big/ H_e \tag{3.3.49}$$

where H_e is as in equation (3.3.37), replacing the loading function f with the failure function F in the partial derivatives. As with the hardening plasticity formulation, we perform the stress correction procedure iteratively until we have $F^{*}/\|\tilde{\boldsymbol{\sigma}}'^{*}\| < \varepsilon_s$.

The following section puts the components of the formulation outlined in the previous and current sections into context, detailing the algorithm used to step the solution forward through time.

3.3.2.4 Time Stepping Procedure

We base our time stepping procedure on the implicit Crank-Nicolson scheme [cf. 235], which facilitates iterative solution for the displacements and internal forces for a given time step. We write the system of ordinary differential equations in time given by equation (3.3.3) for a time step $[t, t+\Delta t]$ as,

$$\mathbf{M}\left(\frac{\dot{\mathbf{a}}_u^{(t+\Delta t,\,j+1)}-\dot{\mathbf{a}}_u^{(t)}}{\Delta t}\right)=\frac{1}{2}\left(\mathbf{F}_E^{(t)}-\mathbf{F}_I^{(t)}\right)+\frac{1}{2}\left(\mathbf{F}_E^{(t+\Delta t)}-\mathbf{F}_I^{(t+\Delta t,\,j+1)}\right)$$
$$\frac{\mathbf{a}_u^{(t+\Delta t,\,j+1)}-\mathbf{a}_u^{(t)}}{\Delta t}=\frac{1}{2}\left(\dot{\mathbf{a}}_u^{(t)}+\dot{\mathbf{a}}_u^{(t+\Delta t,\,j+1)}\right) \tag{3.3.50}$$

where j is an iteration counter for the nonlinear stress correction. We assume the following linearizations,

$$\begin{aligned}\mathbf{a}_u^{(t+\Delta t,\,j+1)}&\approx\mathbf{a}_u^{(t+\Delta t,\,j)}+\Delta\mathbf{a}_u^{(j)}\\ \mathbf{F}_I^{(t+\Delta t,\,j+1)}&\approx\mathbf{F}_I^{(t+\Delta t,\,j)}+\mathbf{K}_{uu(0)}\Delta\mathbf{a}_u^{(j)}\end{aligned} \tag{3.3.51}$$

where $\mathbf{K}_{uu(0)}$ is the global stiffness matrix accounting for grain and interface stiffness, and the subscript $\{\cdot\}_{(0)}$ indicates that we use the initial (elastic) stiffness of the interfaces for efficiency. Rearranging equations (3.3.50) yields the following system of linear equations,

$$\hat{\mathbf{K}}\Delta\mathbf{a}_u^{(j)}=\boldsymbol{\Psi}_\sigma^{(j)} \tag{3.3.52}$$

where,

$$\hat{\mathbf{K}}=\frac{2}{\Delta t^2}\mathbf{M}+\frac{1}{2}\mathbf{K}_{uu(0)} \tag{3.3.53}$$

$$\begin{aligned}\boldsymbol{\Psi}_\sigma^{(j)}=\frac{1}{2}\left(\mathbf{F}_E^{(t)}-\mathbf{F}_I^{(t)}\right)+\frac{1}{2}\left(\mathbf{F}_E^{(t+\Delta t)}-\mathbf{F}_I^{(t+\Delta t,\,j)}\right)-\cdots\\ \cdots-\frac{2}{\Delta t^2}\mathbf{M}\left(\mathbf{a}_u^{(t+\Delta t,\,j)}-\mathbf{a}_u^{(t)}\right)+\frac{2}{\Delta t}\mathbf{M}\dot{\mathbf{a}}_u^{(t)}\end{aligned} \tag{3.3.54}$$

which we employ iteratively combined with the stress correction procedure outlined in Section 3.3.2.3 until $||\Delta\mathbf{a}_u^{(j)}||/||\mathbf{a}_u^{(t+\Delta t,j+1)}|| < \varepsilon_s$ where again ε_s is a stopping criterion for the approximate relative error. Once we obtain a converged estimate of $\mathbf{a}_u^{(t+\Delta t)}$, we may compute the velocity $\dot{\mathbf{a}}_u$ at time $t+\Delta t$ as,

$$\dot{\mathbf{a}}_u^{(t+\Delta t)}=\frac{2}{\Delta t}\left(\mathbf{a}_u^{(t+\Delta t)}-\mathbf{a}_u^{(t)}\right)-\dot{\mathbf{a}}_u^{(t)} \tag{3.3.55}$$

Wood [235] provides a comprehensive discussion of the details regarding the stability and error when using the Crank-Nicolson time stepping scheme.

3.3.2.5 Eigenanalysis of the Grain Structure

The VCFEM-DEM formulation models discrete granular materials, which are discontinuous in nature, using two types of element: polygonal elements representing grains and interface elements representing interactions between grains. Both types of element use a continuum mechanics formulation, and as such, the analysis involves construction of a global mass matrix **M** and a global stiffness matrix $\mathbf{K}_{uu}$. Although the overall response of the system involves nonlinear constitutive behaviour, for very small displacements we can assume linear elastic behaviour in the "tangent" sense. Thus, we may rewrite the homogeneous part of equation (3.3.3) as,

$$\mathbf{M}\ddot{\mathbf{a}}_u^{(t)} + \mathbf{K}_{uu}^{(t)}\mathbf{a}_u^{(t)} = \mathbf{0} \tag{3.3.56}$$

where $\mathbf{K}_{uu}^{(t)}$ represents the global tangent stiffness matrix at time *t*. Recall that $\mathbf{K}_{uu}$ includes components from the grain stiffness, which is linear elastic and constant with time, and the interface element stiffness, which changes over time owing to the nonlinear constitutive behaviour. Following standard approaches from structural dynamics [cf. 239,240], we assume a decomposition of the displacement $\mathbf{a}_u^{(t)}$ into a series of modes,

$$\mathbf{a}_u^{(t)} = \mathbf{\Phi}_u \boldsymbol{\alpha}_u^{(t)} \tag{3.3.57}$$

where $\mathbf{\Phi}_u$ is an orthogonal matrix whose columns represent the mode shapes and $\boldsymbol{\alpha}_u^{(t)}$ is a vector of coefficients representing the magnitude of each mode at time *t*. We emphasize that the nonlinear nature of the granular deformation means that

such an assumption only applies in the brief time window [t-δt, t+δt] where δt is an infinitesimal increment of time, since it relies on the assumption of superposition of the deformation modes. Assuming harmonic form for $\boldsymbol{\alpha}_u^{(t)}$ and substituting equation (3.3.57) into equation (3.3.56) leads to the standard eigenvalue problem,

$$\left(\mathbf{K}_{uu} - \omega_{(k)}^2 \mathbf{M}\right)\boldsymbol{\varphi}_{u(k)} = \mathbf{0} \tag{3.3.58}$$

where $\omega_{(k)}$ is the real-valued angular natural frequency of mode k at time t and $\boldsymbol{\varphi}_{u(k)}$ is the k^{th} column of matrix $\boldsymbol{\Phi}_u$.

3.3.3 Biaxial Compression Simulations

3.3.3.1 Simulation setup and parameters

We implemented the dynamic VCFEM-DEM formulation described in the previous section as a code *vcfem_dyn* using the software package Matlab [219]. To examine the capability of this framework, we ran a series of simulations of biaxial compression tests. This type of simulation is a common test of analysis frameworks for modelling strain localization in granular materials in the literature [45,72,74,75,77,79,81,86,88,89,91,93,97,100,101,164,166,172]. Our aim here is not to complete a detailed sensitivity analysis regarding the parameters of the model. We simply present representative results demonstrating its ability to capture multi-scale phenomena in granular materials.

Figure 3.15 shows a sample mesh used in a biaxial compression simulation. The domain consists of a 0.05 m × 0.15 m region representing the granular material and a 0.05 m × 0.025 m region representing a loading cap. Although

numerical simulations do not typically model laboratory apparatus such as the loading cap explicitly, we found that including it reduced the influence of stress concentrations owing to the boundary conditions during strain-controlled loading, while not significantly increasing the simulation time. The sample mesh in Figure 3.15 represents a coarse sand with a uniform particle size *d* of approximately 3.5 mm. The mesh represents the grains as irregular convex polygons, which are mostly (>83%) hexagonal in shape. The granular part of the domain for this mesh

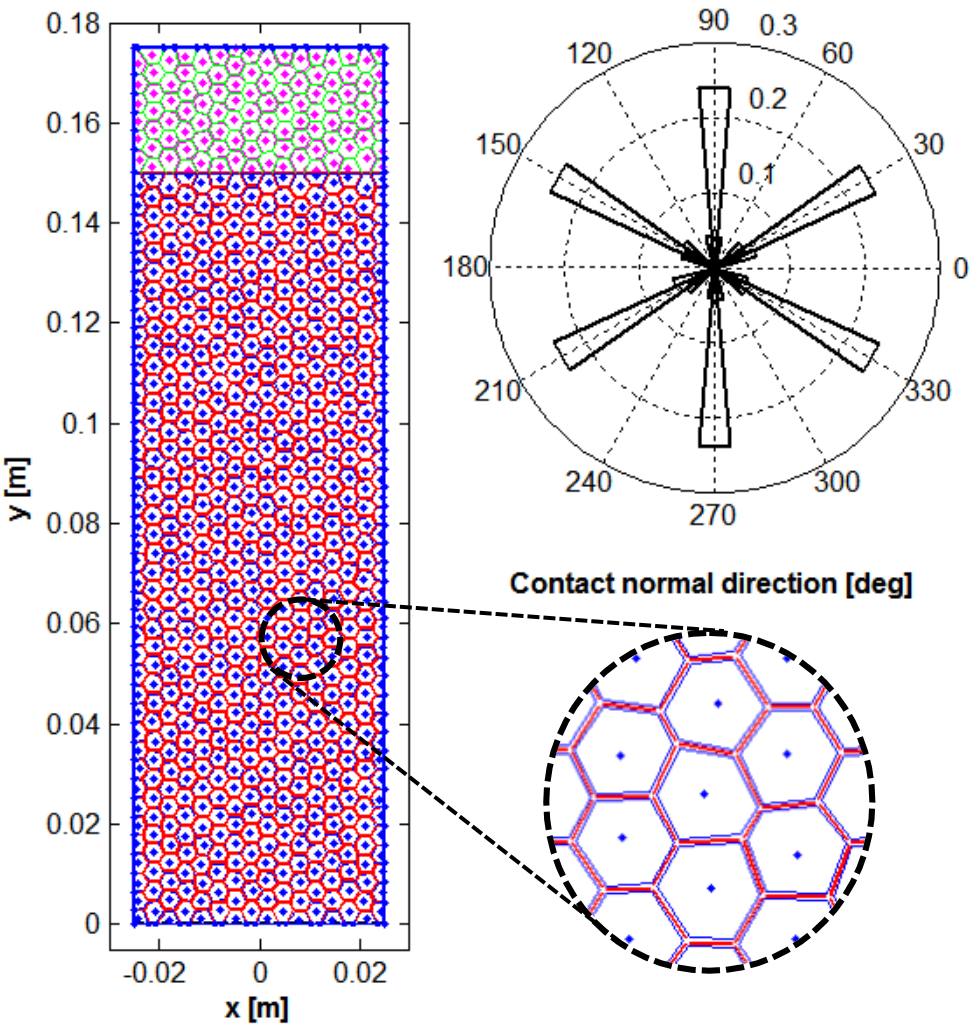

Figure 3.15 Sample VCFEM-DEM mesh for biaxial compression simulations (left), distribution of contact normals (top right) and magnified view of grain and interface elements (bottom right)

has 640 grain elements and 1825 interface elements. Figure 3.15 also shows the distribution of contact normal directions for the sample mesh, which are mostly in the $(n+0.5)\times 60°$ directions for $n \in \{ 0, 1, \ldots, 5 \}$. This mesh is characteristic of those employed in the present study.

Table 3.1 and Table 3.2 show the material properties employed in the present study. For the granular material, we selected grain element properties representative of feldspar [cf. 241] and interface properties such that the elastic shear modulus isthe same as that of the grains, but the normal (constrained) modulus is much higher for the range of confining pressures applied in the simulations. The thickness δ_e of the granular interface elements was set such that the average porosity in the granular domain was approximately 0.25, which is a dense condition for a sand. The parameter e_0 for the interface elements is a model

Table 3.1 Material properties for grain elements

Material	*Symbol*	*Value*	*Units*
Granular	E	40.0	GPa
	ν	0.330	-
	ρ	2.65×10^{3}	kg/m^3
Cap	E	70.0	GPa
	ν	0.330	-
	ρ	2.70×10^{3}	kg/m^3

Table 3.2 Material properties for interface elements

Material	*Symbol*	*Value*	*Units*
Granular	G	15.0	GPa
	λ	1.50×10^{-5}	-
	κ	5.00×10^{-7}	-
	φ_f	30.0	deg
	φ_c	25.0	deg
	e_0	0.900	-
	δ_e	2.83×10^{-4}	m
Cap	G	30.0	GPa
	M	105	GPa
	δ_e	2.83×10^{-4}	m

parameter for the plasticity framework only, and does not correspond to the overall void ratio of the domain. For the cap material, we selected elastic properties representative of aluminum, a cap material commonly used in laboratory compression tests. For the cap "interfaces", we used a linear elastic material model with values of G and M corresponding exactly to the elastic coefficients in the "grains", so we actually model the cap as an intact region with homogeneous and isotropic material properties. Although we assign a value to δ_e in the cap, it has no influence on the simulation results. We let its value be the same as that for the granular interfaces for convenience in the mesh generation. The interface elements on the boundary between the granular and cap materials have the same properties as the granular interfaces.

We apply the biaxial compression simulation in two phases, corresponding to the phases of a drained laboratory compression test. The first phase is a consolidation phase during which we first apply an initial seating pressure of 2 kPa by setting the normal boundary tractions and the initial stresses in the grain elements – $\boldsymbol{\sigma}_0$ in the stress interpolation – and the interface elements all to this value. After stabilization at the seating load, we increase the confining pressure linearly to a maximum value of 200 kPa by increasing the normal tractions and hold this constant again until the specimen stabilizes. The second phase is the strain controlled shearing phase during which we hold the normal tractions on the vertical sides of the specimen constant and apply a vertical strain rate of 1.0 mm/s. The kinematic boundary conditions are $u_y = 0$ along $y = 0$, $u_x = 0$ at $\mathbf{x} = \{ 0, 0 \}^T$ and $u_x = 0$ at $\mathbf{x} = \{ 0, 0.175 \text{ m} \}^T$. The latter condition simulates the constraint against lateral movement of the loading cap that a loading rod would apply.

3.3.3.2 Results and Discussion

Figure 3.16 shows a plot of the mobilized shear in the specimen for three different grain elements during the strain-controlled portion of the simulation for the mesh shown in Figure 3.15. We define the mobilized shear as,

$$\sin(\varphi) = \frac{\frac{1}{2}(\sigma_1 - \sigma_3)}{\frac{1}{2}(\sigma_1 + \sigma_3)} \tag{3.3.59}$$

where σ_1 and σ_3 are the major and minor principal stresses in a grain element. Note that, although the constitutive behaviour within the grains is linear elastic, equilibrium with the surrounding interface elements governs the stress state in a grain. Analyzing the stress state within the grain elements provides a more convenient approach to determining the mobilized shear near a grain element. The stress-strain curves are characteristic of behaviour observed in laboratory compression tests on granular material. During the pre-peak regime, the curve

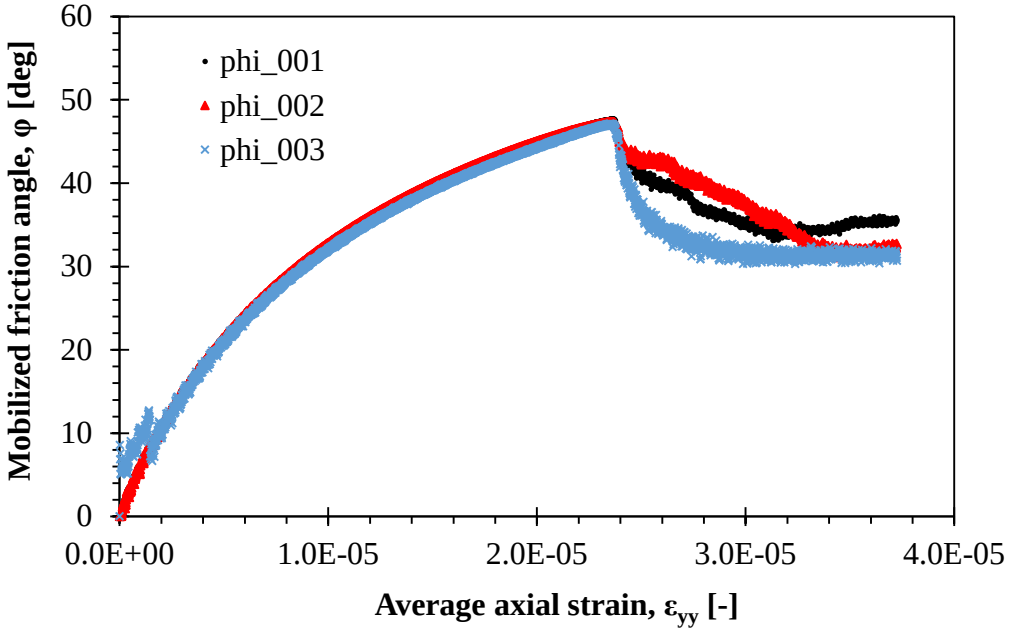

Figure 3.16 Representative stress-strain curves during strain controlled shearing. Different curve numbers correspond to evaluations in different grain elements within the granular domain.

is nonlinear owing to the strain hardening plasticity model used for the interface elements. The peak mobilized friction angle φ_f for this simulation was 47.5°, which is substantially higher than the interface friction angle of 30°, but is consistent with the fact that this simulation represents a very dense granular material with a porosity of 0.25. Following the peak, there is softening until the stress level becomes constant – that is, reaches critical state – at a mobilized friction angle of approximately 33.0°. Again, this is higher than the critical state friction angle of the interface elements, which was 25°, but we attribute this to the density of the specimen. We note that the stress-strain curves for grain elements in different parts of the domain coincide in the pre-peak regime, but diverge in the post-peak regime owing to the rich bifurcation space for the post-peak behaviour.

It is well known [164,166-169,172,173] that post-peak softening cannot be captured at the constitutive modelling level since it develops through macro scale inhomogeneities in stress and strain. Figure 3.17 demonstrates how this occurs in

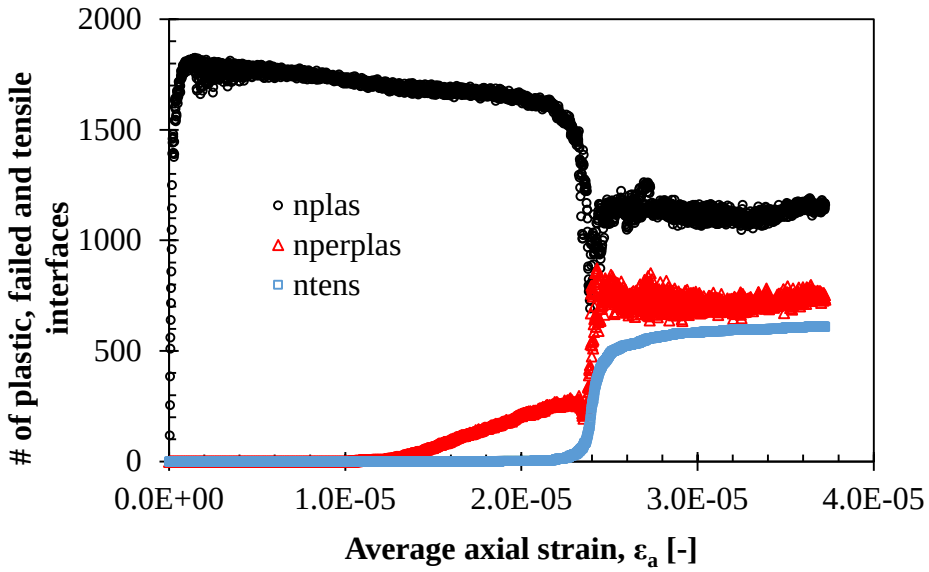

Figure 3.17 Number of plastic and failed interface elements during strain controlled shearing. nplas = # of plastic elements (active loading, but not failed), nperplas = # of elements failed in shear, ntens = # of elements failed in extension.

the VCFEM-DEM model by plotting the number of interface elements in an active loading, shear failure and extension failure state. Note that we count elements in an extension failure state also as being in a shear failure state, since the normal stress is zero. Comparing Figure 3.16 and Figure 3.17, we observe that there is a linear increase in interfaces at shear failure up to the peak, but few in extension failure. Failure occurs when enough failed interfaces exist to form a macroscopic shear failure mechanism – a shear band – leading to a rapid increase in interfaces failing in extension. The rapid increase in interfaces failed in extension corresponds to local dilations in the region near the shear band, which is consistent with observations of shear band failure and strain localization in granular materials. This observation is consistent with the evidence of Hadda et al. [242] for aggregation of so-called c^- contacts in the formation of shear bands in biaxial compression tests. This demonstrates that the VCFEM-DEM modelling framework is capable of capturing the fundamental phenomena that occur during shear failure of a granular material.

Having shown the behaviour during the shearing phase to be consistent with that of typical experimental observations and numerical simulations, we now examine the behaviour of the material during the consolidation phase. Figure 3.18 shows a plot of the global average shear strain in the specimen, computed using Green's Theorem as Section 3.1.2.3 described, during the consolidation phase. We first observe that the shear strain level is very small compared to the strain at failure. What is significant is that the average shear strain is non-zero during the consolidation phase, since one would expect alignment of the principal strain directions and the principal stress directions during isotropic consolidation for an

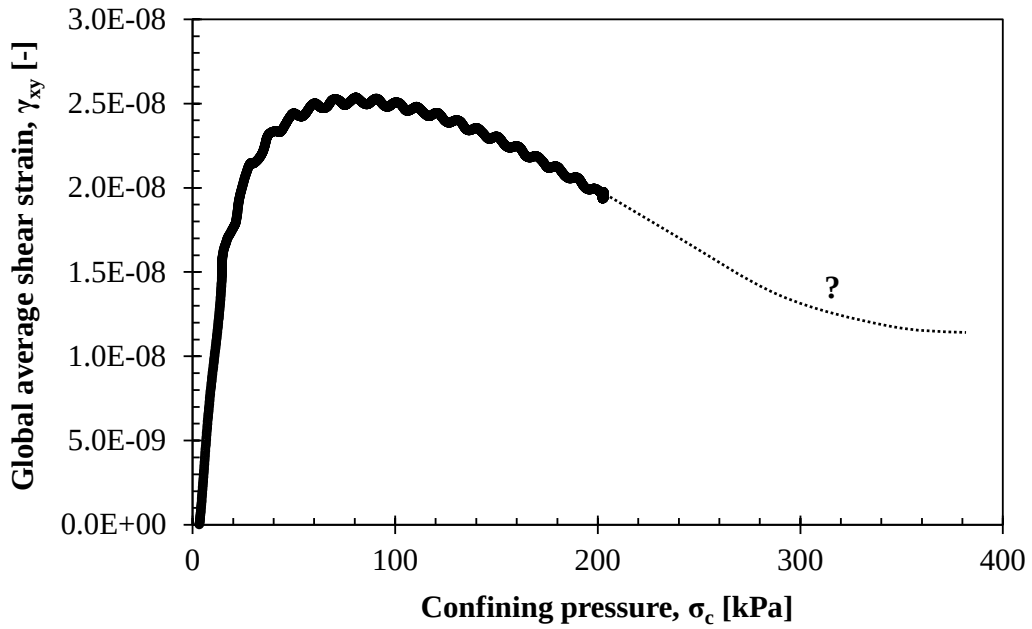

Figure 3.18 Plot of global average shear strain during consolidation phase

isotropic material. We attribute the development of global shear strain, implying rotation of the principal strain directions away from the principal stress directions, to the inherent anisotropy of the grain structure, which the VCFEM-DEM modelling approach captures through the mesh. We also observe that the global shear strain increases to a peak value, but subsequently begins to decrease as the confinement increases. In the present study, we only conducted simulations with maximum confinements of 200 kPa, and such a peak shear strain was not reached in all simulations. Further investigation of this phenomenon is required to understand the implications. However, we propose from these results that geomaterials tested at higher confining pressures may be expected to have more isotropic strength since the high confinement will begin to dominate over the anisotropy of the material fabric. For granular materials at lower levels of confinement, such as near the surface of the Earth where most engineered structures exist, the strength will be anisotropic.

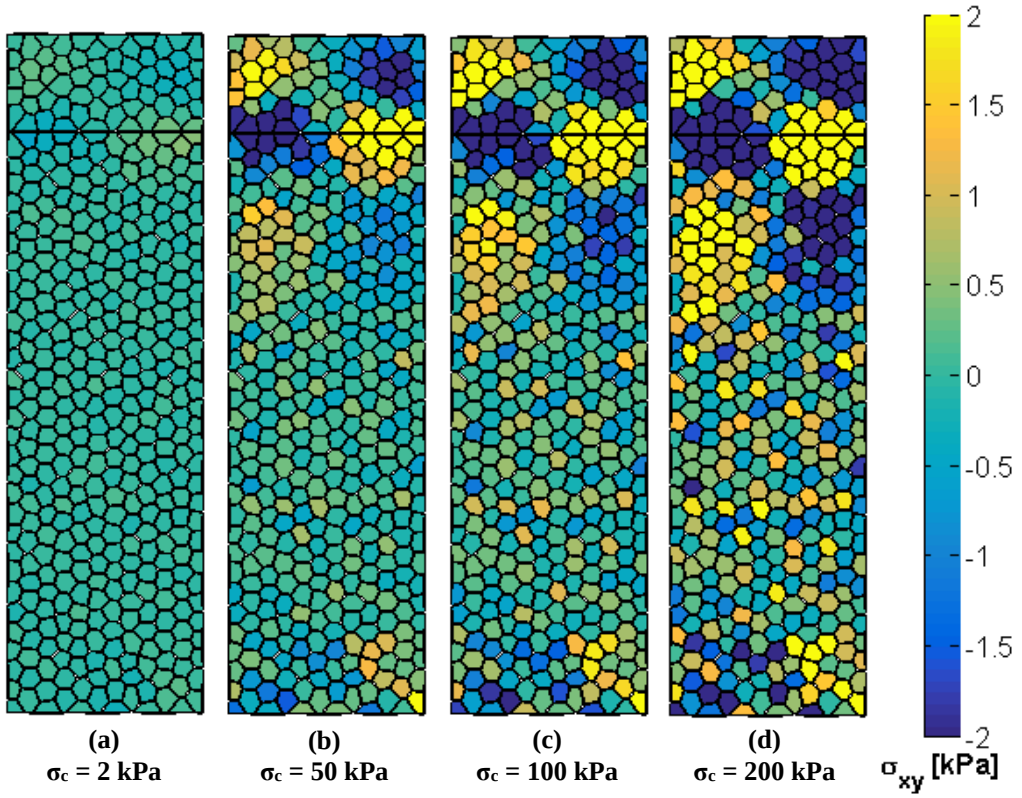

Figure 3.19 Development of inhomogeneous shear stress in specimen during consolidation

The next phenomenon of interest during the consolidation phase is the distribution of shear stress in the specimen. Figure 3.19 plots the average shear stress in the grain elements as the confining pressure increases. The range of shear stresses is ±2 kPa, which is 1% of the maximum confining pressure for this simulation. Though the magnitude of the shear stresses is small, again their pattern is interesting. First, we observe that the top and bottom thirds of the granular region has high shear stress levels stemming from the boundary conditions. In particular, at the interface between the cap and the granular domains where we account for friction using interface elements, a region of high shear stress develops because of the differing compressibility of the feldspar grains and the aluminum cap. The inhomogeneities of shear stress near the cap

and the base reinforce the importance of using specimens with aspect ratios greater than unity in laboratory material tests. Boundary influences aside, the middle third of the specimen still has inhomogeneities in shear stress that are somewhat chaotic, and one cannot attribute to the boundary influences. One can observe small local bands of high shear stress, which will ultimately coalesce into the global shear failure mechanism. Such inhomogeneities in the stress field may be as important to understanding the strength of granular materials as dislocations and imperfections are in understanding the real strength of metals.

We close by examining deformation modes obtained from tangent eigenanalysis of the granular structure. Figure 3.20 demonstrates the two types of deformation modes that we observed. The global modes result from the entire granular structure deforming in unison, and are reminiscent of the mode shapes commonly observed in analysis of multi-storey structures [cf. 240]. These modes result from the combined stiffness of the grain elements and the portion of the interface stiffness that is of the same magnitude. The local modes represent deformations owing to relative grain movement and rotation owing to the portion of the interface stiffness that is significantly different in magnitude compared with the grain element stiffness. The regions of high grain rotation subdivide the specimen into sub-regions, whose size represents a characteristic length scale for the material test, as shown in the two failure modes on the right side of Figure 3.20(b), which correspond to shearing failure. For the 5.0 cm × 15 cm specimen in the present set of simulations, the characteristic length approximately 6.0 to 7.5 cm – roughly one third to half of the specimen height. It is important to realize that the mode shapes and their corresponding eigenvalues change throughout the

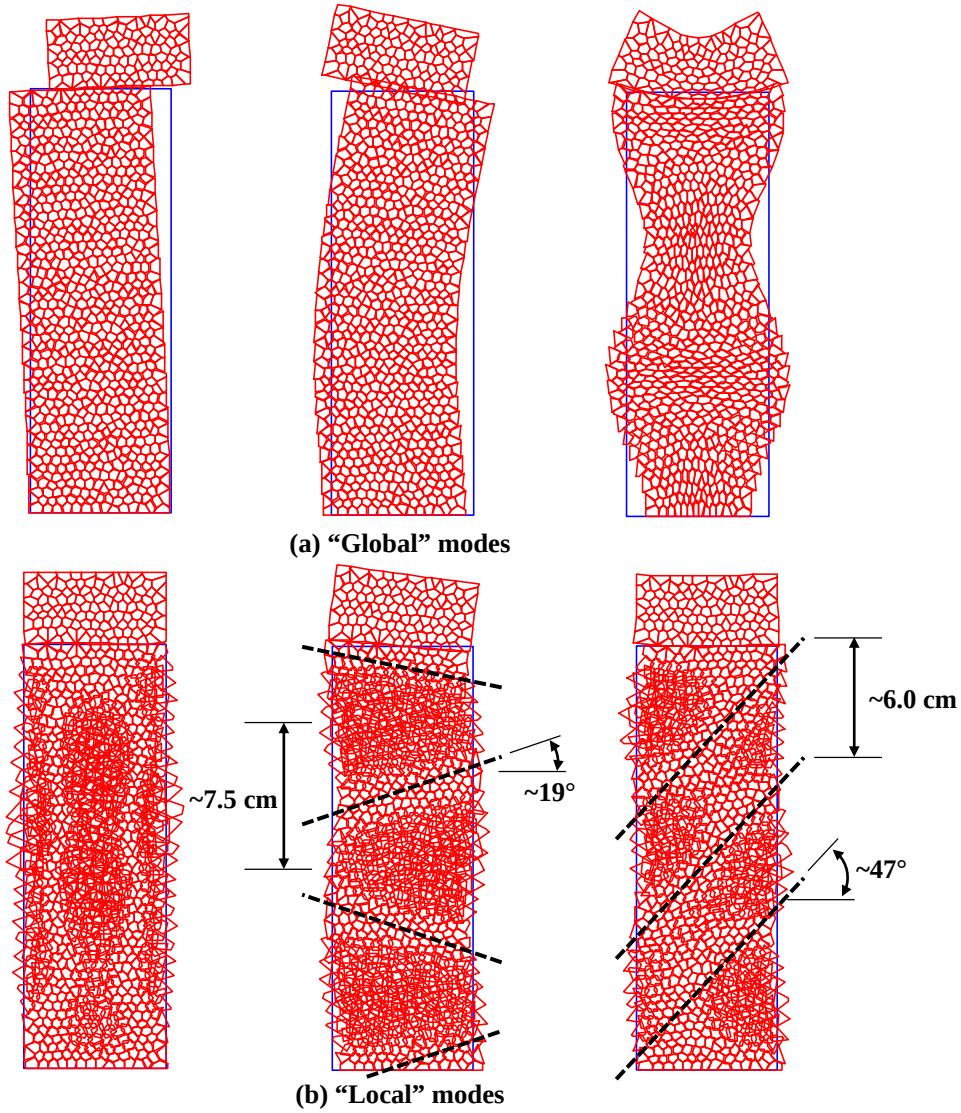

(a) "Global" modes

(b) "Local" modes

Figure 3.20 Tangent eigenmodes in biaxial compression specimen at σ_c = 200 kPa

test, owing to the stress dependency of the interface element stiffness. However, this set of deformation modes, obtained at the end of the consolidation phase under isotropic external loading, already shows deformation patterns similar to the failure modes observed in laboratory compression tests. This is consistent with observations in recent studies that there exists an entire bifurcation domain for the possible diffuse failure modes in a granular material [243-246]. The mode that governs the failure depends on how closely the boundary

conditions correspond with the deformation pattern of each mode. In particular, we note that the local mode on the left of Figure 3.20(b) corresponds to axial splitting commonly observed in unconfined compression of concrete cylinders whereas the local modes on the right correspond to the shear failure commonly observed in axial compression of granular materials with confinement.

3.3.4 Conclusions and Future Work

We formulated and implemented a dynamic VCFEM-DEM model for granular materials that uses hybrid polygonal elements with linear elastic behaviour to represent the grains and interface elements with combined volumetric deviatoric strain hardening to represent the interactions between grains. The results demonstrate its ability to capture the phenomenological characteristics observed throughout a strain-controlled axial compression test on granular material: nonlinear stress strain relation leading to a peak shear strength, followed by softening behaviour governed by the development of a macroscopic shear band mechanism. We also observed interesting phenomena during the isotropic consolidation phase, which would be difficult or impossible to observe during laboratory tests.

There is development of global shear strains under isotropic compression, which we attribute to the inherent anisotropy of the granular fabric. In some cases, the global shear strain increases to a peak and then decreases as the confinement continues to increase. This phenomenon requires further investigation to understand the range of magnitudes of such global shear strains that may occur for specimens of similar fabric orientation and irregularity. Future work should also

examine how such global shear strains vary with the peak confinement, and whether this really influences the peak strength of the granular specimen during the shearing phase.

Also during the confinement phase, we observed inhomogeneities in the shear stress distribution within the specimen. Though small in magnitude compared to the confining stress (~1%), the patterns were indicative of the early stages of shear band development. This may be important in understanding the strength of granular specimens, much as understanding dislocations and imperfections is important to understanding the strength of metals, but it requires further investigation.

Finally, through eigenanalysis of the granular structure, we observed local deformation patterns similar to typical failure modes in granular materials even at the end of the consolidation phase. This indicates the degree to which the granular structure may control the failure, since the “fingerprint” of the shear failure is present even under isotropic loading conditions. Again, the observations in the present study indicate the necessity for further investigation of how the deformation modes change throughout the simulation to understand how this influences the failure of the granular specimen.

The present work examined only specimens with uniform particle size and similar orientations of granular fabric. Future work should also include detailed investigation of the influence of average particle size, particle size distribution, average contact normal direction and contact normal distribution on the results. The VCFEM-DEM modelling framework is capable of investigating such variations, and as such provides an attractive tool for future investigations.

3.4 Conference Presentation #2: Prediction of subsurface load distribution due to soil self-weight using VCFEM-DEM analysis[5]

3.4.1 Introduction

In Sections 3.1-3.3, we were concerned primarily with modelling strain localization resulting from the influence of fabric in granular materials at the laboratory scale. We now apply the VCFEM-DEM methodology to examine the influence of fabric on the distribution of subsurface stresses at the field scale.

In the design and analysis of shallow foundations, engineers typically assume that stress distributes itself uniformly with depth. For a heterogeneous material – which all real granular materials are – the vertical component of subsurface stress σ_{yy} may vary nonlinearly as a function of depth owing to variations in the "fabric" of the material. One would only expect load to transfer uniformly for granular materials of regular shape and packing, as Figure 3.21 shows for regular hexagonal grains. However, many studies show that granular materials do not distribute stress uniformly as one might expect in a homogeneous solid, but rather transfer load through "force chains". A complete review of the literature on force chaining is outside of the scope of the present chapter. Jaeger et al. [18] provide an excellent summary of the peculiarities of the behaviour of granular materials, including the force chaining effect. Dantu [247], Wakabayashi [248] and Drescher and de Josselin de Jong [42] use photoelastic materials as a proxy for real granular materials to visualize the force chains and stress

[5] Karchewski B, Stolle D, Guo P. Prediction of subsurface load distribution due to soil self-weight using Monte Carlo and VCFEM-DEM analyses. Presented at the *Engineering Mechanics Institute Conference (EMI 2014), ASCE, Aug 5-8, Hamilton, ON*, 2014.

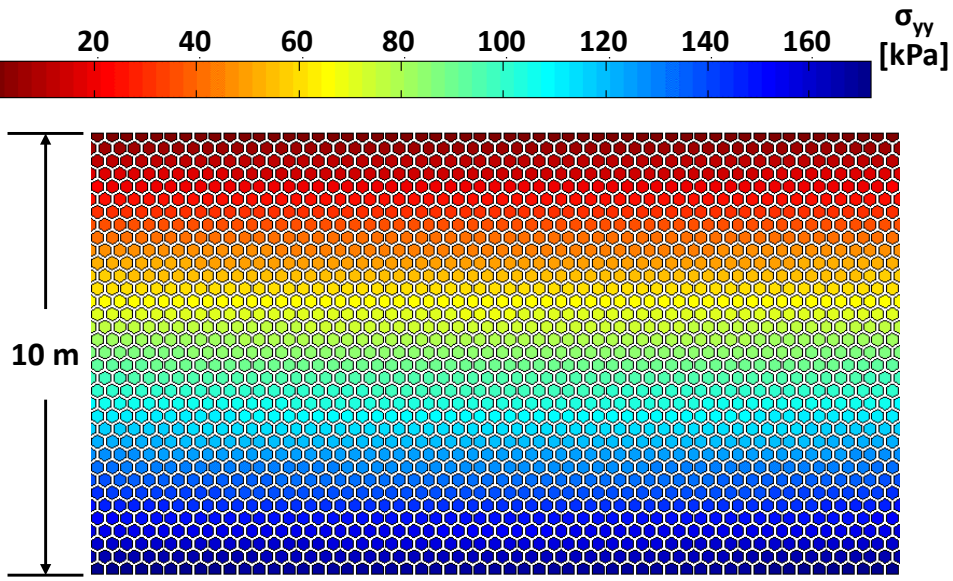

Figure 3.21 Idealized plot of vertical stress distribution with depth for a granular soil, γ = 17.1 kN/m^3

distribution. Travers et al. [249] and Ammi et al. [43] examine the influence of packing disorder (using cylindrical grains) and grain shape (comparing regular polygonal grains with cylindrical grains), respectively, on the packing structure and stress distribution. Kolb et al. [66] experimentally characterize stick-slip instabilities observed when driving various types of granular material at slow velocities with a piston in a two-dimensional cell. They observed that the distribution and characterization of stick-slip events depends strongly on the type of granular material used. Owing to these influences, the effect of the grain structure on the distribution of load in the subsurface is difficult to characterize because of the complex manner in which load distributes through the grains. Harr [250] examines the statistical distribution of subsurface stresses in a granular material owing to surface loads. Several recent theoretical studies point out that the geometric arrangement and compactivity of the granular assembly inherently influences the interparticle force and torque balance – an influence that a so-called

self-consistent continuum theory should incorporate [19-25,65]. One of the aims of the present study is to examine the degree to which irregularity in the grain structure may influence the expected value and standard deviation of vertical stress in the subsurface, and the characteristic length scale over which the grain structure has an influence.

The studies cited in the foregoing literature review were mostly interested in the development of force chains owing to point loads or applied tractions in uniaxial or biaxial compression. In the present study, we examine the influence of force chaining in granular materials on the subsurface distribution of stresses owing to the self-weight of the granular materials. We examine this phenomenon using the static VCFEM-DEM model that we presented the formulation for in Section 3.1.2. We describe only the extension to this model to account for body forces in Section 3.4.2 herein. The demonstrated results of the application of body forces within a hybrid FEM formulation also represent a contribution of academic interest to the hybrid FEM literature, which Chapter 4 expands on further.

3.4.2 Formulation

We present here the formulation of the Voronoi cell elements, focussing only the modifications needed to account for gravity forces. For the remainder of the formulation, we refer to Section 3.1.2.1. We do not present the formulation for the interface elements again here, but rather refer to the formulation presented in Section 3.1.2.2.

We base the formulation for the Voronoi cell elements on the hybrid functional of equation (3.1.1). Tong and Pian [150] propose that one can account

for the influence of body forces by including into the stress interpolation a term that satisfies the particular solution to the equilibrium equations owing to body forces. Thus, we write the stress interpolation as,

$$\boldsymbol{\sigma} = \mathbf{P}_\sigma \boldsymbol{\beta}_\sigma + \mathbf{P}_g \boldsymbol{\beta}_g \tag{3.4.1}$$

where the $\mathbf{P}_g\boldsymbol{\beta}_g$ term represents the particular solution for body forces owing to gravity. Although Tong and Pian propose this, they do not present a demonstrative example. They go on to prove that the solution will be unique if the columns in $\mathbf{P}_g$ are a subset of the columns in $\mathbf{P}_\sigma$. We note that since $\mathbf{P}_g\boldsymbol{\beta}_g$ represents a particular solution to the equilibrium equations corresponding to body forces, it is not important to resolve $\mathbf{P}_g$ and $\boldsymbol{\beta}_g$ separately, though we retain the symbolic form $\mathbf{P}_g\boldsymbol{\beta}_g$ for consistency throughout the formulation. We let,

$$\mathbf{P}_B\boldsymbol{\beta}_B = \begin{Bmatrix} 0 & \rho g y & 0 \end{Bmatrix}^T \tag{3.4.2}$$

where y is the vertical coordinate and ρg is the unit weight of the material where ρ is the density and g is the gravitational acceleration. This form corresponds to a gravitational vector oriented along the same line of action as the y coordinate axis, but in the negative direction. We refer to Section 4.1.2.3 for a more general form. This choice for $\mathbf{P}_g\boldsymbol{\beta}_g$ violates the requirement for uniqueness shown by Tong and Pian [150]. However, we note that choosing the columns of $\mathbf{P}_g$ as a subset of the columns of $\mathbf{P}_\sigma$ and satisfying the particular solution with the $\mathbf{P}_g\boldsymbol{\beta}_g$ term are incompatible goals since the columns of $\mathbf{P}_\sigma$ satisfy the homogeneous equilibrium equations, which prevents them from satisfying the particular solution. We discuss this further in Section 4.1.2.3 on the application of general body forces within the hybrid formulation. Nonetheless, the choice for $\mathbf{P}_g\boldsymbol{\beta}_g$ is apparently the

most sensible option for body forces owing to gravity since it uses only the σ_{yy} component of the stress tensor for gravitational force in the y direction. Interpolating displacements as in equation (3.1.5) and taking the first variation of the hybrid functional with respect to the unknown $\boldsymbol{\beta}_\sigma$ coefficients, we solve for $\boldsymbol{\beta}_\sigma$ in terms of the nodal displacements $\mathbf{a}_u$ as,

$$\boldsymbol{\beta}_\sigma = \mathbf{H}_{\sigma\sigma}^{-1}(\mathbf{G}_{\sigma u}\mathbf{a}_u - \mathbf{H}_{\sigma g}\boldsymbol{\beta}_g) \tag{3.4.3}$$

where $\mathbf{H}_{\sigma\sigma}$ and $\mathbf{G}_{\sigma u}$ are as defined in equations (3.1.7) and (3.1.8) and $\mathbf{H}_{\sigma g}$ is,

$$\mathbf{H}_{\sigma g} = \int_{V_e} \left(\mathbf{P}_\sigma^T \mathbf{D}_e^{-1} \mathbf{P}_g\right) dV \tag{3.4.4}$$

Substituting equation (3.4.3) back into the functional leads to its expression in terms of $\mathbf{a}_u$ only,

$$\Pi_{MCE}\left[\mathbf{a}_u\right] = \tfrac{1}{2}\mathbf{a}_u^T \mathbf{K}_{uu}\mathbf{a}_u - \mathbf{a}_u{}^T \mathbf{F}_g \tag{3.4.5}$$

where $\mathbf{K}_{uu}$ is the element stiffness matrix,

$$\mathbf{K}_{uu} = \mathbf{G}_{\sigma u}^T \mathbf{H}_{\sigma\sigma}^{-1} \mathbf{G}_{\sigma u} \tag{3.4.6}$$

and the element load vector owing to gravity forces is,

$$\mathbf{F}_g = \mathbf{G}_{\sigma u}^T \mathbf{H}_{\sigma\sigma}^{-1} \mathbf{H}_{\sigma g}\boldsymbol{\beta}_g - \mathbf{G}_{gu}^T \boldsymbol{\beta}_g \tag{3.4.7}$$

It is worth noting that the addition of the $\mathbf{P}_g\boldsymbol{\beta}_g$ term to the stress interpolation has no effect on the element stiffness matrix, as one would expect.

3.4.3 Results and Discussion

We now apply this formulation to investigate the distribution of subsurface stress in granular materials owing to self-weight. Figure 3.22 shows three sample meshes of the same average fabric orientation, but varying fabric irregularity

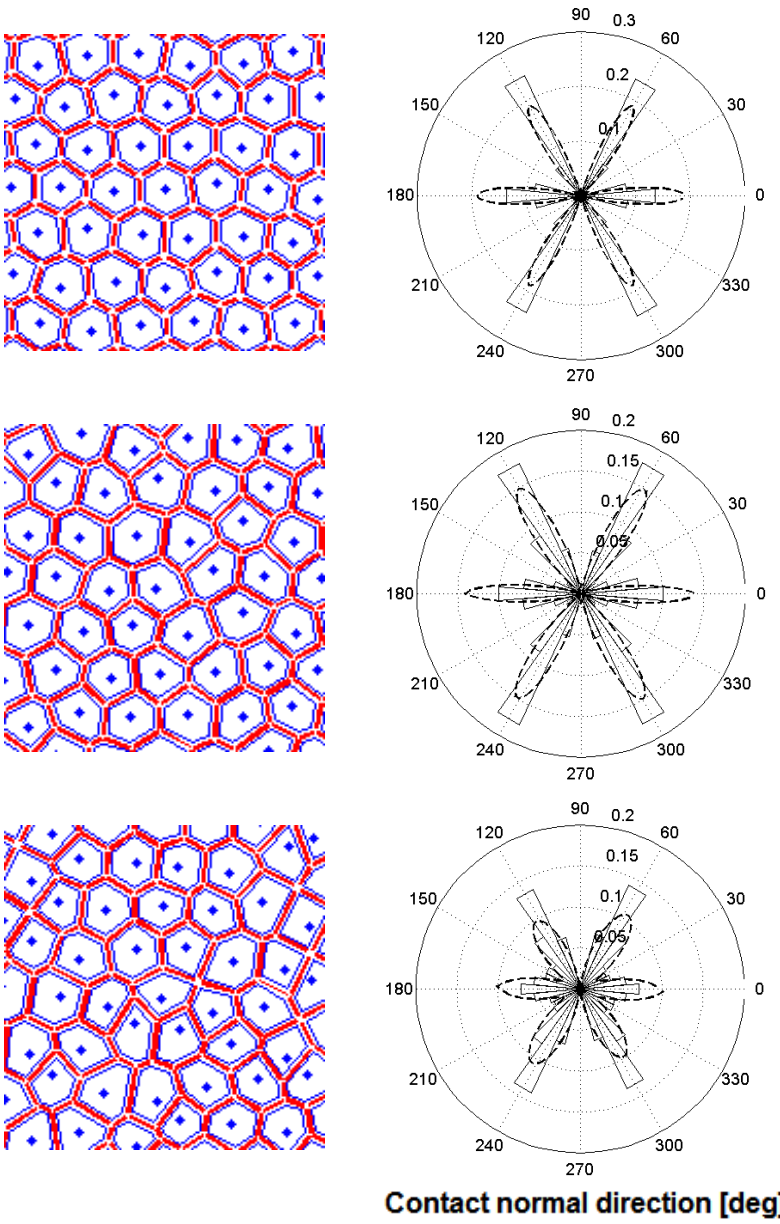

Figure 3.22 Sample VCFEM-DEM meshes with increasing degrees of irregularity (left) and corresponding rose diagrams showing the distribution of contact normal directions in each mesh (right).

characterized by the spread of the distribution of contact normals about the directions $n \times 60°$ for $n \in \{ 0, 1, \ldots, 5 \}$. We use the same elastic properties for the body elements and the same properties for the interface elements as for the simulations in Section 3.1.3. As with any model, these parameters require calibration with experimental or field evidence to model real materials, but our

aim here is only a conceptual demonstration of the capability of the VCFEM-DEM model to capture nonuniform subsurface stress distribution. We set the unit weight of the body elements as $\gamma = \rho g = 17.1$ kN/m^3.

Figure 3.23 shows the average vertical stress component σ_{yy} in each body element for meshes corresponding to the degrees of irregularity shown above. It is clear that increasing irregularity leads to a decrease in uniformity of the subsurface stress distribution. Scrutiny of the regions where stresses are substantially higher or lower than the surrounding material reveals that the stress "fingers" tend to occur in sets of grains with aligned contact planes, causing them to displace in unison. Figure 3.24, Figure 3.25 and Figure 3.26 show plots of the average vertical stress in all grain elements for the low, medium and high irregularity meshes, respectively. Owing to the random nature of the irregular fabrics, we run three analyses for each degree of irregularity – low, medium, high – each having similar contact normal distributions to those shown in Figure 3.22. The slope of the average line, which we determined as the line with 50% of points above it, is consistent with the unit weight of the body elements of 17.1 kN/m^3 in all cases. In addition, we determined the lines corresponding to one standard deviation above and below the mean as the lines passing through the origin and having 32% and 84% of points lying above them, respectively. It is clear that the spread of the distribution of subsurface stress increases with depth in all cases, and that the spread between the γ_μ and $\gamma_{\pm\sigma}$ increases rapidly even for modest increases in the spread of the distribution of contact normal directions. Figure 3.27 shows the distribution of σ_{yy} at selected depths for the high irregularity mesh only, demonstrating that the distribution is normal. The mean stresses at depths of

5.0 m and 7.8 m are consistent with the expected values of 85.5 kPa and 133 kPa, respectively, but the spread about the mean is substantial.

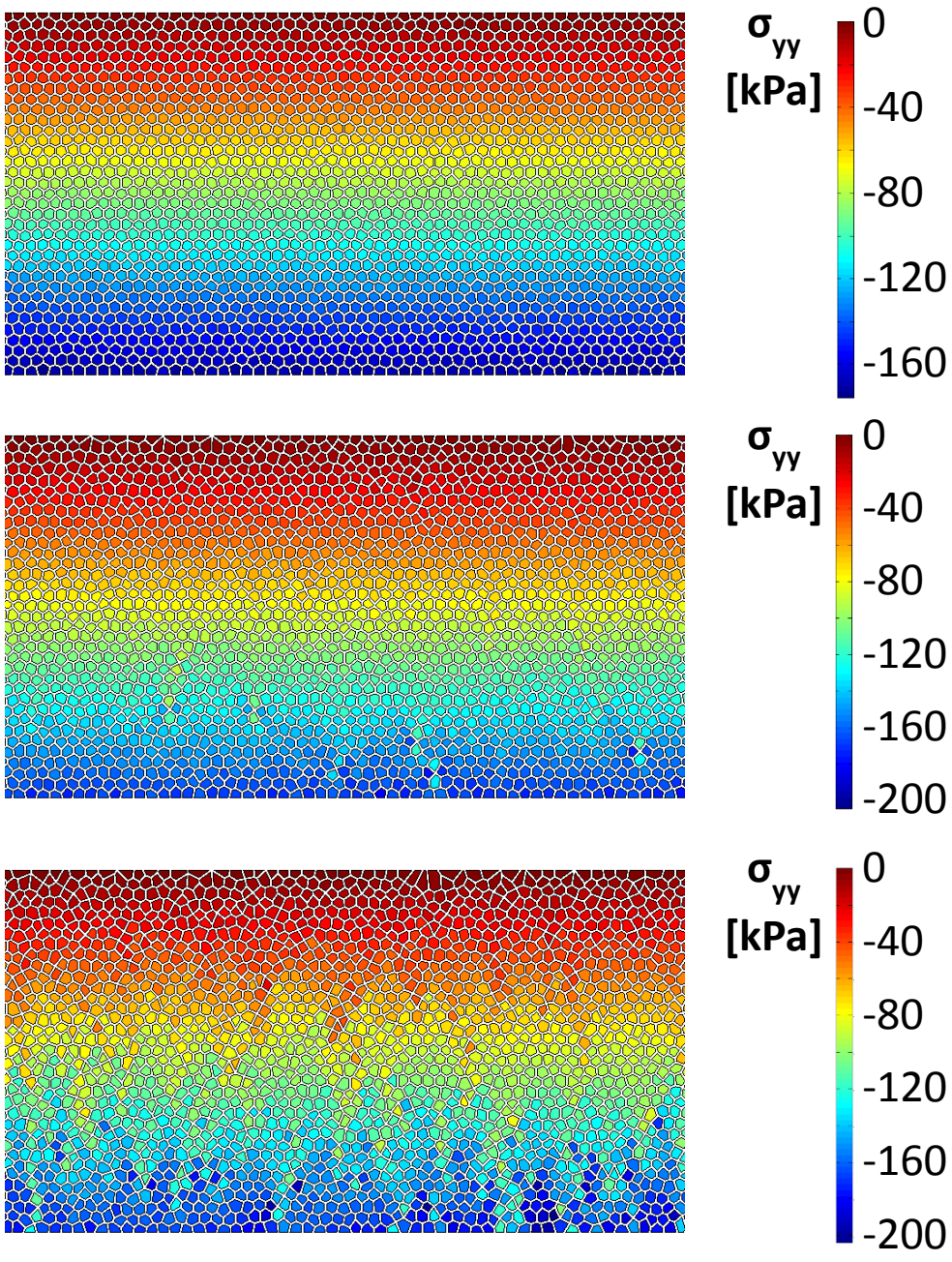

Figure 3.23 Sample plots of subsurface vertical stress generated by VCFEM-DEM analysis for low (top), medium (middle) and high (bottom) degrees of mesh irregularity. Increasing irregularity leads to greater force-chaining. Stress "fingers" correlate to collections of grains with aligned joints.

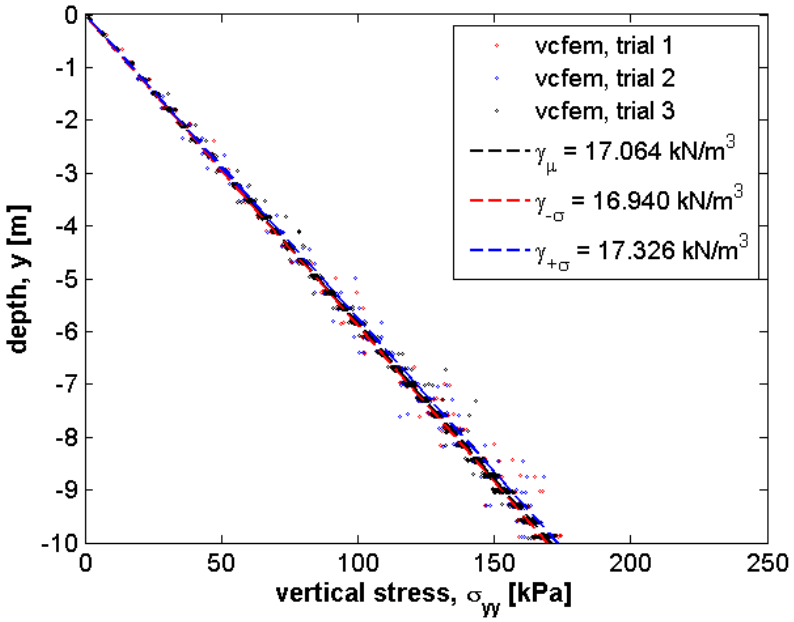

Figure 3.24 Subsurface stress distribution for low degree of mesh irregularity and (inset) typical distribution of joint element normals

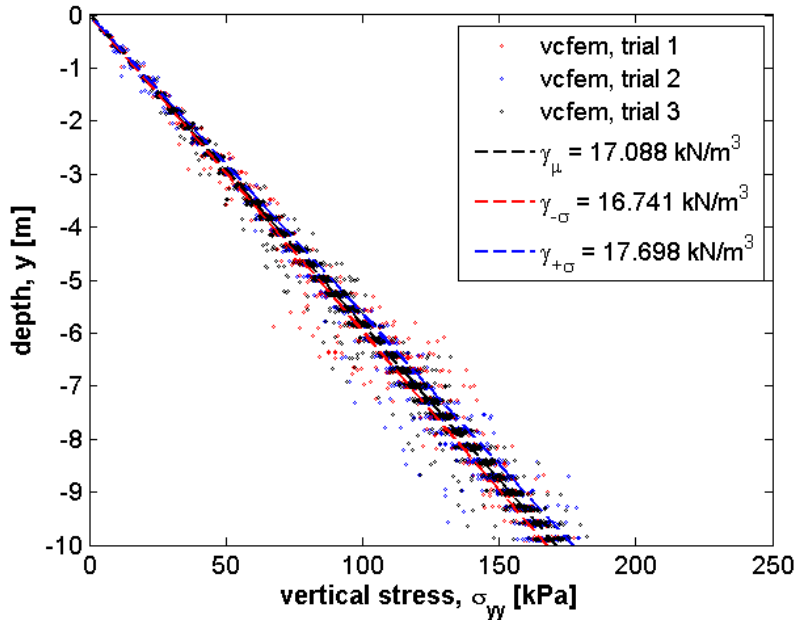

Figure 3.25 Subsurface stress distribution for medium degree of mesh irregularity and (inset) typical distribution of joint element normals

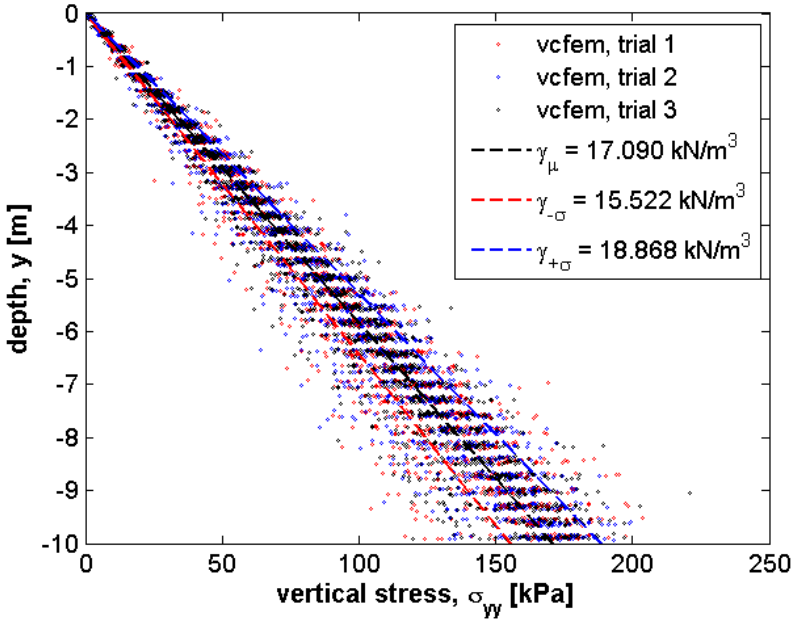

Figure 3.26 Subsurface stress distribution for high degree of mesh irregularity and (inset) typical distribution of joint element normals

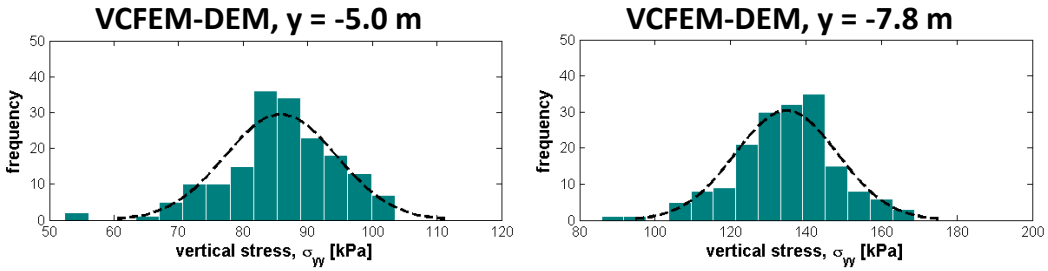

Figure 3.27 Plot of stress distribution at depths of 5.0 m (left) and 7.8 m (right) for 3 VCFEM-DEM trials with high irregularity, $\gamma \approx 17.1$ kN/m^3

3.4.4 Conclusions and Future Work

We conceptually demonstrated the capability of the VCFEM-DEM framework for granular materials to model the subsurface stress distribution at the field scale. The multi-scale nature of geological materials means that micro-scale interactions can influence the macro-scale behaviour. We showed that for materials with irregular grain structure, the variation from the expected value of vertical stress at a given depth could vary significantly. The length scale over

which such variations are important is consistent with the length scale of strain localization in granular materials, which is approximately 3-10 grains. Obviously, this length scale is insignificant at the field scale for granular materials such as sands and gravels where the size of the grains is on the order of millimetres. However, for granular materials such as blocky rock or glacial till where there can be particles whose size is on the order of centimetres or decimetres, the variations in subsurface stress distribution are substantial enough to question whether the assumption that σ_{yy} increases linearly with depth is valid.

In analyzing the subsurface stress distribution using VCFEM-DEM, we also demonstrated the application of body forces in a hybrid FEM formulation. Chapter 4 extends this concept to analysis coupled with seepage.

4 Semi-Coupled Hydro-Mechanical Modelling using VCFEM

4.1 Journal Paper #3: Semi-coupled seepage and deformation analysis of earth dams using the hybrid Voronoi cell finite element method[6]

4.1.1 Introduction

Analysis of coupled hydromechanical behaviour of porous materials is important in many geotechnical engineering problems. For example, in the design of an earth dam with water seeping through it, one requires accurate estimates of the pressure p and specific discharge $\mathbf{q}$ of the pore fluid phase, as well as the stresses $\boldsymbol{\sigma}$, strains $\boldsymbol{\varepsilon}$ and displacements $\mathbf{u}$ of the solid phase. In particular, the pressure and seepage forces are important in the analysis as they significantly influence the "effective" stresses $\boldsymbol{\sigma}'$ in the solid phase, and the effective stress governs the deformation of the solid phase [1-3].

To put the formulation presented herein in context, we divide coupled hydromechanical analysis into three primary categories, as follows,

i. *Fully coupled dynamic analysis*. This type of analysis applies in the short-term where dynamic terms in the governing equations are important. This typically necessitates solution of the complete dynamic equations of motion or a modified version thereof based on simplifying assumptions [cf. 115,251-256]. Zienkiewicz et al. [257] discuss the conditions under which the various simplified versions apply – $\mathbf{u}$-p

[6] Karchewski B, Stolle D, Pekinasova A, Guo P. Semi-coupled seepage and deformation analysis of earth dams using the hybrid Voronoi cell finite element method. Submitted 07/2015 to *Finite Elements in Analysis and Design*.

formulation ignoring fluid acceleration terms (unsteady and convective) for problems involving low frequencies and **u-U** formulation ignoring only convective fluid acceleration for high frequency, very short-term analysis. Zienkiewicz and Shiomi [258] discuss several approaches to writing the **u**-*p* and **u-U** formulations along with the possibility and relative merit of using implicit or explicit time stepping schemes with each approach.

ii. *Quasi-static analysis*. This form – often called consolidation analysis [3,115,257] – ignores all acceleration terms, but retains the velocity of the solid component. Such analysis is appropriate when one desires to determine the time-dependent dissipation of excess pore pressure owing to an increase in applied stress on a porous solid. This process occurs slowly enough to ignore acceleration when the hydraulic conductivity of the medium is small [115,257].

iii. *Semi-coupled static analysis.* This form of analysis applies for long-term steady state conditions when fluid pressure p and specific discharge $\mathbf{q}$ influence the effective stress $\boldsymbol{\sigma}'$ in the solid phase, but motion of the solid has ceased thereby having no influence on the $\mathbf{q}$ or p fields [115]. One ignores all dynamic terms including acceleration of solid and fluid components as well as the velocity of the solid component, thereby partially uncoupling the equations governing the seepage and deformation analyses. We refer to such analysis as “semi-coupled” owing to the fact that the coupling is one-way only.

We focus in the present work is on the last of the three cases, implemented in a hybrid finite element formulation. We distinguish between primary formulation variables that one interpolates directly in the finite element solution, and secondary variables that one determines by differentiation or integration of the interpolated primary variables. Conventional finite element implementations of semi-coupled analysis select a single primary solution variable in each phase of the analysis – typically hydraulic head h for the seepage analysis and displacement $\mathbf{u}$ for the deformation analysis. This choice leads to a penalty in the accuracy of the flux variables $\mathbf{q}$ and $\boldsymbol{\sigma}'$ because these variables are secondary in the analysis. Their computation involves differentiation of the interpolated primary variables h and $\mathbf{u}$. Owing to the subtractive nature of the differentiation operation, amplification of error in the approximate values of the primary variable occurs for the flux variables [145]. The hybrid formulation avoids this by interpolating the flux variables in the domain of an element, satisfying the equilibrium equations a priori. Despite the added complexity of having four primary solution variables in the semi-coupled analysis instead of two, the final form of the equations governing the finite element analysis are no more complex than a conventional analysis in terms of the total number of degrees of freedom. In implementing a coupled hybrid finite element formulation, we also demonstrate the application of body forces owing to gravity, pore pressure and seepage forces. Although the developers of hybrid finite elements propose the implementation of body forces at an early stage [150], there is a notable lack of examples of this in the literature.

Mixed and hybrid finite element methods are an alternative approach to finite element analysis wherein one solves for more than one primary variable [cf. 126,133,134,146-148,208]. Pian [149] and Tong and Pian [150] introduce the concept of hybrid finite elements for stress analysis. Ghosh and co-workers later extend the concept for use with Voronoi cell (polygonal) elements (VCFEM), analysis of materials with local heterogeneities and elastic-plastic analysis [152-155]. Harder et al. [213] examine a family of hybrid finite elements for seepage analysis, although they restrict their implementation to triangular elements. Karchewski et al. [259] extend the hybrid VCFEM to steady seepage analysis including location of a free surface demonstrating the advantages of this approach over conventional finite elements in terms of flux field approximation and global mass balance error.

In the present work, we combine hybrid VCFEM analysis of steady seepage through and deformation of porous media taking into account the semi-coupled hydromechanical behaviour in long-term static analysis. The formulation takes hydraulic head h, specific discharge $\mathbf{q}$, solid displacement $\mathbf{u}$ and effective stress $\boldsymbol{\sigma}'$ as the four primary formulation variables. We achieve coupling of the two analyses by using the solution from the seepage analysis to develop the force vector component owing to the fluid pressure and seepage force fields in the deformation analysis. Section 4.1.2 outlines the governing equations for the semi-coupled analysis, presents the hybrid formulation for the finite element approximation including the details of interpolation of each of the primary variables and shows the hybrid VCFEM implementation. Section 4.1.3 demonstrates the performance of the semi-coupled hybrid VCFEM analysis by

analyzing a simple 1-D case with an analytical solution. To demonstrate practical application to engineering design, we apply the VCFEM analysis to the seepage and deformation of an earth dam, including location of the free surface. Section 4.1.4 summarizes the key contributions and suggests future developments for this formulation.

4.1.2 Formulation

We now briefly define the governing equations for both portions of the semi-coupled analysis. For the constitutive behaviour, we assume a modified form of Darcy's Law for the seepage analysis and linear elasticity for the deformation analysis for simplicity. One may also incorporate elastic-plastic behaviour into the deformation analysis by using approaches presented by Ghosh and co-workers [155,158], and future work with this formulation will include implementation in a hybrid finite element-discrete element approach to modelling geomaterials [cf. 233,234,260]. We assume deterministic material properties, again for simplicity, but there is nothing in the analysis that precludes the use of stochastic analysis where the material properties in an element are random variables generated according to a defined distribution [cf. 261]. Subsections 4.1.2.1 and 4.1.2.2 briefly present the governing equations for the seepage and deformation components of the analysis, respectively, along with their corresponding hybrid VCFEM implementation. Section 4.1.2.3 describes the details of the interpolation of the effective stress field to satisfy equilibrium, including the influence of body forces owing to gravity, pore pressure and seepage forces.

4.1.2.1 Steady seepage analysis

The first phase of the semi-coupled analysis is steady seepage analysis to determine the distribution of pore pressure and seepage flux. Karchewski et al. [259] (Section 2.1.2) present a hybrid VCFEM formulation for field problems in the context of seepage analysis, adapted from hybrid formulations in solid mechanics. The following gives a brief overview of the formulation for completeness of the present work, but for a detailed discussion please consult Section 2.1.2.

First examining the steady seepage portion of the analysis, without loss of generality consider the polygonal domain V with outer surface $S = S_h \cup S_q$, as Figure 4.1 shows. Ignoring any source terms, the Euler equations for steady state seepage analysis in V are,

$$\mathbf{L}_{qh}^{T}\mathbf{q} = 0 \tag{4.1.1}$$

$$\mathbf{i} = \mathbf{L}_{qh}h \tag{4.1.2}$$

$$\mathbf{q} = -\mathbf{K}\mathbf{i} \tag{4.1.3}$$

where $\mathbf{L}_{qh}$ is a linear differential operator, $\mathbf{i}$ is the hydraulic gradient, h is the total hydraulic head, $\mathbf{q}$ is the specific discharge, $\mathbf{K}$ is the hydraulic conductivity tensor and $\{\cdot\}^T$ represents the transpose operation. We use the compact vector notation for representation of symmetric second and fourth order tensor quantities [cf. 116] herein for convenience. We compute the pore pressure p using the familiar relation $p = (h - y)\rho_f g$ where y is the elevation head relative to an arbitrary datum and $\rho_f g$ is the unit weight of the pore fluid. For plane seepage analysis, we define the linear differential operator as $\mathbf{L}_{qh} = \partial/\partial\mathbf{x}$ where $\mathbf{x} = \{ x, y \}^T$ represents the

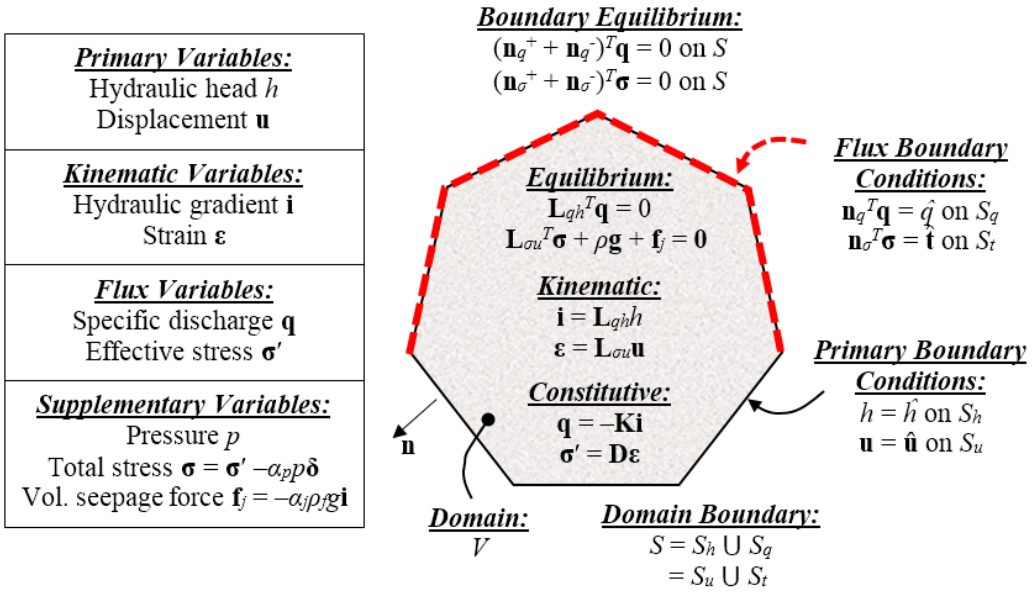

Figure 4.1 Schematic of domain and formulation for coupled VCFEM analysis

Cartesian coordinates of a point. Equations (4.1.1)-(4.1.3) apply both in the overall problem domain V and in any sub-domain V_e of a finite element. In addition to the mass balance in the domain of an element V_e, there is mass balance on internal boundaries S_i between adjacent polygonal elements given by,

$$\left(\mathbf{n}_q^+ + \mathbf{n}_q^-\right)^T \mathbf{q} = 0 \tag{4.1.4}$$

where $\mathbf{n}_q^+$ and $\mathbf{n}_q^-$ are the outward pointing unit normals from the current element and the adjacent element, respectively, on their adjoining interface. Classical boundary conditions for seepage analysis are,

$$h = \hat{h}(\mathbf{x}) \tag{4.1.5}$$

$$\mathbf{n}_q^T \mathbf{q} = \hat{q}(\mathbf{x}) \tag{4.1.6}$$

where $\hat{h}(\mathbf{x})$ is a prescribed hydraulic head on S_h and $\hat{q}(\mathbf{x})$ is a prescribed seepage flux on S_q. Within the context of plane seepage analysis, $\mathbf{n}_q = \{ n_x, n_y \}^T$ where n_x and n_y are the components of $\mathbf{n}_q$ in the x and y directions, respectively.

We base the VCFEM formulation for steady seepage analysis on the following hybrid functional,

$$\Pi_{qh}\left[\mathbf{q}, h^*\right] = \tfrac{1}{2}\int_{V_e}\left(\mathbf{q}^T\mathbf{K}^{-1}\mathbf{q}\right)dV + \int_{S_e} h^*\left(\mathbf{n}_q^T\mathbf{q}\right)dS - \int_{S_q}\left(h^*\hat{q}\right)dS \qquad (4.1.7)$$

which is akin to the modified complementary energy functional for solid mechanics analysis of Tong and Pian [150]. We note that this functional implies weakening of the hydraulic gradient link between equations (4.1.2) and (4.1.3), the interface mass balance of equation (4.1.4) and the natural boundary condition of equation (4.1.6). With regard to the interpolation of h we require that $h^* \subset h$ where h^* and h are the hydraulic head fields on S_e and in V_e, respectively, and continuity of h^* between elements. To accomplish this, we interpolate h^* linearly between adjacent nodal values on S_e as,

$$h^* = \mathbf{N}_h^*\mathbf{a}_h^* \qquad (4.1.8)$$

where $\mathbf{a}_h^* = \{\, a_{h1}, a_{h2} \,\}^T$ are values of hydraulic head at adjacent nodes on an edge, $\mathbf{N}_h^* = \{\, (1-\xi), \xi \,\}^T$ is a shape function matrix interpolating between nodal values along an edge and $\xi = \|\mathbf{x} - \mathbf{x}_1\|/\|\mathbf{x}_2 - \mathbf{x}_1\|$ is a local coordinate. To interpolate h in V_e, we use one of several options for conforming shape functions for polygonal elements [cf. 142],

$$h = \mathbf{N}_h\mathbf{a}_h \qquad (4.1.9)$$

where we note that part of the definition of a "conforming" shape function is that it reduces to the form of equation (4.1.8) on an edge.

The functional also requires satisfaction of equation (4.1.1) in the strong sense, so we interpolate **q** in the domain of an element according to,

$$\mathbf{q} = \mathbf{P}_q \boldsymbol{\beta}_q \tag{4.1.10}$$

where $\mathbf{P}_q$ is a matrix of monomials interpolating $\mathbf{q}$ in the domain of an element – defined such that $\mathbf{q} = \{ \partial\psi/\partial y, -\partial\psi/\partial x \}^T$ where $\psi(\mathbf{x})$ is a potential or "streamline" function thereby satisfying equation (4.1.1), a priori – and $\boldsymbol{\beta}_q$ is a vector of unknown coefficients of the function $\psi(\mathbf{x})$. To wit,

$$\mathbf{P}_q = \begin{bmatrix} 1 & 0 & y & x & 0 & y^2 & 2xy & x^2 & 0 \\ 0 & 1 & 0 & -y & -x & 0 & -y^2 & -2xy & -x^2 \end{bmatrix} \tag{4.1.11}$$

which is valid for elements with up to 10 nodes. We have never encountered an element with >10 nodes for meshes with approximately uniform element size.

Substituting the interpolations from equations (4.1.8) and (4.1.10) into the functional in equation (4.1.7) gives the discretized form of the functional,

$$\Pi_{qh}\left[\boldsymbol{\beta}_q, \mathbf{a}_h\right] = \tfrac{1}{2}\boldsymbol{\beta}_q \mathbf{H}_{qq} \boldsymbol{\beta}_q + \boldsymbol{\beta}_q^T \mathbf{G}_{qh} \mathbf{a}_h - \mathbf{a}_h^T \mathbf{f}_{\hat{q}} \tag{4.1.12}$$

where,

$$\mathbf{H}_{qq} = \int_{V_e} \left(\mathbf{P}_q^T \mathbf{K}^{-1} \mathbf{P}_q \right) dV \tag{4.1.13}$$

$$\mathbf{G}_{qh} = \int_{S_e} \left(\mathbf{n}_q^T \mathbf{P}_q \right)^T \mathbf{N}_h^* dS \tag{4.1.14}$$

$$\mathbf{f}_{\hat{q}} = \int_{S_q} \left(\mathbf{N}_h^{*T} \hat{q} \right) dS \tag{4.1.15}$$

Allowing the first variation of Π_{qh} with respect to the unknown flux coefficients $\boldsymbol{\beta}_q$ to vanish implies,

$$\delta\boldsymbol{\beta}_q^T \left(\mathbf{H}_{qq} \boldsymbol{\beta}_q + \mathbf{G}_{qh} \mathbf{a}_h \right) = 0 \tag{4.1.16}$$

We note that the flux interpolation need not be continuous between elements, since we satisfy mass balance on S_e in an integrated sense through the second term in Π_{qh}. Thus, for arbitrary $\delta\boldsymbol{\beta}_q$, we have,

$$\boldsymbol{\beta}_q = -\mathbf{H}_{qq}^{-1}\mathbf{G}_{qh}\mathbf{a}_h \tag{4.1.17}$$

which after substitution into equation (4.1.12) gives,

$$\Pi_{qh}\left[\mathbf{a}_h\right] = \tfrac{1}{2}\mathbf{a}_h^T\mathbf{K}_{hh}\mathbf{a}_h - \mathbf{a}_h^T\mathbf{Q}_q \tag{4.1.18}$$

where,

$$\mathbf{K}_{hh} = -\mathbf{G}_{qh}^T\mathbf{H}_{qq}^{-1}\mathbf{G}_{qh} \tag{4.1.19}$$

Finally, taking the first variation of Π_{qh} with respect to unknown $\mathbf{a}_h$ gives,

$$\mathbf{K}_{hh}\mathbf{a}_h = \mathbf{Q}_q \tag{4.1.20}$$

which defines the discretized equilibrium for the hybrid finite element.

It is important to realize that the hydraulic conductivity tensor $\mathbf{K} = \mathbf{K}(p)$ for unconfined seepage when $p < 0$. Karchewski et al. [259] (Section 2.1.2.5) present an iterative algorithm for solving equation (4.1.20) accounting for $\mathbf{K} = \mathbf{K}(p)$, based on a similar algorithm that Bathe and Khoshgoftaar [194] propose within the context of a conventional finite element analysis for free surface seepage, so we do not repeat it here. For simplicity, we assume a step function for the $\mathbf{K}(p)$ relation, but one could just as easily use a more complex relation accounting for the soil pore fluid characteristic curve in unsaturated soils.

We observe that although the intermediate manipulations in the hybrid formulation are somewhat more complex than a conventional formulation, the final element conductivity relations are of the same form and contain the same number of degrees of freedom. This implies that the number of global degrees of

freedom will be the same in a hybrid or conventional formulation (i.e. the global number of nodal $\mathbf{a}_h$ values). Once we solve for the global $\mathbf{a}_h$ values, we obtain the flux field in the domain of each element by combining equations (4.1.10) and (4.1.17), producing a smooth flux field that satisfies mass balance without the need for post-processing. With the results for $\mathbf{a}_h$ and $\boldsymbol{\beta}_q$, we may now proceed to the deformation analysis of the solid phase.

4.1.2.2 Deformation analysis

As with the seepage analysis, we begin by examining the governing equations for the deformation analysis. Consider the polygonal domain V with outer surface $S = S_u \cup S_t$, as Figure 4.1 shows. Assuming linear elastic behaviour for the solid phase for simplicity, the Euler equations for the deformation analysis in V are,

$$\mathbf{L}_{\sigma u}^{T}\boldsymbol{\sigma} + \mathbf{f}_b = \mathbf{0} \tag{4.1.21}$$

$$\boldsymbol{\varepsilon} = \mathbf{L}_{\sigma u}\mathbf{u} \tag{4.1.22}$$

$$\boldsymbol{\sigma}' = \mathbf{D}_e\boldsymbol{\varepsilon} \tag{4.1.23}$$

where $\mathbf{L}_{\sigma u}$ is a linear differential operator defined for plane analysis as,

$$\mathbf{L}_{\sigma u} = \begin{bmatrix} \partial/\partial x & 0 & \partial/\partial y \\ 0 & \partial/\partial y & \partial/\partial x \end{bmatrix}^T \tag{4.1.24}$$

$\boldsymbol{\sigma}'$ and $\boldsymbol{\sigma} = \{ \sigma_{xx}, \sigma_{yy}, \sigma_{xy} \}^T$ are the effective and total stresses (tension positive), respectively, $\boldsymbol{\varepsilon} = \{ \varepsilon_{xx}, \varepsilon_{yy}, \gamma_{xy} \}^T$ is strain (extension positive), $\mathbf{u} = \{ u_x, u_y \}^T$ is displacement, $\mathbf{f}_b$ is the volumetric body force vector and $\mathbf{D}_e$ represents the constitutive tensor for the solid skeleton, where for plane strain analysis,

$$\mathbf{D}_e^{-1} = \frac{1+\nu}{E}\begin{bmatrix} 1-\nu & -\nu & 0 \\ -\nu & 1-\nu & 0 \\ 0 & 0 & 2 \end{bmatrix} \tag{4.1.25}$$

where E and ν are the elastic Young's modulus and Poisson's ratio of the solid skeleton, respectively. The inverse of equation (4.1.23) implies that strains in the solid skeleton result only from changes in the effective stress since $\boldsymbol{\varepsilon} = \mathbf{D}_e^{-1}\boldsymbol{\sigma}'$. We account for the influence of the pore fluid on the deformation and stress in the solid phase in two ways: through the effective stress principle [1,2,115],

$$\boldsymbol{\sigma}' = \boldsymbol{\sigma} + \alpha_p p\boldsymbol{\delta} \tag{4.1.26}$$

where p is the pore pressure (compression positive) and $\boldsymbol{\delta} = \{\ 1,\ 1,\ 0\ \}^T$ represents the Kronecker delta, and through the body forces [117],

$$\mathbf{f}_b = \mathbf{f}_g + \mathbf{f}_j = \rho\mathbf{g} + \alpha_j \rho_f g \mathbf{K}^{-1}\mathbf{q} \tag{4.1.27}$$

where ρ is the bulk density of the fluid-solid mixture, $\mathbf{g}$ represents the gravitational acceleration field with $g = \|\mathbf{g}\|$ giving its magnitude, ρ_f is the density of the pore fluid and $\mathbf{i} = -\mathbf{K}^{-1}\mathbf{q}$ is the hydraulic gradient. The values of the α_p and α_j coefficients are typically unity for soils [3], and we follow this assumption herein, but we note that they may be less than unity for other geomaterials such as fractured rock.

Substituting equations (4.1.26) and (4.1.27) into equation (4.1.21) gives,

$$\mathbf{L}_{\sigma u}^T \boldsymbol{\sigma}' = \mathbf{L}_{\sigma u}^T \left(\alpha_p p\boldsymbol{\delta}\right) - \rho\mathbf{g} - \mathbf{f}_j \tag{4.1.28}$$

where we note that the effective stress definition acts as a constraint equation leading to an additional body force $-\mathbf{L}_{\sigma u}^T(\alpha_p p\boldsymbol{\delta})$. The form of equilibrium defined by equation (4.1.28) is more useful than equation (4.1.21) in developing the

hybrid finite element formulation for coupled seepage and deformation analysis since we now have a homogeneous set of equations for $\boldsymbol{\sigma}'$ and a set of particular forms for the body forces owing to pressure, gravity and seepage force. Similar to the interface mass balance of equation (4.1.4), we also define interface equilibrium on the boundary between polygonal elements as,

$$\left(\mathbf{n}_\sigma^+ + \mathbf{n}_\sigma^-\right)^T \boldsymbol{\sigma} = \left(\mathbf{n}_\sigma^+ + \mathbf{n}_\sigma^-\right)^T \left(\boldsymbol{\sigma}' - \alpha_p p \boldsymbol{\delta}\right) = \mathbf{0} \tag{4.1.29}$$

where $\mathbf{n}_\sigma^+$ and $\mathbf{n}_\sigma^-$ represent the outward pointing unit normals from the current element and the adjacent element, respectively, on their adjoining interface. Accounting for the vector notation for tensors, we represent the outward normal as,

$$\mathbf{n}_\sigma = \begin{bmatrix} n_x & 0 & n_y \\ 0 & n_y & n_x \end{bmatrix}^T \tag{4.1.30}$$

To close the formulation for the deformation analysis, the boundary conditions are,

$$\mathbf{u} = \hat{\mathbf{u}}(\mathbf{x}) \tag{4.1.31}$$

$$\mathbf{n}_\sigma^T \boldsymbol{\sigma} = \hat{\mathbf{t}}(\mathbf{x}) \tag{4.1.32}$$

where $\hat{\mathbf{u}}(\mathbf{x})$ gives the prescribed displacements on S_u and $\hat{\mathbf{t}}(\mathbf{x})$ gives the applied tractions on S_t.

Following Tong and Pian [150] and Ghosh and Mallett [153], we define the functional for the deformation analysis of hybrid polygonal finite elements according to a modified complementary energy principle as follows,

$$\Pi_{MCE}\left[\boldsymbol{\sigma}', \mathbf{u}^*\right] = -\tfrac{1}{2}\int_{V_e} \left(\boldsymbol{\sigma}'^T \mathbf{D}_e^{-1} \boldsymbol{\sigma}'\right) dV + \int_{S_e} \mathbf{u}^{*T} \left(\mathbf{n}_\sigma^T \boldsymbol{\sigma}'\right) dS - \int_{S_t} \left(\mathbf{u}^{*T} \hat{\mathbf{t}}\right) dS \tag{4.1.33}$$

We take the effective stress field $\boldsymbol{\sigma}'$ as the flux variable, and assume that it satisfies equation (4.1.28), a priori. The second term, which is the interface

potential representing a weak form of equation (4.1.29), assumes equilibrium of pore pressure p on S_e in the strong sense, which we satisfy through continuity of h, as discussed in the previous section. As with h^* and h, we assume that $\mathbf{u}^* \subset \mathbf{u}$ where $\mathbf{u}^*$ and $\mathbf{u}$ are the displacement fields on the boundary and in the domain of an element, respectively. We interpolate $\mathbf{u}^*$ linearly on the element edges as,

$$\mathbf{u}^* = \mathbf{N}_u^* \mathbf{a}_u \tag{4.1.34}$$

To satisfy equilibrium as defined by equation (4.1.28), a priori, we interpolate the effective stress $\boldsymbol{\sigma}'$ in V_e as,

$$\boldsymbol{\sigma}' = \mathbf{P}_\sigma \boldsymbol{\beta}_\sigma + \mathbf{P}_p \boldsymbol{\beta}_p + \mathbf{P}_g \boldsymbol{\beta}_g + \mathbf{P}_j \boldsymbol{\beta}_j \tag{4.1.35}$$

where $\mathbf{P}_\sigma \boldsymbol{\beta}_\sigma$ represents the interpolation of $\boldsymbol{\sigma}'$ satisfying the homogeneous equilibrium equations and $\mathbf{P}_k \boldsymbol{\beta}_k \; \forall k \in \{ p, g, j \}$ represent the particular solutions for the body forces owing to pore fluid pressure, gravity force and volumetric seepage force, respectively. Following Tong and Pian [150], we construct the first term in equation (4.1.34) to satisfy the homogeneous part of equation (4.1.28) using the Airy's stress function approach [cf. 118] wherein $\mathbf{P}_\sigma$ contains monomial basis functions as follows,

$$\mathbf{P}_\sigma = \begin{bmatrix} 1 & 0 & 0 & y & x & 0 & 0 & y^2 & 2xy & x^2 & 0 & 0 \\ 0 & 1 & 0 & 0 & 0 & y & x & 0 & 0 & y^2 & 2xy & x^2 \\ 0 & 0 & 1 & 0 & -y & -x & 0 & 0 & -y^2 & -2xy & -x^2 & 0 \end{bmatrix} \tag{4.1.36}$$

which is valid for Voronoi cell elements with up to 7 nodes. We add columns with cubic terms for elements with >7 nodes, but this is rare in practice for meshes with uniform element size. The coefficients in $\boldsymbol{\beta}_\sigma$ are unknown and we determine their values through the finite element analysis, whereas we assume that we know

the remaining $\mathbf{P}_k\boldsymbol{\beta}_k$ terms, a priori, since the gravitational acceleration is constant and we know the p and $\mathbf{q}$ fields from the seepage analysis.

Substituting equations (4.1.34) and (4.1.35) into the functional in equation (4.1.33) and allowing the first variation of the result with respect to the unknown stress coefficients $\boldsymbol{\beta}_\sigma$ to vanish gives,

$$\boldsymbol{\beta}_\sigma = \mathbf{H}_{\sigma\sigma}^{-1}\left(\mathbf{G}_{\sigma u}\mathbf{a}_u - \sum_k \mathbf{H}_{\sigma k}\boldsymbol{\beta}_k\right) \tag{4.1.37}$$

where,

$$\mathbf{H}_{\sigma\sigma} = \int_{V_e}\left(\mathbf{P}_\sigma^T\mathbf{D}^{-1}\mathbf{P}_\sigma\right)dV \tag{4.1.38}$$

$$\mathbf{G}_{\sigma u} = \int_{S_e}\left(\mathbf{n}_\sigma^T\mathbf{P}_\sigma\right)^T\mathbf{N}_u^* dS \tag{4.1.39}$$

$$\mathbf{H}_{\sigma k}\boldsymbol{\beta}_k = \int_{V_e}\left(\mathbf{P}_\sigma^T\mathbf{D}^{-1}\mathbf{P}_k\boldsymbol{\beta}_k\right)dV \tag{4.1.40}$$

We now substitute equation (4.1.37) back into the functional to eliminate $\boldsymbol{\beta}_\sigma$ and take the first variation with respect to unknown nodal displacements $\mathbf{a}_u$ to obtain,

$$\mathbf{K}_{uu}\mathbf{a}_u = \mathbf{F}_E \tag{4.1.41}$$

where we define the element stiffness matrix $\mathbf{K}_{uu}$ and "external" load vector $\mathbf{F}_E$ as,

$$\mathbf{K}_{uu} = \mathbf{G}_{\sigma u}^T\mathbf{H}_{\sigma\sigma}^{-1}\mathbf{G}_{\sigma u} \tag{4.1.42}$$

$$\mathbf{F}_E = \mathbf{F}_{\hat{t}} + \sum_k \mathbf{F}_k \tag{4.1.43}$$

where the element load vector is the summation of components arising from applied tractions $\mathbf{F}_{\hat{t}}$ and the various body forces $\mathbf{F}_k$ defined as,

$$\mathbf{F}_{\hat{t}} = \int_{S_t}\left(\mathbf{N}_u^{*T}\hat{\mathbf{t}}\right)dS \tag{4.1.44}$$

$$\mathbf{F}_k = \mathbf{G}_{\sigma u}^T \mathbf{H}_{\sigma\sigma}^{-1} \mathbf{H}_{\sigma k} \boldsymbol{\beta}_k - \mathbf{G}_{ku}^T \boldsymbol{\beta}_k \tag{4.1.45}$$

where,

$$\mathbf{G}_{ku}^T \boldsymbol{\beta}_k = \int_{S_e} \left(\mathbf{N}_u^* \right)^T \left(\mathbf{n}_\sigma^T \mathbf{P}_k \boldsymbol{\beta}_k \right) dS \tag{4.1.46}$$

It is worth noting that the element stiffness matrix involves only the components $\mathbf{G}_{\sigma u}$ and $\mathbf{H}_{\sigma\sigma}$, which derive solely from interpolation of effective stress $\boldsymbol{\sigma}'$ to satisfy the homogeneous equilibrium equations, whereas the $\mathbf{H}_{\sigma k}\boldsymbol{\beta}_k$ and $\mathbf{G}_{ku}{}^T\boldsymbol{\beta}_k$ components appear in the load vectors $\mathbf{F}_k$, which represent the body forces. The following section presents the details of the interpolation of the body forces.

4.1.2.3 Interpolation to satisfy particular solutions for body forces

Tong and Pian [150] show that to guarantee a unique solution when incorporating body forces into the hybrid finite element formulation, the $\mathbf{P}_k\boldsymbol{\beta}_k$ terms should have $\mathbf{P}_k \subset \mathbf{P}_\sigma$ – that is, the columns in $\mathbf{P}_k$ are a subset of the columns in $\mathbf{P}_\sigma$. Although the proof is technically correct, we note that it does not prove useful for selecting appropriate interpolations for body forces. This seems clear when one recalls that in the hybrid formulation we construct $\mathbf{P}_\sigma$ to satisfy the homogeneous stress equilibrium equations, which means that each column individually in $\mathbf{P}_\sigma$ must satisfy the homogeneous equations. This inherently prevents selection of any column or linear combination of columns in $\mathbf{P}_\sigma$ to satisfy a particular solution to the stress equilibrium equations. We attribute the lack of recognition of this fact in the literature to the notable lack of applied examples incorporating body forces into hybrid finite element solutions, as body forces were not of interest in the problems being investigated. We describe next

appropriate interpolations for the body forces in the coupled seepage-deformation analysis including body forces owing to the pore fluid pressure p, weight of the material $\rho\mathbf{g}$, and volumetric seepage force $\mathbf{f}_j$.

We obtain the pressure p from the results of the seepage analysis as,

$$p = \mathbf{N}_h \mathbf{a}_p \tag{4.1.47}$$

where $\mathbf{a}_p$ are the nodal values of pressure and $\mathbf{N}_h$ is as defined in Section 4.1.2.1. Comparing equations (4.1.28) and (4.1.35), we recognize the direct equivalence $\mathbf{P}_p\boldsymbol{\beta}_p = \alpha_p p\boldsymbol{\delta}$, which leads to the following relations,

$$\mathbf{H}_{\sigma p}\boldsymbol{\beta}_p = \int_{V_e} \mathbf{P}_\sigma^T \mathbf{D}^{-1} \left(\alpha_p \mathbf{N}_h \mathbf{a}_p \boldsymbol{\delta} \right) dV \tag{4.1.48}$$

$$\mathbf{G}_{pu}^T \boldsymbol{\beta}_p = \int_{S_e} \mathbf{N}_u^{*T} \left(\mathbf{n}_\sigma^T \alpha_p \mathbf{N}_h^* \mathbf{a}_p \boldsymbol{\delta} \right) dS \tag{4.1.49}$$

where we use the conforming shape functions $\mathbf{N}_h$ in V_e and, for convenience, the linear shape functions $\mathbf{N}_h^*$ on S_e, though they are equivalent by definition.

Comparing equations (4.1.28) and (4.1.35), we have that $\mathbf{L}_{\sigma u}^T(\mathbf{P}_g\boldsymbol{\beta}_g) = -\rho\mathbf{g}$. Thus, $\mathbf{P}_g\boldsymbol{\beta}_g$ is a gravity force potential, which we assume to have σ_{xx}/σ_{yy} in proportion according to the direction of the gravitational field and $\sigma_{xy} = 0$,

$$\mathbf{P}_g\boldsymbol{\beta}_g = -\rho \begin{bmatrix} x & 0 \\ 0 & y \\ 0 & 0 \end{bmatrix} \mathbf{g} \tag{4.1.50}$$

For the present study, $\mathbf{g} = \{\ 0, -g\ \}^T$ so $\mathbf{P}_g\boldsymbol{\beta}_g = \{\ 0, \rho g y, 0\ \}^T$. This does not imply that there can be no shear stresses owing to variations in self-weight, but rather that the body force potential can equilibrate only normal stress components at a

point, with shear stress equilibrium coming through the effective stress field $\boldsymbol{\sigma}'$ by generating shear strains. We compute the bulk density of the material as,

$$\rho = \frac{\left(G_s + SG_f e\right)}{1+e}\rho_w \tag{4.1.51}$$

where G_s and G_f are the specific gravities of the solid grains and the pore fluid, respectively, S is the degree of saturation, e is the void ratio and ρ_w is the density of water. In general, $S = S(p)$ is the soil pore fluid characteristic curve with $S \approx 1$ when $p > 0$ and $S \leq 1$ when $p \leq 0$. Consistent with our use of a step function to represent the hydraulic conductivity tensor $\mathbf{K} = \mathbf{K}(p)$, we also use a step function for $S(p)$ with $S = 1$ when $p > 0$ and $S = 0$ when $p \leq 0$. We acknowledge that this is an oversimplification for unsaturated soils, which we retain for simplicity of the presentation, but there is nothing in our formulation that precludes the use of a more sophisticated function for $S(p)$. We substitute equation (4.1.50) into equations (4.1.40) and (4.1.46) to obtain the forms $\mathbf{H}_{\sigma g}\boldsymbol{\beta}_g$ and $\mathbf{G}_{gu}{}^T\boldsymbol{\beta}_g$.

Finally, we obtain the volumetric seepage force $\mathbf{f}_j$ from the seepage results as,

$$\mathbf{f}_j = \alpha_j \rho_f g \mathbf{K}^{-1}\mathbf{q} = \alpha_j \rho_f g \mathbf{K}^{-1}\mathbf{P}_q\boldsymbol{\beta}_q \tag{4.1.52}$$

and note from comparison of equations (4.1.28) and (4.1.35) that $\mathbf{L}_{\sigma u}{}^T(\mathbf{P}_j\boldsymbol{\beta}_j) = -\mathbf{f}_j$. As with the gravitational body force, $\mathbf{P}_j\boldsymbol{\beta}_j$ represents a body force potential owing to the volumetric seepage force. We again assume that this potential equilibrates normal stress components only and let,

$$\mathbf{P}_j\boldsymbol{\beta}_j = -\alpha_j \rho_f g \begin{bmatrix} x & 0 \\ 0 & y \\ 0 & 0 \end{bmatrix} \mathbf{K}^{-1}\mathbf{P}_q\boldsymbol{\beta}_q \tag{4.1.53}$$

which we substitute into equations (4.1.40) and (4.1.46) to obtain the forms $\mathbf{H}_{\sigma j}\boldsymbol{\beta}_j$ and $\mathbf{G}_{ju}{}^T\boldsymbol{\beta}_j$.

4.1.3 Results and Discussion

We implemented the formulation presented in the previous section as a code *vcfem_coup* using the software package Matlab [219]. We now demonstrate the performance of the coupled hybrid VCFEM formulation – in particular, the implementation of body forces.

First, we solve a simple one-dimensional seepage case for which there is an analytical solution. Figure 4.2 shows a 0.05 m × 0.10 m domain representing a 1-D constant head Darcy experiment. We assume that the domain consists of a uniform medium dense sand with water as the pore fluid. We assume isotropic hydraulic conductivity $K_x = K_y = 1.0\times10^{-3}$ m/s, grain specific gravity G_s = 2.65, fluid specific gravity G_f = 1, void ratio e = 0.4 and elastic coefficients $E = 1.0\times10^5$ kPa and $\nu = 0.3$. For the seepage analysis, we have boundary conditions of $\hat{h} = h_1$ at y = 0 m, $\hat{h} = h_2$ at y = 0.1 m and zero flux on the left and

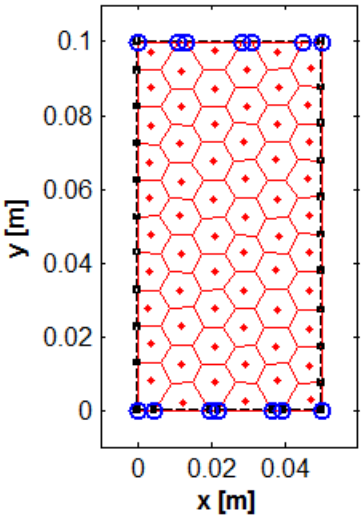

Figure 4.2 Plot of domain and mesh for 1-D coupled analysis

right boundaries. For the deformation analysis, we assume fully fixed displacements on the bottom boundary, fixed lateral displacement on the left and right boundaries and free displacements on the top boundary. The mesh consists of 60 polygonal elements with 10% quadrilaterals, 30% pentagons and 60% hexagons. Owing to the 1-D nature of this example, the solution is not sensitive to mesh density or element shape.

Defining the hydraulic gradient as,

$$i = \frac{h_2 - h_1}{H} \tag{4.1.54}$$

where h_1 and h_2 are the hydraulic head boundary conditions and H = 0.1 m is the height of the domain, we have the analytical solutions for pressure p, lateral and vertical effective stresses σ_{xx}' and σ_{yy}' and vertical displacement u_y,

$$p(y) = \left[(i-1)\,y + h_1\right] G_f \rho_w g \tag{4.1.55}$$

$$\sigma_{xx}'(y) = \frac{\nu}{1-\nu}\sigma_{yy}'(y) \tag{4.1.56}$$

$$\sigma_{yy}'(y) = -\rho_w g H \left[\frac{G_s + G_f e}{1+e} - (1-2i)G_f\right]\left(1 - \frac{y}{H}\right) \tag{4.1.57}$$

$$u_y(y) = -\frac{\rho_w g}{2}\frac{H^2}{E}\left(1 - \frac{2\nu^2}{1-\nu}\right)\left[\frac{G_s + G_f e}{1+e} - (1-2i)G_f\right]\left(2 - \frac{y}{H}\right)\frac{y}{H} \tag{4.1.58}$$

and we assume σ_{xy} = 0 owing to the vertical roller boundary conditions on the left and right sides of the problem. As such, all solutions variables are functions of y only.

We first solve the case where $h_1 = h_2 = 1.5H$ and $i = 0$, which corresponds to hydrostatic conditions. This case isolates the body force components owing to pressure and gravity in the VCFEM analysis since the volumetric seepage forces vanish. Figure 4.3 shows a plot of the results of the VCFEM analysis compared with the analytical solution. We plot the values of p and u_y at the polygonal element nodes and the values of σ_{xx}' and σ_{yy}' at the integration points (see Appendix for details on numerical integration for polygonal elements). There is negligible error in the VCFEM solution for all solution variables. We also solve the case where $h_1 = H$, $h_2 = 1.5H$ and $i = 0.5$ to verify that the body force component owing to volumetric seepage force is correct in the VCFEM implementation. Figure 4.4 shows that the results obtained using the VCFEM agree with the analytical solution exactly.

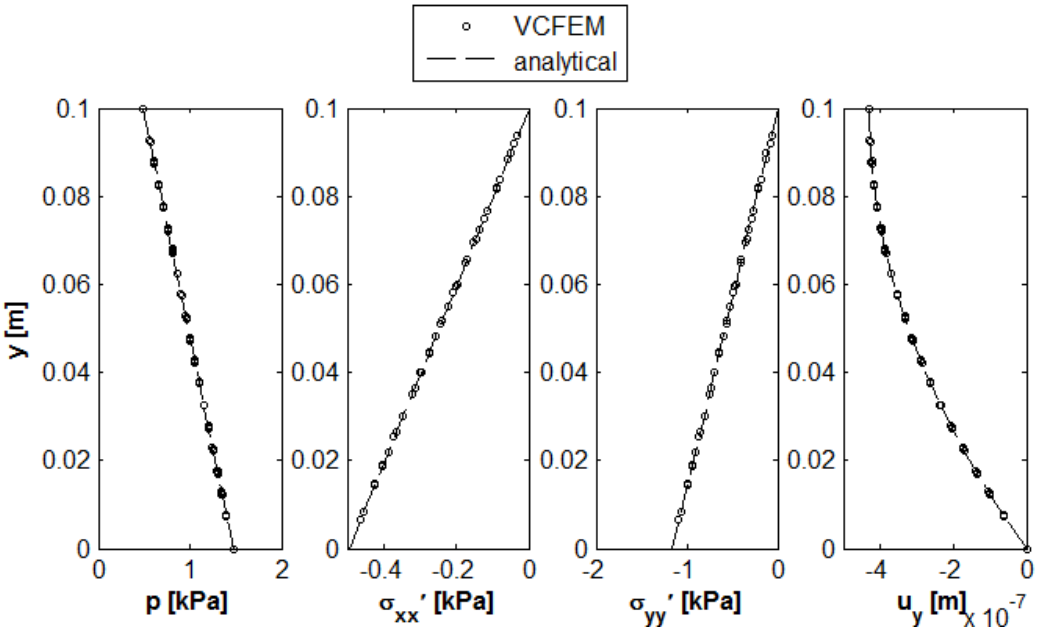

Figure 4.3 Results of 1-D coupled analysis for hydrostatic conditions (hydraulic gradient i = 0)

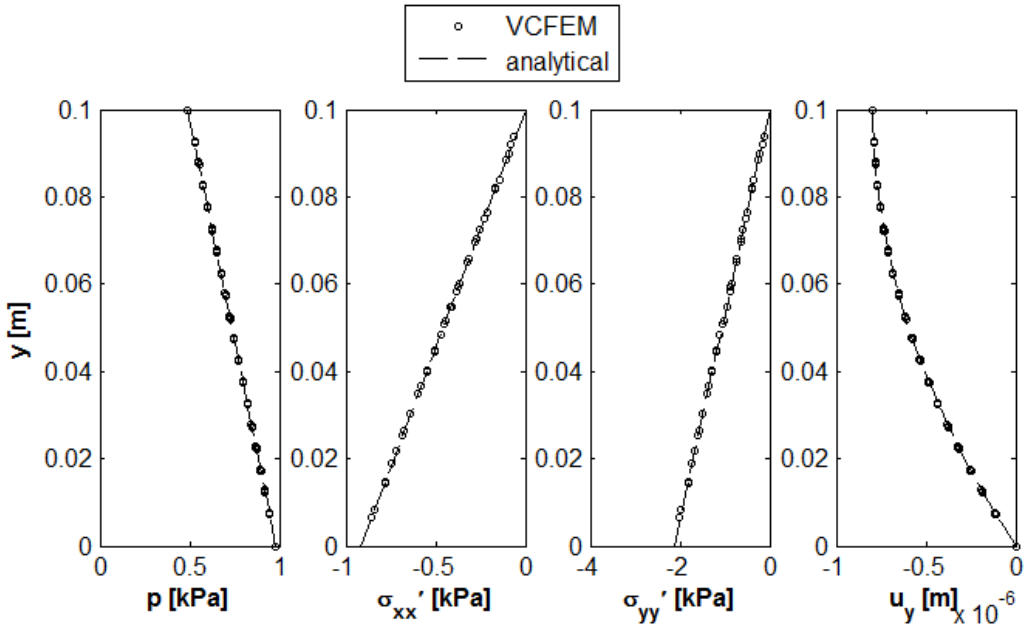

Figure 4.4 Results of 1-D coupled analysis for case with hydraulic gradient i = 0.5

Now, we demonstrate the solution of a problem of practical interest in geotechnical engineering using the coupled hybrid VCFEM with body forces. To this end, we recall that the deformation analysis assumes an elastic constitutive model, which does not account for stress redistributions owing to inelastic deformations. To examine the potential for failure we compute the Mohr-Coulomb failure function for cohesionless material from the effective stress state $\boldsymbol{\sigma}'$ at each integration point,

$$F\left(\boldsymbol{\sigma}'\right)=\tfrac{1}{2}\left|\sigma_1'-\sigma_3'\right|+\tfrac{1}{2}\left(\sigma_1'+\sigma_3'\right)\sin\left(\varphi'\right) \tag{4.1.59}$$

where σ_1' and σ_3' are the major and minor principal stresses (tension positive) obtained from an eigenanalysis of the effective stress state $\boldsymbol{\sigma}'$ and φ' is the effective internal angle of friction. Zones where $F > 0$ correspond to inadmissible stress states according to this failure criterion.

Figure 4.5 shows a 200 m × 70 m rectangular cross section suitable for the preliminary design of an earth dam. We assume the same material properties as in

the 1-D example and an effective internal angle of friction $\varphi' = 30°$. We have hydraulic boundary conditions of $\hat{h}$ = 65 m from y = 0 m to y = 65 m on the upstream side, $\hat{h}$ = 5 m from y = 0 m to y = 5 m on the downstream side, zero flux on the top and bottom boundaries and $\hat{h} = y$ on all other boundaries. The latter boundary condition corresponds to zero gauge pressure, which prevails on boundaries exposed to the atmosphere and internally on the phreatic surface of the pore fluid. The hydraulic conditions correspond to an average horizontal hydraulic gradient $\partial h/\partial x$ = 60/200 = 0.3. For the deformation analysis, we assume fully fixed displacements on the bottom boundary and free displacements on all other boundaries.

We refined the mesh until the analysis results converged, but present here only the results with the converged mesh, which has 754 polygonal elements with most (>88%) being hexagonal. Figure 4.6 shows the results of the seepage analysis to locate the free surface and determine the pressure p and specific discharge $\mathbf{q}$. As Ghosh and Mallett [153] show for deformation analysis and Karchewski et al. [259] (Section 2.1) show for seepage analysis, there is no sensitivity to mesh orientation with the hybrid VCFEM. The pressure field and free surface results are smooth without requiring post-processing.

Figure 4.7 shows a plot of the deformed mesh (displacements magnified for visualization purposes), which qualitatively demonstrates the potential for failure at the toe owing to the seepage forces. Figure 4.8 gives a clearer picture of the failure mechanism by plotting the total and effective stress fields inside the dam. These plots demonstrate the correct implementation of body forces within the hybrid VCFEM. In particular, the total and effective normal stress fields – σ_{xx} and

σ_{yy} vs. σ_{xx}' and σ_{yy}' – are different owing to the influence of pressure p whereas the "total" and "effective" shear stresses – σ_{xy} vs. σ_{xy}' – are identical. There is a bulb of low effective lateral confinement σ_{xx}' near the toe owing to the intensity of the seepage forces, as one would expect from the flow net in Figure 4.6. Figure 4.9 completes the picture, demonstrating a zone of unstable material with $F \gg 0$ near the toe. Obviously a rectangular cross section is an impractical design for an earth dam, but we can use the stress field results from the hybrid VCFEM accounting

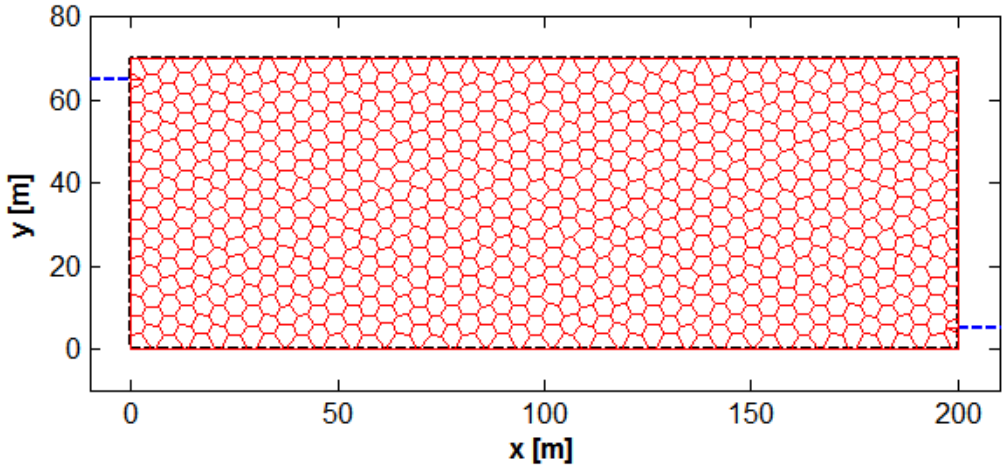

Figure 4.5 Plot of domain and mesh for coupled analysis of rectangular dam

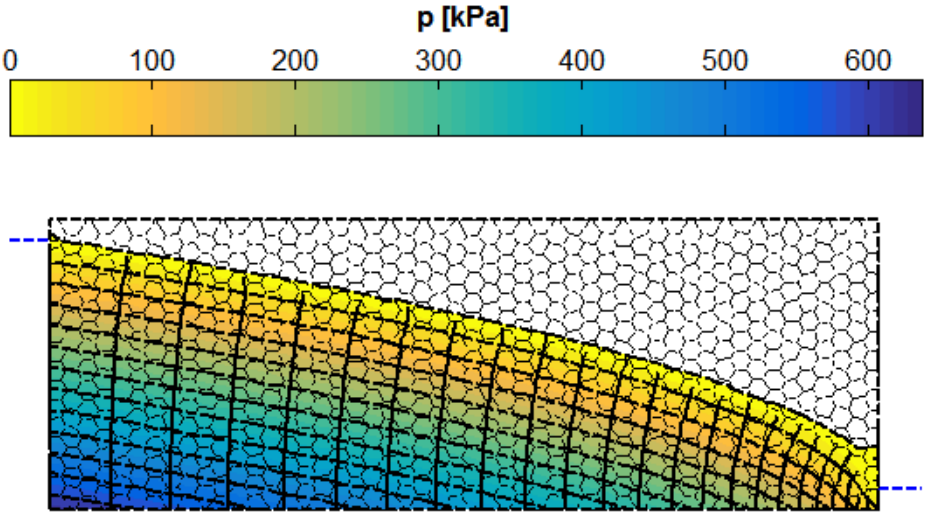

Figure 4.6 Plot of free surface, pressure and flow net for rectangular dam

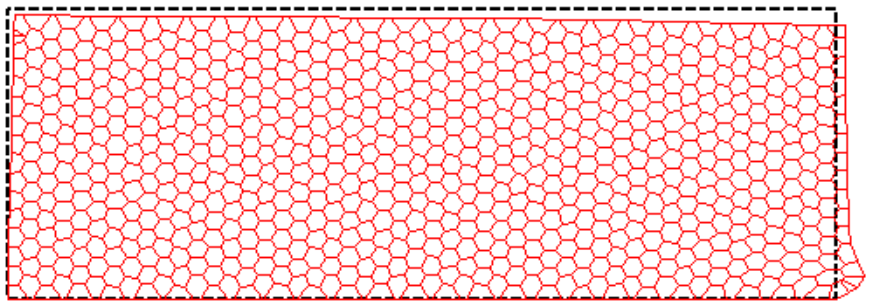

Figure 4.7 Plot of deformed shape for rectangular dam

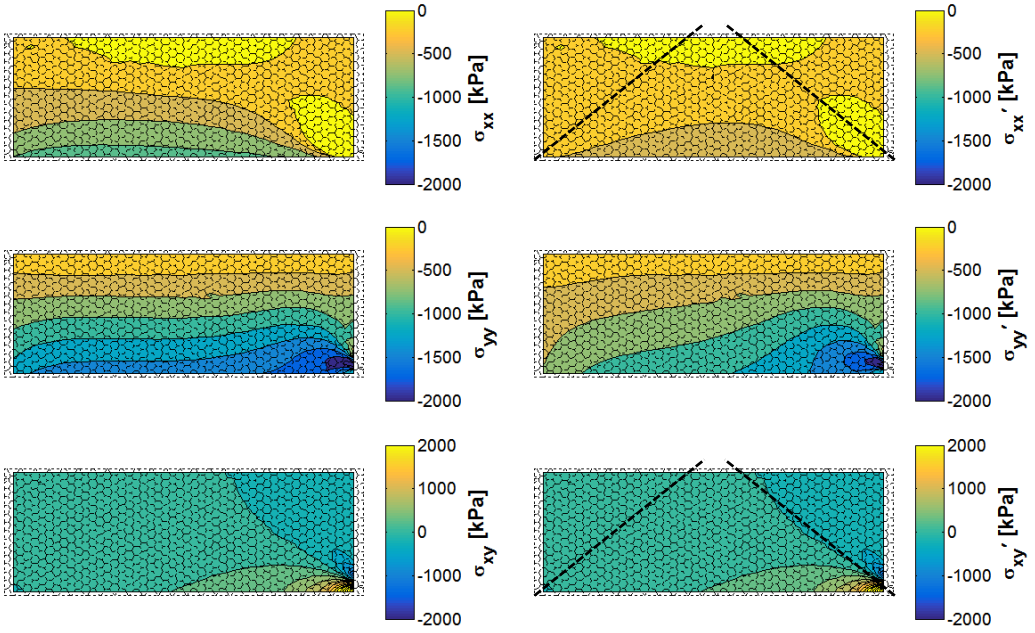

Figure 4.8 Plot of total and effective stresses in rectangular dam

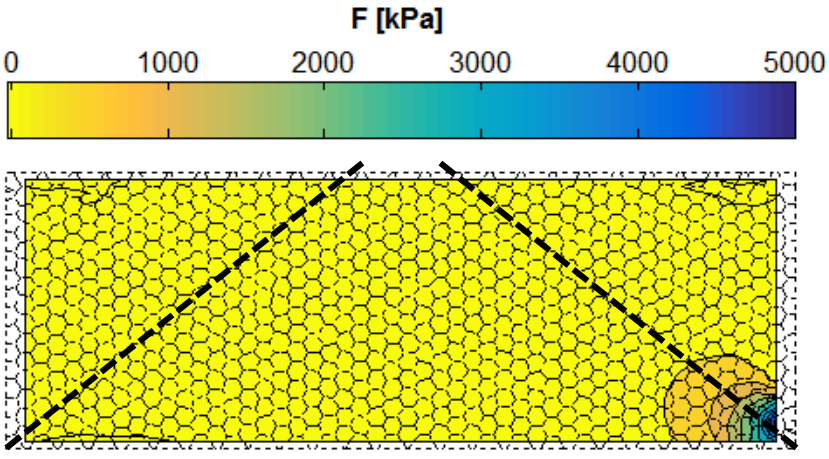

Figure 4.9 Plot of Mohr-Coulomb failure function for rectangular dam

for body forces to determine an efficient and practical side slope angle. Plotting a line through the apex of the zone of low σ_{xx}', high σ_{xy} and high F suggests a slope of 1:1.25 or approximately 39°. We complete the demonstration by analyzing a dam with such a side angle.

Figure 4.10 shows the converged mesh for the analysis of a sloped earth dam, which consists of 414 polygonal elements, which are again mostly (>84%) hexagonal. The mesh has similar element density to that of the rectangular cross section, but has proportionately fewer elements owing to the sloped sides. Figure 4.11 shows the free surface, pressure field and flow net for the sloped dam. Evidently, this cross section leads to a flow field where the discharge on the downstream side spreads out over a larger region implying reduced intensity of the seepage forces within the domain of the dam. Figure 4.12 shows the deformed mesh, which is qualitatively consistent with this flow field. Figure 4.13 shows the results for total and effective stresses where, again, the pressure field affects the normal stresses, but not the shear stresses, as expected. The bulb of low lateral confinement is no longer present, and Figure 4.14 shows that there is now a zone

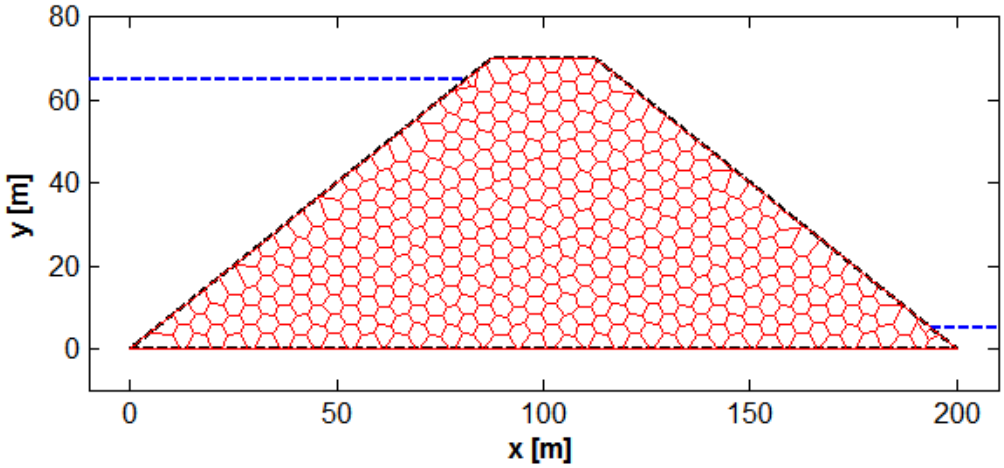

Figure 4.10 Plot of domain and mesh for coupled analysis of sloped dam

of $F > 0$ on the downstream face, as opposed to an intense internal bulb near the toe. This still implies an unstable downstream face with potential for shallow slope failure owing to liquefaction, for which there exist practical engineering solutions such as high conductivity gabions placed on the downstream face. We do not pursue the design details further here, as it is not the focus of the present work and the presented results are sufficient to demonstrate the implementation of the coupled hybrid VCFEM incorporating body forces.

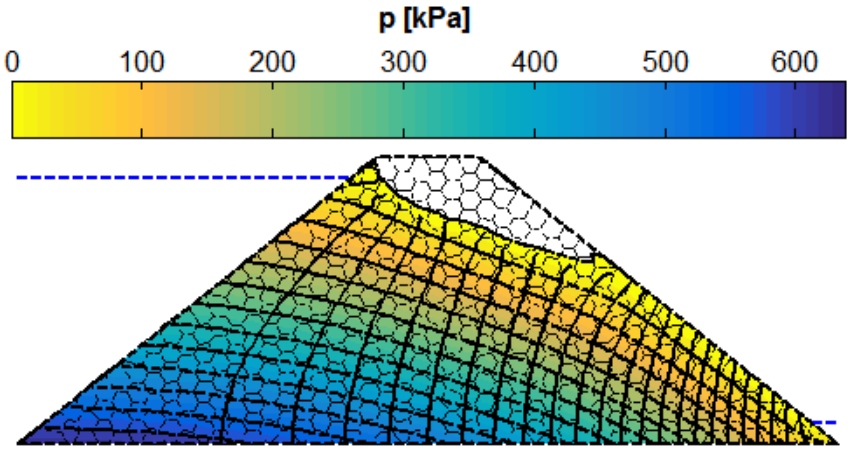

Figure 4.11 Plot of free surface, pressure and flow net for sloped dam

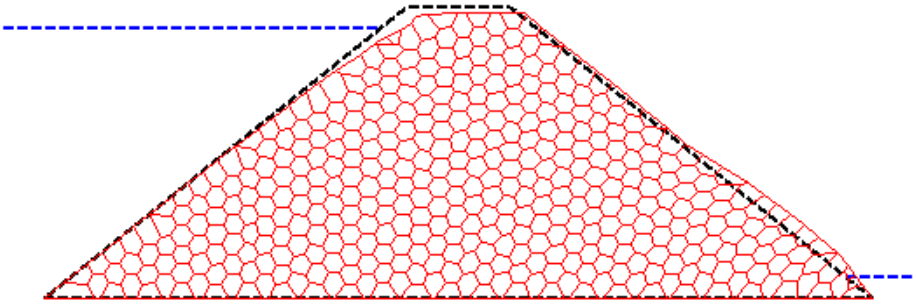

Figure 4.12 Plot of deformed shape for sloped dam

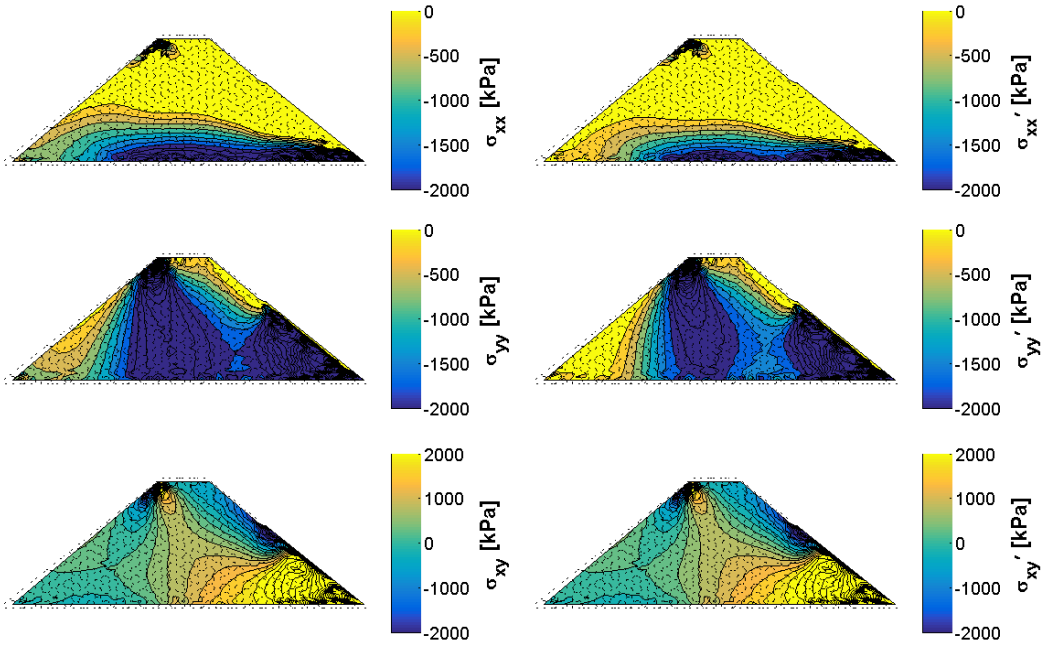

Figure 4.13 Plot of total and effective stresses in sloped dam

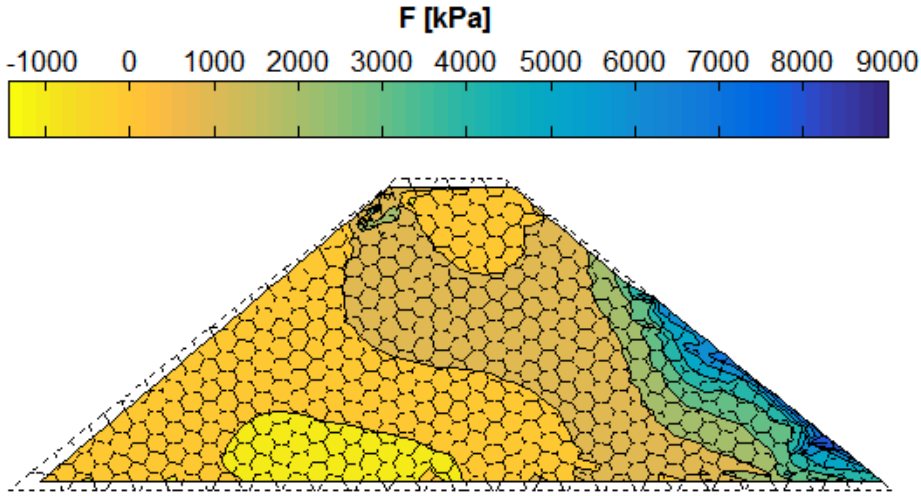

Figure 4.14 Plot of Mohr-Coulomb failure function for sloped dam

4.1.4 Conclusions and Future Work

We presented a hybrid VCFEM formulation for coupled seepage and deformation analysis and demonstrated its performance on a practical geotechnical engineering problem. The key contribution of the present work is the implementation of body forces in a hybrid formulation, which is usable with irregular convex polygonal finite elements with an arbitrary number of nodes.

Although Tong and Pian [150] suggest the possibility of implementing body forces in the hybrid formulation essentially from the outset, and even prove the necessary conditions for the body force interpolation to guarantee a unique solution, there is a notable lack of examples actually doing this in the literature. In computing numerical examples, we discovered that the uniqueness conditions are too restrictive and prevent selection of an interpolation satisfying the particular solutions to the equilibrium equations corresponding to the body forces. Thus, we proposed body force interpolations appropriate for representing gravity forces, seepage forces and pore pressure. In particular, the interpolations for these types of body forces equilibrate normal stresses only, with shear stresses owing to variations in body forces leading to the generation of shear strains in the material.

The analysis herein incorporated only a linear elastic constitutive model, which is inadequate to describe the behaviour of geomaterials, but nonetheless we used this approach to solve a practical problem in geotechnical engineering. The principal author's doctoral thesis work includes the development of a novel approach for multi-scale analysis of geomaterials using a combined finite element-discrete element analysis (VCFEM-DEM) using hybrid polygonal elements to represent grains or volumes of linear elastic material and interface elements to represent the nonlinear constitutive behaviour at the interface between these regions [cf. 233,234,260]. Having implemented coupled seepage and deformation analysis using the hybrid VCFEM as demonstrated in the present work, the next stage of the work will be to incorporate the pressure and seepage forces into the VCFEM-DEM approach to allow multi-scale hydromechanical analysis of geomaterials.

5 Concluding Remarks

Two of the most important phenomena of practical importance in the modelling of geomaterials are the transport of fluid through the pores and the deformation response of the solid component to applied loads. Geological materials are inevitably exposed to the natural environment, so these two phenomena often occur simultaneously. Methods for analyzing certain aspects of these phenomena already exist, each with its own advantages and disadvantages, as Chapter 1 discussed. The present work adds to this body of knowledge by exploring techniques for analyzing geomaterials using VCFEM and VCFEM-DEM.

Coupled seepage and deformation analysis using the VCFEM incorporating body forces allows accurate analysis of earth dams. Chapter 2 demonstrated that the VCFEM for seepage is insensitive to mesh orientation or irregularity, or to the choice of conforming shape function, when using polygonal elements having more than four nodes. Chapter 4 couples the VCFEM seepage analysis with a solid deformation analysis incorporating body forces. The solution of a practical example of the design of an earth dam using the VCFEM required the application of general body forces within a hybrid formulation. Although Tong and Pian [150] proposed the application of body forces in the early stages of the development of hybrid FEM, there is a notable lack of examples in the literature. The present author attributes this to the fact that the developers of hybrid finite elements were mostly interested in problems involving plates and shells [211] where they provide advantages related to satisfying continuity requirements, and

body forces are not of interest. Since body forces such as gravity, pore pressure and volumetric seepage force are important in the analysis of geological materials, the present work developed this aspect, and provided the numerical examples that had been lacking. In doing so, the present author discovered that although the proof of the requirements for uniqueness of solution when applying body forces in the hybrid FEM [150] was technically correct, the requirements were too restrictive to allow an actual solution. Section 4.1.2.3 discussed the details.

Chapter 3 formulated and applied the VCFEM-DEM, a novel approach for simulating granular material behaviour. The application of this method provided new insights into strain localization in granular materials, showing that strain localization is an important phenomenon at all scales. The VCFEM-DEM captured shear banding in biaxial compression tests, demonstrating that global shear strains and inhomogeneities in the shear stress field present after consolidation are early precursors to the failure mode. At the field scale, strain localization can lead to significant non-uniformity in subsurface stress distribution owing to self-weight.

The results of the analyses performed in the present work raised several interesting questions for future research. The results of Chapter 3 revealed that the anisotropy of the grain structure in granular materials has an important influence on the orientation of the failure plane, the strength of the material and the distribution of subsurface stresses. Past studies [cf. 102] have also shown that the grain shape influences the behaviour of granular materials. The VCFEM-DEM has the capacity to model granular materials with complex shapes. The approach can also control the orientation of the fabric of the grain structure and the grain

size distribution carefully. The data structure provided by the interface elements provides a powerful tool for analyzing the development of detailed characteristics of the grain structure such as local changes in void ratio including the directional distribution of volumetric strains throughout the simulations. These advantages provide fertile ground for future investigations into the influences of grain structure and inherent anisotropy in granular materials using the VCFEM-DEM.

Drawing on the success of the VCFEM-DEM for modelling granular materials in Chapter 3, the author is presently at work extending the VCFEM-DEM approach to the analysis of seepage through discontinua such as pore or fracture networks. As with the VCFEM-DEM for granular materials, the mesh configuration is able to represent accurately the physical geometry of geological materials at a wide range of length scales. This will allow multi-scale analysis of the conductivity of fractured rock masses in a novel manner.

Finally, the ultimate thrust of the research using the VCFEM-DEM is coupled simulation of flow through pore/fracture networks and deformation of the granular structure. Such coupled analysis will allow detailed numerical investigation of the behaviour of saturated and unsaturated granular materials, and the fracturing of geological materials owing to rapid changes in fluid pressure in the fractures. The present work demonstrated the capability of the VCFEM and VCFEM-DEM to analyze and provide insight into seepage through porous media, deformation of discrete granular materials and coupled analysis under certain assumptions. The development of a fully coupled model bringing these two aspects together has the author excited about the prospect for new insights into the behaviour of geological materials using the VCFEM-DEM.

6 Appendix

6.1 Quadrature Generation for Voronoi Cell Elements

6.1.1 Introduction

The formulations for hybrid Voronoi cell finite elements in Sections 2.1.2, 3.1.2.1, 3.3.2.2 and 4.1.2 all require formation of element matrices involving integrations of continuous functions – typically polynomials in { x, y } up to order 6, but also conforming shape functions for polygonal elements and local shape functions on edges – over the element surface S_e the element domain V_e. As performing such integrations in closed form would be impractical for numerical calculations owing to the infinite variety of polygonal element shapes, we perform the integrations using numerical integration quadrature rules. This section presents a brief summary of the numerical integration procedures used in the present work for integrals over S_e and V_e.

6.1.2 Formulation

6.1.2.1 General form of integrals for Voronoi cell elements

The Voronoi cell finite element formulations in the present work all require formation of an element "stiffness" matrix $\mathbf{K}$ – sometimes referred to as an element conductivity matrix in cases of seepage analysis,

$$\mathbf{K} = \mathbf{G}^T \mathbf{H}^{-1} \mathbf{G} \tag{6.1.1}$$

where,

$$\mathbf{G} = \int_{S_e} \left(\mathbf{n}^T \mathbf{P} \right)^T \mathbf{N}^* dS \tag{6.1.2}$$

$$\mathbf{H} = \int_{V_e} \mathbf{P}^T \mathbf{C} \mathbf{P} dV \tag{6.1.3}$$

Note that we drop the subscripts used for **K**, **H** and **G** and other matrices in the body of the present work for clarity of the current presentation. Within this section only, **K** refers to the element stiffness matrix and not the hydraulic conductivity tensor. In equations (6.1.2) and (6.1.3) there is the matrix **n** representing the outward normal to S_e, the matrix **P** containing basis functions for flux field interpolation in V_e, the matrix $\mathbf{N}^*$ containing shape functions that interpolate between nodal values on S_e and the matrix **C** representing the constitutive material properties of the element. In the present work, **n** is piecewise constant on S_e, **P** contains up to 3rd order monomial functions in $\mathbb{R}^2$, **N** contains 1st order polynomial functions in $\mathbb{R}$ and **C** is generally constant in V_e except for the case of unconfined seepage where it may be a piecewise constant step function in elements intersected by the free surface dividing the saturated and unsaturated parts of the domain. Tong and Pian [150] give the requirements for the minimum number of unknown flux coefficients m for rank sufficiency of **H** as,

$$m \geq n - r \tag{6.1.4}$$

where n is the number of degrees of freedom in an element and r is the number of zero energy modes, or the number of kinematic constraints, necessary for a unique solution. In the hybrid formulation for linear problems, the **P** matrix derives from derivatives of a potential function. For seepage, there are first order derivatives of a streamline function whereas for solid deformation, there are second order derivatives of Airy's stress function. We assume polynomial form for the potential functions. The requirement of isotropy with respect to the coordinate

system implies that the potential function from which the **P** matrix derives should be a complete polynomial. Combining these requirements, we can determine the maximum order of monomial basis function in **P** for an element with a given number of nodes in each type of formulation. Table 6.1 and Figure 6.1 summarize the results of this analysis, where we observe that for an element with a given number of nodes, the requirements for order of monomial in **P** for the solid deformation formulation are always greater than or equal to the requirements for the seepage formulation. As such, when evaluating the number of integration points required for a polygonal element for either formulation, the requirements for the solid deformation analysis will satisfy the exact integration requirement for both formulations.

Table 6.1 Analysis of required order of monomial basis functions for flux field interpolation in seepage and solid deformation hybrid formulations

Formulation Type	# of kinematic constraints, r	# of dofs/ node	# of nodes/ element	# of dofs/ element, n	# of flux coefficients for rank sufficiency, $m_{req} \geq n - r$	# of flux coefficients using complete polynomial, m_{act}	Maximum order of monomial in P
Seepage (Sec. 2.1.2.4, 4.1.2.1)	1	1	3	3	2	2	0
			4	4	3	5	1
			5	5	4	5	1
			6	6	5	5	1
			7	7	6	9	2
			8	8	7	9	2
			9	9	8	9	2
			10	10	9	9	2
Solid deformation (Sec. 3.1.2.1, 3.3.2.2, 4.1.2.2)	3	2	3	6	3	3	0
			4	8	5	7	1
			5	10	7	7	1
			6	12	9	12	2
			7	14	11	12	2
			8	16	13	18	3
			9	18	15	18	3
			10	20	17	18	3

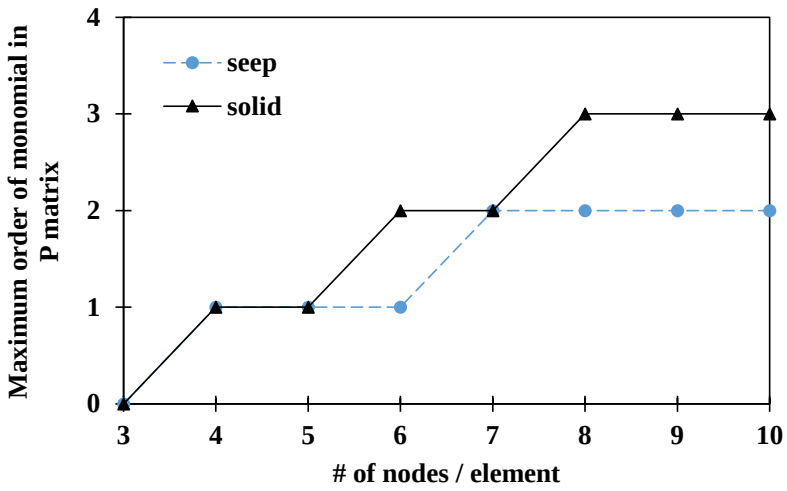

Figure 6.1 Maximum order of monomial in flux interpolation matrix P

In the dynamic VCFEM formulation, we also have an element mass matrix **M** of the form,

$$\mathbf{M} = \int_{V_e} \mathbf{N}^T \rho \mathbf{N} dV \tag{6.1.5}$$

where **N** is a matrix that contains conforming shape functions interpolating between nodal values over a polygonal domain [cf. 135-140,143] and ρ is the density of the material. There is not typically a closed form expression for the shape functions in **N** for polygons with more than four nodes, but they are smooth functions for which a polynomial of sufficient order provides an accurate approximation according to Taylor's theorem.

Owing to the order of the polynomials that we must integrate in equations (6.1.2) and (6.1.3), we should use numerical integration schemes capable of integrating functions of up to fourth order over S_e and up to sixth order over V_e. The shape functions that we must integrate in equation (6.1.5) are not in closed polynomial form, so we will examine the order of integration scheme necessary to achieve accurate numerical integration for a polygon with a given

number of nodes. Section 6.1.2.2 outlines the procedure for numerical integration using standard Gauss quadrature over S_e and Section 6.1.2.3 presents the formulation for generating quadratures to integrate polynomials over convex polygonal domains V_e.

6.1.2.2 Surface integration using standard Gauss quadrature

For the surface integration in equation (6.1.2), we use a numerical integration scheme as follows,

$$\mathbf{G} = \int_{S_e} \left(\mathbf{n}^T \mathbf{P}\right)^T \mathbf{N}^* dS \approx \sum_{i=1}^{N_{edg}} \sum_{j=1}^{N_{int}} \left[\left(\mathbf{n}^T \mathbf{P}\right)^T \mathbf{N}^* \right]_{ij} w_j A_i \tag{6.1.6}$$

where N_{edg} is the number of edges in the polygonal element, N_{int} is the number of integration points on an edge, w_j is the weight assigned to integration point j on an edge and A_i is the area of edge i – for plane strain analysis, the edge length multiplied by a unit thickness. We note that $\mathbf{n}_i$ is constant on an edge and $\mathbf{P} = \mathbf{P}(\mathbf{x})$, but on an edge $\mathbf{x} = \mathbf{N}^* \mathbf{x}_i$ where $\mathbf{x}_i = \{ \mathbf{x}_{i1}, \mathbf{x}_{i2} \}^T$ and $\mathbf{x}_{ik} = \{ x_{ik}, y_{ik} \}$ are the coordinates of node $k \in \{1, 2\}$ on edge i. Using a local coordinate system running from $\xi = 0$ at $\mathbf{x}_{i1}$ to $\xi = 1$ at $\mathbf{x}_{i2}$ we have,

$$\mathbf{N}^*(\xi) = \begin{bmatrix} 1-\xi & 0 & \xi & 0 \\ 0 & 1-\xi & 0 & \xi \end{bmatrix} \tag{6.1.7}$$

which implies that $\mathbf{P} = \mathbf{P}(\xi)$ on an edge as well and since $\mathbf{N}^*(\xi)$ contains only 1st order polynomials in ξ, we can say that the maximum order of polynomial in ξ contained in $\mathbf{P}(\xi)$ is equivalent to the maximum total order of monomial term in $\{ x, y \}$ in $\mathbf{P}(\mathbf{x})$. For example, for a fourth order monomial term x^2y^2, we have,

$$x^2 y^2 = \left[(1-\xi)x_1 + \xi x_2\right]^2 \left[(1-\xi)y_1 + \xi y_2\right]^2$$
$$= \left[(1-\xi)^2 x_1^2 + 2(1-\xi)\xi x_1 x_2 + \xi^2 x_2^2\right]\left[(1-\xi)^2 y_1^2 + 2(1-\xi)\xi y_1 y_2 + \xi^2 y_2^2\right]$$
$$= (1-\xi)^4 x_1^2 y_1^2 + \ldots + \xi^4 x_2^2 y_2^2$$

which is fourth order in ξ. Furthermore, since $\mathbf{N}^*(\xi)$ contains only first order polynomials, the maximum order of the integrand for **G** is the maximum order of monomial basis function in **P** plus unity. Combining this with the results from Figure 6.1, Figure 6.2 shows the order of the integrand in **G**. Using standard Gauss quadrature rules, as shown in Table 6.2, we can integrate polynomials of

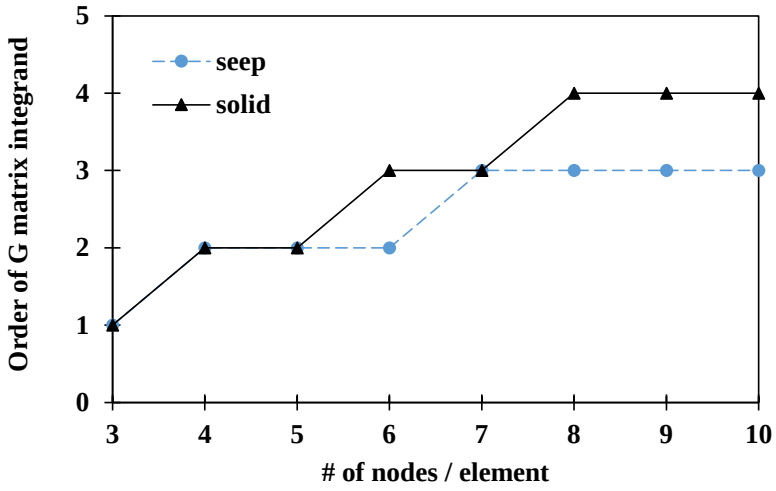

Figure 6.2 Maximum order of integrand for flux balance matrix G

Table 6.2 Standard Gauss-Legendre quadrature rules for use in integrating flux balance matrix G [cf. 145]

# of integration points, N_{int}	Local coordinates of integration points, ξ_j	Integration point weights, w_j
1	$\frac{1}{2}$	1
2	$\frac{1}{2}\left(1 \pm \sqrt{\frac{1}{3}}\right)$	$\frac{1}{2}$
3	$\frac{1}{2}$	$\frac{4}{9}$
	$\frac{1}{2}\left(1 \pm \sqrt{\frac{3}{5}}\right)$	$\frac{5}{18}$

order $2N_{int} - 1$ using an N_{int} point integration rule [145]. Figure 6.3 summarizes the number of integration points per edge required to integrate **G** plotted against the number of nodes in an element.

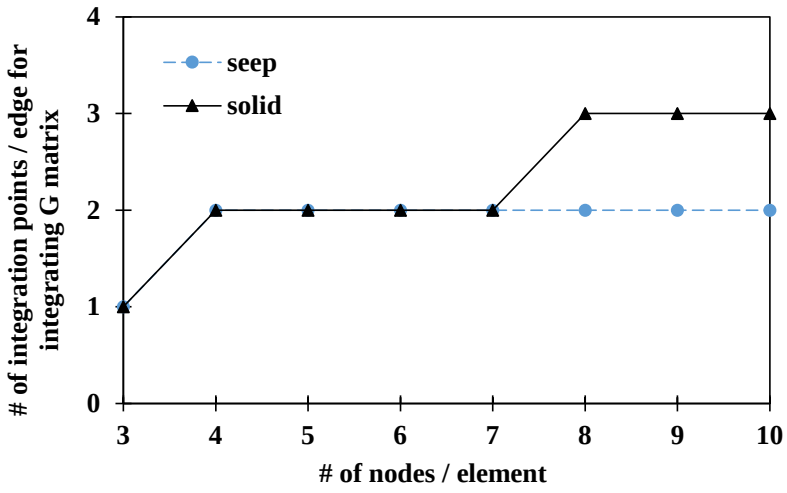

Figure 6.3 Number of integration points used in integrating flux balance matrix G for seepage and solid deformation hybrid formulations

6.1.2.3 Domain integration using generated quadrature for convex polygons

We now examine the numerical integration of integrals over V_e such as in equations (6.1.3) and (6.1.5) of the form,

$$\mathbf{H} = \int_{V_e} \mathbf{P}^T \mathbf{C} \mathbf{P} dV \approx \sum_{i=1}^{N_{int}} \left(\mathbf{P}^T \mathbf{C} \mathbf{P} \right)_i w_i V_e \tag{6.1.8}$$

$$\mathbf{M} = \int_{V_e} \mathbf{N}^T \rho \mathbf{N} dV \approx \sum_{i=1}^{N_{int}} \left(\mathbf{N}^T \rho \mathbf{N} \right)_i w_i V_e \tag{6.1.9}$$

where N_{int} is the number of integration points in an element, w_i is the weight assigned to integration point i and V_e is the volume of the element – for plane strain analysis, the area of the element multiplied by a unit thickness. Although standard quadrature rules exist for triangular, quadrilateral [cf. 134,145] and regular symmetric hexagonal regions [262], standard quadrature rules do not exist

for irregular convex polygons with five or more sides. Mousavi and Sukumar [217] present an efficient approach for generating sets of integration points and weights for such cases. The procedure involves three primary steps:

i. Selection of basis functions $\phi_i(\mathbf{x})$ and evaluation of their exact integrals over the domain V_e.

ii. Generation of candidate integration points $\mathbf{x}_j$ and evaluation of the basis functions at each of these points $\phi_i(\mathbf{x}_j)$.

iii. Solution of a moment fitting equation to determine the corresponding integration point weights w_j.

We briefly summarize the procedure here, but refer to [217] for a more detailed discussion of the derivation of the procedure. We also discuss details of the procedure that we modified, in particular owing to issues that arise from negative integration point weights that result from the procedure of Mousavi and Sukumar [217] in some cases. The goal is to solve a moment fitting equation $\boldsymbol{\phi} = \boldsymbol{\Phi}\mathbf{w}$ of the form,

$$\begin{Bmatrix} \int_{V_e} \omega_1(\mathbf{x})\phi_1(\mathbf{x})dV \\ \int_{V_e} \omega_2(\mathbf{x})\phi_2(\mathbf{x})dV \\ \vdots \\ \int_{V_e} \omega_m(\mathbf{x})\phi_m(\mathbf{x})dV \end{Bmatrix} = \begin{bmatrix} \phi_1(\mathbf{x}_1) & \phi_1(\mathbf{x}_2) & \phi_1(\mathbf{x}_3) & \cdots & \phi_1(\mathbf{x}_n) \\ \phi_2(\mathbf{x}_1) & \phi_2(\mathbf{x}_2) & \phi_2(\mathbf{x}_3) & \cdots & \phi_2(\mathbf{x}_n) \\ \vdots & \vdots & \vdots & \ddots & \vdots \\ \phi_m(\mathbf{x}_1) & \phi_m(\mathbf{x}_2) & \phi_m(\mathbf{x}_3) & \cdots & \phi_m(\mathbf{x}_n) \end{bmatrix} \begin{Bmatrix} w_1 \\ w_2 \\ w_3 \\ \vdots \\ w_n \end{Bmatrix} \tag{6.1.10}$$

where m is the number of basis functions, n is the number of candidate integration points and $\omega_i(\mathbf{x})$ is the weight function associated with basis function $\phi_i(\mathbf{x})$. In the present work, we take $\omega_i(\mathbf{x})$ as unity $\forall i$.

To determine the set of basis functions $\phi_i(\mathbf{x})$ that we must integrate for a given element, we considering the maximum order of monomial in the integrand for the **H** matrix. We assume that the constitutive matrix **C** is constant for an element, thus the maximum order of monomial in the integrand will be twice the maximum order of monomial in **P**. Given the maximum order of monomials in **P** from Table 6.1, Figure 6.4 summarizes the maximum order of monomial in the integrand for **H**. Knowing this, the basis functions $\phi_i(\mathbf{x})$ for a given element should include all monomials $x^i y^j$ for $i+j \leq k$ where k is the maximum order of monomial in the integrand of **H**. Table 6.3 summarizes the number of monomial basis functions m required for elements with up to 10 nodes. Once we determine the required set of basis functions $\phi_i(\mathbf{x})$ we construct the column vector $\boldsymbol{\phi}$ on the left-hand side of equation (6.1.10) by inserting the exact integrals,

$$\boldsymbol{\varphi}_i = \int_{V_e} \omega_i(\mathbf{x}) \phi_i(\mathbf{x}) dV \tag{6.1.11}$$

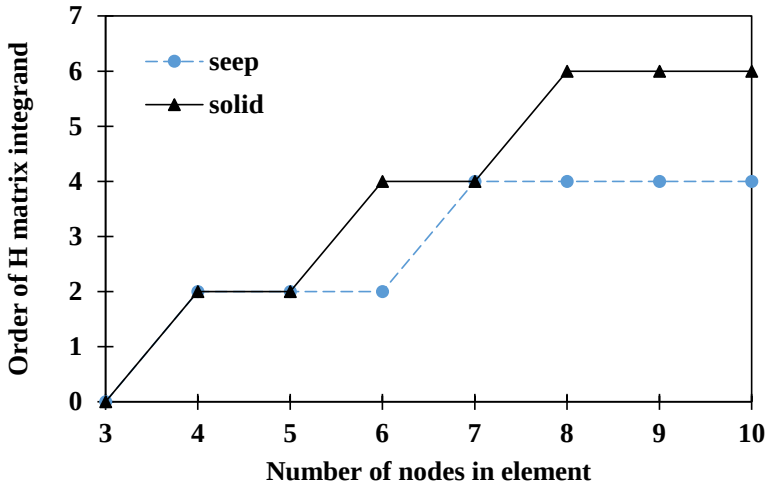

Figure 6.4 Maximum order of monomial in integrand for flux divergence matrix H

Table 6.3 Number of monomial basis functions required for generation of quadrature to integrate flux divergence matrix H

Formulation Type	# of nodes/ element	Maximum order of monomial in H	# of monomial basis functions, *m*
Seepage (Sec. 2.1.2.4, 4.1.2.1)	3	0	1
	4	2	6
	5	2	6
	6	2	6
	7	4	15
	8	4	15
	9	4	15
	10	4	15
Solid deformation (Sec. 3.1.2.1, 3.3.2.2, 4.1.2.2)	3	0	1
	4	2	6
	5	2	6
	6	4	15
	7	4	15
	8	6	28
	9	6	28
	10	6	28

at entry *i*. Lasserre [263,264] presents a scheme for computing integrals of homogeneous continuous and continuously differentiable functions over convex polytopes in N_{dim} dimensions by reduction to integrals over its outer surfaces in (N_{dim} − 1) dimensions. Within the context of the present work, this means reducing the volume integral of $\omega_i(\mathbf{x})\phi_i(\mathbf{x})$ over V_e to a surface integral over S_e, which we may then compute using standard Gauss quadrature rules. Mousavi and Sukumar [217] summarize this integration scheme within the context of generating quadrature rules over convex polyhedra. We present a brief overview of the Lasserre integration scheme here for completeness of the present work. We describe the integration region of a convex polygon V_e as all points **x** such that $\mathbf{Ax} \leq \mathbf{b}$ where **A** is an $N_{edg} \times N_{dim}$ matrix, **b** is an $N_{edg} \times 1$ column vector, N_{dim} is the number of coordinate dimensions – two for a polygon. An edge S_k of V_e is then the part of the line that satisfies $\mathbf{A}_k\mathbf{x} = b_k$ where $\mathbf{A}_k$ is the k^{th} row in **A**, b_k is the k^{th} entry in **b** while still satisfying $\mathbf{Ax} \leq \mathbf{b}$. The surface S_e of V_e is then the set of

edges $S_k \; \forall k \in \{ 1, 2, \ldots N_{edg} \}$. Lasserre integration for integration of homogeneous functions then says that,

$$\int_{V_e} \omega_i(\mathbf{x}) \phi_i(\mathbf{x}) dV = \frac{1}{N_{dim} + N_{ord}} \sum_{k=1}^{N_{edg}} \frac{b_k}{\|\mathbf{A}_k\|} \int_{S_k} \omega_i(\mathbf{x}) \phi_i(\mathbf{x}) \|\mathbf{A}_k\| dS \qquad (6.1.12)$$

where N_{ord} is the order of the homogeneous function $\omega_i(\mathbf{x})\phi_i(\mathbf{x})$. For $\omega_i(\mathbf{x}) = 1$ and monomial $\phi_i(\mathbf{x})$, N_{ord} is the total order of the monomial. We may now compute the surface integrals over the edges S_k using standard Gauss quadrature as follows,

$$\int_{S_k} \omega_i(\mathbf{x}) \phi_i(\mathbf{x}) \|\mathbf{A}_k\| dS \approx \sum_{j=1}^{N_{int}} \left[\omega_i(\mathbf{x}_j) \phi_i(\mathbf{x}_j) \|\mathbf{A}_k\| \right] w_j A_k \qquad (6.1.13)$$

where we interpolate $\mathbf{x}_j = \mathbf{N}^*(\xi_j)\mathbf{x}_k$, given the nodal coordinates $\mathbf{x}_k$ and the area A_k of S_k, and we note that $A_k \neq \|\mathbf{A}_k\|$. We select the quadrature rule from Table 6.2 to obtain the exact integration over S_k, which means that we should have $N_{ord} \leq 2N_{int} - 1$.

Now suppose that we have a set of candidate integration points $\{ \mathbf{x}_1, \mathbf{x}_2, \ldots \mathbf{x}_n \}$ whose locations we assume a priori in a regular grid arrangement over the domain of the element. We construct the matrix $\mathbf{\Phi}$ by evaluating $\phi_i(\mathbf{x}_j) \; \forall \; i \in \{ 1, 2, \ldots m \}, j \in \{ 1, 2, \ldots n \}$ and inserting the values at $\mathbf{\Phi}_{ij}$. Now we solve the linear system in equation (6.1.10). We note that in general $m < n$, so the solution of equation (6.1.10) is underdetermined implying that there is not a unique solution for the set of weights w_j. This is not an issue on its own, but requires special consideration of the algorithm that we use to solve the equation. We use the minimum norm solution provided by the linear solver in Matlab [219], which is based on an orthogonal-triangular (QR) factorization of $\mathbf{\Phi}$. This solution

also has the benefit of resulting in many zero w_j values, which means that we do not need to store their associated weights.

As Mousavi and Sukumar [217] note, the solution sometimes produces negative weights. We found that this is undesirable for cases when we use lumping for the mass matrix **M**, as it may lead to negative nodal masses. Since the integration points with negative weights represent a small minority, and the solution often does not include negative weights, we can solve this by iterative deletion of candidate integration points. The procedure is as follows:

1. Given a set of candidate integration points, construct matrix **Φ** by evaluating $\phi_i(\mathbf{x}_j)\ \forall i,j$ as described previously.
2. Compute the solution **w** to the underdetermined system in equation (6.1.10) using the QR factorization solver.
3. Find all j for which $w_j < -\varepsilon_{tol}$ where ε_{tol} is an error tolerance, necessary owing to the use of floating point numbers of finite precision.
4. Eliminate the candidate points found in step 3.
5. Repeat steps 1-4 until step 3 finds no points.
6. Find all j for which $|w_j| < \varepsilon_{tol}$ and eliminate these points.

Step 3 ensures that there are no integration points with significant negative weights, whereas step 6 deletes points with negligible weight, as these points will not significantly influence the numerical integration result. In practice, we find that this algorithm converges in a small number of iterations (<5) for irregular convex polygonal regions with up to 10 sides. The resulting set of integration points with non-zero weights has $n \leq m$ with cases of $n < m$ resulting from symmetry of the integration region.

6.1.3 Example and Discussion

To demonstrate the technique described in the previous section, consider the irregular hexagon shown in Figure 6.5. Table 6.4 shows the coordinates of the vertices and Table 6.5 shows the properties of the polygon useful for Lasserre integration of the monomial basis functions. Note that the polygon has its centroid at the origin. All numerical integration schemes on polygons in the present work use a local coordinate system such that the centroid is at the origin, to avoid dominance of high order monomial terms in the **P** matrix leading to ill conditioning of the **H** matrix. Throughout this example, the tabulated results show

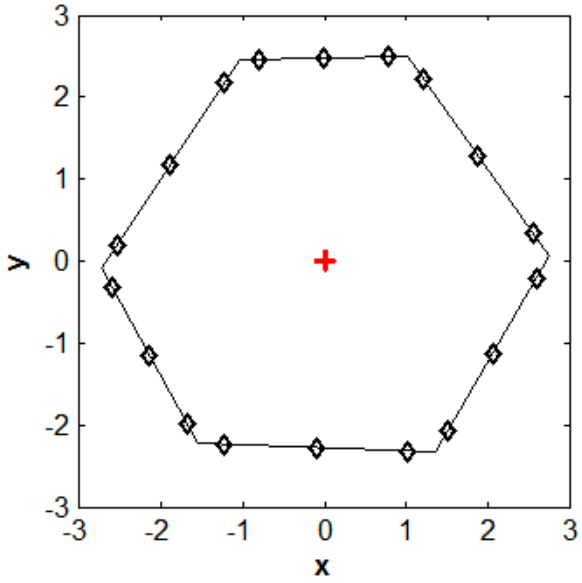

Figure 6.5 Sample irregular hexagon showing location of integration points on S_e

Table 6.4 Vertex coordinates of irregular hexagon

Vertex i	Coordinates x_i	y_i
1	2.751777	0.061217
2	1.005377	2.503237
3	-1.029423	2.458187
4	-2.729623	-0.088803
5	-1.549823	-2.220693
6	1.349877	-2.336763

Table 6.5 Edge data for Lasserre integration over irregular hexagon

Edge	Length	Constraint System, Ax ≤ b			
i	L_i	A_{i1}	A_{i2}	$\|\|A_i\|\|$	b_i
1	3.002228	1.398317	1	1.719095	3.909073
2	2.035299	-0.022140	1	1.000245	2.480978
3	3.062326	-1.498053	1	1.801156	4.000317
4	2.436572	-1.806993	-1	2.065242	5.021212
5	2.902022	-0.040028	-1	1.000801	2.282730
6	2.777703	1.710521	-1	1.981384	4.645757

values to six decimal points of precision, though the calculations were performed using full double precision arithmetic.

To generate the set of quadrature points in the domain of the element and their corresponding weights, it is first necessary to obtain exact integrals of the monomial basis functions. As Table 6.3 shows, a hexagonal element for solid deformation analysis requires integration of monomials up to 4^{th} order, a total of 15 basis functions. Therefore, we require the three point Gauss integration rule from Table 6.2 on each edge. Table 6.6 shows the coordinates of the integration points and the corresponding weights, and Figure 6.5 superimposes their locations on the edges of the hexagon. Table 6.7 shows the results of the Lasserre integration of the monomial basis functions, according to equation (6.1.13). Note that the integral of the constant basis function gives the area of the element, and that the integrals of the first order basis functions vanish since the centroid is at the origin. Integrals of basis functions with even powers of x and y have large positive values, whereas the values are small and may be positive or negative for basis functions with odd powers of x or y.

Next, we generate a grid of candidate integration points over the domain of the element, as Figure 6.6(a) shows. Of course, we only consider grid points that are inside the polygon as candidate integration points. We have the vector $\boldsymbol{\phi}$ from

Table 6.6 Coordinates and weights of integration points on S_e for irregular hexagon

Point	Coordinates		Length	Coefficient	Weight
i	x_i	y_i	L_i	$b_i/\|\|A_i\|\|$	w_i
1	2.554955	0.336437			0.277778
2	1.878577	1.282227	3.002228	2.273912	0.444444
3	1.202199	2.228017			0.277778
4	0.776052	2.498160			0.277778
5	-0.012023	2.480712	2.035299	2.480370	0.444444
6	-0.800097	2.463264			0.277778
7	-1.221038	2.171137			0.277778
8	-1.879523	1.184692	3.062326	2.220972	0.444444
9	-2.538007	0.198247			0.277778
10	-2.596657	-0.329071			0.277778
11	-2.139723	-1.154748	2.436572	2.431295	0.444444
12	-1.682788	-1.980425			0.277778
13	-1.223022	-2.233774			0.277778
14	-0.099973	-2.278728	2.902022	2.280903	0.444444
15	1.023076	-2.323682			0.277778
16	1.507874	-2.066507			0.277778
17	2.050827	-1.137773	2.777703	2.344703	0.444444
18	2.593781	-0.209039			0.277778

Table 6.7 Exact integrations of monomial basis functions over V_e for irregular hexagon using Lasserre integration

Basis function	Monomial integrand	Integral over V_e
i	φ_i	$\int_{Ve} \varphi_i \, dV$
1	1	18.866291
2	x	0.000000
3	y	0.000000
4	x^2	28.551940
5	xy	0.640381
6	y^2	28.745074
7	x^3	-0.105063
8	x^2y	-2.575401
9	xy^2	0.026144
10	y^3	2.675919
11	x^4	89.286776
12	x^3y	2.698386
13	x^2y^2	27.625113
14	xy^3	1.087535
15	y^4	90.112455

the third column of Table 6.7 and we build the matrix $\mathbf{\Phi}$ by evaluating the basis functions at all of the candidate integration points. We solve the underdetermined system in equation (6.1.10) using the Matlab solver as Section 6.1.2.3 described. We obtain 15 non-zero weights, consistent with the fact that there are 15 basis functions. On the first iteration, four of the weights are negative as Figure 6.6(b)

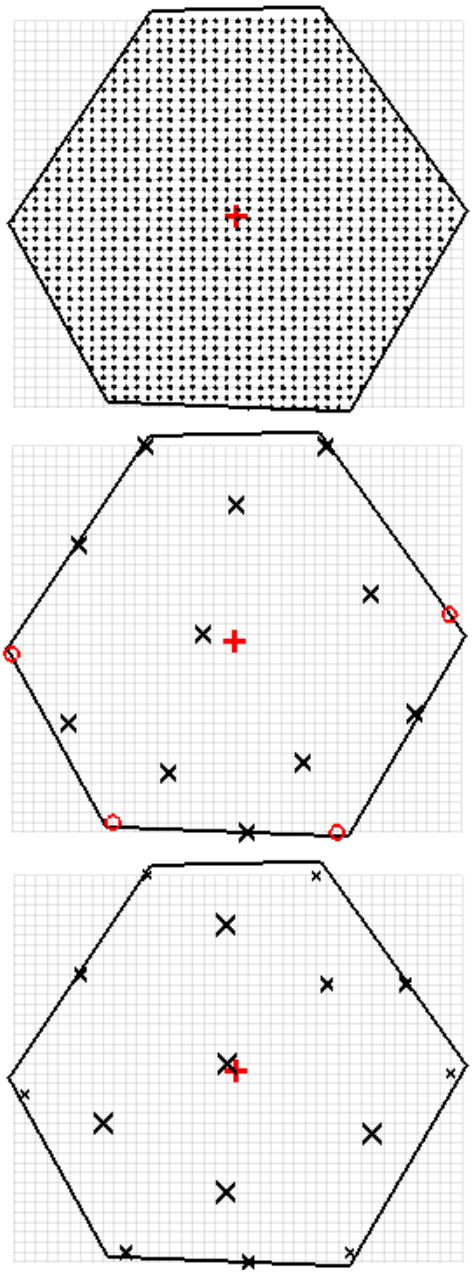

(a) Irregular hexagon tiled with candidate quadrature points.

x_{min} = -2.674809 y_{min} = -2.288363
x_{max} = 2.696963 y_{max} = 2.336257
Δx = 0.134294 Δy = 0.118580

(b) Points with non-zero weights after one iteration. Points with a black X had positive weight. Points with a red O had negative weight.

(c) Points with non-zero weights after five iterations. Size of X indicates the relative magnitude of the weights.

Figure 6.6 Graphical depiction of iterative generation of quadrature points and non-negative weights. Bold red + indicates polygon centroid.

and Table 6.8 show. Negative weights are undesirable, so we delete these four points and repeat the process until we obtain a set of points with positive weights. After five iterations, we obtain a set of 15 integration points with all positive weights, as Figure 6.6(c) and Table 6.9 show. Integration points located closer to

the centre of the element carry the most weight, whereas points near vertices carry the least weight, as one would expect.

Table 6.8 Generated quadrature points and weights for irregular hexagon after one iteration

Point	Coordinates		Weight
i	x_i	y_i	w_i
1	-2.003337	-0.983983	0.136709
2	-1.869043	1.150457	0.079001
3	-1.063277	2.336257	0.015764
4	-0.794689	-1.576883	0.036663
5	-0.391806	0.083237	0.218884
6	0.011077	1.624777	0.127703
7	0.145371	-2.288363	0.082778
8	0.816843	-1.458303	0.113564
9	1.085432	2.336257	0.036515
10	1.622609	0.557557	0.141416
11	2.159786	-0.865403	0.069516
12	-2.674809	-0.153923	** -0.015473 **
13	-1.466160	-2.169783	** -0.016190 **
14	1.219726	-2.288363	** -0.023397 **
15	2.562669	0.320397	** -0.003453 **

Table 6.9 Converged quadrature points and weights for irregular hexagon after five iterations

Point	Coordinates		Weight
i	x_i	y_i	w_i
1	-2.540515	-0.272503	0.017027
2	-1.869043	1.150457	* 0.056086 *
3	-1.600454	-0.628243	** 0.145677 **
4	-1.331866	-2.169783	* 0.025085 *
5	-1.063277	2.336257	0.010260
6	-0.123217	-1.458303	** 0.095526 **
7	-0.123217	0.083237	** 0.161623 **
8	-0.123217	1.743357	** 0.153657 **
9	0.145371	-2.288363	* 0.034558 *
10	0.951137	2.336257	0.016667
11	1.085432	1.031877	* 0.049097 *
12	1.354020	-2.169783	0.014707
13	1.622609	-0.746823	** 0.159708 **
14	2.025492	1.031877	* 0.058906 *
15	2.562669	-0.035343	0.001418

6.1.4 Conclusion

The aim of this Appendaix was to clarify the procedure for generating the quadrature rules used to integrate the **H**, **G** and **M** matrices numerically.

Section 6.1.2 presented the theory behind the quadrature rules, including standard Gauss quadrature rules for surface integrations and the procedure for generating quadrature rules for irregular polygonal domains. Section 6.1.3 provided a demonstrative example to show the complete procedure for generating a set of quadrature points and weights for an irregular hexagon. With these details made clear, the present work is complete.

Bibliography

1. Terzaghi K. Principles of Soil Mechanics. *Engineering News Record* 1925; **95**:19-27.
2. Terzaghi K. *Theoretical Soil Mechanics*. John Wiley & Sons: New York, 1943.
3. Terzaghi K, Peck RB, Mesri G. *Soil Mechanics in Engineering Practice, Third Edition.* John Wiley & Sons, Inc.: New York, 1996.
4. Freeze RA, Cherry JA. *Groundwater*. Prentice Hall: Englewood Cliffs, NJ, 1979.
5. Harr ME. *Groundwater and Seepage*. McGraw-Hill: New York, 1962.
6. Fetter CW. *Contaminant Hydrogeology, Second Edition*. Prentice Hall: Upper Saddle River, NJ, 1999.
7. Jaeger HM, Nagel SR, Behringer RP. The Physics of Granular Materials. *Physics Today* 1996; **49**:32-38, DOI: 10.1063/1.881494.
8. Darcy H. *Les Fontaines Publiques de la Ville de Dijon*. Libraire des Corps Impériaux des Ponts et Chaussées et des Mines: Paris, 1856.
9. Whitaker S. Flow in porous media I: A theoretical derivation of Darcy's law. *Transport in Porous Media* 1986; **1**:3-25, DOI: 10.1007/BF01036523.
10. Coulomb CA. Essai sur une application des règles des maximis et minimis à quelques problemes de statique relatifs à l'architecture. *Memoires de Mathématique et de Physique, Présentés, à l'Academie Royale des Sciences, Paris* 1776; **3**:38.
11. Matsuoka H, Nakai T. Stress-deformation and strength characteristics of soil under three different principal stresses. *Proceedings of the Japanese Society of Civil Engineers* 1974; **232**:59-74.
12. Walsh JB, Brace JF. A fracture criterion for brittle anisotropic rock. *Journal of Geophysical Research* 1964; **69**:3449-3456, DOI: 10.1029/JZ069i016p03449.
13. Hoek E. Strength of jointed rock masses. *Géotechnique* 1983; **33**:187-223, DOI: 10.1680/geot.1983.33.3.187.
14. Oda M. Inherent and induced anisotropy in plasticity theory of granular soils. *Mechanics of Materials* 1993; **16**:35-45, DOI: 10.1016/0167-6636(93)90025-M.
15. Pietruszczak S, Mróz Z. Formulation of anisotropic failure criteria incorporating a microstructure tensor. *Computers and Geotechnics* 2000; **26**:105-112, DOI: 10.1016/S0266-352X(99)00034-8.
16. Pietruszczak S, Mróz Z. On failure criteria for anisotropic cohesive-frictional materials. *International Journal for Numerical and Analytical Methods in Geomechanics* 2001; **25**:509-524, DOI: 10.1002/nag.141.
17. Duveau G, Shao JF, Henry JP. Assessment of some failure criteria for strongly anisotropic materials. *Mechanics of Cohesive Frictional Materials* 1998; **3**:1-26, DOI: 10.1002/(SICI)1099-1484(199801)3:1<1::AID-CFM38>3.0.CO;2-7.
18. Jaeger HM, Nagel SR, Behringer RP. Granular solids, liquids, and gases. *Reviews of Modern Physics* 1996; **68**:1259-1273, DOI: 10.1103/RevModPhys.68.1259.
19. Rothenburg L. Micromechanics of idealized granular systems. *PhD Thesis*, Faculty of Engineering, Carleton University, 1980.
20. Bathurst RJ, Rothenburg L. Observations on stress-force-fabric relationships in idealized granular materials. *Mechanics of Materials* 1990; **9**:65-80, DOI: 10.1016/0167-6636(90)90030-J.
21. Rothenburg L, Bathurst RJ. Micromechanical features of granular assemblies with planar elliptical particles. *Géotechnique* 1992; **42**:79-95, DOI: 10.1680/geot.1992.42.1.79.
22. Kruyt NP, Rothenburg L. Statistical theories for the elastic moduli of two-dimensional assemblies of granular materials. *International Journal of Engineering Science* 1998; **36**:1127-1142, DOI: 10.1016/S0020-7225(98)00003-2.

23. Ball RC, Grinev DV. The stress transmission universality classes of periodic granular arrays. *Physica A* 2001; **292**:167-174, DOI: 10.1016/S0378-4371(00)00580-X.
24. Edwards SF, Grinev DV. The missing stress-geometry equation in granular media. *Physica A* 2001; **294**:57-66, DOI: 10.1016/S0378-4371(01)00102-9.
25. Edwards SF, Grinev DV. Transmission of stress in granular materials as a problem of statistical mechanics. *Physica A* 2001; **302**:162-186, DOI: 10.1016/S0378-4371(01)00462-9.
26. Ouadfel H, Rothenburg L. 'Stress-force-fabric' relationship for assemblies of ellipsoids. *Mechanics of Materials* 2001; **33**:201-221, DOI: 10.1016/S0167-6636(00)00057-0.
27. Kruyt NP, Rothenburg L. Kinematic and static assumptions for homogenization in micromechanics of granular materials. *Mechanics of Material* 2004; **36**:1157-1173, DOI: 10.1016/j.mechmat.2002.12.001.
28. Ballard P, Cambou B, Danescu A, Jean M, Lanier J, Moreau J-J, Radjaï F. *Micromechanics of Granular Materials*. Cambou B, Jean M, Radjaï F (Eds.). ISTE Ltd. and John Wiley & Sons: London, 2009.
29. Rycroft CH. Multiscale Modeling in Granular Flow. *PhD Thesis*, Department of Mathematics, Massachusetts Institute of Technology, 2007.
30. Li X, Yu H-S. On the stress-force-fabric relationship for granular materials. *International Journal of Solids and Structures* 2013; **50**:1285-1302, DOI: 10.1016/j.ijsolstr.2012.12.023.
31. DeGiuli E. Continuum Limits of Granular Systems. *PhD Thesis*, Department of Mathematics, University of British Columbia, 2013.
32. Reynolds O. On the dilatancy of media composed of rigid particles in contact, with experimental illustrations. *Philosophical Magazine, Series 5* 1885; **20**:469-481, DOI: 10.1080/14786448508627791.
33. Rowe PW. The Stress-Dilatancy Relation for Static Equilibrium of an Assembly of Particles in Contact. *Proceedings of the Royal Society of London. Series A, Mathematical and Physical Sciences* 1962; **269**:500-527.
34. Matsuoka H. Dilatancy characteristics of soil. *Soils and Foundations* 1974; **14**:13-24.
35. Wan RG, Guo PJ. A Simple Constitutive Model for Granular Soils: Modified Stress-Dilatancy Approach. *Computers and Geotechnics* 1998; **22**:109-133, DOI: 10.1016/S0266-352X(98)00004-4.
36. Wan RG, Guo PJ. Effect of microstructure on undrained behaviour of sands. *Canadian Geotechnical Journal* 2001; **38**:16-28, DOI: 10.1139/cgj-38-1-16.
37. Wan RG, Guo PJ. Stress Dilatancy and Fabric Dependencies on Sand Behavior. *Journal of Engineering Mechanics* 2004; **130**:635-645, DOI: 10.1061/(ASCE)0733-9399(2004)130:6(635).
38. Wan R, Guo P, Al-Mamun M. Behaviour of granular materials in relation to their fabric dependencies. *Soils and Foundations* 2005; **45**:77-86.
39. Wan R, Guo P. Microstructural formulation of stress dilatancy. *Comptes Rendus Mecanique* 2014; **342**:198-207, DOI: 10.1016/j.crme.2014.01.005.
40. Cosserat E, Cosserat F. *Théorie des Corps déformables*. Hermann et Fils : Paris, 1909.
41. Goodman MA, Cowin SC. A Continuum Theory for Granular Materials. *Archive for Rational Mechanics and Analysis* 1972; **44**:249-266, DOI: 10.1007/BF00284326.
42. Drescher A, de Josselin de Jong G. Photoelastic verification of a mechanical model for the flow of a granular material. *Journal of the Mechanics and Physics of Solids* 1972; **20**:337-351, DOI: 10.1016/0022-5096(72)90029-4.
43. Ammi M, Bideau D, Troadec JP. Geometrical structure of disordered packings of regular polygons; comparison with disc packings structures. *Journal of Physics D: Applied Physics* 1987; **20**:424-428, DOI: 10.1088/0022-3727/20/4/005.

44. Chang SC, Ma L. A micromechanical-based micropolar theory for deformation of granular solids. *International Journal of Solids and Structures* 1991; **28**:67-86, DOI: 10.1016/0020-7683(91)90048-K.
45. de Borst R. A generilisation of J_2-flow theory for polar continua. *Computer Methods in Applied Mechanics and Engineering* 1993; **103**:347-362, DOI: 10.1016/0045-7825(93)90127-J.
46. Steinmann P. A micropolar theory of finite deformation and finite rotation multiplicative elastoplasticity. *International Journal of Solids and Structures* 1994; **31**:1063-1084, DOI: 10.1016/0020-7683(94)90164-3.
47. Günther W. Zur Statik und Kinematik des Cosseratschen Kontinuums. *Abh. Braunschweig. Wiss. Ges.* 1958; **10**:195-213.
48. Koiter WT. Couple-stresses in the theory of elasticity, I and II. *Proceedings of the Royal Netherlands Academy of Sciences* 1964; **B67**:17-44.
49. Mindlin RD. Microstructure in linear elasticity. *Archive for Rational Mechanics and Analysis* 1964; **16**:51-78, DOI: 10.1007/BF00248490.
50. Toupin RA. Theories of elasticity with couple-stresses. *Archive for Rational Mechanics and Analysis* 1964; **17**:85-112, DOI: 10.1007/BF00253050.
51. Neuber H. Über Probleme der Spannungskonzentration im Cosseratkörper. *Acta Mechanica* 1966; **2**:48-69, DOI: 10.1007/BF01176729.
52. Schaefer H. Das Cosserat-Kontinuum. *Zeitschrift für Angewandte Mathematik und Mechanik* 1967; **47**:485-498, DOI: 10.1002/zamm.19670470802.
53. Eringen AC. Theory of micropolar elasticity. In *Fracture, An Advanced Treatise*. Liebowitz H (Ed.). Academic Press: New York, 1968.
54. Lippmann H. Eine Cosserat-Theorie des plastischen Fließens. *Acta Mechanica* 1969; **8**:255-284, DOI: 10.1007/BF01182264.
55. Besdo D. Ein Beitrag zur nichtlinearen Theorie des Cosserat-Kontinuums. *Acta Mechanica* 1974; **20**:105-131, DOI: 10.1007/BF01374965.
56. Reissner E. A further note on finite-strain force and moment stress elasticity. *Zeitschrift für Angewandte Mathematik und Mechanik* 1987; **38**:665-673, DOI: 10.1007/BF00948288.
57. Mühlhaus HB, Vardoulakis I. The thickness of shear bands in granular materials. *Géotechnique* 1987; **37**:278-283, DOI: 10.1680/geot.1987.37.3.271.
58. Mühlhaus HB. Application of Cosserat theory in numerical solutions of limit load problems. *Ingenieur-Archiv* 1989; **59**:124-137, DOI: 10.1007/BF00538366.
59. de Borst R. Simulation of strain localization: a reappraisal of the Cosserat continuum. *Engineering Computations* 1991; **8**:317-332, DOI: 10.1108/eb023842.
60. de Borst R. A generalization of J_2-flow theory for polar continua. *Computer Methods in Applied Mechanics and Engineering* 1993; **103**:347-362, DOI: 10.1016/0045-7825(93)90127-J.
61. de Borst R, Mühlhaus HB. Finite deformation analysis of inelastic materials with micro-structure. In *Proceedings of the IUTAM Symposium on Finite Inelastic Deformations, Hannover*. Besdo D, Stein E (Eds.). Springer: Berlin, 1992.
62. Steinmann P, Willam K. Localization within the framework of micropolar elasto-plasticity. In *Advances in Continuum Mechanics*. Brüller O, Mannl V, Najar J (Eds.). Springer: Berlin, 1991.
63. Dietsche A, Steinmann P, Willam K. Micropolar elasto-plasticity and its role in localization analysis. *International Journal of Plasticity* 1993; **9**:813-831, DOI: 10.1016/0749-6419(93)90053-S.
64. Cambou B (Ed.). *Behaviour of Granular Materials*. Springer-Verlag: Wien, 1998.
65. Huntley JM. Force distribution in an inhomogeneous sandpile. *The European Physical Journal B* 1999; **8**:389-397, DOI: 10.1007/s100510050704.

66. Kolb E, Mazozi T, Clément E, Duran J. Force fluctuations in a vertically pushed granular column. *The European Physical Journal B* 1999; **8**:483-491, DOI: 10.1007/s100510050715.
67. Sterpi D. An analysis of geotechnical problems involving strain softening effects. *International Journal for Numerical and Analytical Methods in Geomechanics* 1999; **23**:1427-1454, DOI: 10.1002/(SICI)1096-9853(199911)23:13<1427::AID-NAG6>3.0.CO;2-B.
68. Rothenburg L, Kruyt NP. Critical state and evolutions of coordination number in simulated granular materials. *International Journal of Solids and Structures* 2004; **41**:5763-5774, DOI: 10.1016/j.ijsolstr.2004.06.001.
69. Hill JM, Selvadurai APS (Eds.). *Mathematics and Mechanics of Granular Materials*. Springer: Dordrecht, 2005. Reprinted from *Journal of Engineering Mathematics* 2005; **52**(1-3).
70. Cambou B, Jean M, Radjaï F (Eds.). *Micromechanics of Granular Materials*. Wiley: Hoboken, 2009.
71. Maugin GA, Metrikine AV (Eds.). *Mechanics of Generalized Continua: One Hundred Years After the Cosserats*. Springer: New York, 2010.
72. Miehe C, Dettmar J, Zäh D. Homogenization and two-scale simulations of granular materials for different microstructural constraints. *International Journal for Numerical Methods in Engineering* 2010; **83**:1206-1236, DOI: 10.1002/nme.2875.
73. Pietruszczak S, Guo P. Description of deformation process in inherently anisotropic granular materials. *International Journal for Numerical and Analytical Methods in Geomechanics* 2013; **37**:478-490, DOI: 10.1002/nag.1106.
74. Tordesillas A, Pucilowski S, Walker DM, Peters JF, Walizer LE. Micromechanics of vortices in granular media: connection to shear bands and implications for continuum modelling of failure in geomaterials. *International Journal for Numerical and Analytical Methods in Geomechanics* 2014; **38**:1247-1275, DOI: 10.1002/nag.2258.
75. Kang DH, Yun TS, Evans TM. Pore orientation of granular materials during biaxial compression. *Computers and Geotechnics* 2014; **59**:1-11, DOI: 10.1016/j.compgeo.2014.03.004.
76. Rudnicki JW, Rice JR. Conditions for the localization of deformation in pressure-sensitive dilatant materials. *Journal of the Mechanics and Physics of Solids* 1975; **23**:371-394, DOI: 10.1016/0022-5096(75)90001-0.
77. Vardoulakis I, Goldscheider M, Gudehus G. Formation of shear bands in sand bodies as a bifurcation problem. *International Journal for Numerical and Analytical Methods in Geomechanics* 1978; **2**:99-128, DOI: 10.1002/nag.1610020203.
78. Roscoe KH. The Influence of Strains in Soil Mechanics. *Géotechnique* 1970; **20**:129-170, DOI: 10.1680/geot.1970.20.2.129.
79. Vardoulakis I. Shear band inclination and shear modulus of sand in biaxial tests. *International Journal for Numerical and Analytical Methods in Geomechanics* 1980; **4**:103-113, DOI: 10.1002/nag.1610040202.
80. Mühlhaus HB, Vardoulakis I. The thickness of shear bands in granular materials. *Géotechnique* 1987; **37**:271-283, DOI: 10.1680/geot.1987.37.3.271.
81. Shuttle DA, Smith IM. Numerical simulation of shear band formation in soils. *International Journal for Numerical and Analytical Methods in Geomechanics* 1988; **12**:611-626, DOI: 10.1002/nag.1610120604.
82. Bardet JP. A comprehensive review of strain localization in elastoplastic soils. *Computers and Geotechnics* 1990; **10**:163-188, DOI: 10.1016/0266-352X(90)90034-S.
83. Vermeer PA. The orientation of shear bands in biaxial tests. *Géotechnique* 1990; **40**:223-236, DOI: 10.1680/geot.1990.40.2.223.

84. Lade PV. Instability, shear banding, and failure in granular materials. *International Journal of Solids and Structures* 2002; **39**:3337-3357, DOI: 10.1016/S0020-7683(02)00157-9.
85. Desrues J, Chambon R. Shear band analysis and shear moduli calibration. *International Journal of Solids and Structures* 2002; **39**:3757-3776, DOI: 10.1016/S0020-7683(02)00177-4.
86. Gajo A, Bigoni D, Muir Wood D. Multiple shear band development and related instabilities in granular materials. *Journal of the Mechanics and Physics of Solids* 2004; **52**:2683-2724, DOI: 10.1016/j.jmps.2004.05.010.
87. Tordesillas A, Peters JF, Gardiner BS. Shear band evolution and accumulated microstructural development in Cosserat media. *International Journal for Numerical and Analytical Methods in Geomechanics* 2004; **28**:981-1010, DOI: 10.1002/nag.343.
88. Gudehus G, Nübel K. Evolution of shear bands in sand. *Géotechnique* 2004; **54**:187-201, DOI: 10.1680/geot.2004.54.3.187.
89. Nübel K, Huang W. A study of localized deformation pattern in granular media. *Computer Methods in Applied Mechanics and Engineering* 2004; **193**:2714-2743, DOI: 10.1016/j.cma.2003.10.020.
90. Gajo A, Muir Wood D, Bigoni D. On certain critical material and testing characteristics affecting shear band development in sand. *Géotechnique* 2007; **57**:449-461, DOI: 10.1680/geot.2007.57.5.449.
91. Rechenmacher A, Abedi S, Chupin O. Evolution of force chains in shear bands in sands. *Géotechnique* 2010; **60**:343-351, DOI: 10.1680/geot.2010.60.5.343.
92. Tordesillas A, Shi J, Tshaikiwsky T. Stress-dilatancy and force chain evolution. *International Journal for Numerical and Analytical Methods in Geomechanics* 2010; **35**:264-292, DOI: 10.1002/nag.910.
93. Oda M, Kazama H, Konishi J. Effects of induced anisotropy on the development of shear bands in granular materials. *Mechanics of Materials* 1998; **28**:103-111, DOI: 10.1016/S0167-6636(97)00018-5.
94. Oda M, Kazama H. Microstructure of shear bands and its relation to the mechanisms of dilatancy and failure of dense granular soils. *Géotechnique* 1998; **48**:465-481, DOI: 10.1680/geot.1998.48.4.465.
95. Evans TM, Frost JD. Multiscale investigation of shear bands in sand: Physical and numerical experiments. *International Journal for Numerical and Analytical Methods in Geomechanics* 2010; **34**:1634-1650, DOI: 10.1002/nag.877.
96. Fu P, Dafalias YF. Fabric evolution within shear bands of granular materials and its relation to critical state theory. *International Journal for Numerical and Analytical Methods in Geomechanics* 2011; **35**:1918-1948, DOI: 10.1002/nag.988.
97. Mahmood Z, Iwashita K. A simulation study of microstructure evolution inside the shear band in biaxial compression test. *International Journal for Numerical and Analytical Methods in Geomechanics* 2011; **35**:652-667, DOI: 10.1002/nag.917.
98. Chupin O, Rechenmacher AL, Abedi S. Finite strain analysis of nonuniform deformation inside shear bands in sands. *International Journal for Numerical and Analytical Methods in Geomechanics* 2012; **36**:1651-1666, DOI: 10.1002/nag.1071.
99. Nguyen N-S, Magoariec H, Cambou B. Analysis of local behaviour in granular materials. *Comptes Rendus Mecanique* 2014; **342**:156-173, DOI: 10.1016/j.crme.2014.01.004.
100. Borja RI, Song X, Rechenmacher AL, Abedi S, Wu W. Shear band in sand with spatially varying density. *Journal of the Mechanics and Physics of Solids* 2013; **61**:219-234, DOI: 10.1016/j.jmps.2012.07.008.
101. Gu X, Huang M, Qian J. Discrete element modeling of shear band in granular materials. *Theoretical and Applied Fracture Mechanics* 2014; **72**:37-49, DOI: 10.1016/j.tafmec.2014.06.008.

102. Desrues J, Andò E. Strain localisation in granular media. *Comptes Rendus Physique* 2015; **16**:26-36, DOI: 10.1016/j.crhy.2015.01.001.
103. Guo P. Undrained shear band in water saturated granular media: A critical revisiting with numerical examples. *International Journal for Numerical and Analytical Methods in Geomechanics* 2013; **37**:353-373, DOI: 10.1002/nag.1101.
104. Guo P, Stolle DFE. Coupled analysis of bifurcation and shear band in saturated soils. *Soils and Foundations* 2013; **53**:525-539, DOI: 10.1016/j.sandf.2013.06.005.
105. Walker DM, Vo K, Tordesillas A. On reynolds' dilatancy and shear band evolution: A new perspective. *International Journal of Bifurcation and Chaos* 2013; **23**:1330034, DOI: 10.1142/S0218127413300346.
106. Chen T, Liu J, Jie Y, Zhang D. Numerical simulations of pattern evolution of shear bands during pure shear of geomaterials. *Tectonophysics* 2015; DOI: 10.1016/j.tecto.2015.04.005.
107. Faraday M. On a Peculiar Class of Acoustical Figures; and on Certain Forms Assumed by Groups of Particles upon Vibrating Elastic Surfaces. *Philosophical Transactions of the Royal Society of London* 1831; **121**:299-340, DOI: 10.1098/rstl.1831.0018.
108. Exadaktylos GE, Vardoulakis IG (Eds.). *Bifurcations, Instabilities, Degradation in Geomechanics*. Springer: Berlin, 2007.
109. Tejchman J. *Shear Localization in Granular Bodies with Micro-Polar Hypoplasticity*. Springer: Berlin, 2008.
110. Nicot F, Wan R. *Micromechanics of Failure in Granular Geomaterials*. Wiley-ISTE: London, 2009.
111. Bonelli S, Dascalu C, Nicot F (Eds.). *Advances in Bifurcation and Degradation in Geomaterials: Proceedings of the 9th International Workshop on Bifurcation and Degradation in Geomaterials*. Springer: New York, 2011.
112. Wan R, Alsaleh M, Labuz J. *Bifurcations, Instabilities and Degradations in Geomaterials*. Springer: Berlin, 2011.
113. Borja RI (Ed.). *Multiscale and Multiphysics Processes in Geomechanics*. Springer: Berlin, 2011.
114. Chau K-T, Zhao J (Eds.). *Bifurcation and Degradation of Geomaterials in the New Millenium: Proceedings of the 10th International Workshop on Bifurcation and Degradation in Geomaterials*. Springer: New York, 2015.
115. Zienkiewicz OC. Basic formulation of static and dynamic behaviours of soil and other porous media. *Applied Mathematics and Mechanics* 1982; **3**:457-468, DOI: 10.1007/BF01908222.
116. Helnwein P. Some remarks on the compressed matrix representation of symmetric second-order and fourth-order tensors. *Computer Methods in Applied Mechanics and Engineering* 2001; **190**:2753-2770, DOI: 10.1016/S0045-7825(00)00263-2.
117. Taylor DW. *Fundamentals of Soil Mechanics*. John Wiley & Sons: New York, 1948.
118. Timoshenko SP, Goodier JN. *Theory of Elasticity, Second Edition.* McGraw-Hill Publishing Company: Toronto, 1951.
119. Tonti E. A mathematical model for physical theories, I & II. *Accademia Nazionale dei Lincei* 1972; **52**:175–181, 350–356.
120. Dirichlet GL. Über die Reduction der positive quadratischen Formen mit drei unbestimmten ganzen Zahlen. *Journal für die reine und angewandte Mathematik* 1850; **40**:209-227.
121. Voronoi MG. Nouvelles applications des parametres continus a la theorie des formes quadratiques. *Journal für die reine und angewandte Mathematik* 1908; **134**:198-287.
122. Aurenhammer F. Voronoi Diagrams – A Survey of a Fundamental Geometric Data Structure. *ACM Computing Surveys* 1991; **23**:345-405, DOI: 10.1145/116873.116880.

123. Green PJ, Sibson R. Computing Dirichlet tessellations in the plane. *The Computer Journal* 1978; **21**:168-173, DOI: 10.1093/comjnl/21.2.168.
124. Ghosh S, Mukhopadhyay SN. A two-dimensional automatic mesh generator for finite element analysis for random composites. *Computers & Structures* 1991; **41**:245-256, DOI: 10.1016/0045-7949(91)90428-O.
125. Rycroft CH. VORO++: A three-dimensional Voronoi cell library in C++. *Chaos* 2009; **19**:041111, DOI: 10.1063/1.3215722.
126. Washizu K. *Variational Methods in Elasticity and Plasticity*. Pergamon Press: New York, 1968.
127. Clough RW. Original formulation of the finite element method. *Finite Elements in Analysis and Design* 1990; **7**:89-101, DOI: 10.1016/0168-874X(90)90001-U.
128. Clough RW. Early history of the finite element method from the view point of a pioneer. *International Journal for Numerical Methods in Engineering* 2004; **60**:283-287, DOI: 10.1002/nme.962.
129. Melosh RJ. Finite element analysis convergence curves. *Finite Elements in Analysis and Design* 1990; **7**:115-121, DOI: 10.1016/0168-874X(90)90003-W.
130. Oden JT. The best FEM. *Finite Elements in Analysis and Design* 1990; **7**:103-114, DOI: 10.1016/0168-874X(90)90002-V.
131. Bathe K-J. *Finite Element Procedures*. Prentice Hall: Englewood Cliffs, NJ, 1996.
132. Cook RD, Malkus DS, Plesha ME, Witt RJ. *Concepts and Applications of Finite Element Analysis, Fourth Edition*. Wiley: New York, 2001.
133. Strang G, Fix G. *An Analysis of the Finite Element Method, Second Edition*. Wellesley-Cambridge Press: Wellesley, MA, 2008.
134. Zienkiewicz OC, Taylor RL, Zhu JZ. *Finite Element Method - Its Basis and Fundamentals, Sixth Edition*. Elsevier: New York, 2005.
135. Belikov VV, Ivanov VD, Kontorovich VK, Korytnik SA, Semenov AY. The non-Sibsonian interpolation: A new method of interpolation of the values of a function on an arbitrary set of points. *Computational Mathematics and Mathematical Physics* 1997; **37**:9-15.
136. Hiyoshi H, Sugihara K. Two generalizations of an interpolant based on Voronoi diagrams. *International Journal of Shape Modeling* 1999; **5**:219-231, DOI: 10.1142/S0218654399000186.
137. Wachspress EL. *A Rational Finite Element Basis*. Academic Press: New York, NY, 1975.
138. Pinkall U, Polthier K. Computing discrete minimal surfaces and their conjugates. *Experimental Mathematics* 1993; **2**:15-36.
139. Malsch EA, Lin JJ, Dasgupta, G. Smooth two dimensional interpolations: a recipe for all polygons. *Journal of Graphics, GPU, and Game Tools* 2005; **10**:27-39, DOI: 10.1080/2151237X.2005.10129192.
140. Sukumar N, Tabarraei A. Conforming polygonal finite elements. *International Journal for Numerical Methods in Engineering* 2004; **61** : 2045–2066, DOI: 10.1002/nme.1141.
141. Sukumar N. Construction of polygonal interpolants: a maximum entropy approach. *International Journal for Numerical Methods in Engineering* 2004; **61**:2159-2181, DOI: 10.1002/nme.1193.
142. Sukumar N, Malsch EA. Recent Advances in the Construction of Polygonal Finite Element Interpolants. *Archives of Computational Methods in Engineering* 2006; **13** : 129–163, DOI: 10.1007/BF02905933.
143. Sukumar N, Bolander JE. Voronoi-based Interpolants for Fracture Modelling. *Tessellations in the Sciences: Virtues, Techniques and Applications of Geometric Tilings*, van de Weijgaert R et al., eds., Springer-Verlag, 2009.

144. Sukumar N, Bolander JE. Numerical Computation of Discrete Differential Operators on Non-Uniform Grids. *Computer Modeling in Engineering & Sciences* 2003; **4**:691-706, DOI: 10.3970/cmes.2003.004.691.
145. Chapra SC, Canale RP. *Numerical Methods for Engineers, Sixth Edition*. McGraw-Hill Higher Education: New York, 2010.
146. Atluri SN, Gallagher RH, Zienkiewicz OC (Eds.). *Hybrid and Mixed Finite Element Methods*. John Wiley & Sons: New York, 1983.
147. Brezzi F, Fortin M. *Mixed and Hybrid Finite Element Methods*. Springer-Verlag: New York, 1991.
148. Pian THH, Wu W-C. *Hybrid and Incompatible Finite Element Methods*. Chapman & Hall/CRC: New York, 2006.
149. Pian THH. Derivation of element stiffness matrices by assumed stress distributions. *AIAA Journal* 1964; **2** : 1333–1336, DOI: 10.2514/3.2546.
150. Tong P, Pian THH. A variational principle and the convergence of a finite element method based on assumed stress distribution. *International Journal of Solids and Structures* 1969; **5**:463–472, DOI: 10.1016/0020-7683(69)90036-5.
151. Pian THH, Tong P. Basis of finite element methods for solid continua. *International Journal for Numerical Methods in Engineering* 1969; **1**:3-28, DOI: 10.1002/nme.1620010103.
152. Ghosh S, Mukhopadhyay SN. A material based finite element analysis of heterogeneous media involving Dirichlet tessellations. *Computer Methods in Applied Mechanics and Engineering* 1993; **104** : 211–247, DOI: 10.1016/0045-7825(93)90198-7.
153. Ghosh S, Mallett RL. Voronoi cell finite elements. *Computers & Structures* 1994; **50**:33-46, DOI: 10.1016/0045-7949(94)90435-9.
154. Ghosh S, Lee K, Moorthy S. Multiple scale analysis of heterogeneous elastic structures using homogenization theory and Voronoi cell finite element method. *International Journal of Solids and Structures* 1995; **32** : 27-62, DOI: 10.1016/0020-7683(94)00097-G.
155. Ghosh S, Moorthy S. Elastic-plastic analysis of arbitrary heterogeneous materials with the Voronoi Cell finite element method. *Computer Methods in Applied Mechanics and Engineering* 1995; **121**:373-409, DOI: 10.1016/0045-7825(94)00687-I.
156. Ghosh S, Moorthy S. Three dimensional Voronoi cell finite element model for microstructures with ellipsoidal heterogeneities. *Computational Mechanics* 2004; **34**:510–531, DOI: 10.1007/s00466-004-0598-5.
157. Ghosh S. *Micromechanical Analysis and Multi-Scale Modeling using the Voronoi Cell Finite Element Method*. CRC Press: New York, 2011.
158. Hu C, Ghosh S. Locally enhanced Voronoi cell finite element model (LE-VCFEM) for simulating evolving fracture in ductile microstructures containing inclusions. *International Journal for Numerical Methods in Engineering* 2008; **76**:1955-1992, DOI: 10.1002/nme.2400.
159. Goodman RE, Taylor R, Brekke T. A model for the mechanics of jointed rock. *Journal of the Soil Mechanics and Foundations Division, ASCE* 1968; **94** : 637-659.
160. Zienkiewicz OC, Best B, Dullage C, Stagg KG. Analysis of nonlinear problems in rock mechanics with particular reference to jointed rock systems. *Proceedings of the 2nd International Conference of the Society of Rock Mechanics*, Belgrade 1970; **3** : 501-509.
161. Katona MG. A simple contact-friction interface element with applications to buried culvert, in Desai CS and Saxena SK (Eds.). *Proceedings of the Symposium on Implementation of Computer Procedures and Stress-Strain Laws in Geotechnical Engineering*, Chicago IL 1981; **1**:45-63.
162. Herrmann LR. Finite element analysis of contact problems. *Journal of the Engineering Mechanics Division, ASCE* 1978; **104** : 1043-1057.

163. Desai CS, Zaman MM, Lightner JG, Siriwardane HJ. Thin-layer element for interfaces and joints. *International Journal for Numerical and Analytical Methods in Geomechanics* 1984; **8** : 19-43, DOI: 10.1002/nag.1610080103.
164. Wang X, Chan D, Morgenstern N. Numerical modelling of shear bands by element bands. *International Journal for Numerical Methods in Engineering* 2002; **54**:1131-1159, DOI: 10.1002/nme.464.
165. Selvadurai APS, Yu Q. Mechanics of a discontinuity in a geomaterial. *Computers and Geotechnics* 2005; **32**:92-106, DOI: 10.1016/j.compgeo.2004.11.007.
166. Pietruszczak S, Mróz Z. Finite element analysis of deformation of strain-softening materials. *International Journal for Numerical Methods in Engineering* 1981; **17**:327-334, DOI: 10.1002/nme.1620170303.
167. Belytschko T, Fish J, Engelmann BE. A finite element with embedded localization zones. *Computer Methods in Applied Mechanics and Engineering* 1988; **70**:59-89, DOI: 10.1016/0045-7825(88)90180-6.
168. Wan RG, Chan DH, Morgenstern NR. A finite element method for the analysis of shear bands in geomaterials. *Finite Elements in Analysis and Design* 1990; **7**:129-143, DOI: 10.1016/0168-874X(90)90005-Y.
169. Pietruszczak S, Niu X. On the description of localized deformation. *International Journal for Numerical and Analytical Methods in Geomechanics* 1993; **17**:791-805, DOI: 10.1002/nag.1610171104.
170. Larsson R, Steinmann P, Runesson K. Finite element embedded localization band for finite strain plasticity based on a regularized strong discontinuity. *Mechanics of Cohesive-Frictional Materials* 1998; **4**:171-194, DOI: 10.1002/(SICI)1099-1484(199903)4:2<171::AID-CFM81>3.0.CO;2-X.
171. Chen J-S, Wu C-T, Belytschko T. Regularization of material instabilities by meshfree approximations with intrinsic length scales. *International Journal for Numerical Methods in Engineering* 2000; **47**:1303-1322, DOI: 10.1002/(SICI)1097-0207(20000310)47:7<1303::AID-NME826>3.0.CO;2-5.
172. Wang X, Chan D, Morgenstern N. Kinematic modelling of shear band localization using discrete finite elements. *International Journal for Numerical and Analytical Methods in Geomechanics* 2003; **27**:289-324, DOI: 10.1002/nag.274.
173. Samaniego E, Belytschko T. Continuum–discontinuum modelling of shear bands. *International Journal for Numerical Methods in Engineering* 2000; **62**:1857-1872, DOI: 10.1002/nme.1256.
174. Cundall PA. A computer model for simulating progressive, large scale movements in blocky rock systems. *Proceedings of the Symposium of the International Society of Rock Mechanics, Nancy, France*, 1971.
175. Cundall PA, Strack ODL. A discrete numerical model for granular assemblies. *Géotechnique* 1979; **29**:47-65, DOI: 10.1680/geot.1979.29.1.47.
176. Cundall PA. Formulation of a three-dimensional distinct element model – Part I. A scheme to detect and represent contacts in a system composed of many polyhedral blocks. *International Journal of Rock Mechanics and Mining Sciences & Geosciences Abstracts* 1988; **25** : 107-116, DOI: 10.1016/0148-9062(88)92293-0.
177. Hart R, Cundall PA, Lemos J. Formulation of a three-dimensional distinct element model – Part II. Mechanical calculations for motion and interaction of a system composed of many polyhedral blocks. *International Journal of Rock Mechanics and Mining Sciences & Geosciences Abstracts* 1988; **25** : 117-125, DOI: 10.1016/0148-9062(88)92294-2.
178. Ting JM, Khwaja M, Meachum LR, Rowell JD. An ellipse-based discrete element model for granular materials. *International Journal for Numerical and Analytical Methods in Geomechanics* 1993; **17**:603-623, DOI: 10.1002/nag.1610170902.

179. Ng T-T. Numerical simulations of granular soil using elliptical particles. *Computers and Geotechnics* 1994; **16**:153-169, DOI: 10.1016/0266-352X(94)90019-1.
180. Lin X, Ng T-T. A three-dimensional discrete element model using arrays of ellipsoids. *Géotechnique* 1997; **47**:319-329, DOI: 10.1680/geot.1997.47.2.319.
181. Barbosa RE, Ghaboussi J. Discrete finite element method for multiple deformable bodies. *Finite Elements in Analysis and Design* 1990; **7**:145-158, DOI: 10.1016/0168-874X(90)90006-Z.
182. Boon CW. Distinct Element Modelling of Jointed Rock Masses: Algorithms and Their Verification. *PhD Thesis*, St. Cross College, University of Oxford, 2013.
183. Radjaï F, Dubois F (Eds.) *Discrete-element Modeling of Granular Materials*. Wiley: Oxford, 2011.
184. Bardenhagen SG, Brackbill JU, Sulsky D. The material-point method for granular material. *Computer Methods in Applied Mechanics and Engineering* 2000; **187** : 529-541, DOI: 10.1016/S0045-7825(99)00338-2.
185. Bardenhagen SG, Guilkey JE, Roessig KM, Brackbill JU, Witzel WM, Foster JC. An Improved Contact Algorithm for the Material Point Method and Application to Stress Propagation in Granular Material. *Computer Modeling in Science & Engineering* 2001; **2** : 509-522, DOI: 10.3970/cmes.2001.002.509.
186. Jassim I, Stolle D, Vermeer P. Two-phase dynamic analysis by material point method. *International Journal for Numerical and Analytical Methods in Geomechanics* 2013; **37** : 2502-2522, DOI: 10.1002/nag.2146.
187. Munjiza A, Owen DRJ, Bicanic N. Combined finite-discrete element method in transient dynamics of fracturing solids. *Engineering Computations* 1995; **12**:145-174, DOI: 10.1108/02644409510799532.
188. Munjiza A. *The Combined Finite-Discrete Element Method*. Wiley: London, 2004.
189. Mahabadi OK, Lisjak A, Munjiza A, Grasselli G. Y-Geo: New Combined Finite-Discrete Element Numerical Code for Geomechanical Applications. *International Journal of Geomechanics* 2012; **12** : 676-688, DOI: 10.1061/(ASCE)GM.1943-5622.0000216.
190. Aalto J. Finite element seepage flow nets. *International Journal for Numerical and Analytical Methods in Geomechanics* 1984; **8**:297–303, DOI: 10.1002/nag.1610080307.
191. Tracy FT, Radhakrishnan N. Automatic Generation of Seepage Flow Nets by Finite Element Method. *Journal of Computing in Civil Engineering* 1989; **3**:268–284, DOI: 10.1061/(ASCE)0887-3801(1989)3:3(268).
192. Bardet J-P, Tobita T. A practical method for solving free-surface seepage problems. *Computers and Geotechnics* 2002; **29**:451–475, DOI: 10.1016/S0266-352X(02)00003-4.
193. Zienkiewicz OC, Mayer P, Cheung YK. Solution of Anisotropic Seepage by Finite Elements. *Journal of the Engineering Mechanics Division, ASCE* 1966; **92**:111–120.
194. Bathe K-J, Khoshgoftaar MR. Finite element free surface seepage analysis without mesh iteration. *International Journal for Numerical and Analytical Methods in Geomechanics* 1979; **3**:13–22, DOI: 10.1002/nag.1610030103.
195. Nath B. A novel finite element method for seepage analysis. *International Journal for Numerical and Analytical Methods in Geomechanics* 1981; **5**:139–163, DOI: 10.1002/nag.1610050204.
196. Elsworth D. A boundary element-finite element procedure for porous and fractured media flow. *Water Resources Research* 1987; **23**:551–560, DOI: 10.1029/WR023i004p00551.
197. Lemon AM. A Hybrid Method for Automatic Flow Net Generation. *MS Thesis*, Department of Civil and Environmental Engineering, Brigham Young University, 2000.
198. Jones NL, Lemon AM, Tracy FT. A hybrid approach to flow net generation. *International Journal for Numerical and Analytical Methods in Geomechanics* 2001; **25**:1339–1349, DOI: 10.1002/nag.183.

199. Casagrande A. Seepage Through Dams. *Journal of the New England Water Works Association* 1937; **51**:131-172. Reprinted in *Contributions to Soil Mechanics 1925-1940*, Boston Society of Civil Engineers: Boston, 1940, pp. 295-336.
200. France PW, Parekh CJ, Peters JC, Taylor C. Numerical analysis of free surface seepage problems. *Journal of the Irrigation and Drainage Division, ASCE* 1971; **97**:165-179.
201. Borja RI, Kishnani SS. On the solution of elliptic free-boundary problems via Newton's method. *Computer Methods in Applied Mechanics and Engineering* 1991; **88**:341-361, DOI: 10.1016/0045-7825(91)90094-M.
202. Bresciani E, Davy P, de Dreuzy JR. A finite volume approach with local adaptation scheme for the simulation of free surface flow in porous media. *International Journal for Numerical and Analytical Methods in Geomechanics* 2012; **36**:1574-1591, DOI: 10.1002/nag.1065.
203. Jie YX, Liu Y. Simulated annealing based algorithm for node generation in seepage analysis with meshless method. *Mechanics Research Communications* 2012; **43**:96-100, DOI: 10.1016/j.mechrescom.2012.03.007.
204. Lacy SJ, Prevost JH. Flow through porous media: A procedure for locating the free surface. *International Journal for Numerical and Analytical Methods in Geomechanics* 1987; **11**:585-601, DOI: 10.1002/nag.1610110605.
205. López-Querol S, Navas P, Peco J, Arias-Trujillo J. Changing impermeability boundary conditions to obtain free surfaces in unconfined seepage problems. *Canadian Geotechnical Journal* 2011; **48** : 841-845, DOI: 10.1139/t10-102.
206. Felippa CA. Parametrized multifield variational principles in elasticity: II. Hybrid functionals and the free formulation. *Communications in Applied Numerical Methods* 1989; **5**:89–98, DOI: 10.1002/cnm.1630050205.
207. Felippa CA. A survey of parametrized variational principles and applications to computational mechanics. *Computer Methods in Applied Mechanics and Engineering* 1994; **113**:109–139, DOI: 10.1016/0045-7825(94)90214-3.
208. Mikhlin SG. *The numerical performance of variational methods*. Wolters-Noordhoff Publishing: Groningen, 1971.
209. Peng JP, Salon SJ. Hybrid finite element boundary element solutions using half-space Green's functions. *Journal of Applied Physics* 1984; **55**:2198–2200, DOI: 10.1063/1.333609.
210. Onuki T. Hybrid finite element and boundary element method applied to electromagnetic problems. *IEEE Transactions on Magnetics* 1990; **26**:582–587, DOI: 10.1109/20.106384.
211. Pian THH, Sze K-Y. Hybrid stress finite element methods for plate and shell structures. *Advances in Structural Engineering* 2001; **4**:13–18, DOI: 10.1260/1369433011502309.
212. Ying W, Henriquez CS. Hybrid Finite Element Method for Describing the Electrical Response of Biological Cells to Applied Fields. *IEEE Transactions on Biomedical Engineering* 2007; **54**:611–620, DOI: 10.1109/TBME.2006.889172.
213. Harder C, Paredes D, Valentin F. A family of Multiscale Hybrid-Mixed finite element methods for the Darcy equation with rough coefficients. *Journal of Computational Physics* 2013; **245** : 107–130, DOI: 10.1016/j.jcp.2013.03.019.
214. Rubinstein R, Punch EF, Atluri SN. An analysis of, and remedies for, kinematic modes in hybrid-stress finite elements: Selection of stable, invariant stress fields. *Computer Methods in Applied Mechanics and Engineering* 1983; **38** : 63–92, DOI: 10.1016/0045-7825(83)90030-0.
215. Fraeijs de Veubeke B. Displacement and equilibrium models in the finite element method, Chapter 9 in *Stress Analysis*. Zienkiewicz OC and Holister GS (eds.). John Wiley & Sons: New York, 1965, pp. 145-197.
216. Dow JO. *A Unified Approach to the Finite Element Method and Error Analysis Procedures*. Elsevier: New York, 1999.

217. Mousavi SE, Sukumar N. Numerical integration of polynomials and discontinuous functions on irregular convex polygons and polyhedrons. *Computational Mechanics* 2010; **47** : 535–554, DOI: 10.1007/s00466-010-0562-5.
218. Borja RI. Composite Newton-PCG and quasi-Newton iterations for nonlinear consolidation. *Computer Methods in Applied Mechanics and Engineering* 1991; **86** : 27-60, DOI: 10.1016/0045-7825(91)90137-U.
219. MATLAB 8.2, The MathWorks Inc., Natick, MA, 2013.
220. Herbert R. Time variant ground water flow by resistance network analogues. *Journal of Hydrology* 1968; **6** : 237-264, DOI: 10.1016/0022-1694(68)90102-9.
221. Lambe TW, Whitman RV. *Soil Mechanics*. Wiley: New York, 1969.
222. Bazyar MH, Graili A. A practical and efficient numerical scheme for the analysis of steady state unconfined seepage flows. *International Journal for Numerical and Analytical Methods in Geomechanics* 2012; **36** : 1793-1812, DOI: 10.1002/nag.1075.
223. Williamson RL. Parametric studies of dynamic powder consolidation using a particle-level numerical model. *Journal of Applied Physics* 1990; **68**:1287-1296, DOI: 10.1063/1.346730.
224. Borg JP, Vogler TJ. Aspects of simulating the dynamic compaction of a granular ceramic. *Modelling and Simulation in Materials Science and Engineering* 2009; **17**:1-22, DOI: 10.1088/0965-0393/17/4/045003.
225. Vu-Quoc L, Zhang X, Walton OR. A 3-D discrete-element method for dry granular flows of ellipsoidal particles. *Computer Methods in Applied Mechanics and Engineering* 2000; **187**:483-528, DOI: 10.1016/S0045-7825(99)00337-0.
226. Stolle D, Guo P. Limit equilibrium slope stability analysis using rigid finite elements. *Canadian Geotechnical Journal* 2008; **45**:653-663, DOI: 10.1139/t08-010.
227. De Borst R, Vermeer PA. Possibilities and limitations of finite elements for limit analysis. *Géotechnique* 1984; **34** : 199-210, DOI: 10.1680/geot.1984.34.2.199.
228. Simo JC, Taylor RL. A return mapping algorithm for plane stress elastoplasticity. *International Journal for Numerical Methods in Engineering* 1986; **22** : 649-670, DOI: 10.1002/nme.1620220310.
229. Liu Y, Stolle D, Guo P, Emery J. Stress-path dependency of resilient behaviour of granular materials. *International Journal of Pavement Engineering* 2014; **15**:614-622, DOI: 10.1080/10298436.2013.808340.
230. Jeremic B, Yang Z, Sture S. Numerical Assessment of the Influence of End Conditions on Constitutive Behavior of Geomaterials. *Journal of Engineering Mechanics* 2004; **130**:741-745, DOI: 10.1061/(ASCE)0733-9399(2004)130:6(741).
231. Silbert LE, Liu AJ, Nagel SR. Normal modes in model jammed systems in three dimensions. *Physical Review E* 2009; **79** : 021308-1-021308-7, DOI: 10.1103/PhysRevE.79.021308.
232. Mehta A (Ed.). *Granular Matter: An Interdisciplinary Approach*. Springer-Verlag: New York, 1994.
233. Karchewski B, Guo P, Stolle D. Simulation of lab scale tests on granular media using assumed stress polygonal finite elements and nonlinear joint elements. *Proceedings of the 67th Canadian Geotechnical Conference, Regina, SK*, 2014.
234. Karchewski B, Stolle D, Guo P. Prediction of subsurface load distribution due to soil self-weight using Monte Carlo and VCFEM-DEM analysis. Presented at *Engineering Mechanics Institute Conference, ASCE, Hamilton, ON*, 2014.
235. Wood WL. Practical Time-stepping Schemes. Clarendon Press: Oxford, 1990.
236. Pietruszczak S. *Fundamentals of Plasticity in Geomechanics*. CRC Press: New York, 2010.
237. Schofield A, Wroth P. *Critical State Soil Mechanics*. McGraw Hill: Maidenhead, 1968.
238. Muir Wood D. *Soil Behaviour and Critical State Soil Mechanics*. Cambridge University Press: Cambridge, 1990.

239. Clough RW, Penzien J. *Dynamics of Structures, Third Edition*. Computers & Structures, Inc.: Berkeley, 2003.
240. Chopra AK. *Dynamics of Structures*. Prentice Hall: Englewood Cliffs, 1995.
241. Carmichael RS (Ed.). *Practical Handbook of Physical Properties of Rocks and Minerals*. CRC Press: Boca Raton, FL, 1989.
242. Hadda N, Nicot F, Wan R, Darve F. Microstructural self-organization in granular materials during failure. *Comptes Rendus Mecanique* 2015; **343**:143-154, DOI: 10.1016/j.crme.2014.09.009.
243. Laouafa F, Prunier F, Daouadji A, Al Gali H, Darve F. Stability in geomechanics, experimental and numerical analyses. *International Journal for Numerical and Analytical Methods in Geomechanics* 2011; **35**:112-139, DOI: 10.1002/nag.996.
244. Wan RG, Pinheiro M, Guo PJ. Elastoplastic modelling of diffuse instability response of geomaterials. *International Journal for Numerical and Analytical Methods in Geomechanics* 2011; **35**:140-160, DOI: 10.1002/nag.921.
245. Daouadji A, Darve F, Al Gali H, Hicher P-Y, Laouafa F, Lignon S, Nicot F, Nova R, Pinheiro M, Prunier F, Sibille L, Wan R. Diffuse failure in geomaterials: Experiments, theory and modelling. *International Journal for Numerical and Analytical Methods in Geomechanics* 2011; **35**:1731-1773, DOI: 10.1002/nag.975.
246. Wan R, Pinheiro M, Daouadji A, Jrad M, Darve F. Diffuse instabilities with transition to localization in loose granular materials. *International Journal for Numerical and Analytical Methods in Geomechanics* 2011; **37**:1292-1311, DOI: 10.1002/nag.2085.
247. Dantu P. Contribution a l'étude mécanique et géometrique des milieux pulverulents. *Proceedings of the 4th International Conference on Soil Mechanics and Foundation Engineering, London* 1957; 411-418.
248. Wakabayashi T. Photo elastic method for determination of stress in powder mass. *Proceedings of the 9th Japan National Congress for Applied Mechanics* 1959; 133-140.
249. Travers T, Ammi M, Bideau D, Gervois A, Messager JC, Troadec JP. Uniaxial Compression of 2D Packings of Cylinders. Effects of Weak Disorder. *Europhysics Letters* 1987; **4**:329-332, DOI: 10.1209/0295-5075/4/3/012.
250. Harr ME. *Mechanics of Particulate Media: A Probabalistic Approach*. McGraw-Hill: New York, 1977.
251. Biot MA. Mechanics of Deformation and Acoustic Propagation in Porous Media. *Journal of Applied Physics* 1962; **33**:1482-1498, DOI: 10.1063/1.1728759.
252. Green AE, Naghdi PM. On basic equations for mixtures. *Quarterly Journal of Mechanics & Applied Mathematics* 1969; **22**:427-438, DOI: 10.1093/qjmam/22.4.427.
253. Morland LW. A simple constitutive theory for a fluid-saturated porous solid. *Journal of Geophysical Research* 1972; **77**:890-900, DOI: 10.1029/JB077i005p00890.
254. Zienkiewicz OC, Chan AHC, Pastor M, Paul DK, Shiomi T. Static and dynamic behaviour of soils: a rational approach to quantitative solutions. I. Fully saturated problems. *Proceedings of the Royal Society of London* 1990; **A429**:285-309.
255. Zienkiewicz OC, Chan AHC, Pastor M, Paul DK, Shiomi T. Static and dynamic behaviour of soils: a rational approach to quantitative solutions. II. Semi-saturated problems. *Proceedings of the Royal Society of London* 1990; **A429**:311-321.
256. De Boer R. Highlights in the historical development of the porous media theory: Toward a consistent macroscopic theory. *Applied Mechanics Reviews* 1996; **49**:201-262, DOI: 10.1115/1.3101926.
257. Zienkiewicz OC, Chang CT, Bettess P. Drained, undrained, consolidating and dynamic behaviour assumptions in soils. *Géotechnique* 1980; **30**:385-395, DOI: 10.1680/geot.1980.30.4.385.

258. Zienkiewicz OC, Shiomi T. Dynamic behaviour of saturated porous media; The generalized Biot formulation and its numerical solution. *International Journal for Numerical and Analytical Methods in Geomechanics* 1984; **8**:71-96, DOI: 10.1002/nag.1610080106.
259. Karchewski B, Pekinasova A, Stolle D, Guo P. Investigation of a hybrid polygonal finite element formulation for confined and unconfined seepage. Submitted 01/2015 to *International Journal for Numerical and Analytical Methods in Geomechanics*.
260. Karchewski B, Guo P, Stolle D. Multi-scale analysis of deformation modes in granular material using a dynamic hybrid polygonal finite element-discrete element formulation. Submitted 07/2015 to the *4th GeoChina International Conference, July 25-27, Shandong, China*.
261. Le TMH, Gallipoli D, Sanchez M, Wheeler SJ. Stochastic analysis of unsaturated seepage through randomly heterogeneous earth embankments. *International Journal for Numerical and Analytical Methods in Geomechanics* 2012; **36**:1057-1076, DOI: 10.1002/nag.1047.
262. Lyness JN, Monegato G. Quadrature rules for regions having regular hexagonal symmetry. *SIAM Journal on Numerical Analysis* 1977; **14**:283-295, DOI: 10.1137/0714018.
263. Lasserre JB. Integration on a convex polytope. *Proceedings of the American Mathematical Society* 1998; **126**:2433-2441, DOI: 10.1090/S0002-9939-98-04454-2.
264. Lasserre JB. Integration and homogeneous functions. *Proceedings of the American Mathematical Society* 1999; **127**:813-818, DOI: 10.1090/S0002-9939-99-04930-8.